

DESIGN, CHARACTERIZATION, VISUALIZATION AND NAVIGATION OF
SWIMMING MICRO ROBOTS IN CHANNELS

by
FATMA ZEYNEP TEMEL

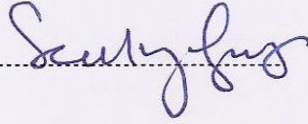
Submitted to the Graduate School of Sabanci University
in partial fulfillment of the requirements for the degree of
Doctor of Philosophy

SABANCI UNIVERSITY
AUGUST 2013

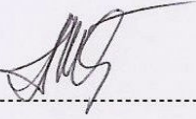
DESIGN, CHARACTERIZATION, VISUALIZATION AND NAVIGATION OF
SWIMMING MICRO ROBOTS IN CHANNELS

APPROVED BY:

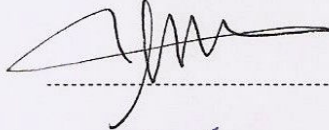
SERHAT YEŞİLYURT
(Dissertation Supervisor)



ASIF ŞABANOVIÇ



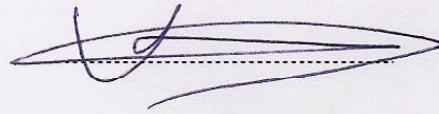
İBRAHİM TEKİN



ALİ KOŞAR



ATA MUĞAN



DATE OF APPROVAL :



© Fatma Zeynep Temel 2013
All Rights Reserved

...to my most beloved family...

DESIGN, CHARACTERIZATION, VISUALIZATION AND NAVIGATION OF SWIMMING MICRO ROBOTS IN CHANNELS

Fatma Zeynep TEMEL
Mechatronics Engineering, PhD. Thesis, 2013
Thesis Supervisor: Assoc. Prof. Serhat YEŞİLYURT

Keywords: Swimming Micro Robots in Channels, Bio-Inspired Medical Robotics, Magnetic Actuation and Navigation, Low Reynolds Number Swimming, Hydrodynamic Interactions, Computational Fluid Dynamics (CFD), Micro-Particle Image Velocimetry (micro-PIV)

ABSTRACT

Recent advances in micro- and nano-technology and manufacturing systems enabled the development of small ($1\mu\text{m} - 1\text{ mm}$ in length) robots that can travel inside channels of the body such as veins, arteries, similar channels of the central nervous system and other conduits in the body, by means of external magnetic fields. Bio-inspired micro robots are promising tools for minimally invasive surgery, diagnosis, targeted drug delivery and material removal inside the human body. The motion of micro swimmers interacting with flow inside channels needs to be well understood in order to design and navigate micro robots for medical applications.

This thesis emphasizes the in-channel swimming characteristics of robots with helical tails at low Reynolds number environment. Effects of swimming parameters, such as helical pitch, helical radius and the frequency of rotations as well as the effect of the radial position of the swimmer on swimming of the helical structures inside channels are analyzed by means of experiments and computational fluid dynamics (CFD) models using swimmers at different sizes. Micro particle image velocimetry (micro-PIV) experiments are performed to visualize the flow field in the cylindrical channel while micro robot has different angular velocities.

The effects of solid plane boundaries on the motion of the micro swimmers are studied by experiments and modeling studies using micro robots placed inside rectangular channels. Controlled navigation of micro robots inside fluid-filled channel networks is performed using two different motion mechanism that are used for forward and lateral motion, and using the strength, direction and frequency of the externally applied magnetic field as control inputs. Lastly, position of the magnetic swimmers is detected using Hall-effect sensors by measuring the magnetic field strength.

KANAL İÇİNDE YÜZEN MİKRO ROBOTLARIN TASARIMI, KARAKTERİZASYONU, GÖRÜNTÜLENMESİ VE NAVİGASYONU

Fatma Zeynep TEMEL
Mekatronik Mühendisliği, Doktora Tezi, 2013
Tez Danışmanı: Doç. Dr. Serhat YEŞİLYURT

Anahtar Kelimeler: Kanal İçinde Yüzen Mikro Robotlar, Doğadan Esinlenen Medikal Robotik, Manyetik Tahrik ve Yönlendirme, Düşük Reynolds Sayısında Yüzme, Hidrodinamik Etkileşimler, Hesaplamalı Akışkanlar Dinamiği (HAD), Mikro Parçacık Görüntülemeli Hız Ölçümü (mikro-PIV)

ÖZET

Mikro ve nano teknoloji alanlarında ve üretim yöntemlerinde görülen gelişmeler, uzunluğu 1µm – 1 mm arasında değişen küçük robotların imal edilmesine ve vücut içerisindeki damar, arter veya kanallarda dışardan uygulanan manyetik alanlar yardımıyla hareket ettirilebilmesine olanak sağlamıştır. Dönen sarmal kuyruklu gibi doğadan esinlenmiş ilerleme mekanizmaları kullanılarak tasarlanan mikro robotlar, minimal invaziv cerrahi operasyonlar, teşhis koyma, hedeflenen bir noktaya ilaç transferi ve vücuttan parça alma gibi işlemleri gerçekleştirmek için gelecek vaat etmektedir. Özellikle tıbbi operasyonlarda kullanılması hedeflenen mikro robotların tasarımı ve yönlendirmelerinin yapılabilmesi için, buldukları kanal içinde kendi hareketleri sonucunda oluşan akış ile etkileşimlerinin anlaşılması gerekmektedir.

Bu tez çalışması, düşük Reynolds sayısında sarmal kuyruklu robotların kanal içindeki davranışları üzerine yoğunlaşmıştır. Farklı boylardaki yüzücülerin sarmal adım uzunluğu, sarmal yarıçap, dönme frekansı gibi yüzme parametrelerinin ve yüzücülerin kanal içinde buldukları pozisyonun, robotların yüzme davranışlarına olan etkileri, deneyler ve hesaplamalı akışkanlar dinamiği (HAD) modelleri kullanılarak analiz edilmiştir. Mikro-parçacık görüntülemeli hız ölçümü deneyleri ile silindirik kanallardaki mikro robotların farklı açısız hızlarında oluşan akış görüntülenmiştir.

Mikro robotların katı bir düzlem çevresindeki hareketinin etkilerini araştırmak üzere, mikro robotların dikdörtgen kesitli kanallar içerisindeki hareketi deneyler ve modelleme çalışmaları ile incelenmiştir. Mikro robotların hareket mekanizmaları ve farklı frekanslarda gözlemlenen davranış değişikliklerinden de faydalanarak, farklı kanal yapıları içindeki navigasyonları gerçekleştirilmiştir. Dışardan uygulanan manyetik alanın şiddeti, yönü ve frekansı, mikro robotların kanal ağ yapıları içindeki yönünü ve pozisyonunu kontrol etmek için girdi olarak kullanılmıştır. Son olarak, manyetik mikro robotların kanal içindeki konumları, Hall-etki sensörleri kullanılarak tespit edilmiştir.

ACKNOWLEDGEMENTS

I would like to express my gratitude to all those who guided and helped me to complete my journey in obtaining my PhD degree.

First and foremost, I would like to thank my dissertation advisor, Dr. Serhat Yeşilyurt, for his continuous support, encouragement and patience during the last four years. I always consider myself very lucky to have him as my supervisor, especially after hearing many horror stories about PhD studies. He has been and will always be a role model to me for showing how a successful researcher, supervisor and lecturer should be, not only with his enthusiasm for research, discipline in work and ethical stance in life but also with his great personality.

I am deeply grateful to Dr. Ata Mugan for always encouraging me to take more and more steps in research and in academia. I also would like to thank my dissertation committee for their valuable time and ideas; Dr. Asif Şabanoviç for his incredible wisdom in every aspect of life, Dr. İbrahim Tekin for teaching magnetics in the most understandable way for me and Dr. Ali Koşar for introducing me to different fields of microfluidics. I also would like to thank Dr. Güllü Kızıldaş Şendur for her help and guidance.

I would also like to thank my colleagues in our research group, Dr. Ahmet Fatih Tabak, Dr. Lale Işikel Şanlı, Aydek Gökçe Erman and Alperen Acemoğlu for helping me in this thesis and for sharing their time while having a break for coffee or tea along with nice conversations.

I also want to thank my dear friends, especially Dr. Merve Acer for her emotional support, helping me getting through the difficult times and making me feel that I was not and will not be alone during my journeys, Erinç Erel Çağlar & Tolga Çağlar for their support and entertainment, and Tolga Cengiz Beşiktaş, Emre Kaygın, Mine Uydan Atay and Serbay Atay for standing with me since our master studies in Germany.

My special thanks are for my family, my parents Hatice and Mehmet Ali Temel and my brother Veli Kıvanç Temel, for their unconditional love, endless support and unlimited patience. It would be impossible to complete my PhD studies without having them in my life. I wish I could thank and show my appreciation enough to my parents not only for their love, encouragement and support at every stage of my personal and professional life, but also for my brother, who has been my best friend all my life. I am thankful every single day of my life and with all my heart that I have Kıvanç as my brother. To them I dedicate this thesis.

This thesis was supported in part by Technological and Scientific Research Council of Turkey (TUBITAK) under the grant number 111M376.

TABLE OF CONTENTS

1	INTRODUCTION	1
2	LITERATURE REVIEW	4
3	MOTIVATION AND BACKGROUND.....	17
4	SWIMMING OF BIO-INSPIRED SWIMMERS IN CHANNELS	23
4.1	Methodology.....	24
4.1.1	Experimental Studies	24
4.1.2	Computational Fluid Dynamics Studies.....	27
4.1.2.1	Boundary conditions	28
4.1.2.2	Simulation parameters	30
4.2	Results	31
4.2.1	Experimental Results	31
4.2.2	CFD Results	33
4.2.2.1	Forward velocity	33
4.2.2.2	Body rotation rates	38
4.2.2.3	Body resistance coefficient	39
4.2.2.4	Radial forces and torques	39
4.2.2.5	Efficiency	42
4.3	Discussion.....	44
5	SWIMMING OF ARTIFICIAL MAGNETIC SWIMMERS IN CYLINDRICAL CHANNELS.....	46
5.1	Experimental Studies.....	47
5.1.1	Fabrication of the Artificial Swimmer	47
5.1.2	Experimental Setup	48
5.1.3	Results	52
5.1.3.1	Experiments in glycerol	52
5.1.3.2	Experiments in water	56
5.2	Theoretical Modeling	57
5.2.1	Equation of Motion	57

5.2.1.1	Wall effects	59
5.2.1.2	Magnetic torque	61
5.2.2	Results	62
5.3	Computational Fluid Dynamics (CFD) Modeling.....	66
5.3.1	Modeling	67
5.3.2	Results	70
5.3.2.1	Velocity fields	71
5.3.2.2	Swimming speed	74
5.3.2.3	Forces and torques on the swimmer.....	77
5.3.2.4	Efficiency	81
5.4	Flow Visualization.....	83
5.4.1	Experimental Setup	84
5.4.2	Micro Particle Image Velocimetry Setup.....	85
5.4.3	Results	88
5.5	Discussion.....	90
6	SWIMMING OF ARTIFICIAL SWIMMERS IN RECTANGULAR CHANNELS.....	94
6.1	Experimental Studies	94
6.1.1	Methodology	94
6.1.2	Results	98
6.2	CFD Studies.....	108
6.2.1	Methodology	109
6.2.1.1	Boundary conditions	111
6.2.1.2	Simulation parameters	112
6.2.2	Results	113
6.3	Discussion.....	122
7	SENSING AND APLICATION OF ARTIFICIAL SWIMMERS IN CHANNELS.....	124
7.1	Moving In Channel Networks	124
7.1.1	Methodology	124
7.1.2	Results	128
7.1.2.1	Navigation in Y-shaped channels	128
7.1.2.2	Navigation in T-shaped channels.....	128
7.1.2.3	Obstacle avoidance	129
7.2	Magnetic Navigation	131
7.3	Sensing.....	134

7.3.1	Methodology	134
7.3.2	Results	134
7.4	Discussion.....	136
8	CONCLUSION	138
8.1	Contributions	141
8.2	Future Work.....	142
9	REFERENCES	144

LIST OF FIGURES

Figure 2.1	Purcell’s Scallop Theorem explains that the motion of bacteria at low Reynolds number is time-independent [7].	5
Figure 2.2	(a) The swimmer, mechanism used to convert angular oscillation to translational oscillation and experimental setup [15]. (b) Experimental setup used to calculate thrust force of a bio-inspired propulsion mechanism [16]. (c) Helmholtz coil setup, untethered screw device and container used for experiments [19]. (d) Bundling sequence mimicking bacterial flagella bundling [23]. (e) Experiments performed to investigate the flow field of a helical tail using ultraviolet fluorescent [24].	7
Figure 2.3	(a) Electromagnetic actuation system proposed by Yu <i>et al.</i> [26]. (b) Electromagnetic actuation setup consists of saddle coils proposed by Choi <i>et al.</i> [27]. (c) OctoMag prototype designed and constructed at ETH Zurich consists of eight electromagnets [28]. (d) Rotating permanent magnet manipulator proposed by Fountain <i>et al.</i> [29].	9
Figure 2.4	(a) Driving principle of magnetic swimming mechanism using planar waves proposed by Sudo <i>et al.</i> [34]. (b) Beating pattern of the motion of a magnetic flexible filament attached to a red blood cell by Dreyfus <i>et al.</i> [35]. (c) Artificial bacterial flagella swimming motion controlled by magnetic fields by Zhang <i>et al.</i> [20]. (d) Nano-structured helices controlled under magnetic fields by Ghosh and Fisher [3]. (e) Transportation procedure by a micromachine with a microholder under magnetic fields by Tottori <i>et al.</i> [36]. (f) The motion experienced by the helices and the tubules under the action of magnetic fields by Schuerle <i>et al.</i> [37].	10
Figure 2.5	(a) Mechanical model of <i>E. coli</i> swimming near a solid surface and physical picture for the out-of-plane rotation of the bacterium by Lauga <i>et al.</i> [50]. (b) Scheme of a blood vessel with minor bifurcations and forces acting on a particle at different positions by Arcese <i>et al.</i> [52].	13
Figure 2.6	PIV results of four separate measurements at the same periodic position for rigid rotating helices for (a) top view and (b) side view by Kim <i>et al.</i> [81].	15
Figure 3.1	Applications of swimming micro robots [1].	17

Figure 4.1	(a) Dimensional parameters of the swimming robot. (b) Layout of the robot with the helical tail of amplitude 3 mm and having 3 waves on its tail. (c) Schematic representation of the experimental setup.....	26
Figure 4.2	(a) The radial position of robot in CFD model is changed along \mathbf{z} -axis until the distance between the robot and channel wall, w_d , is equal to 0.1 mm. (b) Mesh distribution of having 4 full waves on its tail and $A = 4$ mm, traveling near the wall with distance to the wall, w_d , equals 0.1 mm.....	29
Figure 4.3	Velocity of robots, from experiments (navy), from CFD simulations for robots traveling near the wall with distance to wall, w_d , equals 1mm (cyan), for robots traveling near the wall with distance to the wall, w_d , equals 0.2 mm (yellow), and for robots traveling near the wall with distance to the wall, w_d , equals 0.1 mm (red) for amplitudes, A , equals (a) 1 mm, (b) 2 mm, (c) 3 mm and (d) 4 mm.	35
Figure 4.4	Velocity of robots are normalized with the rotational frequency of the tail, f . Results are from experiments ('circles'), from CFD simulations for robots traveling with distance to wall, w_d , equals 1mm ('squares'), for robots traveling with distance to wall, w_d , equals 0.2 mm ('diamonds'), and for robots traveling with distance to the wall, w_d , equals 0.1 mm ('triangles') for amplitudes, A , equal to (a) 1 mm, (b) 2 mm, (c) 3 mm and (d) 4 mm, and for number of waves, N_λ , between 2 and 6.....	36
Figure 4.5	Simulation results of velocity of the robots are normalized with the wave speed, $S_w = \omega/k$, as a function of the radial position of the robot for A equals (a) 1 mm, (b) 2 mm, (c) 3 mm and (d) 4 mm; and for $N_\lambda = 2$ ('square'), 3 ('downward triangles'), 4 ('upward triangles') and 6 ('diamonds').....	37
Figure 4.6	Body rotation rates are normalized with the angular velocity of the tail, from experiments (navy), from CFD simulations for robots traveling with a distance to wall, w_d , equals 1 mm (cyan), for robots traveling with a distance to wall, w_d , equals 0.2 mm (yellow), and for robots traveling near the wall with distance to the wall, w_d , equals 0.1 mm (red) for amplitudes, A , equals (a) 1 mm, (b) 2 mm, (c) 3 mm and (d) 4 mm.....	38
Figure 4.7	Simulation results of body resistance coefficients of the robots with respect to the radial position of the robot for A equals (a) 1 mm, (b) 2 mm, (c) 3 mm and (d) 4 mm; and for $N_\lambda = 2$ ('square'), 3 ('downward triangles'), 4 ('upward triangles') and 6 ('diamonds').....	40
Figure 4.8	Radial force on \mathbf{z} -direction of the robots as a function of the radial position of the robot for A equals (a) 1 mm, (b) 2 mm, (c) 3 mm and (d) 4 mm; and for $N_\lambda = 2$ ('square'), 3 ('downward triangles'), 4 ('upward triangles'), 6 ('diamonds') are obtained from simulations. (e) Schematic representation of forces acting on the robot swimming near the wall.....	41

Figure 4.9	Torque on \mathbf{z} -direction of the robots as a function of the radial position of the robot for A equals (a) 1 mm, (b) 2 mm, (c) 3 mm and (d) 4 mm; and for $N_\lambda = 2$ ('square'), 3 ('downward triangles'), 4 ('upward triangles'), 6 ('diamonds') are obtained from simulations. (e) Schematic representation of torques acting on the robot swimming near the wall. (f) Top-view of the swimming robot from the experiments.	42
Figure 4.10	Efficiency of the robots with respect to the radial position of the robot for A equals (a) 1mm, (b) 2 mm, (c) 3 mm and (d) 4 mm; and for $N_\lambda = 2$ ('square'), 3 ('downward triangles'), 4 ('upward triangles') and 6 ('diamonds') with the results are obtained from simulations.....	44
Figure 5.1	Swimming micro robots made in the laboratory. (a) Helix making process, (b) L2W3 - shorter and thicker, (c) L2W4 - longer and thinner.	48
Figure 5.2	Experimental setup consists of electromagnetic coil pairs and USB microscope camera (left). Schematic view of micro swimmer (right)....	52
Figure 5.3	Dependence of linear velocity of micro swimmer L2W3 on magnetic field strength and rotation frequency.	54
Figure 5.4	Dependence of linear velocity of micro swimmer L2W4 on magnetic field strength and rotation frequency.	54
Figure 5.5	Comparison of L2W3 and L2W4 in terms of linear velocity. Applied magnetic field strength is 7.02 mT.....	55
Figure 5.6	Comparison of experimental data collected at 7.60 mT with the RFT model.....	55
Figure 5.7	Dependence of linear velocity of micro swimmer L2W4 on magnetic field strength and rotation frequency in water. The behavior after step-out frequency is a reason to be suspicious about inertial effects	57
Figure 5.8	Swimmer body penetrating imaginary inner concentric cylinder: Penetration depth δp is computed in r-coordinate of the lab frame	60
Figure 5.9	Simulation based rotational \mathbf{s} -velocity: Effect of step-out frequency and spontaneous counter-rotation of L2W4; operating at 6.85 mT with $f = 20$ Hz.....	63
Figure 5.10	Time-averaged \mathbf{x} -velocity vs magnetic actuation frequency. Experiment vs RFT for L2W3 at 6.85 mT	64
Figure 5.11	Time-averaged \mathbf{x} -velocity vs magnetic actuation frequency. Experiment vs RFT for L2W3 at 7.22 mT	64
Figure 5.12	Time-averaged \mathbf{x} -velocity vs magnetic actuation frequency. Experiment vs RFT for L2W4 at 6.85 mT	65
Figure 5.13	Time-averaged \mathbf{x} -velocity vs magnetic actuation frequency. Experiment vs RFT for L2W4 at 7.22 mT	65
Figure 5.14	Simulation based yz-trajectory for L2W4 operating at 7.22 mT with $f = 20$ Hz.....	66

Figure 5.15	(a) Micro robot used in the experiments consists of a magnetic head and a metal right-handed helical tail. (b) Drawing of the micro robot in CFD model that consists of a spherical head and a left-handed helical tail inside a cylindrical channel.	68
Figure 5.17	Closed contour surfaces, which are colored by <i>gray</i> for positive (backward $-u/d_h f = 0.17$ and $u = 0.61$ mm/s) and <i>black</i> for negative positive (forward $-u/d_h f = -0.17$ and $u = -0.61$ mm/s) velocities, for swimmer (a) in unbounded fluid; (b) in the circular channel at the center; and (c) near the channel wall; for all cases $\phi = \pi$, i.e., $t = \pi/\omega$. Swimmer is covered with the <i>black</i> contour surface, which represents the flow moving with the swimmer.	72
Figure 5.18	Axial velocity profile induced by unbounded swimmer (dashed black lines) and swimmers inside the channel (dash-dotted blue lines for in-center swimmer and solid red lines for near-wall swimmer) along the segments parallel to the channel's long axis at $y = d_h/2$ and $z = 0$ for unbounded and center and at $y = d_h/2$ and $z=0.3$ mm for near-wall swimmers, for rectangular positions: (a) $\phi = \pi/2$ ($t = \pi/2\omega$), (b) $\phi = \pi$ ($t = \pi/\omega$), (c) $\phi = 3\pi/2$ ($t = 3\pi/2\omega$), (d) $\phi = 2\pi$ ($t = 2\pi/\omega$).....	73
Figure 5.19	Axial velocity profile across the channel for axial positions: (a) one-head diameter in front of the swimmer, (b) at the middle of the head, (c) at the middle of the tail, (d) about 1 mm after the tail for $\phi = \pi/2$ ($t = \pi/2\omega$) (dotted black), $\phi = \pi$ ($t = \pi/\omega$) (dashed blue), $\phi = 3\pi/2$ ($t = 3\pi/2\omega$) (solid red), $\phi = 2\pi$ ($t = 2\pi/\omega$) (dash-dotted green).....	74
Figure 5.20	Experimental (solid lines with asterisks), in-center (solid lines with circles) and near-wall (dashed lines with squares) swimmer speed of micro robot having base-case parameters with respect to (a) frequency where $A = 0.125 \mu\text{m}$ and $N_\lambda = 4$, (b) amplitude where $f = 10$ Hz and $N_\lambda = 4$, and (c) number of waves where $f = 10$ Hz and $A = 0.125 \mu\text{m}$..	76
Figure 5.21	x -force acting on the head normalized by the theoretical spherical drag ($3\pi\mu d_h U$) with respect to dimensionless time for unbounded (dash-dotted line), in-center (dashed line), and near-wall (solid line) swimmers.	78
Figure 5.22	Time-averaged y - and z -forces for near-wall swimmers (solid lines with circles and squares) with respect to (a) frequency, (b) amplitude and (c) number of waves in comparison to drag force on the head (solid lines with asterisks). (d) Schematic representation of forces acting on the robot swimming near the wall.	79
Figure 5.23	Time-averaged torques in y - and z -directions for near-wall swimmers (solid lines with circles and squares) with respect to (a) rotational frequency, (b) wave amplitude and (c) number of waves on the helical tail in comparison to the x -torque (dashed lines with asterisks). (d) Schematic representation of torques on the base-case robot swimming near the wall. (e) Top-view of the micro robot in experiments (actual robot has a right-handed helical tail, mirror-image is shown here).	81

Figure 5.24	(a) Frequency, (b) wave amplitude and (c) number of waves dependence of efficiency for in-center (solid lines with circles) and near wall (solid lines with squares) swimming micro robots.....	83
Figure 5.25	20 mm × 20 mm × 20 mm Plexiglas cube on a lamella with a 1 mm diameter cylindrical channel and magnetic swimmer at the bottom.....	84
Figure 5.26	Electromagnetic coil pairs to produce rotational magnetic field along vertical axis placed on the Leica microscope.....	85
Figure 5.27	Double-frame micro-PIV imaging system consists of a cooling unit, a Neodymium-doped yttrium lithium fluoride (Nd:YLF) laser having a maximum output of 150W, a Phantom v130 high speed camera connected to Leica DMILM inverted microscope.	87
Figure 5.28	Dantec Dynamics DualPower dual cavity Nd:LYF laser.	87
Figure 5.29	Velocity vector map obtained for 2 Hz (a) at the end of the cylindrical head from micro-PIV, (b) at the end of the cylindrical head from CFD, (c) at the tip of the tail from micro-PIV, (d) at the tip of the tail from CFD. Maximum velocities are measured from micro-PIV as 2.8 mm/s.	89
Figure 5.30	Velocity vector map obtained for 8 Hz (a) at the end of the cylindrical head from micro-PIV, (b) at the end of the cylindrical head from CFD, (c) at the tip of the tail from micro-PIV, (d) at the tip of the tail from CFD. Maximum velocities are measured from micro-PIV as 11.2 mm/s.....	90
Figure 6.1	Millimeter size magnetic helical swimmers inside channels. (a) Swimmer no.1 (right-handed) and (b) swimmer no.2 (left-handed).....	96
Figure 6.2	An image processing sequence of converting the frames from RGB to grayscale, detecting the intensity of each pixel, distinguishing helical swimmer by adjusting intensities of pixels and defining centroid of the helical swimmer is used to measure the forward and lateral velocities of micro swimmers.....	98
Figure 6.3	Motion of right-handed helical swimmer moving to the negative x -direction (swimmer no.1) or left-handed helical swimmer moving to the positive x -direction (swimmer no.2) inside rectangular channel when rotational frequency, f , equals (a) 1 Hz and (b) 5 Hz. In the figure, \mathbf{F}_t , \mathbf{F}_g , \mathbf{F}_f and ω represent traction force, gravitational force, fluid force and angular velocity, respectively.	100
Figure 6.4	Position change of helical right-handed swimmer (no.1) in x -direction (blue line) and in y -direction (green line) inside rectangular channel during its motion.	102
Figure 6.5	(a) Dependence of linear velocities of micro swimmer no.1 (right-handed swimmer) on rotation frequency and channel surface. Negative frequencies represent backward motion and positive frequencies represent forward motion. (b) Picture of rough-surface, width of the channel (rough surface) is equal to 1.3 mm.	102

Figure 6.6	Dependence of linear velocities of left-handed swimmer (no.2) on rotation frequency and channel surface. Negative frequencies represent forward motion and positive frequencies represent backward motion.	104
Figure 6.7	Initial and final positions of the helical swimmers when rotating with a frequency of 1 Hz or -1 Hz, which represents moving forward and backward with a rotation frequency equal to 1 Hz, respectively. Three different initial positions are chosen: positive y -corner, mid-point, negative y -corner.....	106
Figure 6.8	Initial and final positions of the helical swimmers when rotating with a frequency of 2 Hz or -2 Hz which represents moving forward and backward with a rotation frequency equal to 2 Hz, respectively. Three different initial positions are chosen: positive y -corner, mid-point, negative y -corner.....	107
Figure 6.9	Initial and final positions of the helical swimmers when rotating with a frequency of 3 Hz or -3 Hz. which represents moving forward and backward with a rotation frequency equal to 3 Hz, respectively Three different initial positions are chosen: positive y -corner, mid-point, negative y -corner.....	108
Figure 6.10	(a) Micro robot used in the experiments consists of a magnetic head and a metal right-handed helical tail. (b) Drawing of the micro robot in CFD model that consists of a cylindrical head and a right-handed helical tail.	109
Figure 6.11	Helical swimmer placed in the rectangular channel and simulations are performed for different positions of the swimmer in the channel. A thin layer with high viscosity represents the channel walls.	112
Figure 6.12	Flow and pressure field around the head of the helical swimmer inside rectangular channel while helical swimmer is rotating with 1 Hz and is in contact with viscous boundary layer. Color bar shows the pressure distribution in Pa in the cross-sectional plane.	114
Figure 6.13	Flow and pressure fields around the head of the helical swimmer inside rectangular channel while helical swimmer is away from the channel boundaries with a distance of (a) $w_{dy} = 424 \mu\text{m}$, $w_{dz} = 30 \mu\text{m}$, (b) $w_{dy} = 40 \mu\text{m}$, $w_{dz} = 114 \mu\text{m}$, (c) $w_{dy} = 109 \mu\text{m}$, $w_{dz} = 274 \mu\text{m}$ to simulate the rotation at higher frequency values. Color bar shows the pressure distribution in Pa in the cross-sectional plane.	115
Figure 6.14	Linear (forward) velocities of micro swimmer with respect to its position inside rectangular channel. Only one quarter of the channel is presented and color bar shows the velocity values in mm/s..	116
Figure 6.15	Dependence of lateral velocities of micro swimmer on the position inside the channel.	117
Figure 6.16	Dependence of vertical velocities of micro swimmer on the position inside the channel.	118

Figure 6.17	Dependence of lifting force acting in z-direction on rotation frequency for the case swimmer is rotated about y-axis by 5° which is shown in the inset.	120
Figure 6.18	Dependence of angular velocities about y-axis on helical swimmer's position inside rectangular channel.	121
Figure 6.19	Dependence of angular velocities about z-axis on helical swimmer's position inside rectangular channel.	122
Figure 7.1	Channel structures with (a) Y-shaped connections and (b) T-shaped connections.	125
Figure 7.2	Experimental setup consists of (a) orthogonally placed three electromagnetic coil pairs (b) which are driven by Maxon Motor Drives connected to a NI-DAQ and controlled by a joystick (c) using Labview.	126
Figure 7.3	Orthogonally placed three electromagnetic coil pairs are driven with same frequency but with different currents. Coils placed in x- and y-direction are in phase whereas z-direction coil pair has a 90° phase shift.	127
Figure 7.4	(a) Helical swimmer moves in positive x-direction with the applied positive rotational magnetic field along x-axis if the frequency is high. For low rotational frequencies lateral motion occurs also in positive y-axis. The torque applied for direction is represented with $\mathbf{T}_{M,d}$, u is the velocity along x-axis and v is the velocity along y-axis. (b) Traction force, \mathbf{F}_T , due to the applied magnetic torque, $\mathbf{T}_{M,p}$, at low frequencies provides a velocity in lateral direction. \mathbf{F}_f and \mathbf{F}_g are friction and gravity forces, respectively	128
Figure 7.5	Motion of the helical swimmer inside (a) Y-shaped and (b) T-shaped rectangular channels. Magnetization of the permanent magnet on the helical swimmer is always perpendicular to the helix axis; net torque on the swimmer is due to the cross-product of the externally applied magnetic field with the magnetization of the head.	129
Figure 7.6	(a) Schematic representation of motion of helical swimmer inside rectangular channel when it comes across an obstacle. (b) Snapshots of forward motion of the helical swimmer placed inside rectangular channel. Green arrows show the position of the helical swimmer. Rotation frequency is 5 Hz. When $t = 20$ s swimmer does not move forward although it continues it is rotating at the same frequency. After $t = 30$ s, the frequency is dropped to 1 Hz and swimmer started to move in lateral direction, thus it avoided the obstacle.	130
Figure 7.7	Applied current to the y-axis electromagnetic coil pair to change the lateral position of the swimmer. Magnitude of the sinusoidal current is multiplied with a constant "c" to determine the magnitude of DC current.	132

Figure 7.8	Some scenarios and the minimum magnetic field force to be applied to maintain the initial lateral position with a magnetic force against traction force or to change the lateral position of the micro swimmer by applying a reverse magnetic force. “Min.c” refers to the ratio between magnitudes of DC current and sinusoidal current. “Start” and “Finish” refer to the initial and final position of the magnetic swimmer, respectively.....	133
Figure 7.9	(a) Phidget Interface Kit 8/8/8 board (b) Phidget 1108 Hall-effect magnetic sensor	135
Figure 7.10	Magnetic helical swimmer is placed inside a glycerol-filled glass channel which is placed onto the Hall-effect magnetic sensors.....	135
Figure 7.11	Magnetic field values with respect to time obtained from Hall-effect sensors	136

LIST OF SYMBOLS

a	Distance along the axis of the coil from the center
A	Amplitude (helical radius)
b	Friction coefficient
\mathbf{B}	Magnetic induction
\mathbf{C}	Local resistance matrix on the tail
\mathbf{C}_B	Mobility matrix of the body
\mathbf{C}_T	Mobility matrix of the tail
C_{BN}	Normal force coefficient of the body
C_{BR}	Tangential force coefficient of the body
C_{TN}	Normal force coefficient of the tail
C_{TR}	Tangential force coefficient of the tail
c_n	Normal resistive force coefficient
c_t	Tangential resistive force coefficient
\mathbf{D}_h	Drag matrix for rigidly-attached head of the micro swimmer
\mathbf{D}_r	Diagonal 3-by-3 translational body drag coefficient matrix
\mathbf{D}_t	Diagonal 3-by-3 rotational body drag coefficient matrix
d_b	Diameter of the body
d_{cap}	Outer diameter of the cap
d_{ch}	Diameter of the channel
d_h	Diameter of the spherical head
d_{tail}	Diameter of the tail
δ_p	Penetration depth of the swimmer
δ_{xj}	Kronecker's delta
\mathbf{e}_x	Unit vector in the \mathbf{x} -direction
\mathbf{F}	External force vector
\mathbf{F}_d	Total drag force

\mathbf{F}_p	Total propulsion force
\mathbf{F}_T	Traction force
F_x	Total force on the swimmer in the \mathbf{x} -direction
$F_{x,body}$	Axial force on the body
f	Frequency
g	Gravity constant
\mathbf{H}	magnetic field
$H(\cdot)$	Heaviside step function
I	Current
\mathbf{I}	Identity matrix
I_{SC}	Current applied to the small coils
I_{BC}	Current applied to the big coils
k	Wave number
L	Length
L_b	Total Length of the body
L_{cap}	Length of the cap
L_{ch}	Length of the channel
L_{tail}	Apparent length of tail
ℓ_{tail}	Curvilinear (actual) length of helical tail
\mathbf{M}	Magnetization
\mathbf{m}	Magnetic dipole moment
$mass$	Mass of an object
μ	Viscosity
N	Number of turns
N_λ	Number of waves
\mathbf{n}	Surface normal vector
\mathbf{n}_x	x-component of the local surface normal
\mathbf{n}_y	y-component of the local surface normal
\mathbf{n}_z	z-component of the local surface normal
η	Efficiency
p	Pressure
\mathbf{P}_{tail}	Position vector of the tail

P	Position vector of surface points of the swimmer with respect to swimmer's center of mass
Φ	Phase angle
ϕ	Rotation angle of the swimmer
Ψ	Constraint matrix
r_b	Radius of the body
r_{cap}	Outer radius of the cap
r_{ch}	Radius of the channel
r_{coil}	Radius of the coil
r_h	Radius of the spherical head
r_{tail}	Radius of the tail wire
r_{sw}	Radial position of the robot
r_{hs}	Radius of the helical swimmer
R	Rotation between the local Frenet-Serret frame on the helical tail and the swimmer frame
R_h	6-by-6 resistance matrix for the magnetic head
R_t	6-by-6 resistance matrix for the helical tail
R_θ	Transformation matrix between lab coordinate systems
Re	Reynolds number
Re_f	Frequency Reynolds number
\mathfrak{R}	The matrix handling rotations from swimmer frame to stationary lab frame
ρ	Density
S	Skew-symmetric matrix for the cross products between the position and velocity vectors in the swimmer frame
S	Total surface of the swimmer
S_b	Surface of the robot body
S_{tail}	Surface of the robot tail
S_w	Wave speed
s_t	Stiffness tuning parameter
σ	Stress tensor
t	Time
T_d	Total drag torque
T_{ext}	External torque
T_x	Rotational torque in the axial direction

$T_{x,body}$	Rotational torque acting on the body in the x -direction
T_{ch}	Depth of rectangular channel
t_{sw}	Position of the robot in the z -direction
$\boldsymbol{\tau}_M$	Torque on a dipole in free space
θ	Angle
\mathbf{u}	Linear velocity vector
U	Forward (axial) velocity
u	Forward velocity of the fluid
v	Volume of the particle
V	Lateral velocity
W	Vertical velocity
\mathbf{W}	Skew-symmetric matrix for the body center of mass
W_{ch}	Width of rectangular channel
w_d	Distance between the robot and channel wall
w_{dy}	Distance between the robot and channel wall along y-direction
w_{dz}	Distance between the robot and channel wall along z-direction
w_{d_c}	Minimum local distance of the center line of the tail to the surface of the channel
w_{sw}	Position of the robot in the y -direction
ω	Angular velocity
ω_{tail}	Rotation rate (angular velocity) of the tail
$\boldsymbol{\Omega}$	Angular velocity vectors
Ω_b	Rotation rate (angular velocity) of the body
Ω_x	Swimmer rotation rate about x-direction
Ω_y	Swimmer rotation rate about y-direction
Ω_z	Swimmer rotation rate about z-direction
x_{tail}	Axial position of the helical tail measured from the joint
x_{COM}	x-coordinates of the joint
y_{COM}	y-coordinates of the joint
z_{COM}	z-coordinates of the joint
ζ_0	Free space permeability
ζ_{eff}	Actual permeability

TABLE OF ABBREVIATIONS

BEM	Boundary Element Method
CCD	Charged Couple Device
CFD	Computational Fluid Dynamics
DC	Direct Current
DOF	Degree of Freedom
MEMS	Micro-electro-mechanical Systems
MRI	Magnetic Resonance Imaging
PIV	Particle Image Velocimetry
RFT	Resistive Force Theory
RPM	Rotating Permanent Magnet
SBT	Slender Body Theory

1 INTRODUCTION

Micro-electro-mechanical-systems (MEMS) technology, which offers combination of electrical and mechanical components at very small scales, proposes a great deal of opportunities. Micro-fluidic, biomedical and chemical applications are especially the areas where MEMS can be used for micromanipulation or medical procedures, as an example. Among these applications, micro-fluidics is particularly significant with the idea of developing micro swimmers which have great potential as tools that can promote minimally invasive surgery and perform several medical tasks, such as diagnosis, targeted therapy, drug delivery and removing material from human body.

Micro robots have the potential to dramatically change many aspects of medicine by navigating inside the blood vessels or other channels in body to perform targeted diagnosis and therapy [1]. For instance, length of treatment period (duration of therapy) can be shortened significantly, procedures special to people and illness can be achieved and drugs can only be delivered to the unhealthy organs and tissues.

Among the studies found in literature about swimming micro robots, examinations of controllable forward propulsion mechanisms take an important place. Observing nature is the starting point of most of the projects in this area. There are a number of studies in literature investigating the movements of both macro and micro scale swimming organisms. Moving organisms like bacteria and spermatozoa use two different kinds of propulsion mechanisms. One of them is planar wave propagation, which is a result of a flexible tail moving like cilia. Other one is helical wave propagation which is a result of a corkscrew motion of a helix shape tail. It has been presented that helical wave propagation generated using rigid helical tails is advantageous in terms of the forward velocity and thrust force [1]. Recent studies showed that it is possible to produce magnetic helical micro robots and to make them rotate and propel using rotating magnetic fields [2, 3], which is exploited commonly as

an actuation method for simplicity and effects magnetic fields to human body are already well known [4].

Although there are a number of groups working on this area, studies are mainly conducted for swimmers that are placed in pools rather than inside channels. Considering the application area of micro robots, one of which is medical procedures, in-channel flow conditions that occur because of the motion of micro robots is crucial to understand clearly. Although there are a few publications showing the increase in thrust force when the micro robot is swimming near a wall, in-channel swimming needs to be studied in detail.

Focus of this thesis is in-channel swimming behavior of bio-inspired and artificial swimmers with helical tails inside viscous fluid filled channels. Experimental and computational fluid dynamics (CFD) studies are performed using bio-inspired two link cm-scale swimmers with helical tails in cylindrical channel and artificial one link mm-scale magnetic swimmers with helical tails in both cylindrical and rectangular channels. It is understood that radial position of the robot, helical tail wave characteristics and rotation frequency are important parameters on swimmers' velocities, fluid forces and torques acting on the swimmers and efficiencies of the swimmers.

Furthermore, micro-Particle Image Velocimetry (micro-PIV) method is used to visualize resultant flow fields due to the rotation of helical mm-sized swimmers inside cylindrical channels for different rotational frequencies. Lastly, experiments on magnetic sensing and controlled navigation of mm-sized magnetic helical swimmers are conducted for the sake of completeness and to make an initial assessment on how magnetic micro swimmers can be controlled in conduits.

This thesis begins with a summary of the studies performed by other research groups in the Chapter 2 and emphasizes the importance of in-channel experimental and CFD studies in Chapter 3. Experimental and CFD results of bio-inspired helical two-link swimmers are presented in the fourth chapter. Fifth chapter consists of sections of experimental, theoretical, CFD and micro-PIV studies performed using artificial magnetic helical swimmers. Micro-PIV experiments are presented in the fourth section of this chapter. Experimental and CFD studies with magnetic helical swimmers in rectangular channels are presented in the sixth chapter. The seventh chapter is an extension of the fifth chapter and consists of the experimental studies about sensing, navigation and control of magnetic helical swimmers in cylindrical and

rectangular channels.

This thesis focuses on the in-channel swimming behavior of bio-inspired and artificial swimmers with helical tails inside viscous fluid filled channels in order to point out the differences from unbounded swimming and the points to be considered in designing micro swimmers and developing their control algorithms. Design and control of micro-robots for in vivo medical applications can benefit greatly from the results and detailed analysis presented in this thesis. Significant findings of this thesis are understanding of the flow field inside channels due to the rotation and motion of helical swimmers, determining the effect of parameters such as the wavelength and amplitude of the helical waves, and the proximity of swimmers to channel walls, for developing useful control algorithms for these swimmers.

2 LITERATURE REVIEW

Miniaturized swimming robots have great potential to revolutionize modern medicine; risks of many life-threatening operations and procedures can be reduced significantly. For instance, potent drugs can be delivered to target organs, tissues and cells; arterial build-up can be removed to enhance blood flow in vital organs; diagnostic information can be collected and delivered from directly within organs and tissues, etc. Recent developments in manufacturing of integrated devices with electrical, mechanical, chemical and biological components at very small scales rendered bio-inspired medical swimming micro robots realizable [1, 4, 5, 6]. A comprehensive survey of development of micro robots and their potential impact in medicine is provided by Nelson *et al.* [1].

Propulsion mechanisms of macro scale objects in fluids are inadequate for micro scales where Reynolds number is much smaller than 1 and viscous forces dominate inertial ones. Purcell's Scallop Theorem (Figure 2.1) demonstrates that a standard propeller is useless for propulsion in micro scales [7]. However, microscopic organisms such as bacteria and spermatozoa can move up to speeds around tens of body lengths per second [8, 9, 10] with propulsion generated by their flagellar structures, which are either rotating helices or flexible filaments that undergo undulatory motion.

Bacteria such as *Vibrio alginolyticus*, *Escherichia coli* and *Rhodobacter sphaeroides* propel themselves with the rotation of their helical flagella, which are actuated by molecular motors [10] within the body that can rotate as high as at 1 kHz, in the case of *V. alginolyticus* [8, 9, 10]. The speed of the organism depends on the body shape and size, as well as parameters of the flagellar actuation, such as wavelength, frequency, and amplitude [8, 9, 10]. Moreover, swimming of bacteria in rectangular channels having widths (1.3 - 1.5 microns) slightly larger than the diameter of the body of the organism is reported by DiLuzio *et al.* [11]. The result is significant in showing that the actuation mechanism generates hydrodynamic propulsion in narrow channels

overcoming molecular interaction forces between the organism and the channel walls [11].

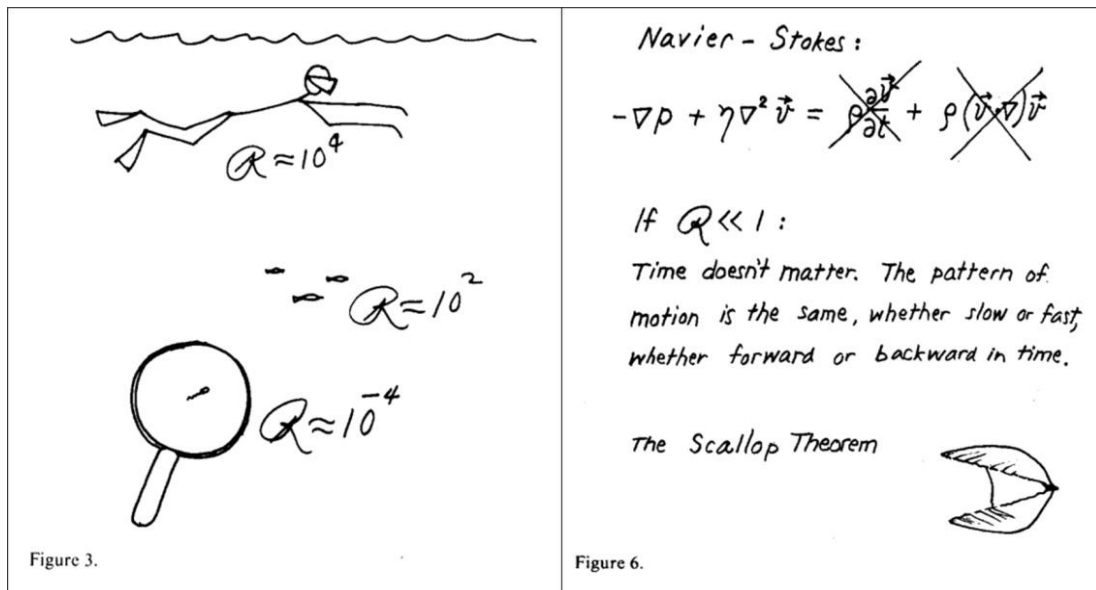


Figure 2.1 Purcell’s Scallop Theorem explains that the motion of bacteria at low Reynolds number is time-independent [7].

Natural micro swimmers such as bacteria and spermatozoa can propel themselves using either one of two propulsion mechanisms: planar wave propulsion or helical wave propulsion. Although helical wave propulsion is the preferred method for experiments since it is considered more efficient compared to planar wave propulsion [12], in literature experiments using both mechanisms are performed. Generating and storing power in micro-scales as well as building actuation mechanisms such as molecular motors in nano-scales pose difficulties due to challenges of micro-manufacturing [13, 14]. Thus, macro-scale experiments are considered a method to study the effects of swimming parameters of two-link swimmers and the swimming behavior of low Reynolds number swimmers.

Experiments with scaled-up robots swimming in viscous fluids have been used to demonstrate the efficacy of the actuation mechanism as well as validate hydrodynamic models, since low Reynolds number flows are governed by Stokes equations regardless of the length scale. The Reynolds number, which characterizes the relative strength of inertial forces with respect to viscous ones, is given by, $Re = \rho U \ell_s / \mu$, where ρ and μ are density and the viscosity of the fluid, and U and ℓ_s are the velocity and length scales of the flow; therefore as long as Reynolds number is the same, hydrodynamic characters of flows at micro and macro scales would be the same. However, it is clear that as the

length scale is reduced to molecular scales, the continuum hypothesis fails. According to Purcell [7], a man would experience the same forces and effects as a bacterium if he tries to swim in a pool that is full of molasses; since both situations would have the same low Reynolds number and same physical conditions.

There are a number of works reported in literature that takes advantage of the hydrodynamic similarity of low Reynolds numbers and uses experiments in viscous fluids at cm-scales to study the swimming of bacteria in micro-scales. Yu *et al.* [15] used a mechanism to convert rotational motion from a motor to oscillatory motion and obtained thrust force from planar wave propagation on a flexible cilia (Figure 2.2a). Experimental investigations resulted with measuring propulsive forces with a force sensor and a camera; authors concluded that the results are in agreement with theoretical model [15].

A bio-inspired helical propulsion mechanism is proposed by Behkam and Sitti [16] to calculate the thrust force. In the scaled-up characterization experiments, the deflection of a very thin (1.6 mm) cantilever beam due to the rotation of helical tail in silicon oil-filled tank is measured to calculate the thrust force (Figure 2.2b). Another scaled-up model is presented by Honda *et al.* [17] where rotating magnetic field is used as external actuation to obtain propagation of a cm-long helical swimming robot in a silicon oil-filled cylindrical channel. The linear relationship between the swimming speed of the robot and the excitation frequency is observed by authors and results agreed well with the hydrodynamic model developed by Lighthill [18] based on the slender body theory. Mahoney *et al.* [19] manufactured a screw like robot having 5.6 mm length and 1.4 mm diameter and investigated its motion inside a soft tissue (Figure 2.2c). Unstable motion of robots is observed when the rotational frequency of applied magnetic field exceeds a certain value [19] similar to [2, 3, 20]. Forward propulsion force and rotation torque are calculated for a flexible rotating flagella in another study by Coq *et al.* [21]. Chen *et al.* [22] performed experiments with a robot having four helical tails controlled by four individual DC motors placed inside a silicon oil-filled channel and presented that the forward velocity of the robot changes proportionally with respect to the rotation velocities of motors. In addition, authors indicated that the robot can be navigated with the help of four individual tails [22].

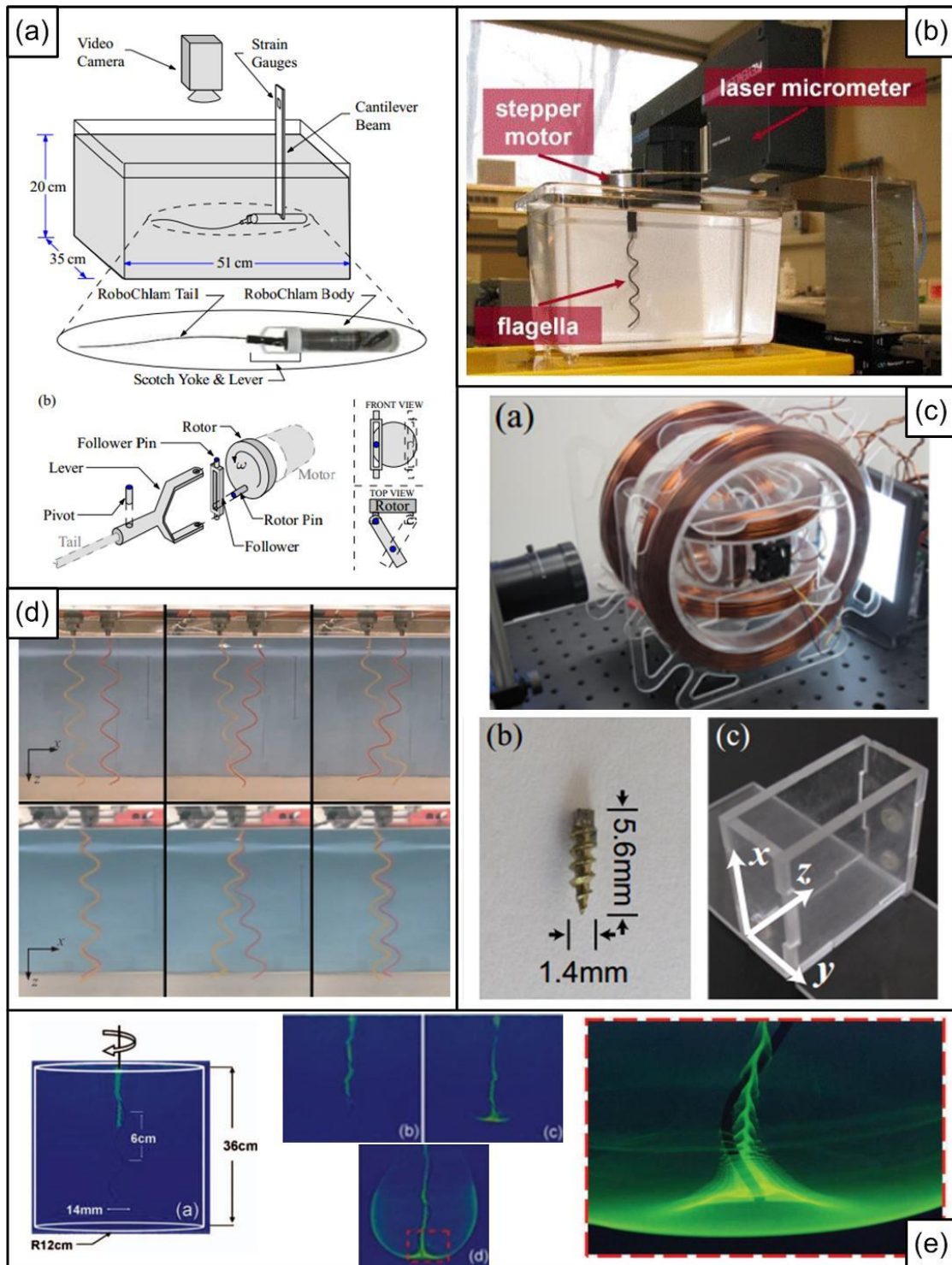


Figure 2.2 (a) The swimmer, mechanism used to convert angular oscillation to translational oscillation and experimental setup [15]. (b) Experimental setup used to calculate thrust force of a bio-inspired propulsion mechanism [16]. (c) Helmholtz coil setup, untethered screw device and container used for experiments [19]. (d) Bundling sequence mimicking bacterial flagella bundling [23]. (e) Experiments performed to investigate the flow field of a helical tail using ultraviolet fluorescent [24].

Visualization of flow field around rotating helices is demonstrated by Kim *et al.* [23]; authors analyzed digital video images of a macroscopic scaled-up model that demonstrated the purely mechanical phenomenon of bacterial flagella bundling; the macroscopic scale model allows determining the effects of parameters that are difficult to study in micro-scale such as rate and direction of motor rotation (Figure 2.2d).

Sakar *et al.* [24] performed experiments using ultraviolet fluorescent with a helical tail in a cylindrical tube (24 cm diameter and 32 cm depth) where Reynolds number is equal to 0.8 and investigated the flow field (Figure 2.2e). Although Reynolds number is below one, authors observed unstable and time-dependent flow since the flow is not completely in viscous regime [24].

Although there are different actuation methods proposed for micro-scale swimmers in the literature, like the mini DC brushless motor used in [6], the use of external magnetic fields has many advantages that circumvent the need for on-board power source that enables autonomous untethered motion of the micro robot [12]. In addition, medical equipment using magnetic fields can be reconfigured for actuation of micro robots such that external magnetic fields compatible with medical procedures were demonstrated successfully for the actuation of swimming micro-robots [25]. Helmholtz coils [26, 27, 28] and permanent magnets [29] are used to induce external magnetic fields to render forces and torques on magnetic micro robots for propulsion.

Swimming mechanisms using planar and helical wave propulsion are used in experiments to demonstrate bio-inspired micro swimmers moving with the help of externally applied magnetic fields [30, 31, 32, 33]. A study using planar waves is conducted by Sudo *et al.* using micro robots on the order of a millimeter, and the effect of tail width and length on the swimming velocity are investigated [34]. Dreyfus *et al.* also used planar wave propagation by linking superparamagnetic colloids with double stranded DNAs which has a total length of 24 μm and showed that the velocity and direction of motion is controlled by adjusting the external fields [35]. Although the examples using planar wave propulsion in literature, commonly used propulsion mechanism for micro swimmers is the rotation of helical tails, since rotating magnetic fields can easily be generated [12].

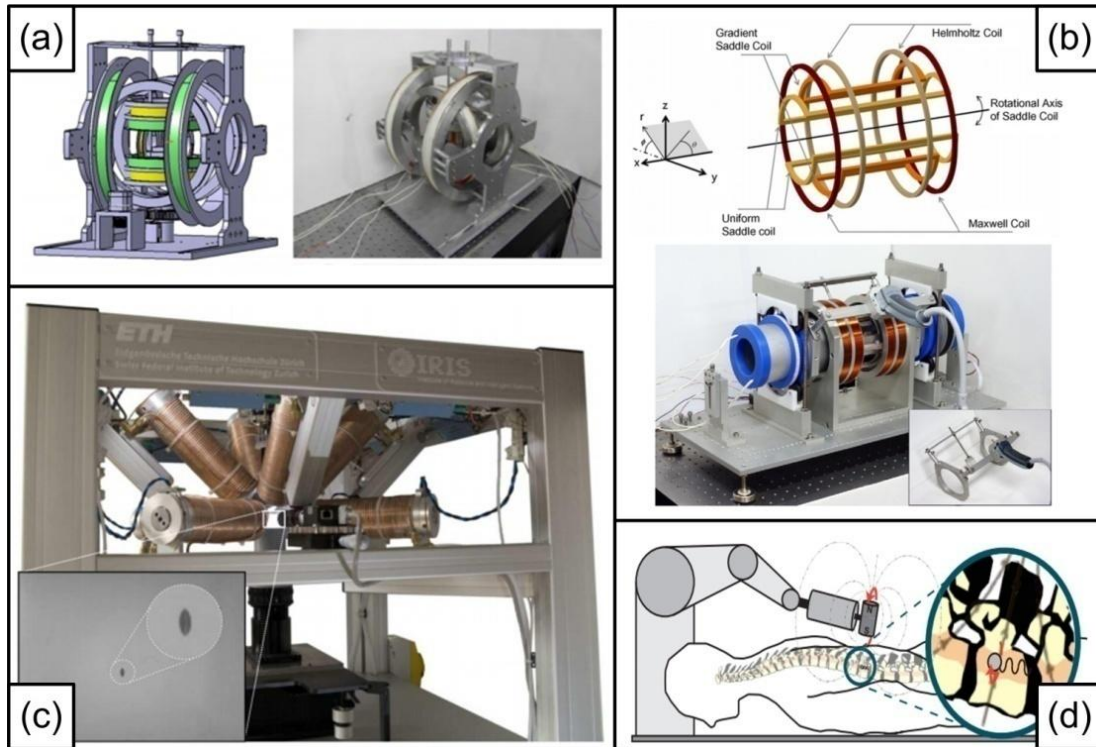


Figure 2.3 (a) Electromagnetic actuation system proposed by Yu *et al.* [26]. (b) Electromagnetic actuation setup consists of saddle coils proposed by Choi *et al.* [27]. (c) OctoMag prototype designed and constructed at ETH Zurich consists of eight electromagnets [28]. (d) Rotating permanent magnet manipulator proposed by Fountain *et al.* [29].

Helical artificial bacterial flagella are manufactured from GaAs by Zhang *et al.*, measured as $1.8 \mu\text{m}$ in width, $30 \mu\text{m}$ in length, 200 nm in thickness and attached to a soft magnetic nickel on one side [2, 20]. Authors demonstrated that the flagella swim along its helical axis with the externally applied rotating magnetic field in that direction obtained by electromagnetic coil pairs, and concluded that size of the head and strength of the applied magnetic field affect the linear swimming velocity. In addition, 3D steering of helical micro swimmers is accomplished by a low strength, rotating magnetic field with micrometer positioning precision inside a water filled tank [2, 20]. Another study on swimming micro structures was carried out by Ghosh and Fisher [3], who manufactured and operated chiral colloidal propellers having $200\text{-}300 \text{ nm}$ width and $1\text{-}2 \mu\text{m}$ length: swimmers were made of silicon dioxide and a thin layer of ferromagnetic material (cobalt) was deposited on one side. Rotational magnetic fields were used to navigate the magnetic nano-structured propellers in water with micrometer level precision [3]. Furthermore, two new methods of manufacturing robots with helical

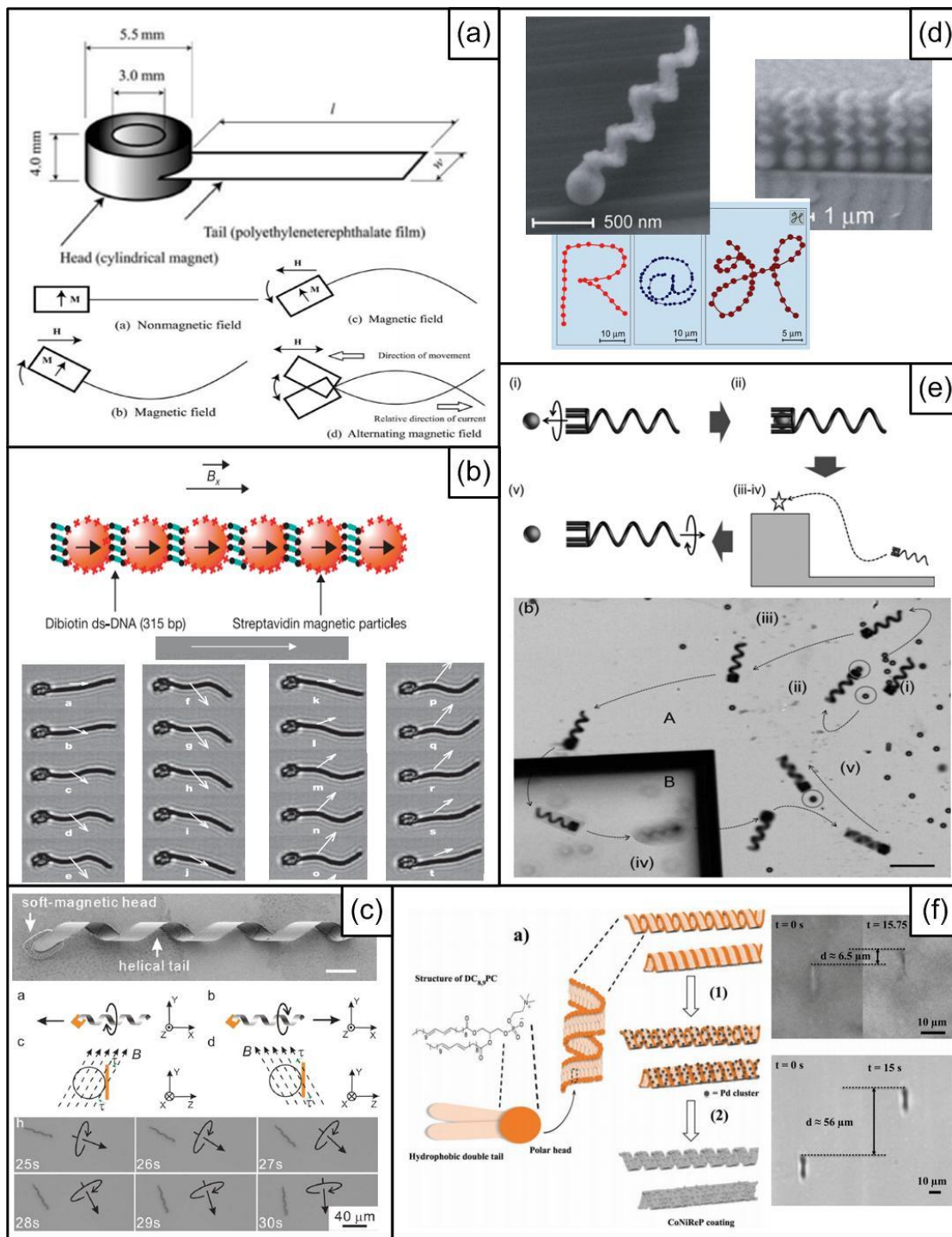


Figure 2.4 (a) Driving principle of magnetic swimming mechanism using planar waves proposed by Sudo *et al.* [34]. (b) Beating pattern of the motion of a magnetic flexible filament attached to a red blood cell by Dreyfus *et al.* [35]. (c) Artificial bacterial flagella swimming motion controlled by magnetic fields by Zhang *et al.* [20]. (d) Nano-structured helices controlled under magnetic fields by Ghosh and Fisher [3]. (e) Transportation procedure by a micromachine with a microholder under magnetic fields by Tottori *et al.* [36]. (f) The motion experienced by the helices and the tubules under the action of magnetic fields by Schuerle *et al.* [37].

tails are tested. First is the construction of 8.8 μm long micro carriers that consist of micro holders and helical structures using 3D laser processing and physical vapor deposition [36]. Tottori *et al.* coated micro carriers with two thin Ni/Ti layers using electron beam evaporator, so that the micro machines are controlled with the aid of externally applied magnetic fields [36]. Second is the coating of liposome, which has self-formed two-layered spiral structures or tubules, by CoNiReP in order to obtain rigid and magnetically controllable structures [37]. The motion of these helices was then observed under a 5 DOF system that consists of eight electromagnets [37].

Hydrodynamic modeling of natural micro-swimmers has been an interest for more than 50 years. A thorough review of hydrodynamic models of low Reynolds number swimming is presented by Lauga and Powers [38]. Taylor [39] presented an analysis of the flow induced by small amplitude planar waves propagating on an infinite sheet immersed in a viscous fluid analogous to the propulsion mechanism of spermatozoa. Gray and Hancock [40] modeled swimming of a sea-urchin spermatozoa based on the fluid forces calculated by the resistive force theory, which offers a general framework for the calculation of resultant propulsion and drag forces from the integration of local forces in normal and tangential directions that are proportional to the velocity components in those directions over the tail. Lighthill [18] postulated a line distribution of stokelets on slender bodies and obtained resistive force coefficients for rotating rigid helical tails. Purcell [7] presented a general view on the motion of micro structures in fluids and explained the time and geometric conditions to obtain desired thrust effect with the "Scallop Theorem." Brennen and Winet [41] presented a broad review of propulsion mechanisms and parameters of microorganisms along with theoretical models. Higdon [42] examined the interaction between cilia of a spermatozoa moving with the help of helical wave propagation and fluids with high viscosities. Author obtained results defining the relationship between helical wave geometry and the fluid forces induced by helical wave propulsion, required energy consumption and efficiency of aforementioned swimming method [42]. Wiggins and Goldstein [43] investigated interaction of thin flexible tails with fluids, at the equilibrium point of bending stresses of tail and fluid stresses. As a result of this study, the links between fluid forces and structural stresses, and effects on the forward propulsion force have been revealed [43]. Manghi *et al.* performed Stokes simulation studies using Rotne-Prager Green functions and calculated the resultant propulsion force of a flexible nano-size filament rotates as a result of the balance between thermal, hydrodynamic and elastic forces [44]. Keaveny

and Maxey [45] inspired from the experiments performed using magnetic particles added to red blood cells and calculated magnetic forces and fluid forces numerically together with the kinematic equations of cilia structure. Raz and Leshansky [46] carried out simulation studies to analyze a spherical load moving with the propulsion force occurs as a result of necklace-shaped rotating magnetic particles.

There are a number of studies on modeling swimming microorganisms inside channels, tubes and near planar solid boundaries in literature. Brennen and Winet [41] pointed out that the resistive force coefficients (i.e. [18 and 40]) used to model the motion of helical or planar wave propulsion of a tail would be different for near-wall situations. Katz [47] studied asymptotic analysis of the planar wave propulsion between two infinite plates or near an infinite plate using perturbation methods and lubrication theory. Results indicate that velocity of the swimmer increases when the distance between plates increases or the distance between the single plate and the swimmer increases [47]. Following this work, Katz *et al.* [48] calculated resistive force coefficients using the slender body theory with distributed stokelets over slender bodies swimming near solid walls. In a similar study, Blake [49] concluded that the ratio of resistance force coefficients of a thin object moving next to a solid boundary should be greater than two. Lauga *et al.* [50] modeled circular motion of *E. coli* near solid boundaries using drag coefficients derived by Katz *et al.* [48] and validated the model with experimental results. Recently, in-channel swimming of infinite helices and filaments that undergo undulatory motion is studied by Felderhof [51] with an asymptotic expansion, which is valid for small amplitudes; results show that the speed of an infinitely long helix placed inside a fluid-filled channel is always larger than the free swimmer and depends on the tail parameters such as the wavelength and the amplitude.

Moreover, analytical models that describe the equation of motion for artificial structures swimming in blood vessels are reported in recent years. Arcese *et al.* [52] developed an analytical model that includes contact forces, weight, van der Waals and Coulomb interactions with the vessel walls and hydrodynamic propulsion forces in non-Newtonian fluids to address the control of magnetically guided therapeutic micro robots in the cardiovascular system.

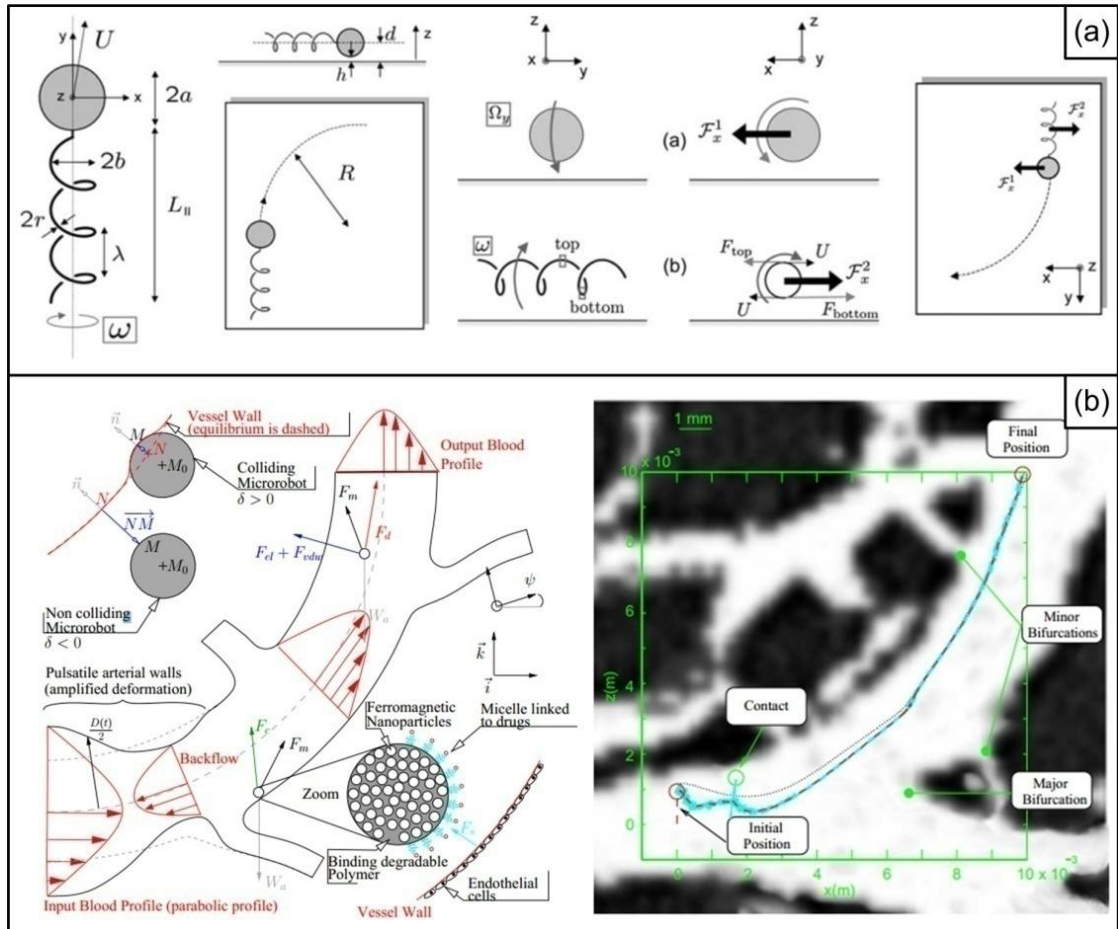


Figure 2.5 (a) Mechanical model of *E. coli* swimming near a solid surface and physical picture for the out-of-plane rotation of the bacterium by Lauga *et al.* [50]. (b) Scheme of a blood vessel with minor bifurcations and forces acting on a particle at different positions by Arcese *et al.* [52].

In addition to analytical models, there are numerous examples of numerical solutions of the flow equations for micro swimmers in unbounded media and near planar walls; representative ones are the following. Motion of *vibrio alginolyticus* was modeled numerically by Goto *et al.* [53] with the boundary element method (BEM); authors showed the results of the model agree well with observations on the strains of the organism that exhibit geometric variations. Ramia *et al.* [54] used a numerical model based on BEM and calculated that the micro swimmer's velocity increases by only %10 when swimming near a planar wall, despite the increase in drag coefficients.

No-slip boundary conditions are adopted for swimming of microorganisms in unbounded media and near planar walls. However, from a general perspective no-slip boundary condition assumption is questioned and investigated in several studies [55, 56, 57, 58, 59]. In micro scales, wetting becomes an important parameter to specify boundary conditions, since hydrophobicity affects the slip length dramatically [59, 60,

61]. Blood vessels and other conduits in the human body are covered with hydrophilic surface tissue, which is the endothelium and used to render polymers hydrophilic [62, 63]. Although in earlier studies it is reported that slip exists both on hydrophilic and hydrophobic surfaces and the degree of slip differs according to the wetting of the surface [61], with improvements on contact angle measurement techniques, boundary conditions on the hydrophilic surfaces is indicated as no-slip [58, 59, 64, 65]. In addition, most of the bacteria show hydrophilic surface properties [66, 67], thus no-slip boundary conditions are assumed for swimming of bacteria, as used in [68, 69].

Another question is about the Newtonian fluids used in experiments and modeling studies. The red blood cells, which present in the blood, cause it to behave like a non-Newtonian fluid [70]. The blood plasma, on the other hand, is a Newtonian fluid and more than 50% of it is water. A micro swimmer would experience the same effects with particles (cells) in the blood, therefore, at the micro-nano level, blood can be considered as Newtonian fluid while performing experimental or modeling studies [70]. In addition, the experimental results of Liu *et al.* [71], who studied visco-elastic effect of the non-Newtonian fluid using Boger fluid in their scaled-up setup, which is used to measure the force-free swimming speed of a rotating rigid helix, show that the difference in the forward velocities of rotating helices in viscous and visco-elastic fluids is not crucial.

In recent years, studies about the visualization of the flow field around rotating helices became significant besides the studies about the motion of swimming robots. One of the most common methods in flow visualization and analysis is particle image velocimetry (PIV) [72, 73, 74]. The main advantages of PIV can be listed as:

- Performing measurements without interrupting the flow (non-invasive)
- Being an optic-based and accepted metrology method
- Being a method with full field of view
- Being able to perform quantitative measurements of velocity vectors at many points in the flow at the same time
- Obtaining full field of view velocity vectors from two consecutive image frames.

As a result, studies are performed with the help of PIV systems on propulsion of flying and swimming living creatures [75, 76, 77], reasons for the flows become unstable [78, 79] and analyzing transport and mixing processes of fluids and chemicals in micro fluidic devices [80]. PIV is also widely used to investigate on the swimming

mechanisms and aquatic locomotion of swimming organisms [75, 76, 77]. For instance, a study conducted by Kim *et al.* [81] is performed to measure the velocity field for rotating rigid and flexible helices, and study the flagellar bundling of E.coli or other bacteria, by building a scaled-up model, which ensures Reynolds number to be low, using macro-scale particle image velocimetry (PIV) system.

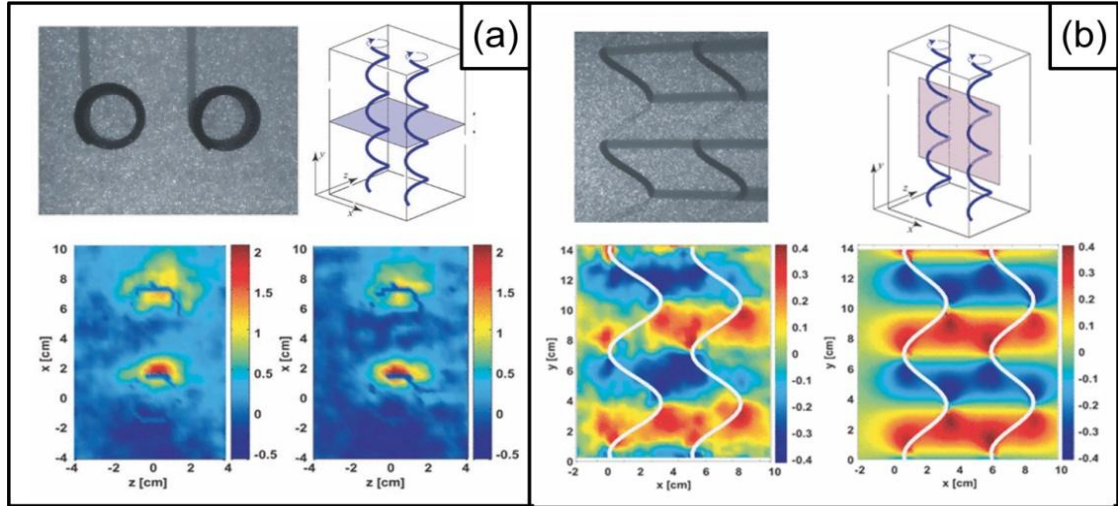


Figure 2.6 PIV results of four separate measurements at the same periodic position for rigid rotating helices for (a) top view and (b) side view by Kim *et al.* [81].

The need to analyze the flows within the micrometer-size channels become inevitable with the development of microfluidic and lab-on-a-chip devices and as a result the technological extension of PIV, micro-PIV method is emerged [80, 82, 83, 84]. The main difference between PIV and micro-PIV is due to the illumination methods used in two techniques, whereas image processing approaches and flow rate calculations are the same. The aim of both illumination methods is to minimize the intensity interference of fluorescent spheres in the different velocity layers in the flow. In PIV experiments, only a part of the flow is illuminated with a laser light sheet, thickness of which should be smaller than the depth of focus of the imaging system. Since it is difficult to obtain a stable, few micrometers thick layer of the laser light, volume illumination approach is preferred rather than the sheet illumination in micrometer-scale system. In micro-PIV, a volume in the flow is illuminated, however, depth of focus and field of view determines the layer which is observed [74, 84]. One of the most important criteria in the PIV systems is measured dynamic velocity range [85] and determined by the speed of the cameras (frames per second captured) used in the PIV systems. Because of the high cost of the high resolution cameras, double frame

cameras are widely used as an alternative with their low costs, however, high cost pulsed lasers are required to be able to achieve desired high-quality results.

3 MOTIVATION AND BACKGROUND

In near future, considering the technological developments, micro robots are expected to be the tools that can serve for many complicated medical procedures. Simple surgical operations such as clearing blood clots inside hard-to-reach arteries in vital organs can be performed by millimeter-sized robots which can be delivered inside a nearby artery, navigated through the arterial network, manipulated to perform a task such as releasing of an anti-clotting agent, and navigated back for recovery. In addition, the risks and injuries will decrease by using micro robots in such applications as ablation of harmful tissues by rotational motion inside tissues, destroying the unhealthy tissues by vibrating micro robot, or ablation of tissues by heating the micro robot up using radiofrequency (Figure 3.1) [1].

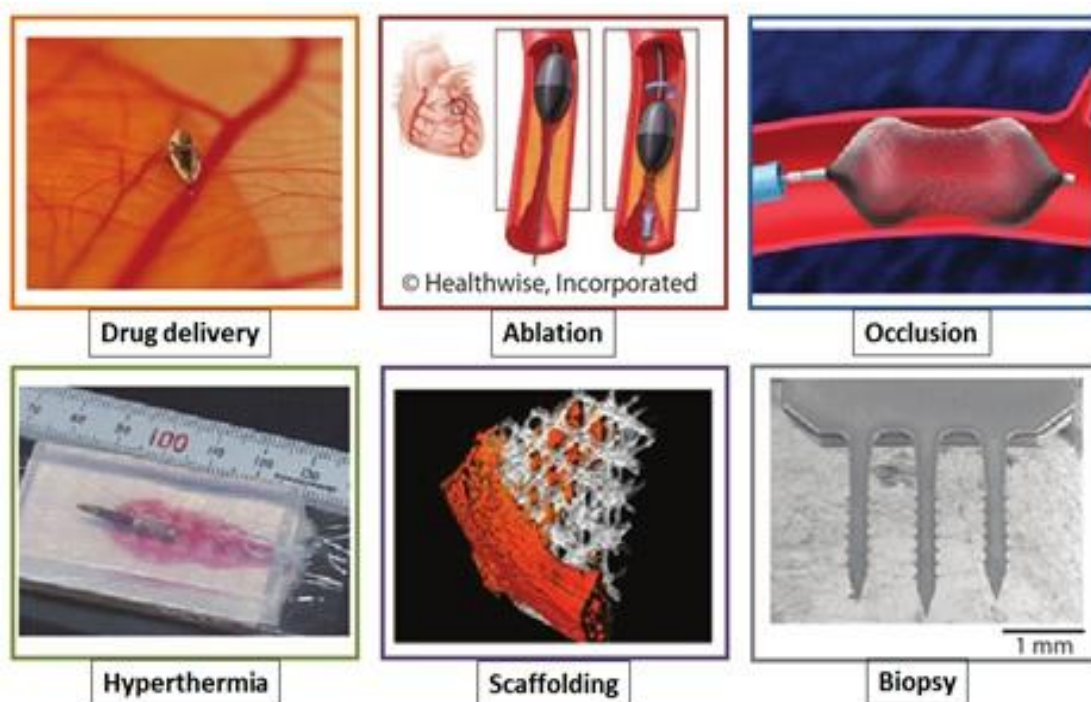


Figure 3.1 Applications of swimming micro robots [1].

Circulatory system inside the human body consists of veins and arteries having diameters ranging between 10 μm and 25 mm. Arteries having diameter greater than 1

mm have strong blood flow such that manipulation of micro robots will be difficult. On the other hand, channels in central nervous system are suitable places for micro robots which can be used effectively and navigated in channels about 1.5 mm in diameter to vacancies in brain to perform simple operations. Using micro robots for such surgical operations will expand the ability and the areas that cannot be reached by currently used cabled catheter which is an alternative to open brain surgery. Urinary system is another place for micro robot usage with 2.5 mm diameter and 250 mm length channels. Treating kidney stone (renal calculus) and prostate cancer are potential applications that micro robots can perform in the urinary system [1].

Autonomous micro robots, which are aimed to be used in bodily channels of circulatory, nervous and urinary systems, must be precisely navigated inside channels to the desired place; thus it is important for micro robots to be accurately controlled by operators. Thus, in-channel experiments are significant for micro robots to be used in *in vivo* applications inside blood vessels and similar conduits.

In-channel swimming is addressed by a number of studies in literature. A cm-long spiral swimming robot is actuated by Honda *et al.* [17] using external rotating magnetic field to obtain propagation in a silicon-oil-filled, 15-mm-diameter channel. Authors showed that motion of the robot has a linear relationship with the actuation frequency and concluded that the motion of the robot is proportional the actuation frequency and can be predicted by the slender body theory of Sir Lighthill [18]. Hydrodynamic interactions between swimming organisms and solid surfaces were investigated by Berke *et al.* [86] by measuring the distribution of *E.coli* swimming between glass plates and results were compared with a hydrodynamic model. Another study about bacteria swimming near solid surfaces was conducted by Giacché *et al.* [87] using a boundary element method based model to predict the near-wall motion of flagellated microorganisms and validated their model with a set of experiments with *E.coli*. Similarly, Fountain *et al.* [29] used a rotating permanent magnet (RPM) manipulator with a helical micro robot having a diameter of 1.625 mm and made experiments in lumen using gradients in a non-uniform magnetic field. Authors concluded that RPM manipulator is viable for 1DOF propulsion and gradual steering maneuvers [29]. Martel *et al.* [4] demonstrated that Magnetic Resonance Imaging (MRI) can be used as an actuation method for dragging magnetized particles and Mathieu and Martel validated that in physiological circumstances with a magnetic sphere which has 1.5 mm diameter

in size by using magnetic field gradient [88]. Authors also used Maxwell coil pairs placed inside MRI to steer a magnetic micro particle in a micro-vascular channel [88].

Thorough understanding of the induced flow due to the rotation of micro robots inside fluid-filled channels and hydrodynamic interactions between micro robots and channel boundaries are required for controlled-navigation of micro robots inside bodily channels such as spinal cord or arteries. This thesis aims to examine the behavior of micro robots in channels and their interaction with fluid and surrounding channel boundaries. In order to achieve this goal, various studies are performed:

- Experiments: Swimmers are placed in fluid filled tubes with circular and rectangular cross sections. Autonomous mm-scale one link magnetic swimmers are actuated by rotating magnetic fields provided by Helmholtz coil pairs. Experiments were performed to understand the effects of actuation frequency, helical tail wave parameters, radial position of the robot, and strength of the magnetic field. Image processing software is used to determine the robots' motion in forward and lateral directions.
- Resistive Force Theory (RFT): A 6-DOF time-dependent hydrodynamic model is built for mm-scale one link magnetic helical swimmers in cylindrical channels based on Resistive Force Theory (RFT) including a technique to implement cylindrical channel effects, and magnetic step-out frequency phenomena.
- Computational fluid dynamics (CFD): CFD models for a two link cm-scale and one link mm-scale swimming robots in cylindrical channel are developed and validated with experiments and used to study the effects of the radial position of the robots as well as the wavelength and wave amplitude of the helical tails on the swimming speed, efficiency and forces acting on the body inside circular channels. In order to understand the flow field induced by the magnetic micro robot and the interaction of the micro robot with the channel wall, CFD-based analysis of the flow field is presented which calculates forward, lateral and vertical velocities of the swimmer no.1 as a function of the position of the swimmer.
- Micro-Particle Image Velocimetry (PIV): Images of flow at different cross-sectional planes using micro-PIV is obtained and compared with CFD results to visualize and fully understand the flow field induced by the

rotation of mm-scale helical swimmers.

- Sensing: Hall-effect sensors are used to predict the place of mm-scale magnetic swimmers inside channels.
- Navigation: Magnetic navigation of mm-scale helical swimmers inside rectangular channels is demonstrated by using the direction and the frequency of rotating magnetic field in Y-shaped and T-shaped channels and for obstacle avoidance inside channels.

This thesis focuses on the in-channel swimming behavior of bio-inspired and artificial swimmers with helical tails inside viscous fluid filled channels in order to point out the differences from unbounded swimming and the points to be considered in designing micro swimmers and developing their control algorithms. Design and control of micro-robots for in vivo medical applications can benefit greatly from the results and detailed analysis presented in this thesis.

Experimental and computational fluid dynamics (CFD) studies are performed using bio-inspired two link cm-scale swimmers with helical tails in cylindrical channel are presented in Chapter 4. In this chapter, a CFD model is developed, validated with the experiments and used to study effects of the radial position of the robots as well as the wavelength and wave amplitude of the helical tails on the swimming speed, efficiency and forces acting on the body inside circular channels. Radial position of the robot is very important in the hydrodynamic analysis of in-channel swimming: first, the radial position of the robot can be controlled, for example, by magnetic forces albeit crudely when necessary; and second, in cases when the radial position cannot be controlled and governed by other forces acting on the robot, its effects need to be understood well and incorporated in simple hydrodynamic relationships, such as the resistive force theory [23], in analytical models that incorporate all the forces acting on the robot, e.g. as in [52]. Contact forces arise when swimmer touches the rigid cylindrical wall is neglected in this study, since they produce a sudden impact and do not affect the swimming behavior as observed in experiments; neither tails of the robots stop rotating, nor an irregularity in the forward velocity is observed. Experiments are conducted with a bio-inspired cm-scale robot inside a circular channel filled with a silicone oil to mimic the low Reynolds number swimming conditions of small scale organisms [89].

Artificial one link mm-scale magnetic swimmers with helical tails are used to

perform experiments inside fluid-filled cylindrical channels which are presented in Chapter 5. Swimming experiments of mm-sized micro robots in glycerol and water-filled mini channels that are actuated by a rotating external magnetic field generated by two pairs of counter facing electromagnetic coils are presented. Experiments are carried out for two swimming micro robots which consist of heads made of permanent magnets and rigid helical tails of different dimensions, which simulate micro-fluidic regime since the same flow conditions as micro-scale rotation arise when they are in glycerol-filled mini channels. Moreover, a 6-dof time-dependent hydrodynamic model is built based on RFT including: a novel technique to implement cylindrical channel effects, and magnetic step-out frequency phenomena. Experimental results are used to validate the proposed hydrodynamic model with appropriate tuning of body resistance coefficients due to irregular shapes of the magnetic heads and the overall flow conditions that differ from simple viscous drag on the body, which is commonly used to obtain analytical body resistance coefficients.

In addition to the experiments and theoretical studies, Chapter 5 includes CFD simulations of the artificial one link swimmer and visualization of the flow inside the cylindrical channel using micro-PIV. Simulation-based analysis of the flow field induced by the one-link swimmer inside a circular channel is performed to calculate hydrodynamic forces and torques acting on the swimmer and the swimming efficiency as a function of the wavelength and amplitude of the helical tail and the radial position of the swimmer. A three-dimensional steady-state CFD model is developed and solved with the commercial finite-element software COMSOL Multiphysics [91]. Furthermore, micro-Particle Image Velocimetry (micro-PIV) method is used to visualize resultant flow fields due to the rotation of helical micro swimmers inside cylindrical channels for different rotational frequencies.

In the experiments performed using helical micro robots near plane boundaries, it is observed that two motion mechanisms are used for forward and lateral motion, which are explained in Chapter 6. Experiments are performed using helical magnetic micro swimmers inside rectangular channels on rough and smooth surfaces and at different angular velocities to study the effects of surface roughness and rotation frequency on the forward velocity. Micro robots are placed inside glycerol-filled rectangular channels move forward due to the rotation of helical tails in the direction of helical axis and move laterally by rolling due to the wall traction. Moreover, high and low frequency behavior of micro robots inside rectangular channel differs due to the resultant flow

fields. In CFD models, a viscous fluid layer is proposed to simulate the wall and simulations are validated with experiments. Calculated translational and angular velocities are used to predict the position and orientation of the micro swimmers inside rectangular channels.

In the last chapter, experiments on magnetic sensing and controlled navigation of magnetic helical swimmers are investigated to understand how magnetic micro swimmers can be controlled in conduits. Hall-effect sensors are used to predict the position of micro swimmer inside channel by measuring magnetic field strength. In addition, motion mechanism of micro robot is used to overcome obstacles inside channels and micro robots are navigated through channel networks by controlling the strength, direction and rotational frequency of the externally applied magnetic field.

4 SWIMMING OF BIO-INSPIRED SWIMMERS IN CHANNELS

Experiments with scaled-up robots swimming in viscous fluids at low Reynolds number are used to demonstrate the efficacy of the actuation mechanism as well as validate hydrodynamic models; since flow physics remains the same, i.e. creeping flow conditions for low Reynolds numbers are preserved. According to Purcell [7], a man would experience the same forces and effects as a bacterium if he tries to swim in a pool that is full of molasses; low Reynolds number environment have the same physical effects regardless of length scale. Several studies are performed in macro scale to study and model motion in micro scale and presented in literature [6, 17, 23, 81].

In this chapter, computational fluid dynamics (CFD) model for a two-link swimming robot in cylindrical channel is discussed. The developed CFD model is validated with the previous experiments presented in [89]. The effects of the radial position of the robot and the wavelength and wave amplitude of the helical tail on the swimming speed, efficiency and forces acting on the body inside circular channels are presented. Radial position of the robot is very important in the hydrodynamic analysis of in-channel swimming: first, the radial position of the robot can be controlled, for example, by magnetic forces albeit crudely when necessary; and second, in cases when the radial position cannot be controlled and governed by other forces acting on the robot, its effects need to be understood well and incorporated in simple hydrodynamic relationships, such as the resistive force theory [18], in analytical models that incorporate all the forces acting on the robot, e.g. as in [52]. Contact forces, which arise when the swimmer touches the rigid cylindrical wall, are neglected in this study, since they produce a sudden impact and do not affect the swimming behavior as observed in experiments; neither tails of the robots stop rotating, nor an irregularity in the forward velocity is observed.

Experiments are conducted with a bio-inspired cm-scale robot inside a circular channel filled with a silicone oil to mimic the low Reynolds number swimming conditions of small scale organisms. The numerical model is based on the solution of

three-dimensional Stokes equations subject to no-slip boundary conditions on the body and the tail of the robot and on channel walls as widely used in earlier/similar studies [7, 38, 51, 54]. The approach presented here is valid for scales greater than about 100 nm where the continuum hypothesis remains valid and no-slip boundary conditions hold. Swimming in nanometer scales, close contact with channel walls and non-Newtonian behavior of bodily fluids are outside the scope of this thesis. Fully-coupled solution of Stokes equations with those limitations remains a challenge and the subject of our ongoing efforts.

The two-link swimming robot used in the experiments has two counter rotating components: a capsule body and a helical tail [89, 90]. Experiments are conducted with fifteen different tails attached to the body; wavelength (helical pitch) and amplitude (radius of the helix) are varied for each tail. Forward velocity of the robot and rotational frequencies of the tail and the body are measured.

During experiments, it is observed that the swimming robot does not align with channel's long axis and it swims near the wall at the bottom rather than the center of the channel. In order to clarify robot's position and orientation when swimming inside a circular channel and calculate forces and torques acting on the swimming robot, a CFD model is developed using the commercial finite-element package, COMSOL Multiphysics [91]. The CFD model is validated with the experimental results. Simulations are performed for the same geometric parameters of the robot and the channel as the ones used in the experiments, except the radial position of the robot in the channel, which was difficult to measure in experiments. For each tail, radial position of the robot is varied between 0 and 8.9 mm in the simulations, and for each specified position of the robot the angular rotation of the helical tail is varied between $\pi/6$ and 2π : in total $16 \times 8 \times 12 = 1536$ three-dimensional simulations are performed in addition to mesh convergence studies for selected tails and radial positions.

4.1 Methodology

4.1.1 Experimental Studies

The robot used in the experiments is untethered and consists of a body and a helical tail. The body of the robot is made of a glass tube of outer diameter of 1.6 cm

and thickness of 1 mm and a plastic cover with outer diameter of 1.8 cm and length of 1 cm. Inside the glass tube, a power source, Li-polymer battery (3.7 V, 65 mAh) of dimensions $17.3 \times 13.5 \times 13.5 \text{ mm}^3$; a brushless DC motor of diameter of 6 mm and length of 14 mm with 3V DC nominal voltage and 200 mA nominal current; and a small switch of dimensions $7 \times 3 \times 3 \text{ mm}^3$ are held together with an adhesive putty that ensures rotational symmetry and neutral buoyancy of the body. Table 4.1 summarizes common dimensions of robots.

In order to study effects of the pitch (wavelength) and radius (amplitude) of the helical tail on swimming speed of the robot, 15 different helical tails are made of steel wire of diameter 1 mm. Tails are manufactured manually by wrapping the steel wire around rigid bars of desired diameter to obtain amplitudes, A , of 1, 2, 3 and 4 mm, which corresponds to a ratio between amplitudes and channel diameter, A/r_{ch} , $1/18$ (0.056), $2/18$ (0.112), $3/18$ (0.167) and $4/18$ (0.223). Then the coil is plastically deformed by extending it to desired wavelengths that correspond to 2, 3, 4 and 6 turns, N_i , on the helical tail, which has a fixed length, 6 cm; the total length of the wire varies with the wavelength and amplitude. Only the tail with the largest amplitude, 4 mm, and the smallest number of turns, 2, was not achieved satisfactorily and eliminated from the ensemble.

Table 4.1 Common dimensional properties for robots and channel

Radius of the body, r_b	0.8 cm
Total length of the body, L_b	4 cm
Outer radius of the cap, r_{cap}	0.9 cm
Length of the cap, L_{cap}	1 cm
Apparent length of tails, L_{tail}	6 cm
Length of couplings	1 cm
Diameter of tail wire, $2r_{tail}$	1 mm
Diameter of the channel, $2r_{ch}$	3.6 cm

Fixed plastic couplings are used to secure each tail to the shaft of the dc-motor that protrudes from the capsule. The robot consisting of the capsule and the tail is placed inside an open-ended circular glass channel with the diameter of 3.6 cm and length of 30 cm inside an aquarium filled with silicone oil with a viscosity of 3.5 Pa·s as shown in Figure 4.1c. The body, which is used for all robots, is neutrally buoyant;

however robots rest at the bottom of the horizontally placed channels due to the weight of the steel wire tail.

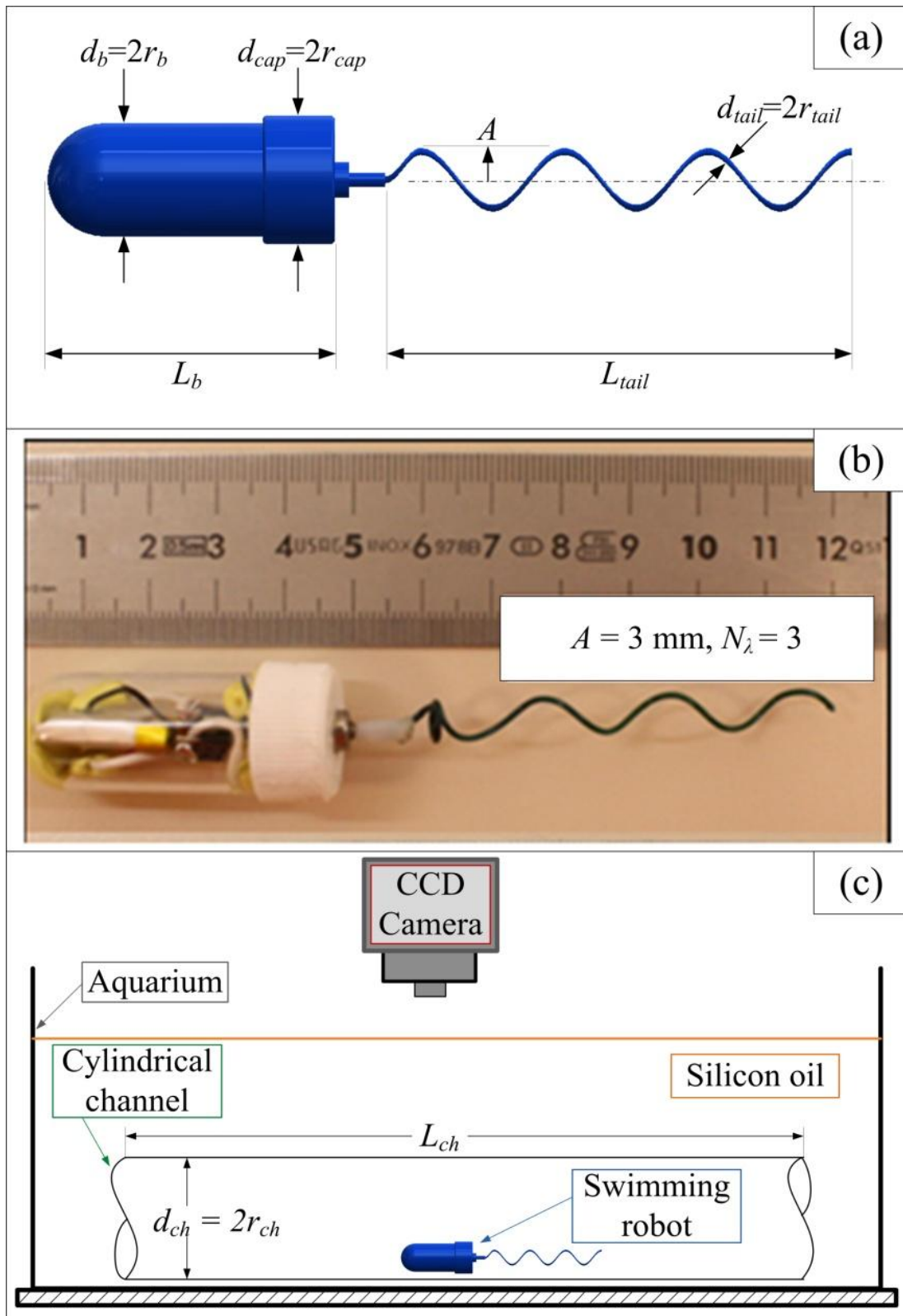


Figure 4.1 (a) Dimensional parameters of the swimming robot. (b) Layout of the robot with the helical tail of amplitude 3 mm and having 3 waves on its tail. (c) Schematic representation of the experimental setup.

For each experiment, the battery that supplies power for the dc-motor is charged fully, the switch is turned on manually and the robot is placed inside the channel near the mid-axis. The motion of the robot is recorded with a CCD camera. Frequencies of tail and body rotations and forward velocity of the robot are calculated from orientations of the body and the tail, and from the position of the robot in recorded images.

4.1.2 Computational Fluid Dynamics Studies

Swimming of robots inside an open-ended circular channel filled with viscous silicone oil is simulated using a CFD model. Body of the robot is modeled almost identically as the body used in the experiments with the union of a sphere and a cylinder (see Figure 4.1a and Figure 4.2). As a connector between the body and the helical tail, another cylindrical piece is attached to the bottom of the body; finally a helix is used to model the tail. Dimensions of the robots modeled here are the same as the robots used in the experiments.

In the creeping flow regime, inertial forces are negligible, and incompressible flow is governed by viscous forces balanced by the pressure gradient subject to continuity:

$$\mu \nabla^2 \mathbf{u} - \nabla p = 0 \quad \text{and} \quad \nabla \cdot \mathbf{u} = 0 \quad (4.1)$$

where μ is viscosity, \mathbf{u} is the velocity vector and p is pressure.

In the absence of inertial forces, the flow induced by the rotation of the helical tail and the motion of the robot has no memory; instantaneous snapshot solutions of the velocity field and the pressure are obtained from (4.1) using boundary conditions for the given position of the robot and the helical tail. The centerline position of the wire, which forms a right-handed helical tail, is given by

$$\mathbf{P}_{tail} = [x_{tail} \quad A \cos(kx_{tail} + \varphi) \quad -A \sin(kx_{tail} + \varphi)] \quad (4.2)$$

where x_{tail} is the axial position of the helical tail measured from the joint, A is the amplitude (helical radius), $k = 2\pi/\lambda$ is the wave number, λ is the wavelength (helical pitch), and $\varphi = \omega t$ is the phase angle that corresponds to the rotation of the helix with angular velocity of ω .

For the forward velocity of the robot, which is an unknown and specified as a boundary condition, the constraint equation for force-free swimming condition is specified as the zero-net force in the swimming direction and obtained from the integration of fluid stresses over the surface of the robot:

$$\int_{S_{tail} \cup S_{body}} \sigma \cdot \mathbf{n}_x dS = 0 \quad (4.3)$$

where σ is the stress tensor, \mathbf{n}_x is the x -component of the local surface normal, and $S_{tail} \cup S_b$ is the whole surface of the robot including its tail and body. Similarly, for the unknown body rotation rate and the given rotational frequency of the tail, zero-net torque constraint is specified as an additional equation:

$$\int_{S_{tail} \cup S_b} [(y - y_{COM})(\sigma \cdot \mathbf{n}_z) - (z - z_{COM})(\sigma \cdot \mathbf{n}_y)] dS = 0 \quad (4.4)$$

where $(y, z)_{COM}$ are (y, z) -coordinates of the joint and $\mathbf{n}_{(y, z)}$ are y - and z -components of the surface normal.

4.1.2.1 Boundary conditions

Inlet and outlet of the channel are set to open boundary conditions, i.e. the normal stresses are zero:

$$(-p\mathbf{I} + \sigma)\mathbf{n} = 0 \text{ at } x = 0, L_{ch} \quad (4.5)$$

No-slip boundary conditions are used at the solid surfaces, which are the channel wall and the swimmer's surface. The slip length between glass (solid) and silicon oil (liquid) interfaces is on the order of 20 nm [55], and does not constitute a limiting issue in the experiments. Furthermore no-slip boundary conditions hold well in a variety of micro flows [65], and it is assumed that no-slip conditions remain valid for swimming of structures and organisms that are at least tens of microns long for channels that have similar dimensions. Thus, no-slip boundary conditions at the channel walls are:

$$\mathbf{u} = 0 \text{ at } r = r_{ch} \quad (4.6)$$

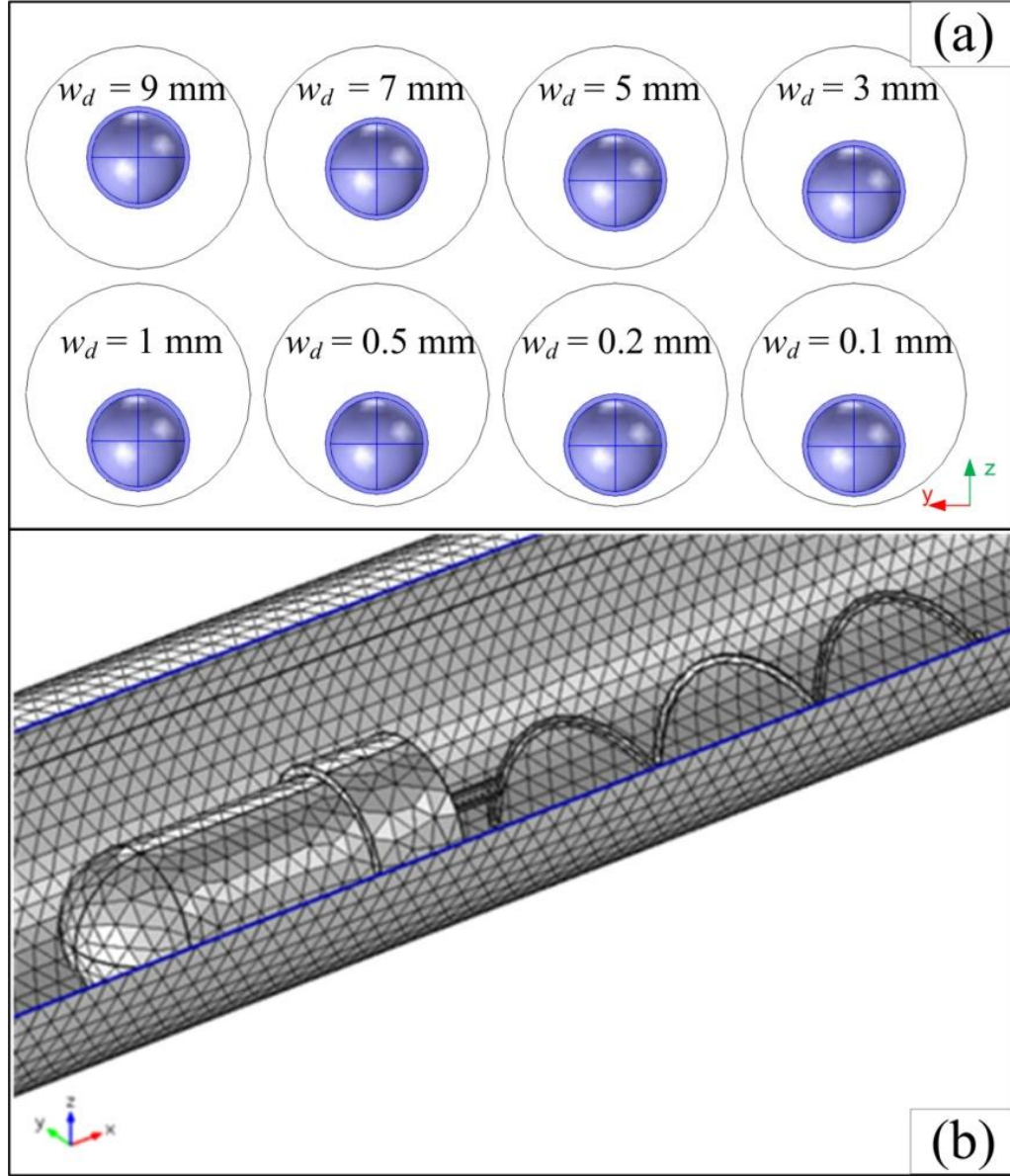


Figure 4.2 (a) The radial position of robot in CFD model is changed along \mathbf{z} -axis until the distance between the robot and channel wall, w_d , is equal to 0.1 mm. (b) Mesh distribution of having 4 full waves on its tail and $A = 4 \text{ mm}$, traveling near the wall with distance to the wall, w_d , equals 0.1 mm.

The swimming robot moves with a forward velocity, U , while the body and the tail counter-rotate at different rates. Therefore, no-slip moving-wall boundary conditions for the body and the tail are specified as:

$$\mathbf{u}(\mathbf{x}) = [U, 0, 0] + [0, y, z - r_{sw}] \times [\Omega_b, 0, 0] \text{ for } \mathbf{x} \in S_b \quad (4.7)$$

and

$$\mathbf{u}(\mathbf{x}) = [U, 0, 0] + [0, y, z - r_{sw}] \times [\omega_{tail}, 0, 0] \text{ for } \mathbf{x} \in S_{tail} \quad (4.8)$$

where r_{sw} is the position of the robot in the \mathbf{z} -direction and varied between 0 (centerline) and a value, which corresponds to a small gap between the body and the channel wall; Ω_b is the body rotation rate; and ω_{tail} is the rotation rate of the tail.

4.1.2.2 Simulation parameters

Governing equations given by (4.1) subject to constraint equations (4.3) and (4.4) and boundary conditions (4.5) to (4.8) are solved with the finite-element method (FEM) software, COMSOL Multiphysics [91].

The finite-element model consists of approximately 90000 tetrahedral elements and 450000 degrees of freedom. The linear system of equations is solved using the PARDISO direct solver. For each configuration of the tail and the radial position of the robot the average velocity and the body rotation rate are obtained from 12 different angular positions in $\pi/6$ increments; each simulation takes about 3 to 5 minutes on a high end workstation with 12 cores operating at 2.7 GHz and sharing 96 GB of RAM. Figure 4.2b shows the mesh distribution when the distance between the robot and the channel wall, w_d , equals 0.1mm with the finest mesh.

In simulations, radial position of each robot in the channel is varied between 0 and 8.9 mm, which is specified only in the \mathbf{z} -direction with respect to the centerline of the channel for $y = 0$ (see Figure 4.2). For $r_{sw} = 0$, the axis of the robot lies on the centerline of the channel, and for $r_{sw} = 8.9$ mm, the closest distance between the body and the channel wall, w_d , is only 0.1 mm. In order to set the position of robot closer than 0.1 mm, restrictive constraints on the finite-element mesh are necessary for accurate solutions. Moreover, as results indicate any further increase in the proximity of the robot to the channel wall does not change the trend.

4.2 Results

Experiments are performed with fifteen tails having different wavelength and amplitudes to obtain the forward velocity of the robot and the rotation rates of the body and the tail. Experimental results are compared with the ones from CFD simulations to validate the CFD model, which is then used to predict the effect of the radial position on the velocity, forces acting on the robot and efficiency.

4.2.1 Experimental Results

Experimental results are listed in Table 4.2. Hydrodynamic models and numerical results indicate that the forward velocity increases with the frequency and amplitude, but has an optimum for the wavelength, which depends on other parameters such as the size of the body and the length of the tail [18, 42, 53, 54, 92]. In the experiments, the frequency of the tail rotation varies according to the torque balance for each tail; therefore theoretical trends are not discernible easily. The rotation frequency of the tail decreases with increasing number of waves and the amplitude due increasing viscous torque. Therefore the tail's rotation frequency and the forward velocity are at their maximum values for each tail according to the current and power constraints of the battery and the dc motor.

In the experiments, maximum forward velocity is 1.01 mm/s for the robot with a helical tail that has 3 full waves and 3-mm amplitude, for which the frequency of tail rotations is 2.49 Hz; the minimum forward velocity is 0.32 mm/s for the robot with 6 full waves and 4mm amplitude, for which the tail's rotation frequency is the smallest as well, 0.89 Hz.

The frequency of rotations of tails and bodies vary significantly between robots. Frequency of tail rotations is larger for tails with small amplitudes (between 4.3 and 8.2 Hz for $A = 1$ mm) than tails with large amplitudes (between 0.9 and 1.2 Hz for $A = 4$ mm). However, rotational frequency of the body, in principle, is expected to be constant as long as the torque provided by the motor is constant. Variation in body rotation rates could be due to the power-angular velocity relationship of the DC motor, or the contact friction between robots and the channel wall; part of the robot's weight comes from the

tail and increases with the actual length of the wire, which increases with the amplitude and number of helical waves.

Table 4.2 Experimental Results

Robots	Amplitude, A [mm]	Number of Waves, N_λ	Rotational Frequency of the Tail, $\omega_{tail}/2\pi$ [s^{-1}]	Forward Velocity of the Robots, U [mm/s]	Rotational Frequency of the Body, $\Omega_b/2\pi$ [s^{-1}]
R1	1	2	8.19	0.68	0.049
R2	1	3	4.32	0.59	0.035
R3	1	4	4.33	0.47	0.034
R4	1	6	6.13	0.56	0.043
R5	2	2	3.80	0.78	0.060
R6	2	3	3.27	0.83	0.055
R7	2	4	3.14	0.96	0.057
R8	2	6	2.84	0.57	0.057
R9	3	2	2.01	0.81	0.067
R10	3	3	2.49	1.01	0.065
R11	3	4	2.14	0.94	0.057
R12	3	6	1.59	0.44	0.048
R14	4	3	1.18	0.97	0.063
R15	4	4	1.10	0.70	0.055
R16	4	6	0.89	0.32	0.051

Furthermore, exact radial positions of robots were difficult to measure in the experiments; it is expected that robots travel as close as possible to the channel wall due to their weight. Moreover, the stiction of the robot on the channel wall is not observed in experiments; for all cases, rotation of the body and the forward motion always prevailed. Computational fluid dynamics is used to model the flow and obtain forward velocity and body rotation rate for observed tail rotation rates in experiments for each robot to confirm that the motion of robots is dominated by hydrodynamic effects. The possible contacts of robot and channel wall are neglected in CFD simulations, since they were not observed in experiments. In addition, when robot gets very close to the wall, lubrication physics is governed. In the lubrication layer, the thin layer between

two solids, in this case robot and channel wall, Reynolds number is far below 1 [93], thus Stokes equations are valid for hydrodynamic solution of the flow within the layer [93, 94]. Moreover, molecular influences become significant if the thickness of the lubrication layer is smaller than 10 nm [95] and the minimum thickness between robot and channel wall is equal to 100 μm in CFD simulation.

4.2.2 CFD Results

4.2.2.1 Forward velocity

Experimentally obtained forward velocities are compared with CFD simulation results in Figure 4.3. In experiments, it is observed that swimming robot is moving at the bottom of the channel, but the distance between the channel wall and robots could not be determined. In simulations, the radial position is varied between 0 and 8.9 mm, which corresponds to 0.1 mm distance from the wall, for each robot. Furthermore for each radial position of each robot, average forward velocities and body rotation rates are obtained from averaging of 12 angular positions of the tail with increments of $\pi/6$.

Comparisons of experimental and simulation results indicate that most of the robots swim near the wall with a very small clearance. When the distance between the channel and the robots is 0.1 mm and 0.2 mm, velocity of the robots obtained from simulations agree very well with experimental results, particularly for $A = 2$ mm, 3 mm, and 4 mm (Figure 4.3b, c and d). When $A = 1$ mm, simulation results for robots having a distance of 0.2 mm to the channel is in a better agreement than the case for which the distance is 0.1 mm, although the results are very close. Velocities obtained from CFD simulations for the robots travelling near the wall with a clearance of 1 mm are somewhat higher than the velocities obtained in experiments. The velocity values are on the order of 1 mm/s, and the fastest robot has 3 full waves on its helical tail with the amplitude (radius of the helix) equals to 3 mm (R10 in Figure 4.3c).

In the case of one-link swimmer with a helical tail attached to a permanent magnet and reported in [54], forward velocity of the swimmers is larger near the wall than at the center of the channel. Furthermore, although a one-to-one comparison with the one-link magnetic swimmer is not applicable here since dimensional ratios of head and tail are

different in two cases, the decrease in velocities for $A = 4$ mm as N_λ increases is similar for both cases.

Analytical studies show that, swimmers with helical tails in unbounded fluids [18, 42] and in cylindrical channels [53] have an optimal number of wave values that maximizes the swimming speed. Based on an analysis using stokelets, Higdon [42] presented that for the same rotational speed, the optimum number of wave value to reach the maximum swimming speed is equals 3 for a swimmer with L_{tail}/r_b and r_{tail}/r_b equal 10 and 0.02, respectively, where L_{tail} is the length of the flagellum, r_b is the radius of the body and r_{tail} is the radius of the flagellum. Higdon [42] also stated that the optimum number of wave value is highly dependent on the geometry of the swimmer and the decrease in swimming speed for number of wave numbers greater than the optimum value is a result of the efficiency drop, since the helical structures lose their slenderness as wavelength decreases. In Fig. 3, the existence of and change in optimal number of wave value with respect to the tail geometry is observed. For $A = 2, 3$ and 4 mm, optimal number of wave values are 3, 2 and 1 (last result is according to simulations), respectively.

When $A = 1$ mm, swimming speed shows a different trend than the rest. The rotational frequencies of tail and body drop for robots R2 and R3, which might be a reason of uneven tails due to their hand-made manufacturing process, or insufficient charge of batteries although they were charged before every experiment.

In Figure 4.4, forward velocities are normalized with the rotational frequency of the tail to eliminate the effect of the frequency on the forward velocity, so that the effect of the amplitude and the wavelength is emphasized. In fact, U/f , represents the stroke, which is the distance traveled for a full rotation of the tail. CFD simulations agree very well with experimental results particularly for robots swimming near the channel wall with a distance of 0.1 mm and 0.2 mm especially for $A = 2$ mm.

According to experiments and near-wall simulations the stroke, U/f , increases with the amplitude. Although the simulation results predict that the U/f increases with N_λ for $A = 1$ mm, experimental results indicate that there is an optimal value of the number of waves on the tail (Figure 4.4a). Simulation results agree with the experimentally measured results in predicting that there are optimal values of N_λ for $A = 2$ and 3 mm (Figure 4.4b-c), and that U/f decreases with N_λ for $A = 4$ mm (Figure 4.4d).

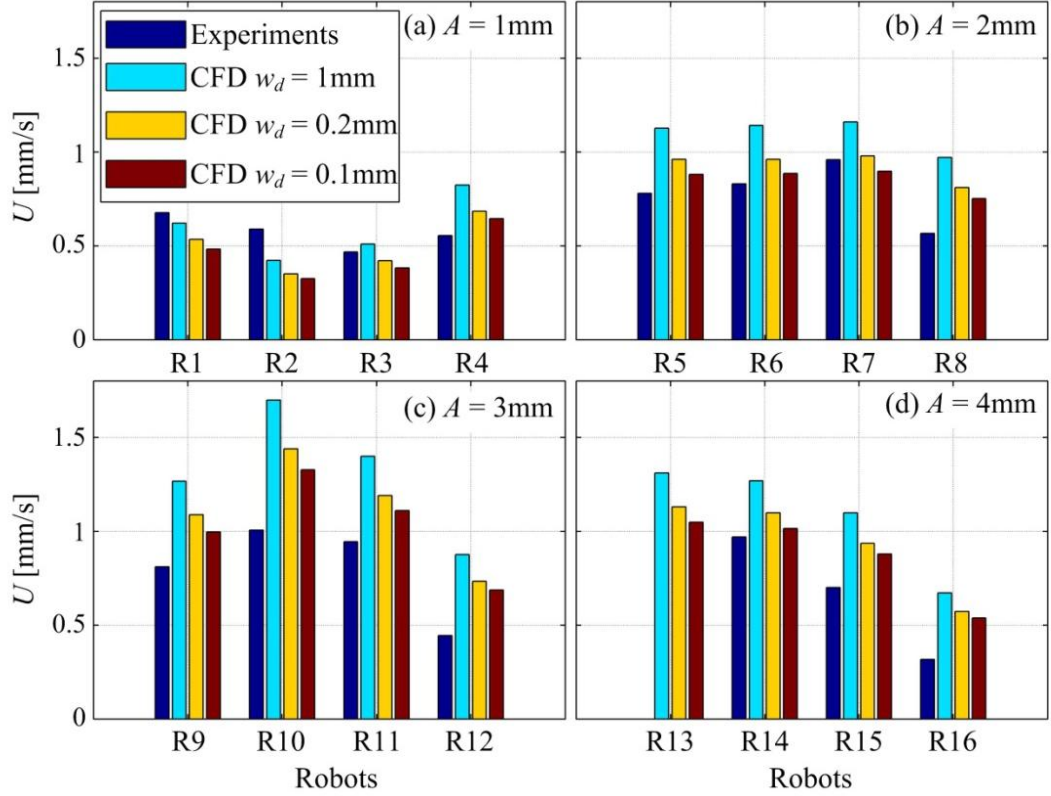


Figure 4.3 Velocity of robots, from experiments (navy), from CFD simulations for robots traveling near the wall with distance to wall, w_d , equals 1mm (cyan), for robots traveling near the wall with distance to the wall, w_d , equals 0.2 mm (yellow), and for robots traveling near the wall with distance to the wall, w_d , equals 0.1 mm (red) for amplitudes, A , equals (a) 1 mm, (b) 2 mm, (c) 3 mm and (d) 4 mm.

The effect of the radial position on the velocity of the robot is shown in Fig. 5, where the radial position of the swimmer, r_{sw} , is normalized with the channel radius, r_{ch} . For all amplitudes and number of waves, the stroke is higher for robots closer to the wall than the ones at the center up to almost 30%; in particular when the normalized radial position, r_{sw}/r_{ch} , is about 0.4. Similarly, 30% increase in the forward velocity is observed for the one-link swimmer as well for r_{sw}/r_{ch} about 0.5 [96]. This improvement in the forward velocity can be attributed to the reduction in the body resistance coefficient near the wall. For radial positions greater than the optimal value that corresponds to the minimum resistance of the body, velocities of robots decrease sharply due to increased viscous for near the wall; it is plausible that expected velocity of the robot goes to zero when the distance from the wall goes to zero given that the interaction between the robot and the channel wall is based on hydrodynamic effects. Traction forces due to van der Waals or Coulomb interactions are expected to dominate when the proximity to the channel wall is on the order of tens of nanometers; however, accurate modeling of traction forces remains a challenge.

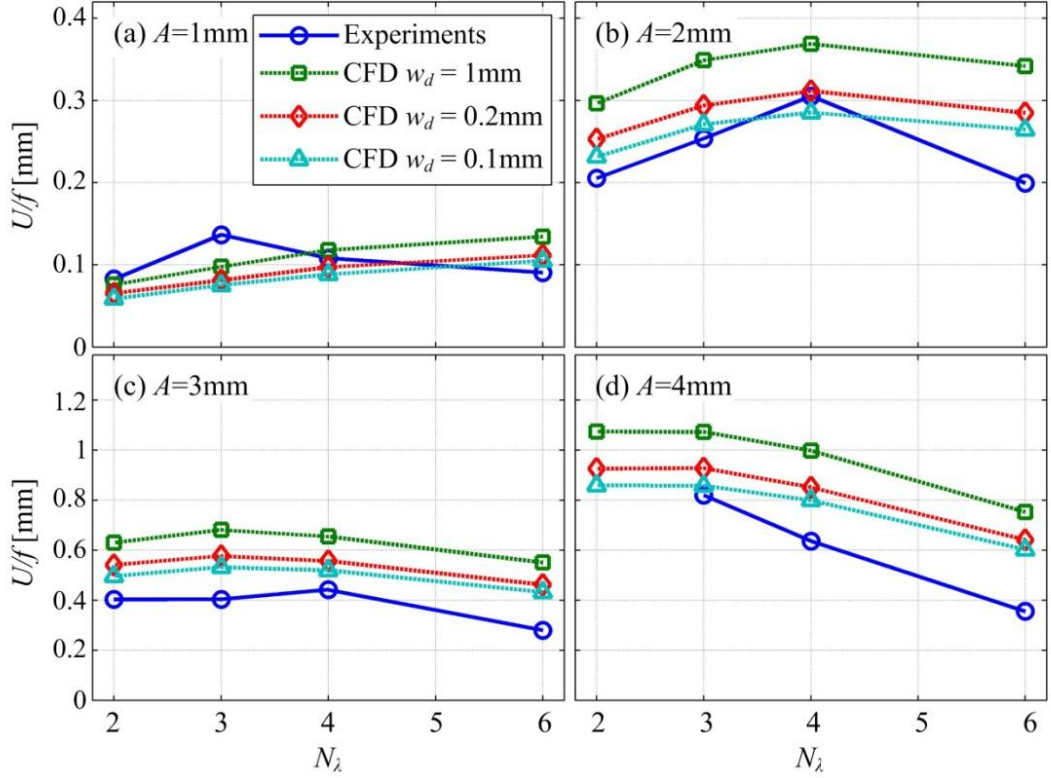


Figure 4.4 Velocity of robots are normalized with the rotational frequency of the tail, f . Results are from experiments (‘circles’), from CFD simulations for robots traveling with distance to wall, w_d , equals 1 mm (‘squares’), for robots traveling with distance to wall, w_d , equals 0.2 mm (‘diamonds’), and for robots traveling with distance to the wall, w_d , equals 0.1 mm (‘triangles’) for amplitudes, A , equal to (a) 1 mm, (b) 2 mm, (c) 3 mm and (d) 4 mm, and for number of waves, N_λ , between 2 and 6.

In Figure 4.5, it is also observed that the number of waves has a positive effect for $A = 1$ mm (Figure 4.5a), for which the stroke increases with the number of waves for all radial positions; although the increase with the radial position is not as much for $N_\lambda = 2$ as other values of N_λ . For $A = 2$ mm, the stroke is the highest for all radial positions in the case of $N_\lambda = 4$, and the lowest for $N_\lambda = 2$; strokes are almost identical for $N_\lambda = 3$ and 6 at all radial positions (Figure 4.5b). For $A = 3$ mm, strokes are very similar for all number of waves and radial positions; however the increase in the stroke with the radial position is not as pronounced as other values of N_λ than 6 (Figure 4.5c). This is also the case for $A = 4$ mm, for which the stroke for $N_\lambda = 6$ is significantly lower than others followed by the stroke for $N_\lambda = 4$, which does not increase as much as it does for $N_\lambda = 2$ and 3 near the wall (Figure 4.5d).

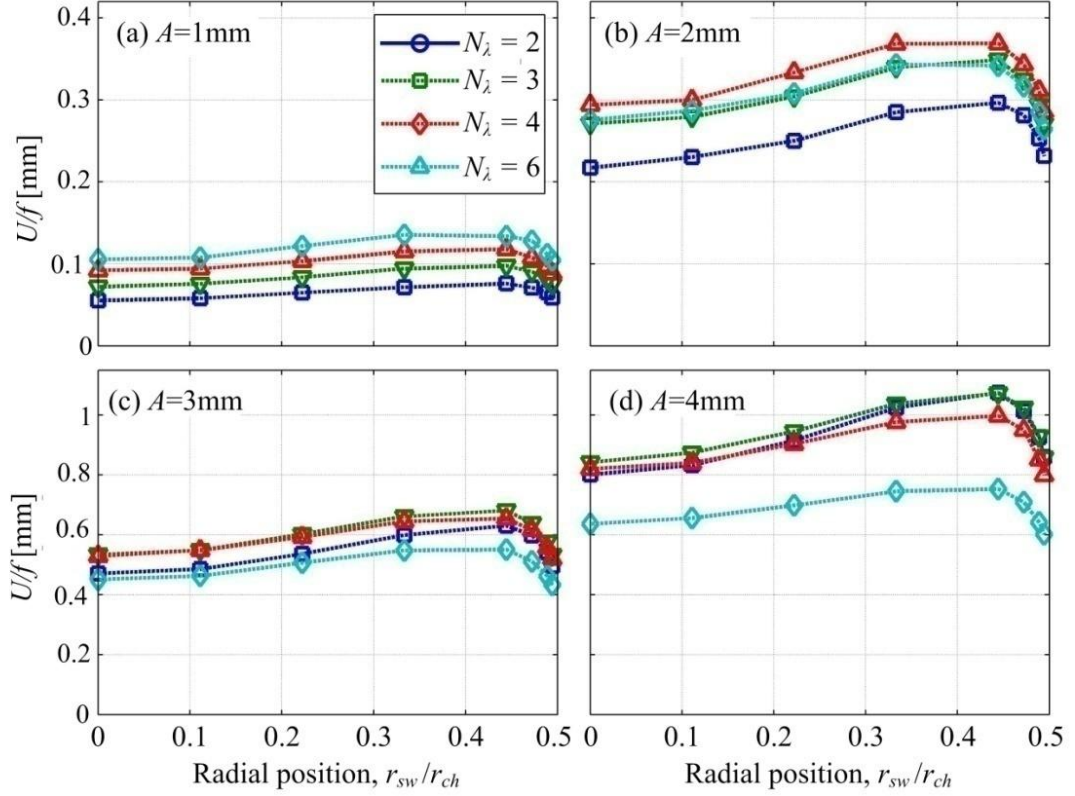


Figure 4.5 Simulation results of velocity of the robots are normalized with the wave speed, $S_w = \omega/k$, as a function of the radial position of the robot for A equals (a) 1 mm, (b) 2 mm, (c) 3 mm and (d) 4 mm; and for $N_\lambda = 2$ ('square'), 3 ('downward triangles'), 4 ('upward triangles') and 6 ('diamonds').

Furthermore, differences between experiments and CFD results in Figure 4.4 can be attributed to, in part, the actual radial position of the robot for each tail in the experiments. Although the closest radial position to the channel wall is set to 0.1 mm in the simulations, the radial position of each robot is expected to vary in the experiments. Therefore, one can conclude that robots travel closer to the channel wall for $A = 3$ mm and 4 mm, as experimentally measured velocities are smaller than the ones predicted by the CFD model, and robots slow down as they travel closer to the channel wall as shown in Figure 4.5. For $A = 2$ mm, radial position of the robots in the experiments is more or less 0.1 mm, although the experimental result is below the CFD result for $N_\lambda = 6$; for $A = 1$ mm, robots travel farther from the wall. The interpretation presented here, also agrees with the weight of individual tails that increase with the wire length (curvilinear length) of each tail, which is given by $\ell_{tail} = [L_{tail}^2 + 4\pi^2 A^2 N_\lambda^2]^{1/2}$, where L_{tail} is the length of the helix. As the weight of the robot increases due to increasing amplitude and number of waves, the average distance between the robot and the channel wall must decrease.

4.2.2.2 Body rotation rates

Normalized body rotation rates with respect to angular velocities of tails are compared in Figure 4.6. Simulation results indicate that the normalized body rotation rate increases with the number of waves and agree very well with experimental results when the distance from the wall, w_d , is set to 0.1 mm and 0.2 mm. Furthermore, for $A = 2$ mm, simulation results for $w_d = 0.2$ mm agree much better with experiments than the simulation results for the rest do indicates that R5-7 swim not very close to the wall. Simulation and experimental results show that according to the geometry of the tail, the position of robots changes but distance between robot and channel wall is always below 0.2 mm.

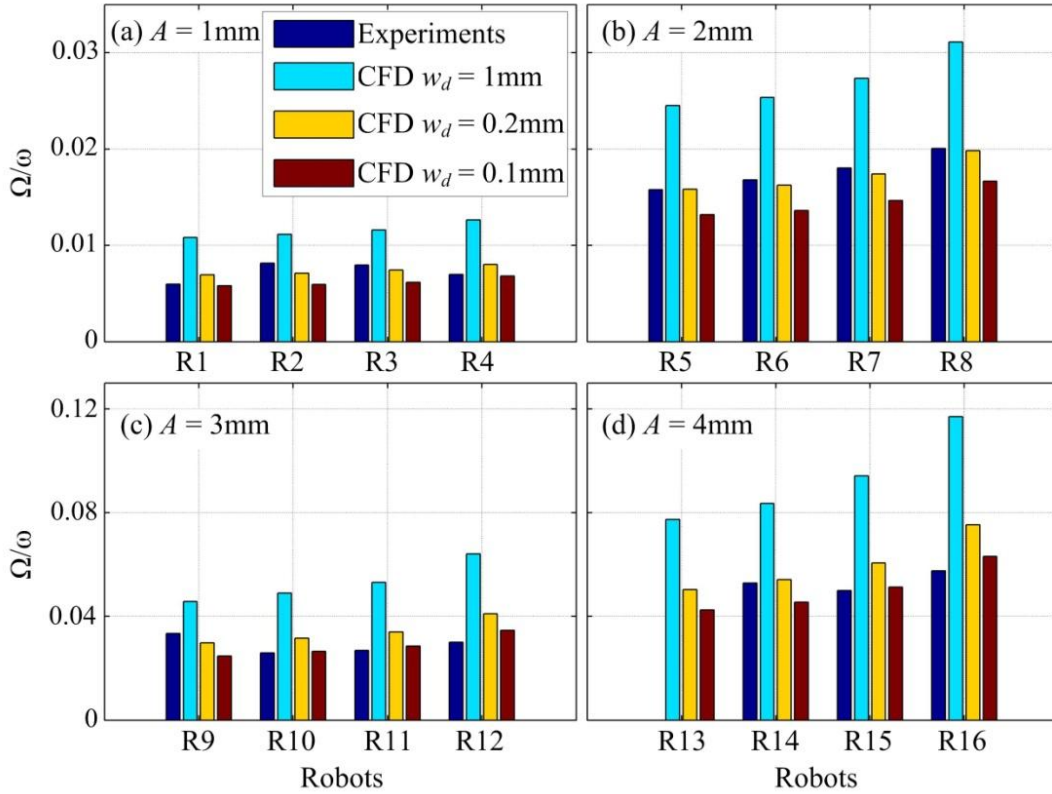


Figure 4.6 Body rotation rates are normalized with the angular velocity of the tail, from experiments (navy), from CFD simulations for robots traveling with a distance to wall, w_d , equals 1 mm (cyan), for robots traveling with a distance to wall, w_d , equals 0.2 mm (yellow), and for robots traveling near the wall with distance to the wall, w_d , equals 0.1 mm (red) for amplitudes, A , equals (a) 1 mm, (b) 2 mm, (c) 3 mm and (d) 4 mm.

4.2.2.3 Body resistance coefficient

In Figure 4.7, the body resistance coefficient, which is the ratio of the axial force on the body to the axial (forward) velocity of the robot, $F_{x,body}/U$, is plotted against the radial position for each robot using the results of the CFD model. As the number of waves and the amplitude of the helical tail increase, body resistance coefficients stay constant for center-swimming as expected, and indicate that tail parameters do not have a significant effect on the body resistance coefficient. However, as the radial position increases, body resistance coefficients decrease to a minimum value where the velocity of the robot almost reaches its maximum (Figure 4.5 and Figure 4.7). As robots get further closer to the channel wall, the body resistance coefficient reaches to the same value as the one at the center of the channel.

For all amplitudes and number of waves, the body resistance coefficient takes a minimum value for the normalized radial position of about 0.4. According to Happel and Brenner [97], resistance of a small sphere traveling inside a cylindrical channel reaches its minimum value for normalized radial position nearly equals to 0.3 at low Reynolds numbers confirming the advantage of off-center swimming.

4.2.2.4 Radial forces and torques

Forces acting on the swimming robot along the radial direction (i.e. the negative \mathbf{z} -direction for $y = 0$) are calculated from CFD simulations and presented in Figure 4.8 as a function of the radial position. As the number of waves on the helical tail and the amplitude increase, there is not a clear indication of a net radial force on the robot for r_{sw}/r_{ch} values between 0 and 0.3. Occasional variations are attributed to lower order of accuracy in the calculation of forces than the accuracy in the calculation of the velocity [91, 98]; force calculations are based on the stress tensor, which uses derivatives of velocity components, which are projected on to second-order polynomials in the finite-element representation. In order to ameliorate the problem finer mesh than the one used in the simulations is necessary; however for the three-dimensional simulations presented here, any further improvement in the finite-element mesh remains too restrictive, and is not critical for the purposes of this work.

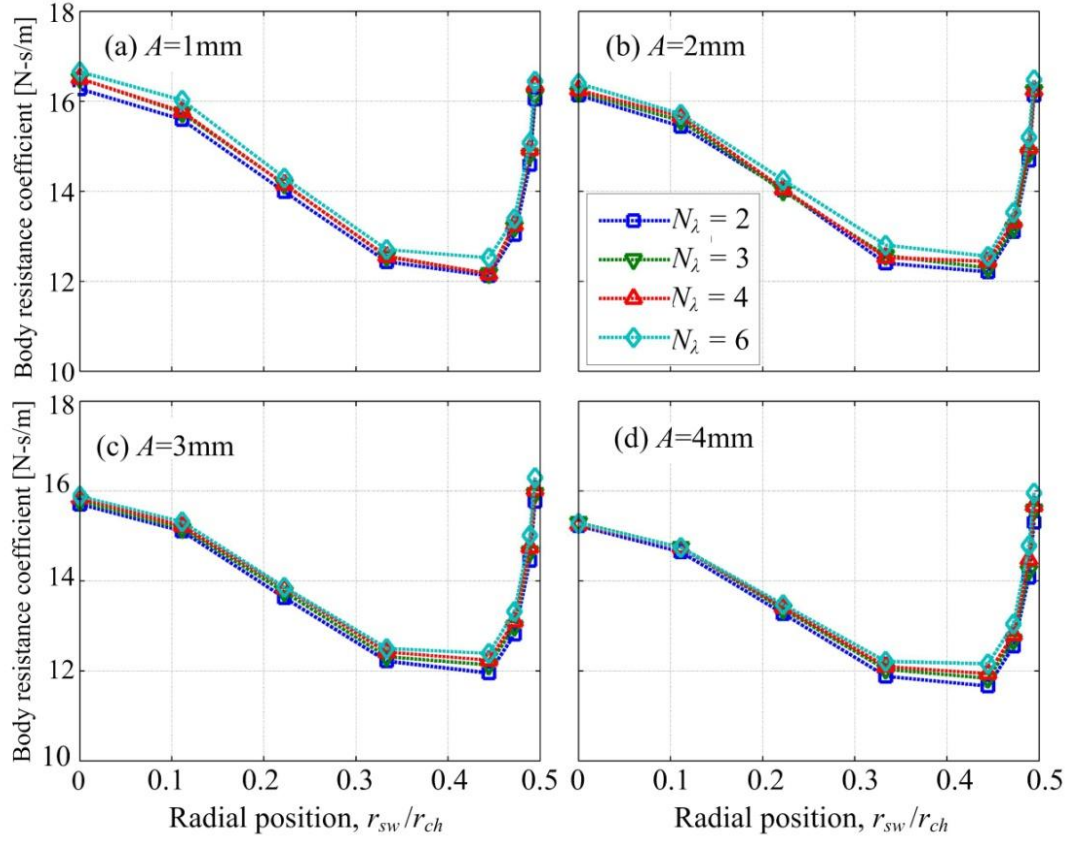


Figure 4.7 Simulation results of body resistance coefficients of the robots with respect to the radial position of the robot for A equals (a) 1 mm, (b) 2 mm, (c) 3 mm and (d) 4 mm; and for $N_\lambda = 2$ ('square'), 3 ('downward triangles'), 4 ('upward triangles') and 6 ('diamonds').

Tail parameters do not have a significant effect on the radial force. As the robot gets closer to the wall, radial force increases first up to $w_d = 0.2$ mm, then a sudden fall and change of sign is observed in Figure 4.8 for all amplitudes and wavelengths. Very close to the wall, i.e. $w_d = 0.1$ mm, the \mathbf{z} -direction force becomes negative, i.e. the radial force is positive, indicating a push towards the wall due to hydrodynamic effects only, when the robot is parallel to the channel's axis. Based on this result and the weight of the robot, a constant contact between the robot and the wall is expected, unless the orientation of the robot is different than the one assumed in the simulations. The increase in the \mathbf{z} -direction force is also observed for the one-link magnetic swimmer in [96] but the sudden fall is not observed.

Since the body and the tail counter-rotate, lateral forces on each link occur in opposite directions. Net positive \mathbf{y} -direction (also the tangential direction) force indicates that the rotation of the tail dominates the force due to the rotation of the head (Figure 4.8e).

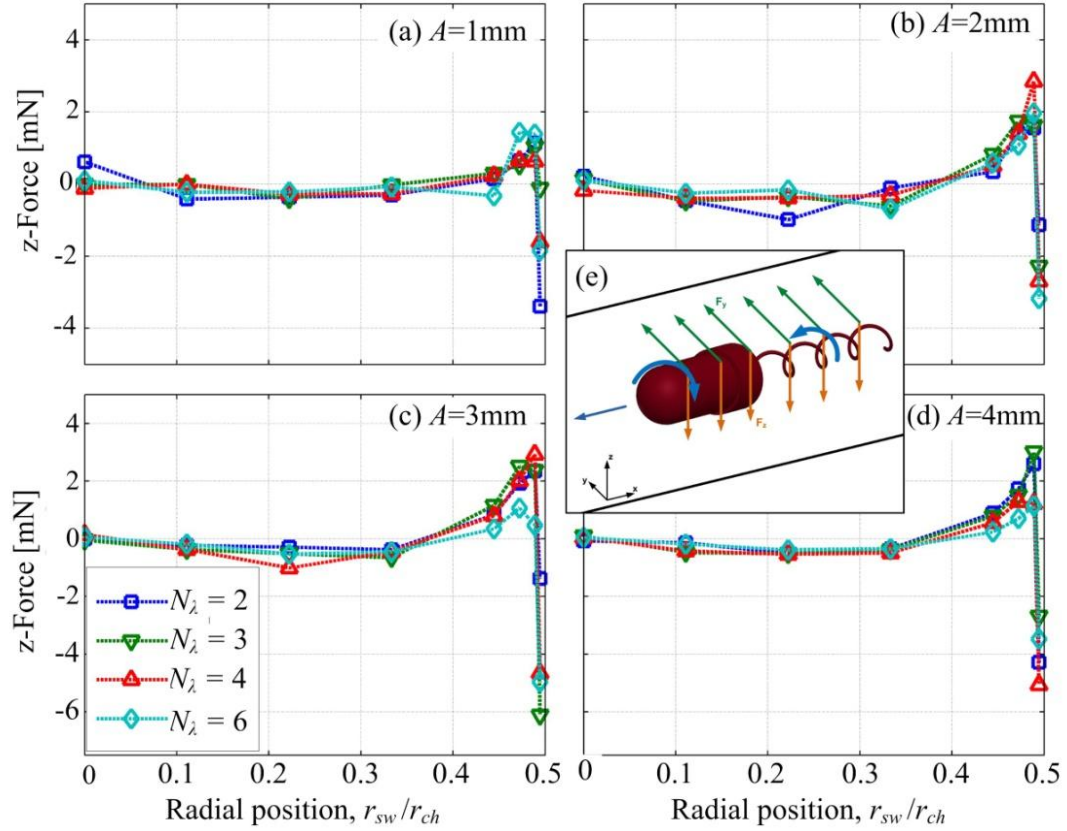


Figure 4.8 Radial force on \mathbf{z} -direction of the robots as a function of the radial position of the robot for A equals (a) 1 mm, (b) 2 mm, (c) 3 mm and (d) 4 mm; and for $N_\lambda = 2$ ('square'), 3 ('downward triangles'), 4 ('upward triangles'), 6 ('diamonds') are obtained from simulations. (e) Schematic representation of forces acting on the robot swimming near the wall.

Torques acting on the swimming robot are calculated in CFD simulations and presented in Figure 4.9. As the number of waves and the amplitude increase, magnitude of the torque along the \mathbf{z} -direction also increases between $r_{sw}/r_{ch} = 0$ and 0.45. As the distance from the wall decreases further, magnitude of the \mathbf{z} -torque decreases. The difference between the \mathbf{z} -torque values of robots having different number of waves on the helical tail becomes discernible as the amplitude of the helical wave increases (Figure 4.9). In all cases, robots having tails with 6 waves are affected the most from the net negative \mathbf{z} -torque consistent with experiments (Figure 4.9). Lastly, a small positive \mathbf{y} -direction torque is observed for all cases indicating that the body pushes itself away from the wall (Figure 4.9).

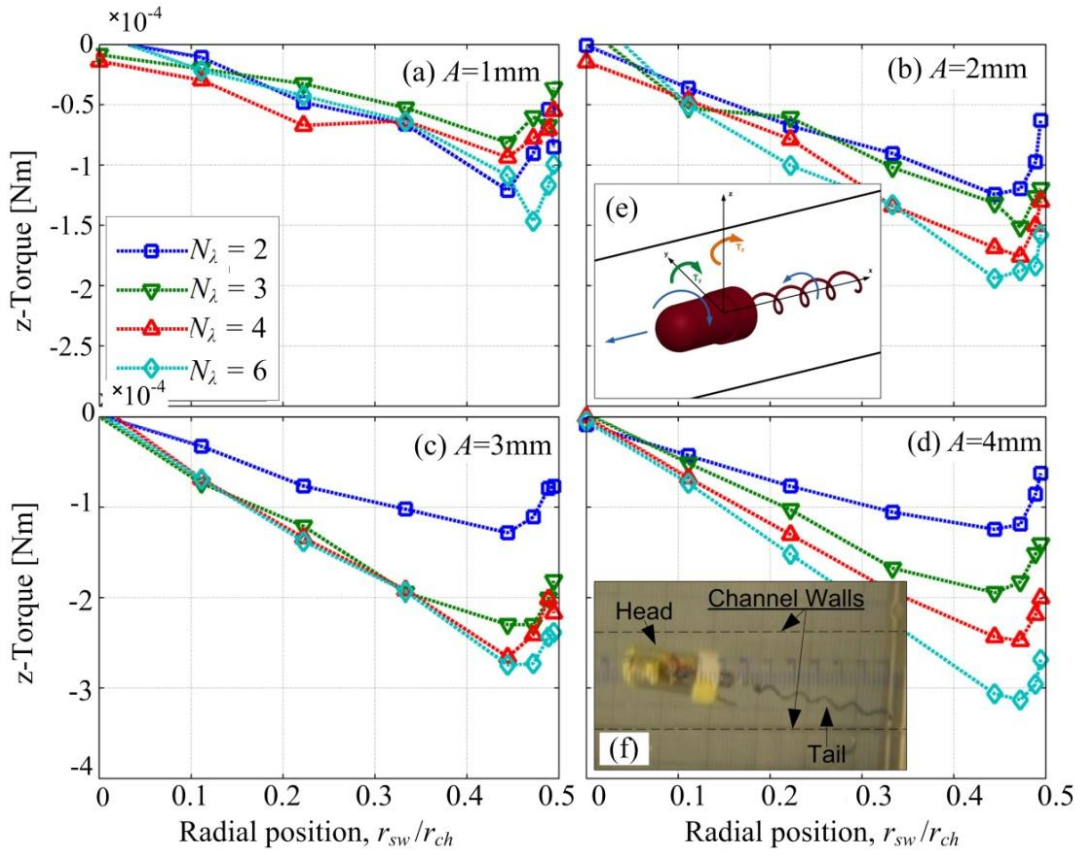


Figure 4.9 Torque on \mathbf{z} -direction of the robots as a function of the radial position of the robot for A equals (a) 1 mm, (b) 2 mm, (c) 3 mm and (d) 4 mm; and for $N_\lambda = 2$ ('square'), 3 ('downward triangles'), 4 ('upward triangles'), 6 ('diamonds') are obtained from simulations. (e) Schematic representation of torques acting on the robot swimming near the wall. (f) Top-view of the swimming robot from the experiments.

4.2.2.5 Efficiency

Efficiency of swimming robots is calculated from the ratio of the rate of work done to move the robot in the swimming direction and the rate of work done to rotate the tail, as defined by Purcell for low Reynolds number swimmers [7]. The net force on the robot in the direction of its motion is zero, thus only the drag force on the body is considered for the work done in the swimming direction, as also adopted in other studies for the definition of the efficiency of micro swimmers [18, 42]. The net rate of work done by the rotation of the tail is calculated from the net angular velocity of the tail with respect to the body. Thus, the efficiency of swimming robots is obtained from:

$$\eta = \frac{U \int_{S_{body}} \sigma \cdot \mathbf{n}_x dS}{T_{x,body}(\omega_{tail} + \Omega_b)} \quad (4.9)$$

Here U is the forward velocity, σ is the stress tensor, \mathbf{n}_x is the \mathbf{x} -component of the surface normal, $T_{x,body}$ is the rotational torque acting on the body in the \mathbf{x} -direction, ω_{tail} is the angular velocity of the tail and Ω_b is the angular velocity of the body.

Efficiencies of swimming robots are shown in Figure 4.10. For $A = 1$ mm, the efficiency of the robot increases with the number of waves on the tail and varies slightly with respect to the radial position of the robot: it increases with the radial position of the robot up to a maximum around 0.1% for $N_\lambda = 6$ near the wall, then decreases with the further increase of the radial position (Figure 4.10).

For $A = 2$ mm, there is a significant increase in the efficiency of the robot, compared to $A = 1$ mm, about 0.35% near the wall for $N_\lambda = 3$ or $N_\lambda = 4$, for which the efficiency is significantly larger than for $N_\lambda = 6$ (Figure 4.10b). For $A = 2$ mm, number of waves (helical turns) that leads to the least efficient design is 2. The effect of the radial position on the efficiency is clearly visible: there is an optimal position for robots for about $r_{sw}/r_{ch} = 0.44$ (i.e. $w_d = 1$ mm).

For $A = 3$ and 4 mm (Figure 4.10c-d), efficiencies are larger than for $A = 1$ and 2 mm; about 0.6% for $A = 3$ mm and almost 1% for $A = 4$ mm. For $N_\lambda = 6$, efficiency remains almost constant with respect to the amplitude and with the radial position of the robot. For $A = 3$ mm, most efficient designs have $N_\lambda = 2, 3$ and 4 with slight changes in values, and a cross-over between the values at the center and near the wall for $N_\lambda = 2$ and 4: the former is slightly more (less) efficient at the center than the latter at the center (near the wall) as shown in Figure 4.10c.

Although the difference between $N_\lambda = 2$ and 3 is still very small, the distinction between the efficiencies of robots with $N_\lambda = 2, 3$ and 4 is clearer for $A = 4$ mm. However, robots with $N_\lambda = 2$ is clearly more efficient than for $N_\lambda = 3, 4$ and 6 in decreasing order especially near the wall where the efficiency is almost 1% (Figure 4.10d). Lastly, the effect of the radial position is very small for the robot with $N_\lambda = 6$: the efficiency remains unchanged for all positions except very close to the wall, for which the efficiency exhibits a decline as the radial position increases.

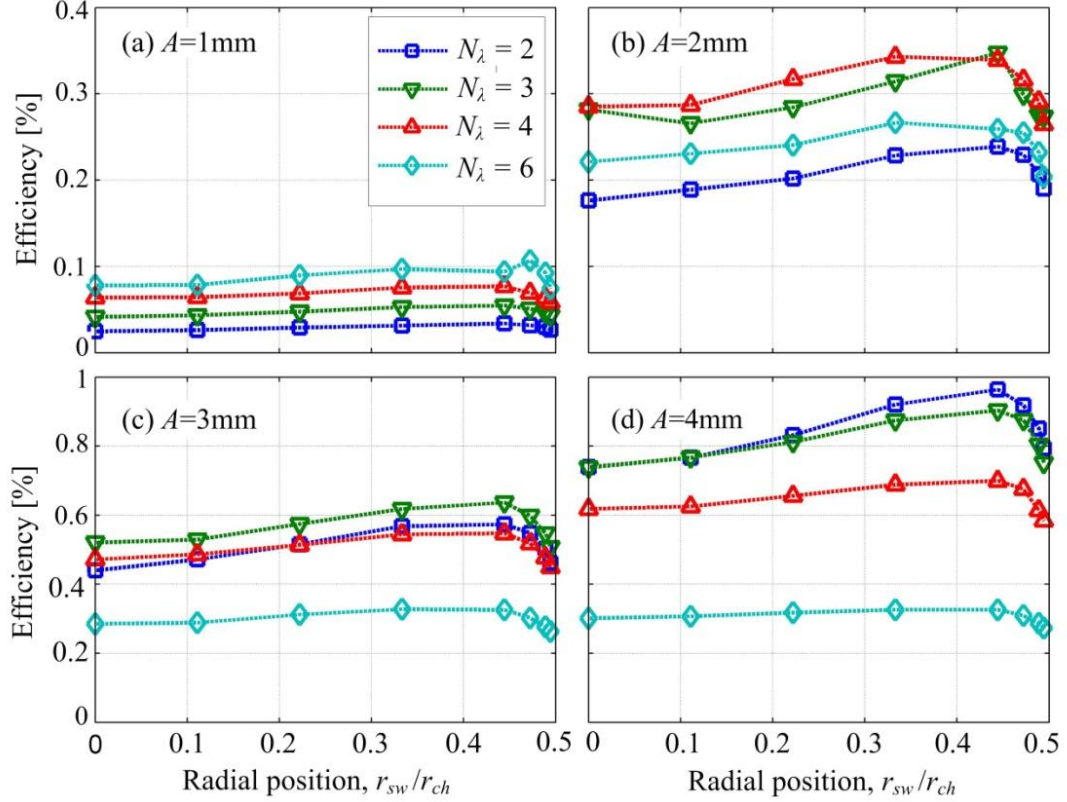


Figure 4.10 Efficiency of the robots with respect to the radial position of the robot for A equals (a) 1mm, (b) 2 mm, (c) 3 mm and (d) 4 mm; and for $N_\lambda = 2$ (‘square’), 3 (‘downward triangles’), 4 (‘upward triangles’) and 6 (‘diamonds’) with the results are obtained from simulations.

Overall, the pattern indicates that efficiency increases with the wave amplitude (radius) of helical tails. However, the number of waves has a nonlinear effect: larger number of waves for small amplitudes leads to higher efficiencies, and vice versa. Moreover, the efficiency is consistently larger for robots traveling near the wall than the ones traveling at the center.

4.3 Discussion

The experimental and simulation results are presented for cm-scale autonomous swimming robots inside a viscous-fluid filled channel to mimic the swimming of micro robots in aqueous solutions inside blood vessels and other conduits. A computational fluid dynamics (CFD) model is used to solve three-dimensional Stokes equations that govern the flow, and validated with the experiments. Forward swimming and body-angular velocities of the robots are measured in experiments and compared with CFD simulation results for the same robots traveling at radial positions vary between the

center of the channel and 0.1 mm away from the wall in order to understand the effect of the radial position inside the channel. Simulation results for robots swimming near the wall agree very well with experimental results, where the robots swim very near the wall as well.

The radial force on the robot is negligible in the core region of the channel, slightly negative towards the center for the robots closer to the wall before it changes sign and sharply increases when the robot is very close to the wall. The pull towards the wall can combine with the gravity and improve the contact with the wall. There is an indication that the contact force may have a role in the slowing down of the body rotation rate for robots with heavy tail. However, the forward velocity is not hampered by contact forces.

Swimming velocity and the efficiency of the robots peak at a radial position, which corresponds to 1 mm distance from the wall for all wave amplitudes and number of waves; almost 25% increase in the efficiency is observed for the robot with $A = 4$ mm and $N_z = 2$ and traveling near the wall, compared to the one with the same parameters traveling at the center of the channel. Efficiency of the robots increase with the amplitude, however the effect of the wavelength is nonlinear: small wavelengths have higher efficiency at small amplitudes, or vice versa.

Body resistance coefficients of the robots are calculated in CFD simulations, according to which the resistance coefficients decreases with the radial position of the robots up to almost 25% near the wall, compared to the value at the center. Furthermore, the tail parameters, namely the amplitude and wavelength, have a small effect on the body resistance coefficient of the swimming robots, which have significantly larger bodies compared to tails.

Results provide guidelines for the design of micro robots for *in vivo* operations inside vessels, arteries and similar body conduits. Swimming velocities of the robots strongly depend on the geometry of the channel as well as amplitude and the wavelength of the helical tail as well as the radial position of the robot. Lastly, fluid forces can be calculated reliably from the solution of three-dimensional Stokes equations with CFD models and used to obtain accurate resistance coefficients for the representation of hydrodynamic effects in analytical models that may include other forces such as contact friction and other interactions with the channel walls.

5 SWIMMING OF ARTIFICIAL MAGNETIC SWIMMERS IN CYLINDRICAL CHANNELS

In this chapter, swimming experiments of mm-sized robots in glycerol and water-filled mini channels are discussed. Experiments are carried out for two swimming micro robots which consist of heads made of permanent magnets and rigid helical tails of different dimensions. The robots in the experiments are 360 μm and 460 μm in diameter and 2.45 mm and 2.17 mm in length; with these dimensions swimming of the robots in glycerol-filled mini channels corresponds to micro-fluidic regime. Use of water as a working fluid in the experiments demonstrates the efficacy of micro robots in the low inertia regime where the Reynolds number is greater than one.

Moreover, a 6-dof time-dependent hydrodynamic model is built based on Resistive Force Theory (RFT) including: a technique to implement cylindrical channel effects, and magnetic step-out frequency phenomena. Experimental results are used to validate the proposed hydrodynamic model with appropriate tuning of body resistance coefficients due to irregular shapes of the magnetic heads and overall flow conditions that differ from simple viscous drag on the body, which is commonly used to obtain analytical body resistance coefficients.

In order to understand the flow field induced by the micro robot and the interaction of the micro robot with the channel wall, simulation-based analysis of the flow field is presented which calculates hydrodynamic forces and torques acting on the swimmer and the swimming efficiency as a function as a function of the wavelength and amplitude of the helical tail and the radial position of the swimmer. A three-dimensional steady-state computational fluid dynamics (CFD) model is developed and solved with the commercial finite element software COMSOL Multiphysics [91]. Simulations are conducted for two different positions of the swimmer aligned with the channel axis, at the center and near the wall.

Simulation results are validated with the results obtained from micro-PIV experiments.

5.1 Experimental Studies

In what follows, the components of the experimental setup and results are discussed. Fabrication and properties of the helical swimmers are explained as well as the properties of the electromagnetic coils which provide rotating magnetic fields for actuation. Results of the experiments are presented with respect to different rotational frequencies and magnetic field strengths.

5.1.1 Fabrication of the Artificial Swimmer

For medical applications, human circulatory system is the most important application area for untethered swimming of micro robots, since it is possible to reach every place of the body by vessels [1]. In order to use micro robots for performing *in vivo* missions such as targeted drug delivery, removing plaque, destroying blood clots, they should be navigated controllably in blood vessels, arteries and capillaries which have diameters ranging from a few microns to centimeters [1]. Micro swimmers manufactured in our laboratory have diameters less than half a millimeter and lengths at most 3 mm. With this dimensions they seem ready to be used in medium artery (4 mm), vein (5 mm), aorta (25 mm) and vena cava (30 mm) in terms of size [1].

Helical artificial swimmers used in the experiments consist of a permanent magnetic head and a helical tail, which is made of metal wire. Magnetic head is the element that moves together with the rotating magnetic field (explained in the next section). Helical tail is attached to the magnetic head with a strong adhesive, thus a one-link swimmer is obtained unlike natural micro swimmers that have counter rotating body and flagella.

In order to have high magnetization factor in small volumes, large pieces of neodymium-iron-boron ($\text{Nd}_2\text{Fe}_{14}\text{B}$) magnet powder are used. Nearly spherical lumps of magnets have dimensions that measure $150\ \mu\text{m} \times 160\ \mu\text{m} \times 160\ \mu\text{m}$ (L2W3 in Figure 5.1) and $160\ \mu\text{m} \times 170\ \mu\text{m} \times 170\ \mu\text{m}$ (L2W4 in Figure 5.1), respectively. Each robot has a different size of magnetic particles because of the irregularity of the large pieces in the powder.

Helical tail was made of metal wires of diameter is $110\ \mu\text{m}$. Helices were produced by coiling the wires up on cylinders with different diameter (Figure 5.1).

Wave lengths or wave numbers of helices were adjusted by simply deforming the helices. The dimensions of micro swimmers can be seen in Table 5.1.

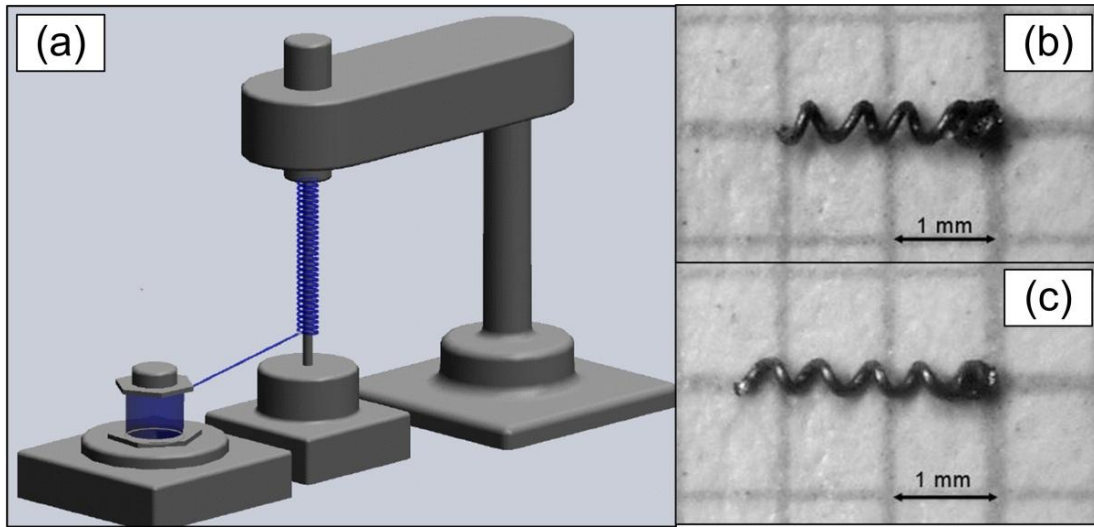


Figure 5.1 Swimming micro robots made in the laboratory. (a) Helix making process, (b) L2W3 - shorter and thicker, (c) L2W4 - longer and thinner.

Table 5.1 Dimensions of Micro Swimmers

	Length [mm]	Number of waves	Length of tail [mm]	Diameter of head [mm]	Helix diameter [mm]
L2W3	2.17	3	1.71	0.46	0.41
L2W4	2.45	4	2.09	0.36	0.36

5.1.2 Experimental Setup

The use of alternating and rotating magnetic fields for propagation and steering of magnetic devices is a popular method of actuation for untethered robots [17, 20, 34, 35, 99, 100]. Usually, orthogonal electromagnetic coil pairs are used such as Helmholtz or Maxwell coils for achieving rotating magnetic fields. Pawashe *et al.* [100] used six independent electromagnetic coil pairs and obtained a stick-slip motion of a micro robot, whereas Zhang *et al.* [20] used three orthogonal coil pairs and attained uniform rotating magnetic field.

The forward and backward propagation of the micro swimmers are provided by applying rotating magnetic field. For manipulation of the robots four coils were placed by pairs being perpendicular to each other as seen in Figure 5.2. The magnetic head can

rotate by means of the applied magnetic field only when magnetic torque on the head overcomes the viscous resistance of the fluid on the robot inside the channel.

The torque needed to rotate the micro swimmer is provided by the electromagnetic coils. If we represent magnetic dipole moment with \mathbf{m} , magnetic induction with \mathbf{B} , magnetic field with \mathbf{H} , and free space permeability with ζ_0 , the torque on a dipole in free space is [101]

$$\boldsymbol{\tau}_M = \mathbf{m} \times \mathbf{L} = \zeta_0 \mathbf{m} \times \mathbf{H} \quad (5.1)$$

The magnetic particles having a magnetic moment vector \mathbf{m} tend to align with the direction of the magnetic induction [101]. Magnetic dipole moment is a property of the material, and is given by the magnetization (\mathbf{M}) and the volume of the particle (ν).

$$\mathbf{m} = \mathbf{M} \times \nu \quad (5.2)$$

Thus, one may recast (5.1) as follows:

$$\tau_M = \zeta_0 \nu M H \sin \theta \quad (5.3)$$

where θ is the angle between \mathbf{B} and \mathbf{m} . Magnetic field along the axis of a circular coil depends on the current passing through coil, I , radius of the coil, r_{coil} , number of turns, N , and distance along the axis of the coil from the center, a , and is found by deriving Biot-Savart law as [101]

$$H = \frac{NIr_{coil}^2}{2(r_{coil}^2 + a^2)^{3/4}} \quad (5.4)$$

In order to rotate the magnetic particle attached to the helical tail, the magnetic torque supplied from the external field must be equal to the viscous torque on the whole swimmer:

$$\mathbf{C}_B \begin{bmatrix} \mathbf{u} \\ \boldsymbol{\Omega} \end{bmatrix} + \mathbf{C}_T \begin{bmatrix} \mathbf{u} \\ \boldsymbol{\Omega} \end{bmatrix} = \begin{bmatrix} \mathbf{F} \\ \boldsymbol{\tau}_M \end{bmatrix} \quad (5.5)$$

where, for a full six degree of freedom motion, \mathbf{C}_B and \mathbf{C}_T are the mobility matrices of the body and tail, \mathbf{u} is the velocity vector, $\boldsymbol{\Omega}$ is the rotational velocity vector, \mathbf{F} is the external force applied (which is zero here), and $\boldsymbol{\tau}_M$ is the magnetic torque. Since the body and tail are not separate links and attached to each other, \mathbf{u} and $\boldsymbol{\Omega}$ are same for body and tail.

$$\left(\begin{bmatrix} C_{B_N} & 0 \\ 0 & C_{B_R} \end{bmatrix} + \begin{bmatrix} C_{T_N,1} & C_{T_N,2} \\ C_{T_R,1} & C_{T_R,2} \end{bmatrix} \right) \begin{bmatrix} \mathbf{u} \\ \boldsymbol{\Omega} \end{bmatrix} = \begin{bmatrix} \mathbf{F} \\ \boldsymbol{\tau}_M \end{bmatrix} \quad (5.6)$$

Components of mobility matrices of body and tail are different from each other. Derivation of the mobility matrix components can be found in [102]. Normal and tangential force coefficients for tail can be calculated theoretically with the derivations Sir Lighthill stated in 1976 [99]. For a spherical body, C_{B_N} and C_{B_R} are written as

$$C_{B_N} = -6\pi\mu r_h^2 \quad (5.7)$$

$$C_{B_R} = -8\pi\mu r_h^3 \quad (5.8)$$

where μ is the viscosity of the fluid and r_h is the radius of the spherical head [102].

The electromagnetic coils in our setup are not identical (see Table 5.2). In order to obtain a uniform magnetic field everywhere in the working space, ideally, the distance between the coils must be equal to the average radius of the coils. The magnetic field is uniform enough for the workspace, which is used in the experiments and consists of a glass pipette of 1-mm-inner diameter; observations are made for about 10-mm swimming range of the robot.

Electromagnetic coils are mounted as shown in Figure 5.2. Alternating current is applied to obtain a rotating magnetic field. The current is transmitted to the coils from the power generators via Maxon ADS_E 50/10 motor drives that are connected to DS1103PPC controller board.

Table 5.2 Dimensions of Coils

Coils	y-axis	z-axis
Measured resistance [Ω]	14	7.5
Wire diameter [mm]	0.45	0.8
Number of turns	1400*	750
Coil diameter [mm]	30	90
Distance between coils [mm]	20	60

*Since the data sheet is not available, this information was obtained by calculations and may not be precise.

The magnitude of current and frequency of the sinusoidal currents are adjusted by the ControlDesk software. Maxon motor drives are operated with dSPACE and the signal is converted from digital to analog. Each coil is connected to one Maxon motor drive. Alternating current is applied to coil pairs with a phase shift to obtain the rotating magnetic field. The current applied to the small and big coils are defined as $I_{SC} = I_{0,SC}\sin(2\pi ft)$ and $I_{BC} = I_{0,BC}\cos(2\pi ft)$ respectively.

Propagation of micro swimmers is observed with TIMM-400 S/W v. 0.1-100 Microscope having a resolution of 720×576 pixels in which a USB digital camera that can record maximum 30 frames per second is mounted.

The micro swimmers are placed in glass pipettes filled with glycerol and water. The pipettes are placed on the x-axis which is shown schematically in Figure 5.2. Experiments are conducted for five different magnetic field strengths in glycerol with micro swimmers L2W3 and L2W4. The L2W4 is also used in water under three different magnetic field strengths.

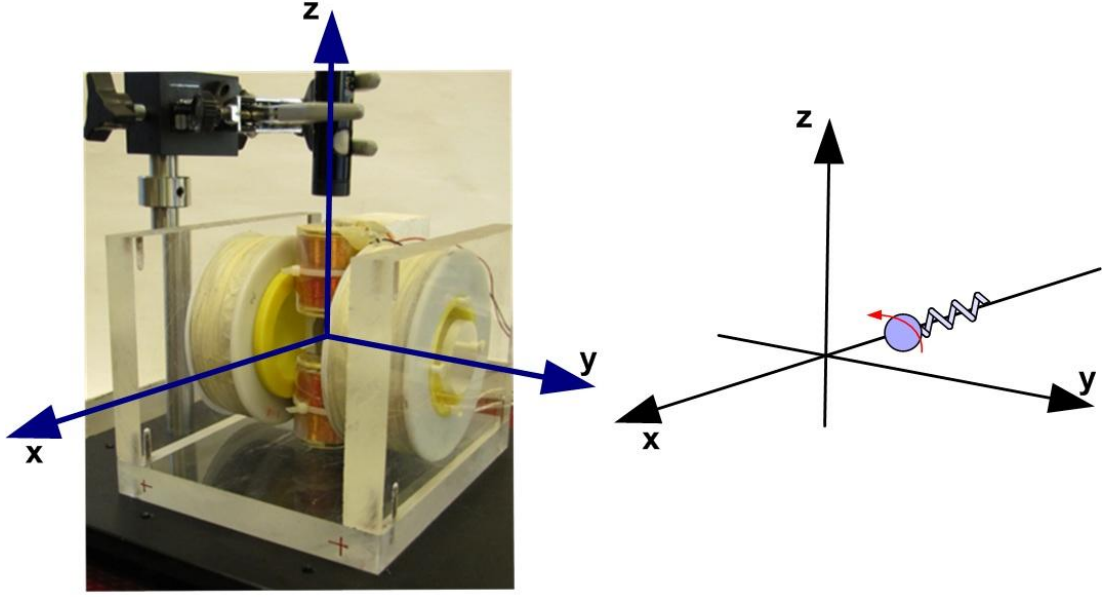


Figure 5.2 Experimental setup consists of electromagnetic coil pairs and USB microscope camera (left). Schematic view of micro swimmer (right).

5.1.3 Results

5.1.3.1 Experiments in glycerol

The micro swimmer L2W3 and L2W4 are placed in a glass pipette having an inner diameter of 1 mm, and pipette is filled with glycerol having a dynamic viscosity of 0.1 Pa·s. Reynolds number is calculated for both head and tail assuming the head is perfect sphere at 10 Hz. Density of the fluid, linear velocity of micro swimmer, radius of head, rotation frequency, diameter of the tail and amplitude of helical tail wave are represented with ρ , U , r_h , f , d_{tail} and A respectively.

$$\text{Re}_{head_L2W3} = \frac{\rho U r_h}{\mu} = 2.4 \cdot 10^{-3} \quad (5.9)$$

$$\text{Re}_{tail_L2W3} = \frac{2\pi f \rho A d_{tail}}{\mu} = 12.8 \cdot 10^{-3} \quad (5.10)$$

$$\text{Re}_{head_L2W4} = \frac{\rho U r_h}{\mu} = 2.4 \cdot 10^{-3} \quad (5.11)$$

$$\text{Re}_{tail_L2W4} = \frac{2\pi f \rho A d_{tail}}{\mu} = 18.1 \cdot 10^{-3} \quad (5.12)$$

Although the Reynolds numbers are greater than the Reynolds number of bacteria in water, they are still much smaller than 0.1. Thus, inertial effects are negligible with respect to viscous forces.

In Figure 5.3 and Figure 5.4, linear velocities of micro swimmer L2W3 and L2W4 in glycerol are represented with respect to magnetic field strength and rotating frequency. Five different magnetic field strengths changing from 6.85 mT to 7.60 mT are used in the experiments; rotating frequency is varied from 5 Hz to 50 Hz.

The linear velocity is obtained by dividing the distance to the time that micro swimmer takes to travel. For both robots the same behavior is observed. The linear increase in velocity continues up to a maximum point, where the swimmer starts to slow down due to insufficient magnetic torque, which is no longer can make the swimmer rotate with the frequency of rotating magnetic field. This behavior can also be seen both in micro [2] and macro scales [12]. Maximum linear velocity is obtained as 2.65 mm/s for L2W3 and 3.5 mm/s for L2W4, under the effect of 7.60 mT. Because of the linear relationship between velocity and frequency, it is clear that applying stronger magnetic field at higher frequencies will result with increment in linear velocity. The frequency value at which the micro swimmers reach their maximum linear velocity is known as step-out frequency.

In Figure 5.5 the comparison in velocities of L2W3 and L2W4 can be seen. The data represented are obtained under 7.02 mT magnetic field strength. As expected, L2W4 travels faster than L2W3, since the former has a longer tail with more waves, which increases the propulsive force, and a smaller head that decreases the drag.

Resistive force theory [40] is applied to the swimmers in order to compare the experimental results. In Figure 5.6, the comparison of experimental results with normal and tuned RFT for L2W4 at 7.60 mT is represented. The theoretical normal and tangential drag coefficients for tail and body are calculated from [99, 102] and then tuned to include the wall effects.

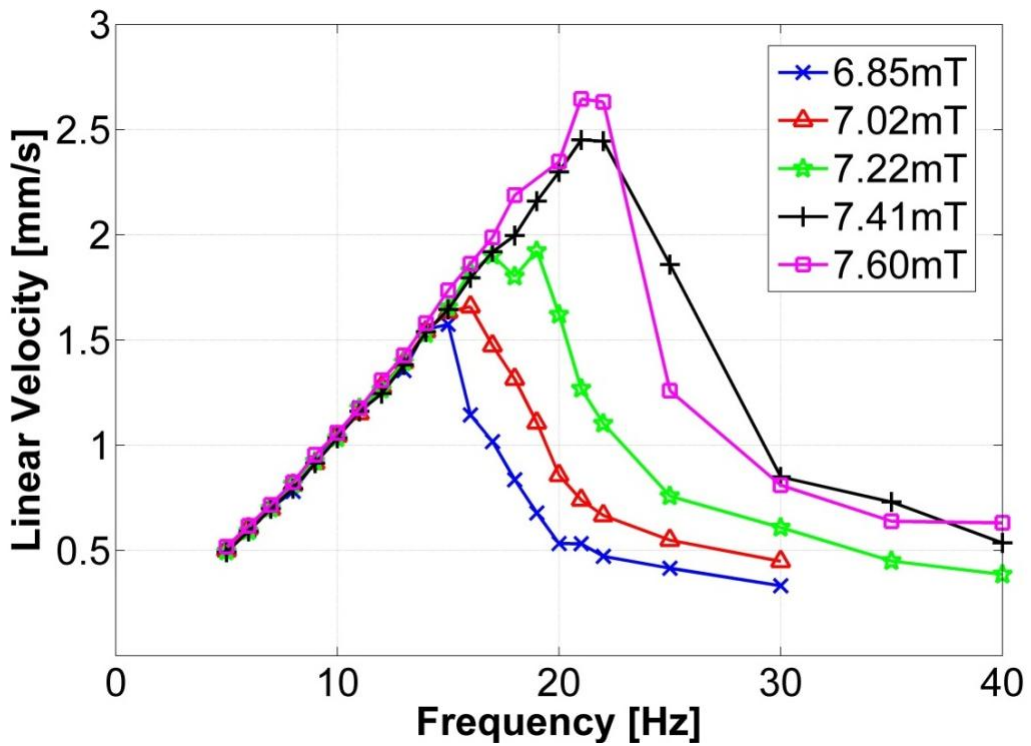


Figure 5.3 Dependence of linear velocity of micro swimmer L2W3 on magnetic field strength and rotation frequency.

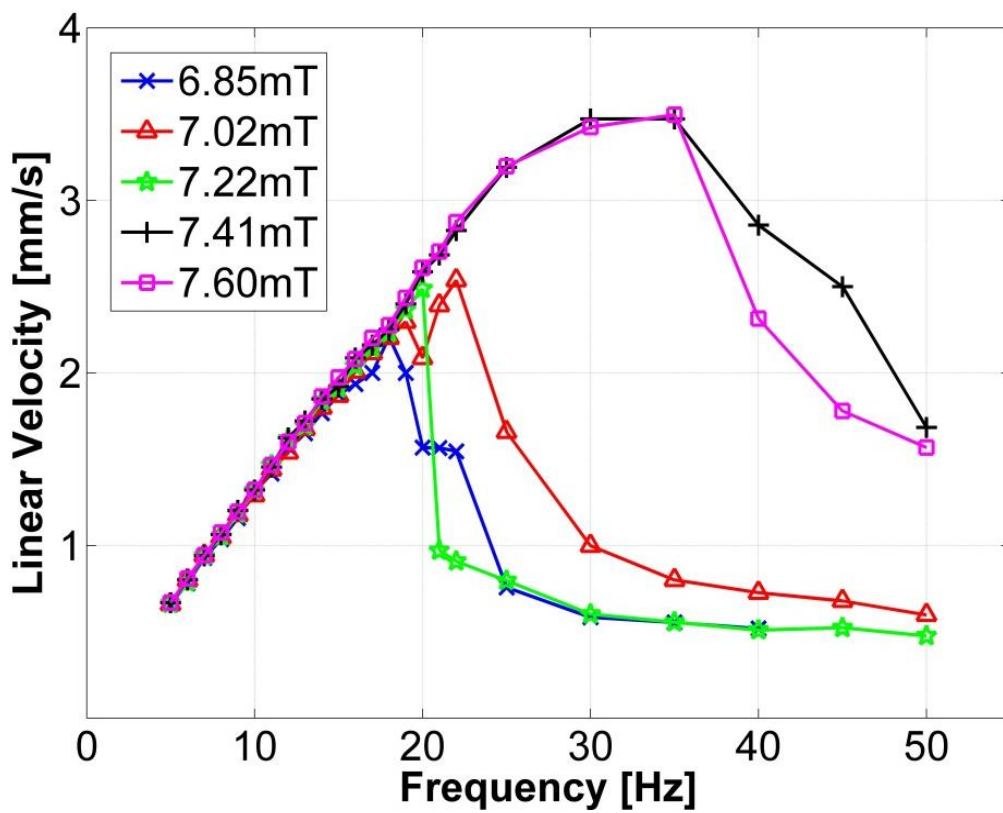


Figure 5.4 Dependence of linear velocity of micro swimmer L2W4 on magnetic field strength and rotation frequency.

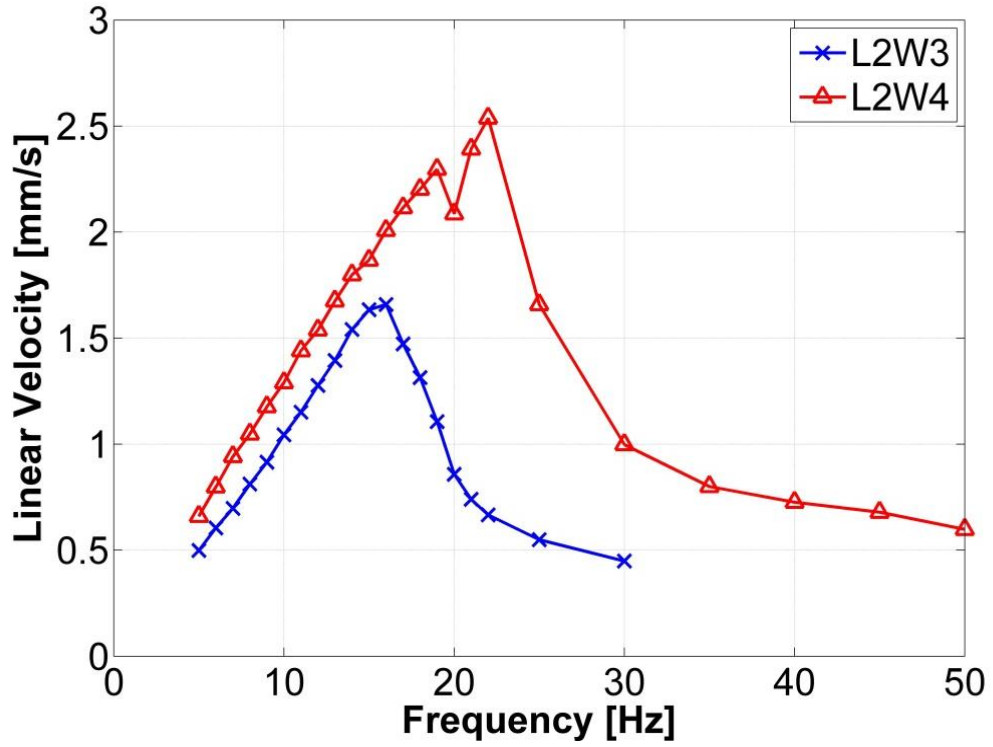


Figure 5.5 Comparison of L2W3 and L2W4 in terms of linear velocity. Applied magnetic field strength is 7.02 mT.

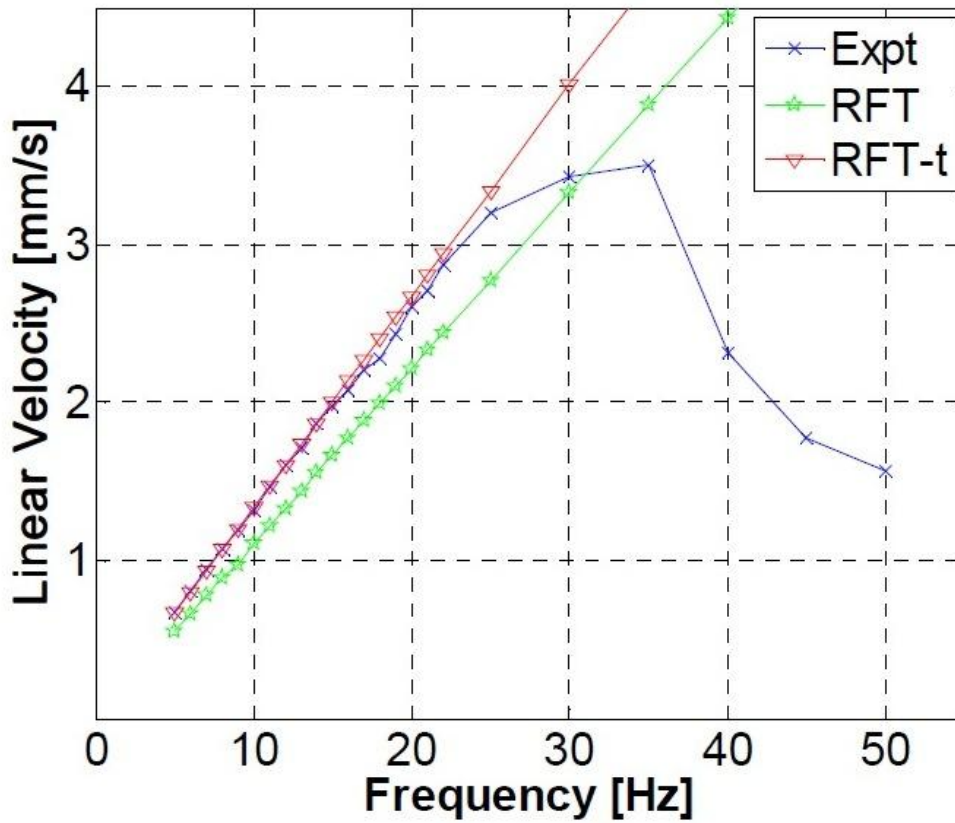


Figure 5.6 Comparison of experimental data collected at 7.60 mT with the RFT model.

5.1.3.2 Experiments in water

The micro swimmer L2W4 was placed in a glass pipette having an inner diameter of 1 mm, and pipette is filled with water which has a dynamic viscosity of 0.001 Pa·s. Previous assumptions about Reynolds number and inertial and viscous effects are no longer applicable to the experiments in water. At 30 Hz, the Reynolds numbers of the head's and tail's motions are as follows:

$$\text{Re}_{\text{head_L2W4}} = \frac{\rho U r_h}{\mu} = 0.55 \quad (5.13)$$

$$\text{Re}_{\text{tail_L2W4}} = \frac{2\pi f \rho A d_{\text{tail}}}{\mu} = 5.43 \quad (5.14)$$

In Figure 5.7, the results of the experiments in water are presented. Three different magnetic field strength are applied; 5.70 mT, 6.00 mT, 6.45 mT. Up to 50 Hz, the effect of magnetic field strength does not make a difference in linear velocities. At 20 Hz, micro swimmer is slower in water than it is in glycerol, so we can conclude that inertial effects are not negligible and deteriorates the propulsion of the helical tail. Increasing frequency more than 50 Hz results in an unpredictable velocity behavior, due to more pronounced inertial effects, as $\text{Re}_{\text{tail_L2W4}}$ is on the order of 10.

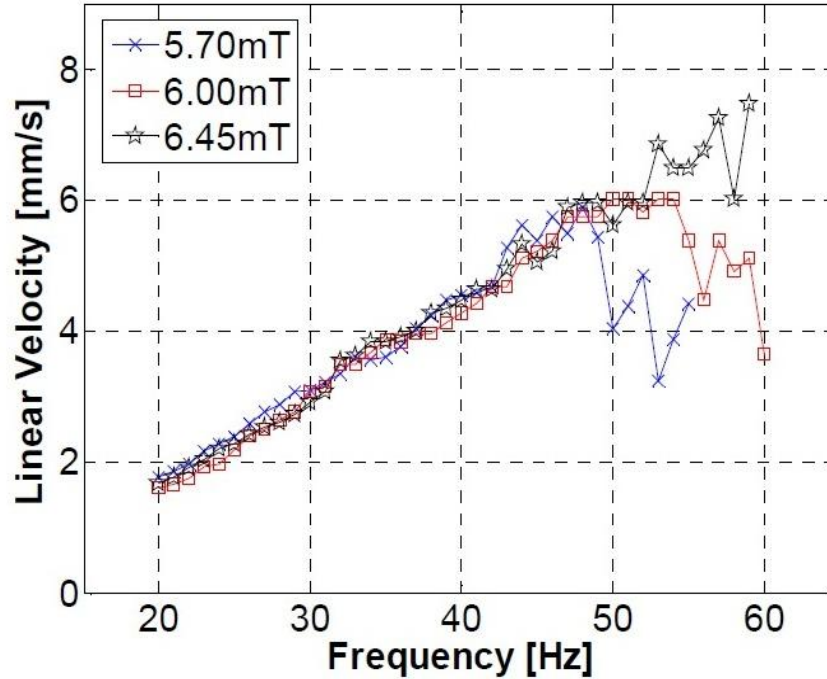


Figure 5.7 Dependence of linear velocity of micro swimmer L2W4 on magnetic field strength and rotation frequency in water. The behavior after step-out frequency is a reason to be suspicious about inertial effects

5.2 Theoretical Modeling

A 6-dof time-dependent hydrodynamic model is built based on Resistive Force Theory (RFT) [40] including: a novel technique to implement cylindrical channel effects, and magnetic step-out frequency phenomena. Experimental results are used to validate the proposed hydrodynamic model with appropriate tuning of body resistance coefficients due to irregular shapes of the magnetic heads and the overall flow conditions that differ from simple viscous drag on the body, which is commonly used to obtain analytical body resistance coefficients. Numerical and experimental data for time-averaged forward velocity are found to agree well.

5.2.1 Equation of Motion

Linear and angular velocities and trajectory of helical swimmers are obtained from the solution of the equation of motion with the propulsion force due to the rotation

of the tail when the external magnetic torque is applied, total drag force and drag torque on the swimmer as follows:

$$\begin{aligned}\mathbf{F}_d + \mathbf{F}_p &= 0 \\ \mathbf{T}_d + \mathbf{T}_{ext} &= 0\end{aligned}\tag{5.15}$$

Here subscripts p , d and ext denote propulsion, drag and the external effects, respectively.

Force and torque vectors due to hydrodynamic propulsion and fluid drag are constructed by the resistive force theory [40]: the force and torque vectors are obtained from the linear and angular velocity vectors with a linear resistance relationship as follows:

$$\begin{bmatrix} \mathbf{F}_d + \mathbf{F}_p \\ \mathbf{T}_d \end{bmatrix} = (\mathbf{R}_t + \mathbf{R}_h) \begin{bmatrix} \mathbf{u} \\ \boldsymbol{\Omega} \end{bmatrix}\tag{5.16}$$

where \mathbf{u} and $\boldsymbol{\Omega}$ are linear and angular velocity vectors in swimmer frame, and \mathbf{R}_t and \mathbf{R}_h are 6-by-6 resistance matrices for the helical tail and the magnetic body, respectively [102]. The resistance matrix for a rigid helical tail decomposes as follows:

$$\mathbf{R}_t = \int_0^{L_{tail}} \begin{bmatrix} \mathbf{RCR}' & -\mathbf{RCR}'\mathbf{S} \\ \mathbf{SRCR}' & -\mathbf{SRCR}'\mathbf{S} \end{bmatrix} ds\tag{5.17}$$

where L_{tail} is the apparent tail length, s is the spatial s -coordinate in the swimmer frame, \mathbf{R} is the rotation between the local Frenet-Serret frame on the helical tail [103] and the swimmer frame, \mathbf{S} is the skew-symmetric matrix for the cross products between the position and velocity vectors in the swimmer frame, the diagonal matrix \mathbf{C} is the local resistance matrix on the tail, and superscript $'$ denotes transpose.

Due to the angular symmetry of the cylindrical cross section of the tail, normal and binormal components of the local resistive force are proportional to the normal and binormal components of the local velocity with the same normal resistive force coefficient, which is given by [41]:

$$c_n = \begin{cases} \frac{4\pi\mu}{\ln(\lambda/r_{tail}) + 0.193 - 3\lambda/8w_{d-c}}, & \frac{\lambda}{2w_{d-c}} \leq 1 \\ \frac{4\pi\mu}{\ln(2w_{d-c}/r_{tail})}, & \frac{\lambda}{2w_{d-c}} > 1 \end{cases} \quad (5.18)$$

The tangential component of the resistive force is proportional to the velocity in that direction with the tangential resistive force coefficient [41]:

$$c_t = \begin{cases} \frac{2\pi\mu}{\ln(\lambda/r_{tail}) - 0.807 - 3\lambda/16w_{d-c}}, & \frac{\lambda}{2w_{d-c}} \leq 1 \\ \frac{2\pi\mu}{\ln(2w_{d-c}/r_{tail})}, & \frac{\lambda}{2w_{d-c}} > 1 \end{cases} \quad (5.19)$$

In (5.18) and (5.19), w_{d-c} is the minimum local distance of the center line of the tail to the surface of the channel, r_{tail} is the tail radius, and λ is the helical pitch.

Drag matrix for rigidly-attached head of the micro swimmer, \mathbf{D}_h , is given by:

$$\mathbf{D}_h = \begin{bmatrix} \mathbf{D}_t & -\mathbf{D}_t \mathbf{W} \\ \mathbf{W} \mathbf{D}_t & \mathbf{D}_r \end{bmatrix} \quad (5.20)$$

where \mathbf{D}_t and \mathbf{D}_r are diagonal 3-by-3 translational and rotational body drag coefficient matrices respectively, and \mathbf{W} is the skew-symmetric matrix for the body center of mass. Resistance matrix given by (5.20) is modified in order to account for the wall effects as discussed next.

5.2.1.1 Wall effects

Body and tail drag matrices given by (5.17) and (5.20) are modified in each time step in order to implement the presence of inflexible solid channel boundaries. Hard-constraint kinematic equations, i.e. in case of an elastic collision between the micro swimmer's body and channel walls, are transformed into soft kinematic constraints for an imaginary concentric inner cylinder of radius ($R_{ch}-\epsilon$) as follows:

$$\Psi_{6 \times 6} \begin{bmatrix} \mathbf{u} \\ \boldsymbol{\Omega} \end{bmatrix} := \begin{cases} \begin{bmatrix} \mathbf{R}_\theta (\Re \mathbf{u} + \boldsymbol{\Omega} \times \mathbf{P}) \\ \mathbf{R}_\theta (\boldsymbol{\Omega} \times \mathbf{P}) \\ \mathbf{0}_{6 \times 6} \end{bmatrix} & , \|\mathbf{P}\| \neq 0 \\ \mathbf{0}_{6 \times 6} & , \|\mathbf{P}\| = 0 \end{cases} \quad (5.21)$$

where Ψ is the constraint matrix, \Re is the matrix handling rotations from swimmer frame to stationary lab frame, i.e. \mathbf{xyz} , determined by integrating time dependent quaternion rotations [103], and \mathbf{R}_θ is the transformation matrix between lab coordinate systems, i.e. from \mathbf{xyz} to $\mathbf{xr}\theta$ coordinates.

The vector \mathbf{P} in (5.21) represents the position of surface points of the swimmer with respect to swimmer's center of mass, and is set to zero unless the proximity of the swimmer to channel wall exceeds the limit such that body surface touches or penetrates the imaginary concentric inner cylinder. In effect, $\boldsymbol{\Omega} \times \mathbf{P}$ is used to consider the contact torque on the swimmer. If the limit is exceeded, nonzero elements within Ψ modify the elements of mobility matrix as follows:

$$\mathbf{R}'_{h,ij} = \begin{cases} \frac{s_t}{(\varepsilon - \delta_p)/\varepsilon} \mathbf{R}_{h,ij} & , \Psi_{ij} \neq 0 \\ \mathbf{R}_{h,ij} & , \Psi_{ij} = 0 \end{cases} \quad (5.22)$$

where δ_p is the penetration depth of the swimmer in $\mathbf{xr}\theta$ coordinates as depicted in Figure 5.8, and s_t is the stiffness tuning parameter which is 30 unless otherwise stated.

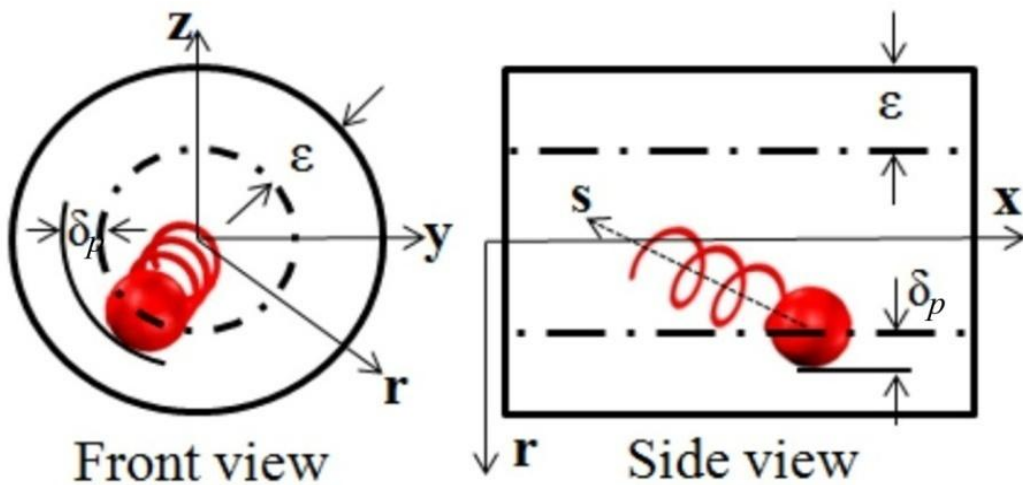


Figure 5.8 Swimmer body penetrating imaginary inner concentric cylinder: Penetration depth δ_p is computed in \mathbf{r} -coordinate of the lab frame

Eq. (5.22) ensures that as the minimum distance decreases, the corresponding mobility matrix elements are multiplied with a large scalar to constrain the motion in that direction. The artificial concentric inner cylinder is fixed as $\varepsilon = r_{ch} / 2$ in order to impose the effect of channel walls on the swimmer body gradually. However, the resistance matrix must have full rank at all times, i.e. $\det(\mathbf{R}_r + \mathbf{R}'_h) \neq 0$.

5.2.1.2 Magnetic torque

External torque vector in (5.15) happens due to the magnetic field applied along the \mathbf{x} -axis in lab frame. The resultant torque felt by the magnetic head of the swimmer is given by revising (5.3) as:

$$\mathbf{T}_{ext} = \boldsymbol{\tau}_M = \mathfrak{R}' \zeta_{eff} \nu \|\mathbf{M}\| \|\mathbf{H}\| \mathbf{n}_x \sin(\theta) \quad (5.23)$$

where ζ_{eff} is the actual permeability, and \mathbf{M} is the magnetization of the magnetic head. The direction of the resultant torque is denoted by the normal vector \mathbf{n}_x . Angle between the external magnetic field and the body is denoted by θ and computed as the integral of the difference between the angular velocities of body and rotational magnetic field:

$$\theta = \int_0^t (2\pi f - \Omega_s) dt' \quad (5.24)$$

where f is the actuation frequency of the magnetic field, and Ω_s is the resultant swimmer rotation along \mathbf{s} -axis, which is initially 0 and updated at each simulation time step beforehand (5.15) is solved. This consequently results in \mathbf{F}_p in (5.15) due to cross-coupling terms in mobility matrix given by (5.17). In the case when the swimmer rotates with the frequency of the magnetic field the angle θ remains constant, however, when the strength of the field is not enough to overcome the fluid's resistance it varies with time.

Continuous steady torque is sustained by means of the rotating magnetic field as long as the swimmer rotates with the field. When the swimmer loses its synch with the magnetic field, effective torque drops and swimmer can no longer rotate at the same rate

with the field, thus, the propulsion becomes erratic. The maximum frequency that the swimmer can follow without loss of propulsion is called step-out frequency.

5.2.2 Results

Helical swimmers are placed inside the glass pipettes with inner diameters of 1 mm and filled with glycerol having a dynamic viscosity of 0.1 Pa·s. At 10 Hz, Reynolds numbers for both head and helical tail are calculated as $Re_{\text{head_L2W3}} = 2.4 \times 10^{-3}$, $Re_{\text{tail_L2W3}} = 12.8 \times 10^{-3}$, $Re_{\text{head_L2W4}} = 2.4 \times 10^{-3}$, and $Re_{\text{tail_L2W4}} = 18.1 \times 10^{-3}$. Thus inertial effects are negligible with respect to viscous forces for both the forward motion of the head and the rotation of the tail.

RFT based model simulations are carried out for 25 complete periods of the rotation of the external magnetic field. Equation of motion (5.15) is solved by Adams-Bashforth-Moulton PECE solver [104]. Each simulation took about 15 to 45 seconds on a single processor of 64-bit Linux workstation with dual quad-core Xeon processors clocked at 2.6 GHz depending on the numerical stiffness of the swimmer's motion. Time-averaged forward velocities of the swimmers are calculated over the entire duration of the motion. The experimental time-averaged \mathbf{x} -direction velocity is calculated by dividing the traveled distance to the travel time of micro swimmer.

Similar behavior is observed for both swimmers L2W3 and L2W4 for forward velocities in lab frame. The linear velocity is proportional to the actuation frequency up to the step-out frequency. In the linear region, rotations of the magnetic field and the swimmer are identical, and the magnetic torque on the swimmer is steady. As the magnetic actuation frequency increases, time-averaged forward velocity decreases due to loss of useful magnetic torque, which is inapt to enforce the swimmer follow continuously with the frequency of rotating magnetic field. As depicted in Figure 5.9, at times the swimmer reverses rotational direction as the cross product of the magnetization of the head and the external field points at the opposite direction, slows down the swimmer, and, even forces the swimmer to move in the opposite direction.

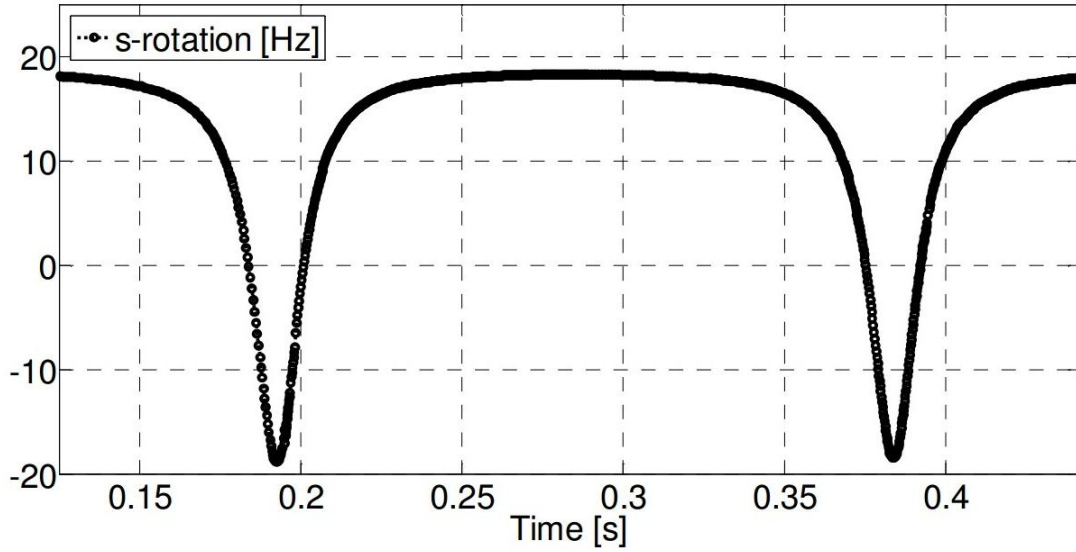


Figure 5.9 Simulation based rotational s-velocity: Effect of step-out frequency and spontaneous counter-rotation of L2W4; operating at 6.85 mT with $f = 20$ Hz.

Figure 5.10 and Figure 5.11 show the comparison of time-averaged x -velocities observed by experiments and computed by RFT based model for micro swimmer robot designated as L2W3 operating with two different magnetic field strengths, i.e. 6.85 mT and 7.22 mT. Simulation results are in good agreement with experiments. They predict the linear relationship between magnetic actuation frequency and time-averaged forward velocity till step-out frequency occurs. After that point onward, consequent nonlinear decrease in forward velocity is partially predicted in all cases as shown in Figure 5.10 and Figure 5.11. It is noted that, linear and rotational s-drag coefficients of swimmer body are multiplied with 0.3 and 1.15, respectively, in order to predict the time-averaged forward velocity of L2W3. Moreover, tuning of body drag coefficients in simulations is only to compensate the effects of possible morphological impurities of the body in experiments; nevertheless, this procedure does not affect the linear behavior shown in Figure 5.10-Figure 5.13. Lastly, to predict the step-out frequency with minimum magnetic torque, magnetization of the head is divided by 1.35 for this robot: in effect, than factor accounts for the angle between the magnetic field and the magnetization.

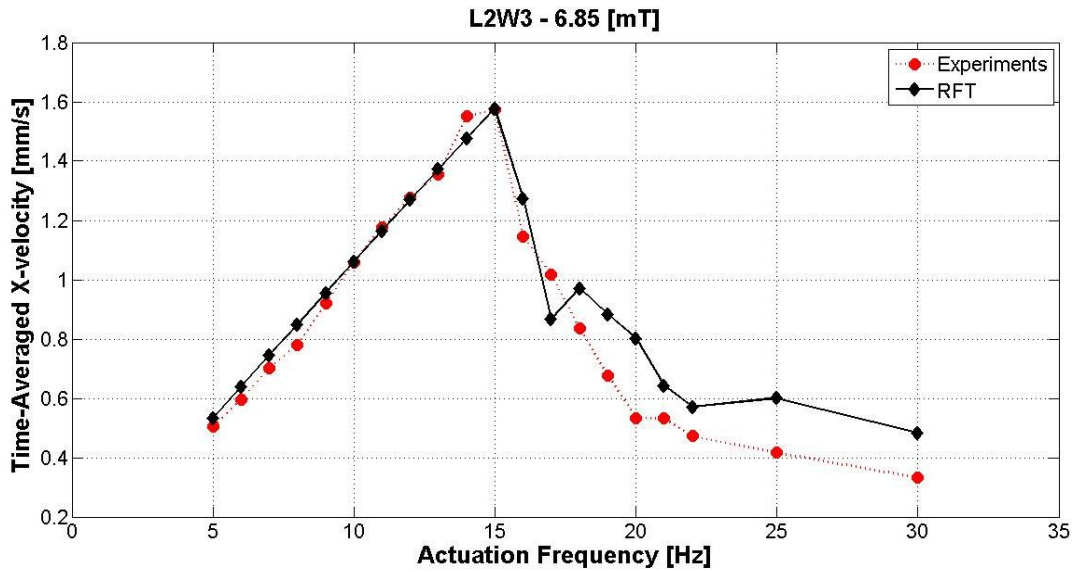


Figure 5.10 Time-averaged x -velocity vs magnetic actuation frequency. Experiment vs RFT for L2W3 at 6.85 mT

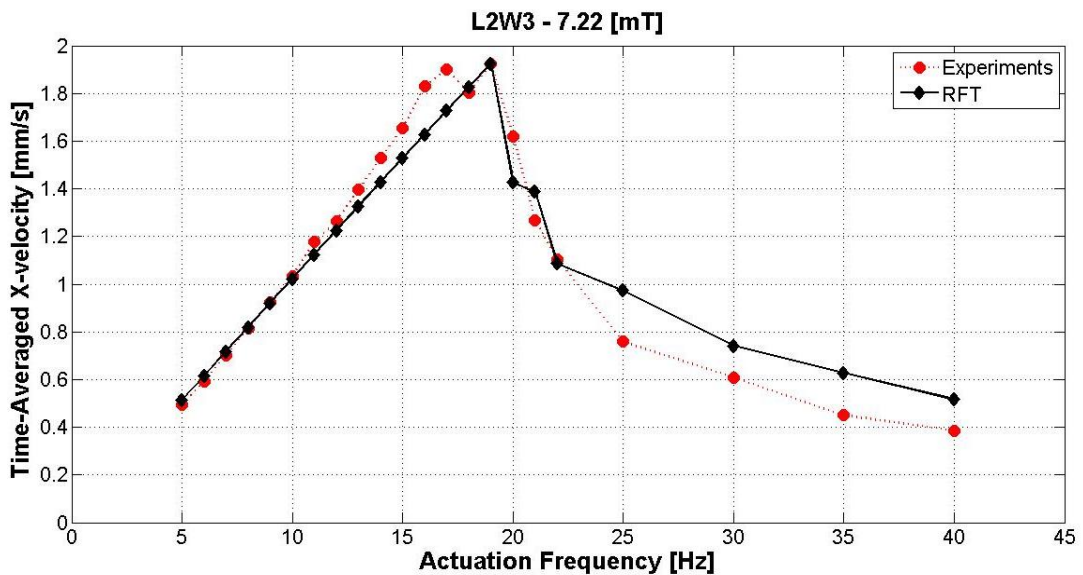


Figure 5.11 Time-averaged x -velocity vs magnetic actuation frequency. Experiment vs RFT for L2W3 at 7.22 mT

Figure 5.12 and Figure 5.13 show the comparison of time-averaged x -velocities observed by experiments and computed by RFT based model for micro swimmer robot designated as L2W4 operating under same magnetic field strengths with L2W3. Simulation results predict the linear relationship between magnetic actuation frequency and time-averaged forward velocity with high accuracy till step-out frequency occurs. Similarly to L2W3 results, consequent nonlinear decrease in forward velocity is partially predicted in all cases as shown in Figure 5.12 and Figure 5.13. It is noted that,

linear and rotational s-drag coefficients of body is multiplied with 3 and 1.1, respectively, in order to predict the time-averaged forward velocity of L2W4. Lastly, magnetization of the head is divided by 1.49 in order to account for the actual magnetic torque based on the step-out frequency for this robot.

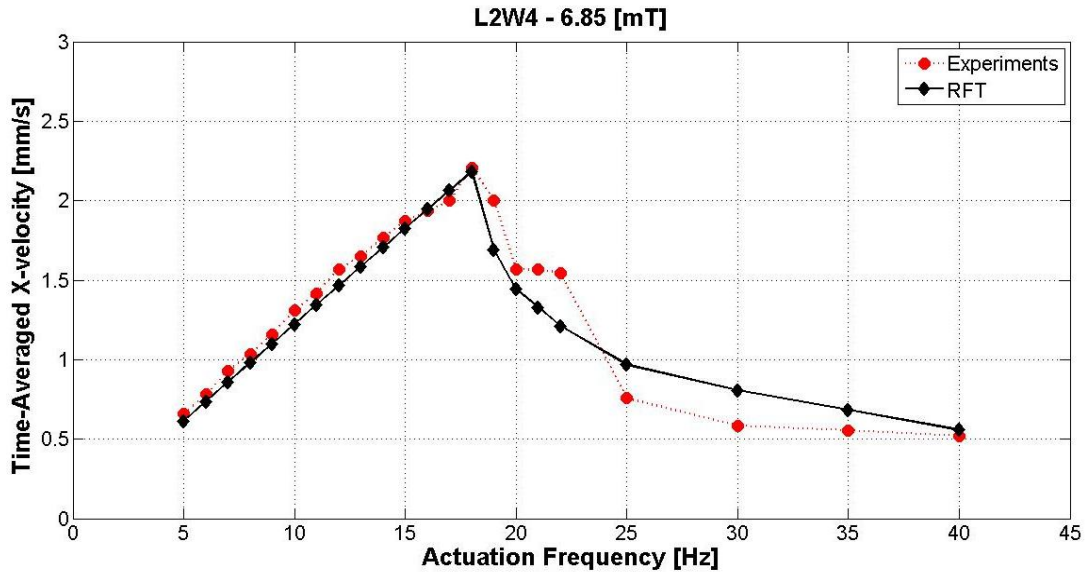


Figure 5.12 Time-averaged x -velocity vs magnetic actuation frequency. Experiment vs RFT for L2W4 at 6.85 mT

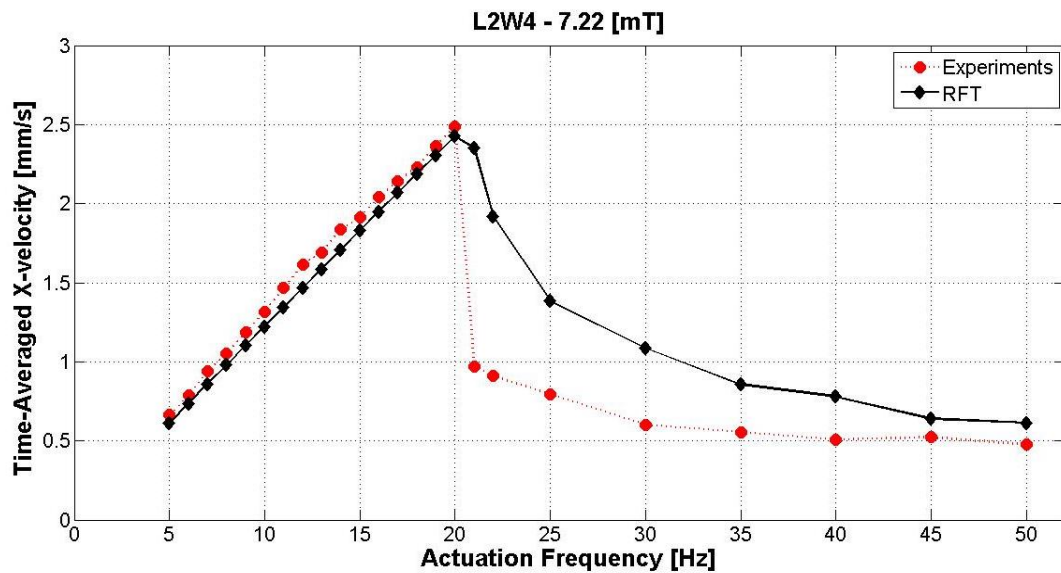


Figure 5.13 Time-averaged x -velocity vs magnetic actuation frequency. Experiment vs RFT for L2W4 at 7.22 mT

Figure 5.14 demonstrate the wall effects on yz -trajectory of the swimmer as magnetic field frequency is smaller than step-out frequency. Implementation of soft constraints on inner cylinder actually limits the position of the micro swimmer on the

yz -plane such that overall motion of the swimmer's center of mass is mostly restricted to artificial inner cylinder as it continuously penetrates and bounces back and remains on the wall (the trajectory illustrated with red in Figure 5.14). However, if (5.22) is not applied, swimmer follows a more monotonous path and does not remain inside the channel (green trajectory in Figure 5.14).

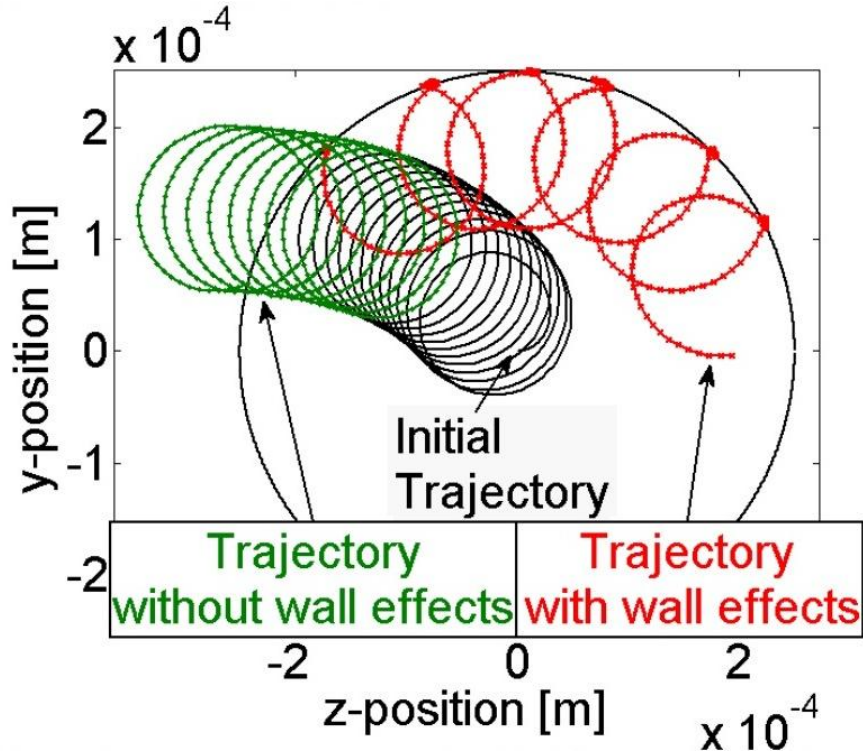


Figure 5.14 Simulation based yz -trajectory for L2W4 operating at 7.22 mT with $f = 20$ Hz

5.3 Computational Fluid Dynamics (CFD) Modeling

Simulation-based analysis of the flow field induced by the on-link swimmer inside a circular channel, hydrodynamic forces and torques acting on the swimmer and the swimming efficiency as a function of the wavelength and amplitude of the helical tail and the radial position of the swimmer. Micro swimmers are modeled based on the one used in experimental work at low Reynolds numbers ($Re \sim 10^{-3}$). A three-dimensional steady-state computational fluid dynamics (CFD) model is developed and solved with the commercial finite-element software COMSOL Multiphysics [91]. Simulations are conducted for two different positions of the swimmer aligned with the channel axis, at the center and near the wall.

5.3.1 Modeling

The micro swimmer modeled here is based on the actual robot used in our experiments which is referred as L2W4. The swimmer used in the experiments consists of a magnetic head attached to a rigid right-handed helical tail with a strong adhesive (Figure 5.15a). Nearly spherical powder of $\text{Nd}_{12}\text{Fe}_{14}\text{B}$ magnet is used for the magnetic head, whereas the tail is made of non-magnetic metal wire which has a thickness of 110 μm and four full waves. Diameter of the magnetic head, length of the helical tail and the amplitude of helical waves are measured as 360 μm , 2.09 mm and 125 μm , respectively. In the CFD model, the magnetic head is assumed to be a perfect sphere and attached to the left-handed helical tail without any gap. The difference between chiralities of the tails makes no difference in the calculated values but only in the directions as confirmed by simulations for robots having the same dimensions but differing only in the chirality of the helices.

The glass channel is filled with glycerol, whose viscosity is $\mu = 0.1 \text{ Pa}\cdot\text{s}$, and density is $\rho = 1000 \text{ kg}\cdot\text{m}^{-3}$ in experiments and simulations. Only a 7.2 mm portion of the channel is taken into account in the model as the flow is well within the viscous regime and the motion of the swimmer does not affect the downstream and upstream portions significantly as confirmed by simulations: fluid motion is suppressed within less than a millimeter distance from the swimmer in the flow regime of simulated robots (i.e. for $\text{Re} \sim 10^{-3}$).

Geometric dimensions are scaled with the diameter of the head (see Table 5.3), which is multiplied by the frequency of rotations to set the velocity scale. Thus Reynolds number used in scaling is the ‘frequency Reynolds number’:

$$\text{Re}_f = \frac{\rho r_h^2 f}{\mu} \quad (5.25)$$

Table 5.3 shows actual dimensions and properties of the fluid and corresponding values used in non-dimensional equations in the CFD model. In Figure 5.15b parameters of the system are shown schematically.

Table 5.3 Geometric parameters of the channel and micro swimmer

Parameter	Actual Value	Dimensionless Value
Radius of channel, r_{ch}	0.5 mm	1.39
Length of channel, L_{ch}	7.2 mm	20
Wire diameter of the tail, d_{tail}	0.11 mm	0.306
Length of tail, L_{tail}	2.09 mm	5.81
Diameter of spherical head, d_h	0.36 mm	1
Density of fluid, ρ	1000 kg/m ³	1
Viscosity of fluid, μ	0.1 Pa.s	1/Re

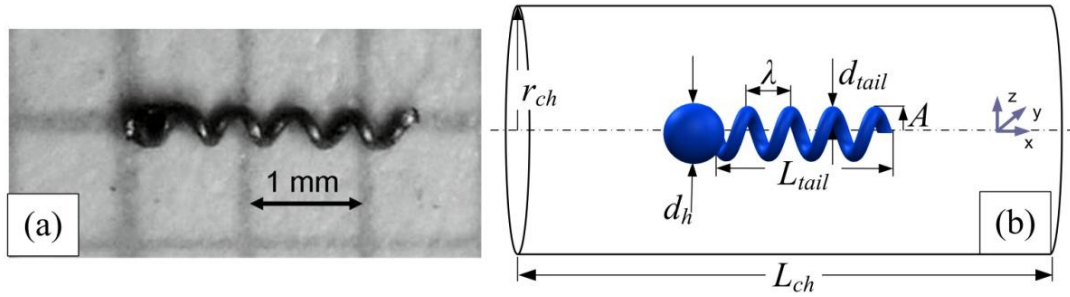


Figure 5.15 (a) Micro robot used in the experiments consists of a magnetic head and a metal right-handed helical tail. (b) Drawing of the micro robot in CFD model that consists of a spherical head and a left-handed helical tail inside a cylindrical channel.

Rotation of the rigid helix, with the unitary frequency in the dimensionless CFD model, is specified as a sinusoidal deformation in **y**- and **z**-directions:

$$P_{tail} = \begin{bmatrix} x_{tail} \\ y_{tail} \\ z_{tail} \end{bmatrix} = \begin{bmatrix} x_{tail} \\ A \cos(\varphi - kx_{tail}) \\ A \sin(\varphi - kx_{tail}) \end{bmatrix} \quad (5.26)$$

where k is the wave number, A is the amplitude of the helical waves, x_{tail} is the distance from the head and $\varphi = \omega t$ is the phase angle that corresponds to the rotation angle of the helix at a given time t and angular velocity ω .

The three-dimensional instantaneous flow around the swimmer inside the channel is modeled with the incompressible Stokes equations for low Reynolds number swimming conditions:

$$\begin{aligned} 0 &= -\nabla p + \frac{1}{\text{Re}_f} \nabla^2 \mathbf{u} \\ \nabla \cdot \mathbf{u} &= 0 \end{aligned} \quad (5.27)$$

where p is the pressure, $\mathbf{u}=[U, V, W]$ is the velocity vector of the fluid and Re_f is the frequency Reynolds number given by (5.25).

No-slip boundary conditions are imposed on the swimmer and on the channel walls including its inlet and outlet. On the swimmer, velocity is specified by forward motion and rotation of the swimmer having unitary rotational frequency. Namely, we have:

$$\mathbf{u} = 0 \text{ at } r = r_{ch}, x = 0 \text{ and } x = L_{ch} \quad (5.28)$$

and

$$\mathbf{u} = (\mathbf{e}_{x2\pi}) \times \mathbf{P} + [U, 0, 0] \text{ on the swimmer} \quad (5.29)$$

where r is the radial position, \mathbf{e}_x is the unit vector in the \mathbf{x} -direction, \mathbf{P} is the position vector on the swimmer surface and U is the forward velocity of the swimmer. We only considered the forward motion in the \mathbf{x} -direction, which is dominant particularly inside the cylindrical channel as also observed in our experiments.

Forward velocity of the swimmer, U , is the only variable needs to be calculated in (5.29); lateral velocities, which are negligible for in-channel swimming, are set to zero. Angular velocity in the direction of the motion of the micro robot is specified in simulations, unlike in experiments, where finite magnetization of the head and the specified external magnetic field strength lead to a constant magnetic torque, which sets a constraint for the \mathbf{x} -direction viscous torque for the swimmer.

In order to obtain the forward velocity of the swimmer, the force-free swimming condition is added as a constraint equation:

$$F_x = \int_S \sigma_{xj} d\mathbf{S}_j = 0 \quad (5.30)$$

where F_x is the total force on the swimmer in the \mathbf{x} -direction, σ_{xj} is the stress tensor components in the \mathbf{x} -direction, $d\mathbf{S}_j = dS [n_x, n_y, n_z]'$ is the differential element at the

surface that points in the j^{th} direction, S is the surface of the swimmer, and n_x , n_y and n_z are surface normal vectors in \mathbf{x} -, \mathbf{y} - and \mathbf{z} -directions.

In (5.30), where standard summation of repeated indices is implied, the stress tensor in the \mathbf{x} -direction, σ_{xj} , for incompressible flow is given by:

$$\sigma_{xj} = -p\delta_{xj} + \mu \left(\frac{\partial u}{\partial x_j} + \frac{\partial u_j}{\partial x} \right) \quad (5.31)$$

where δ_{xj} is the Kronecker's delta, $x_j = \{x, y, z\}$ and $u_j = \{U, V, W\}$.

Commercial finite element software, COMSOL Multiphysics [91], is used to solve (5.27) and (5.30) subject to (5.28) and (5.29). The finite element model consists of 40000 and 96000 tetrahedral elements and 225000 and 530000 degrees of freedom, for center and near-wall swimming conditions, respectively. The linear system of equations is solved using the PARDISO direct solver.

In CFD simulations, radial position and angular velocity of the swimmer and number and amplitude of helical waves on the tail are varied. Calculated velocities, forces, torques and efficiencies are averaged over full rotations of micro robots over a set of angular positions, ϕ in (5.26), that correspond to times at which the snapshot solutions of Stokes equations are obtained.

5.3.2 Results

In CFD simulations, frequencies are varied between 1 and 30 Hz, wave amplitudes between 25 and 125 μm , and number of waves between 1 and 5. Radial position of the swimmer is set to zero for swimmers at the center and to 0.3 mm for swimmers near the channel wall. Base-case reference parameter values are set to those for the robot used in experiments, which are $B = 0.125$ mm for the helical radius (wave amplitude) of the tail, $f = 10$ Hz for frequency, and $N_\lambda = 4$ for number of waves on the tail. Only one parameter is varied for each simulation while the others are kept constant. For the swimmer located at the center of the channel, the helical axis lies on the axis of the channel. In order to mimic unbounded swimming conditions and additional simulation is carried out for comparisons for a swimmer placed inside a channel with

radius equals to 3.6 mm (approximately 10 times the diameter of the head) with the base-case parameters.

5.3.2.1 Velocity fields

Closed contour surfaces colored gray for positive (backward) and black for negative (forward) velocities are shown in Figure 5.16 for swimmers with the base-case values of geometric parameters, (a) in unbounded fluid, (b) in the center of the channel, and (c) near the channel wall. For all cases, the left-handed helical tail of the swimmer rotates in the positive \mathbf{x} -direction and pushes the fluid in the same direction, while the swimmer moves in the opposite direction. The u/d_{hf} ratio in Figure 5.16 is equal to -0.17 for forward flow (black surface) and 0.17 for backward flow (gray surface), whereas forward velocities of the unbounded, in-center and near-wall swimmers are -0.67 mm/s ($u/d_{hf} = -0.186$), -0.7 mm/s ($u/d_{hf} = -0.195$) and -0.76 mm/s ($u/d_{hf} = -0.212$), respectively. The black contour surface ($u = -0.61$ mm/s) represents the fluid that moves with the swimmer. The gray surface ($u = 0.61$ mm/s) is for the flow in the opposite direction (positive \mathbf{x} -direction) with respect to the direction of swimming.

Backward flow induced by the rotation of the helical tail and the forward flow due to the motion of the overall swimmer form two distinct surface contours around the tail. Extent of the backward flow for the unbounded swimmer (gray contour surface in Figure 5.16a) is only limited to the vicinity of the tail (see Figure 5.17) and diminishes immediately behind the tail. Observed flow around the body of the swimmer is due to the motion of the swimmer itself. In Figure 5.16b, surface contours are shown for the swimmer placed at the center of the channel; surface contours resemble those around the unbounded swimmer (Figure 5.16a). However, there is a weak backward flow especially around the head of the swimmer in the case of swimming at the center of the channel.

In Figure 5.16c, surface contours are shown for the swimmer near the channel wall. Axial velocity contours around the tail remain the same as previous cases for unbounded and center-located swimmers. On the other hand, contours around the head of the near-wall swimmer are distinctly different than the ones observed for unbounded and center swimmers. Based on the similarity between the velocity contours of extreme values around helical tails, we suggest that flow near the tail of the swimmer varies very

little with unbounded or in-channel swimming. However, the flow around the head of the near-wall swimmer is significantly different than flows observed for unbounded and center swimmers.

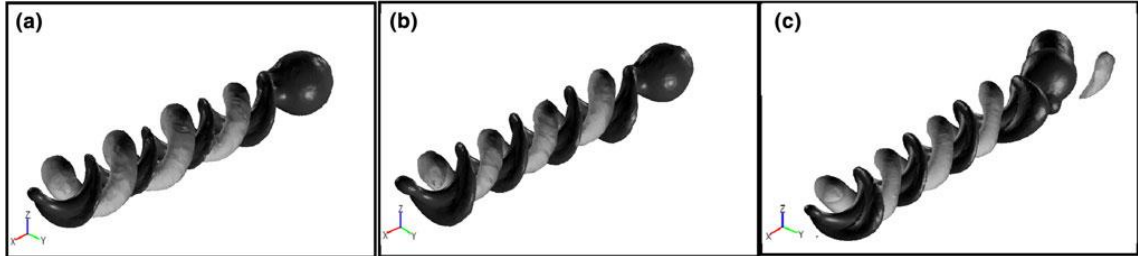


Figure 5.16 Closed contour surfaces, which are colored by *gray* for positive (backward $-u/d_h f = 0.17$ and $u = 0.61$ mm/s) and *black* for negative positive (forward $-u/d_h f = -0.17$ and $u = -0.61$ mm/s) velocities, for swimmer (a) in unbounded fluid; (b) in the circular channel at the center; and (c) near the channel wall; for all cases $\phi = \pi$, i.e., $t = \pi/\omega$. Swimmer is covered with the *black* contour surface, which represents the flow moving with the swimmer.

In Figure 5.17, axial velocity profiles are demonstrated on segments which are along the \mathbf{x} -direction, parallel to the axis of the helical tail and tangent to the head of the swimmer at $y = d_h/2$ and $z = 0$ for unbounded and center swimmers and at $y = d_h/2$ and $z = 0.3$ mm for near-wall swimmers. Axial velocities are shown with respect to the axial position relative to the head and at angular positions, $\phi = \{\pi/2, \pi, 3\pi/2, 2\pi\}$, i.e., $t = \{\pi/2\omega, \pi/\omega, 3\pi/2\omega, 2\pi/\omega\}$. At all times, axial velocity profiles are similar for all swimming conditions around the tails of the swimmer. However, the axial velocity profile around the head of the near-wall swimmer is significantly different than the profiles for center and unbounded swimmers. Rotation of the helical tail squeezes the fluid between the swimmer and the wall, and forces the flow in both directions. Moreover, close to the head of the near-wall swimmer, there is a clear backward flow in the channel due to the displacement of the fluid by the head. The flow in the channel weakens away from the swimmer and vanishes within a millimeter (diameter of the channel, or the half length of the tail) consistently with the Stokes flow regime. Particularly for the in-channel swimmer, flow vanishes in two distance units due to the suppression induces by channel walls. In essence, only the fluid in immediate neighborhood of the swimmer is affected by the motion of the swimmer; the fluid in the rest of the channel remains still.

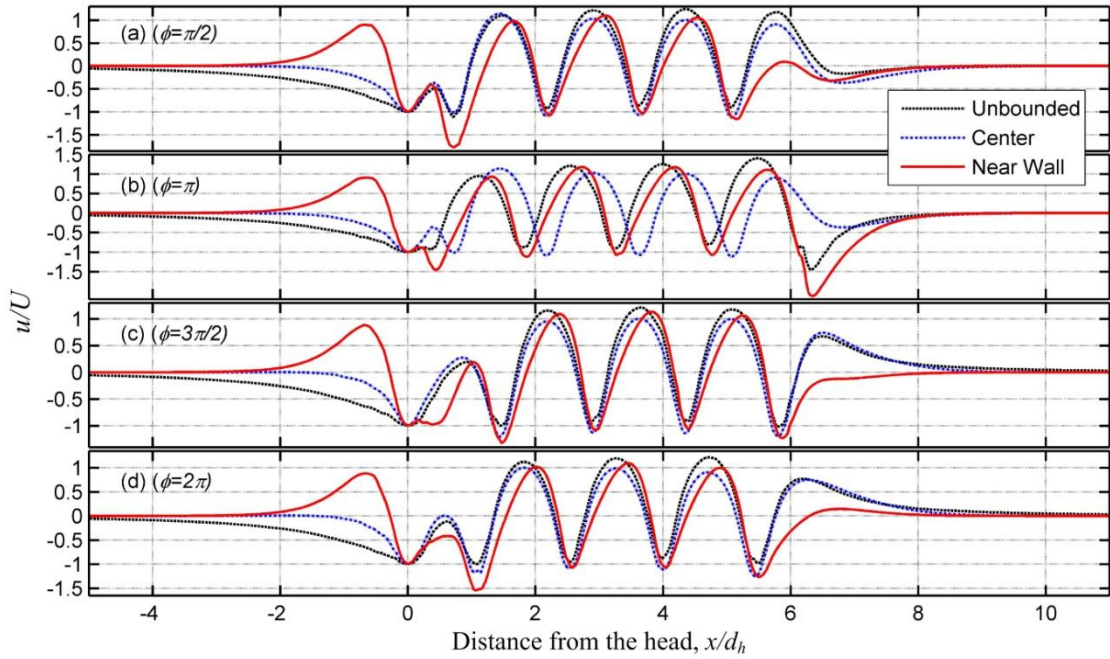


Figure 5.17 Axial velocity profile induced by unbounded swimmer (dashed black lines) and swimmers inside the channel (dash-dotted blue lines for in-center swimmer and solid red lines for near-wall swimmer) along the segments parallel to the channel's long axis at $y = d_h/2$ and $z = 0$ for unbounded and center and at $y = d_h/2$ and $z = 0.3 \text{ mm}$ for near-wall swimmers, for rectangular positions: (a) $\phi = \pi/2$ ($t = \pi/2\omega$), (b) $\phi = \pi$ ($t = \pi/\omega$), (c) $\phi = 3\pi/2$ ($t = 3\pi/2\omega$), (d) $\phi = 2\pi$ ($t = 2\pi/\omega$).

Distribution of the axial velocity of the flow with respect to the \mathbf{y} -position at $z = 0$ is shown in Figure 5.18 for the swimmer placed along the centerline of the channel for axial positions that correspond to: (a) one-head diameter in front of the swimmer; (b) mid-position of the head; (c) mid-position of the tail; and (d) three head-diameters behind the tail (see the sketches in Figure 5.18). In all cases, average axial velocity of the flow in the channel is zero due to the conservation of mass in the close-ended channel. The backward flow of the displaced fluid is clearly observed at all times and axial positions. Despite the symmetry of the spherical head, axial flow is not axisymmetric even in front of the head (Figure 5.18a), indicating that the flow around the helical tail has a significant effect on the upstream flow demonstrating a characteristic feature of the low Reynolds number helical swimming in channels, unlike the swimmer in unbounded fluid for which the flow in front of the swimmer is solely due to the forward motion of the swimmer. In Figure 5.18b, the flow around the head of the swimmer is due to zero-net flow in the close-ended channel: the forward motion of the swimmer pushes the fluid backward away from the swimmer towards the channel

wall. At the mid-section of the tail (Figure 5.18c), the axial flow distribution is due to the rotation of the helical tail and alters its direction according to the angular position of the robot. Behind the swimmer away from the tip of the tail, the axial velocity profile becomes smooth and resembles a simple sine wave with a magnitude reduced by 97.5 % within a millimeter, which is equal to the diameter of the channel (Figure 5.18d).

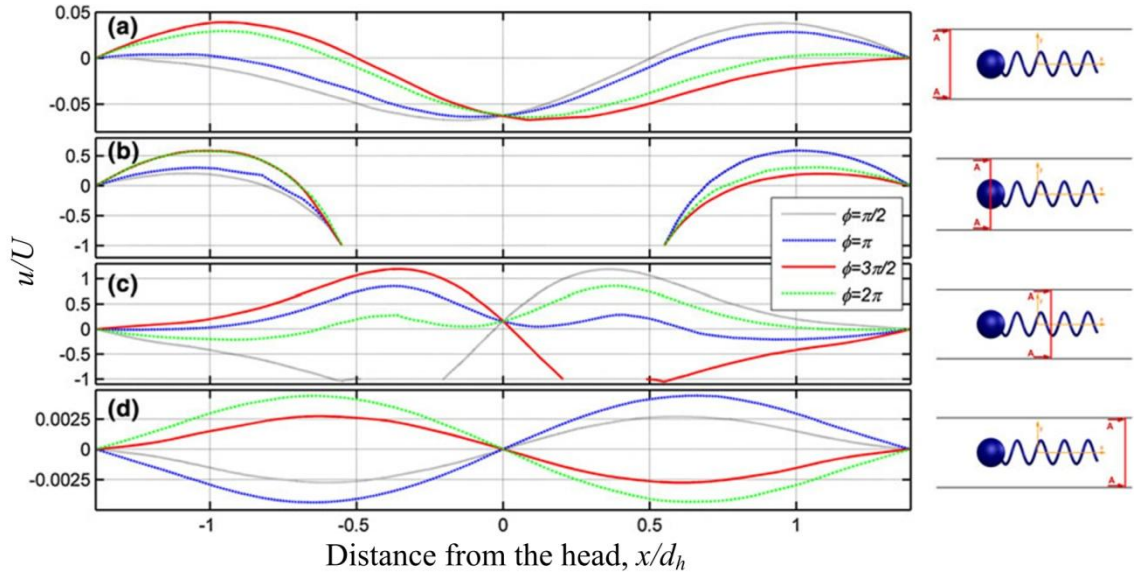


Figure 5.18 Axial velocity profile across the channel for axial positions: (a) one-head diameter in front of the swimmer, (b) at the middle of the head, (c) at the middle of the tail, (d) about 1 mm after the tail for $\phi = \pi/2$ ($t = \pi/2\omega$) (dotted black), $\phi = \pi$ ($t = \pi/\omega$) (dashed blue), $\phi = 3\pi/2$ ($t = 3\pi/2\omega$) (solid red), $\phi = 2\pi$ ($t = 2\pi/\omega$) (dash-dotted green).

5.3.2.2 Swimming speed

Effects of the frequency, amplitude (helical radius), and wavelength (helical pitch) of the helical tail on the swimming speed of the robot were studied for both center and near-wall swimming in circular channels. According to simulation results for base-case parameters ($f = 10$ Hz, $A = 0.125$ μm , and $N_\lambda = 4$), near-wall swimming (1.11 mm/s) is faster than swimming at the center (0.87 mm/s), which is slightly faster than unbounded swimming (0.77 mm/s). Recently, Felderhof [51] carried out an analytical study based on asymptotic expansions for infinite rotating helices in cylindrical tubes; according to his results, in-channel swimming is always faster than unbounded swimming; for large wave numbers discrepancy is even more significant. However, in previous studies carried out for swimming near planar walls, e.g., by Lauga *et al.* [50], the authors concluded that swimming near planar walls reduces the speed of the swimmer for some

natural micro-swimmers such as *E. coli*. According to Lauga *et al.* [50], a microorganism with a helical tail having three waves reaches the same velocity with a slower rotational speed when the swimmer is placed away from a solid boundary. Discrepancy between the results occurs due to the differences of the swimmers studied in Lauga *et al.* [50] and in this study: first the proximity of the organism to the wall is very close in Lauga *et al.* [50], about 1 versus 6 % of the radius of the head, here we compare center-swimming versus distance from the wall about 6 % of the radius of the head; second, counter-rotating body and tail is considered in Lauga *et al.* [50] and the one-link swimmer with the glued body and tail considered here. The distance between the robot and solid wall has an utmost effect; as robots get closer to the channel wall, they tend slowing down and even come to the full-stop when they are in full contact. Moreover, for spherical objects in circular channels, Happel and Brenner [97] show that there is an optimal radial position where the drag force over the sphere is minimum; as the sphere gets further closer to the wall the drag force raises sharply.

The forward velocity of the micro swimmer is investigated in Figure 5.19 with respect to rotational frequency, wave amplitude and number of waves. The effect of the frequency on the swimmer's speed is shown in Figure 5.19a. Swimming speed increases linearly with the frequency for both radial position, similar to the relationship between the speed and frequency for the infinite helix in an unbounded medium as calculated analytically [18, 39], and observed by experiments [3]. According to simulations, swimming speed is about 0.145 times the wave propagation speed on the tail for near-wall swimming and for all frequencies; similarly center-swimming speed is 0.134 times the wave propagation speed. Speeds observed in experiments are slightly faster than those we obtained in simulations. In the experiments, which are conducted with horizontal tubes, the radial position of the swimmer was not measured, but it was clear that gravity causes swimmer to remain very close to the wall at all times.

Figure 5.19b shows the change in swimming speed with respect to the amplitude of helical waves. According to the analytical results for free swimmers [18, 42], swimming speed increases quadratically with the amplitude. In addition, Felderhof [51] concludes that based on his asymptotic solution, infinite helices in circular channels swim proportional to the square of the amplitude. According to the simulation results for near-wall swimmer, swimming speed is proportional to the amplitude with a power greater than 1. The difference between simulation results and aforementioned analytical results is expected due to the effect of the finite amplitude of the helix; quadratic

behavior reported in approximate analytical studies is valid for small amplitudes near zero. Furthermore, for micro swimmers moving at the center of the cylindrical channel, swimming speed does not increase quadratically, but it shows a slight decrease in the rate of increase of the swimming speed as the wave amplitude increases.

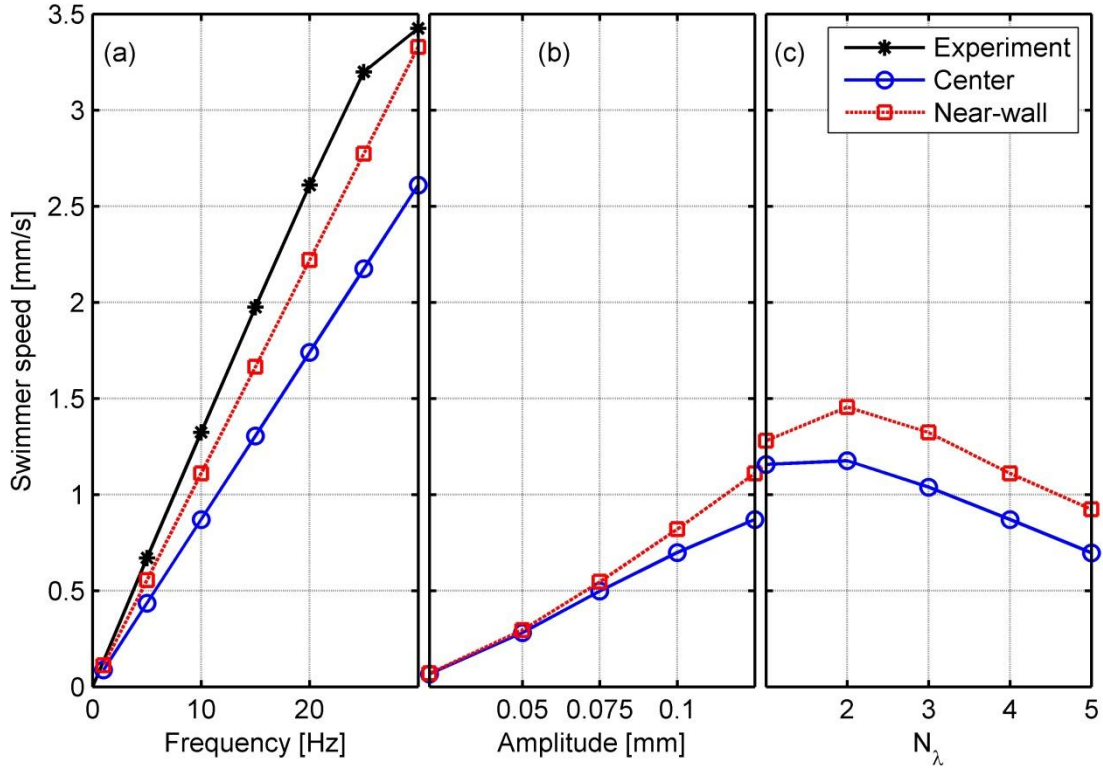


Figure 5.19 Experimental (solid lines with asterisks), in-center (solid lines with circles) and near-wall (dashed lines with squares) swimmer speed of micro robot having base-case parameters with respect to (a) frequency where $A = 0.125 \mu\text{m}$ and $N_\lambda = 4$, (b) amplitude where $f = 10 \text{ Hz}$ and $N_\lambda = 4$, and (c) number of waves where $f = 10 \text{ Hz}$ and $A = 0.125 \mu\text{m}$.

Number of waves affects the speed of the swimmer similarly for both center and near-wall swimming (Figure 5.19c). According to simulation results, swimming speed reaches its maximum value when $N_\lambda = 2$, and decreases linearly for higher N_λ values. According to analytical studies, there is an optimal value of the number of waves that maximizes the swimming speed for swimmers with helical tails in unbounded fluid [18, 42]. For the same rotational speed, based on an analysis using stokelets, Higdon [42] showed that the maximum swimming speed is reached when the number of waves is 3 for a swimmer with L_{tail}/r_b ratio being 10 and r_{tail}/r_b ratio being 0.02, where L_{tail} is the length of the flagellum, r_b is the radius of the body, and r_{tail} is the radius of the flagellum and that the point of the maximum velocity after the optimal point is a result

of the decrease in efficiency due to the disappearance of the slenderness of helical structures as wavelength decreases. For swimming of infinite helices in circular tubes, Felderhof [51] also concludes that in-channel swimming has an optimal value of the wave number depending on the physical parameters of the swimmer and the environment.

5.3.2.3 Forces and torques on the swimmer

The net force in the \mathbf{x} -direction is zero due to free-swimming condition given by (5.30), and the net torque in the \mathbf{x} -direction equals to the external torque (e.g., magnetic). For swimmers with base-case parameters, net torque values in the \mathbf{x} -direction are calculated as 0.4 nN·m for unbounded swimming, 0.487 nN·m for swimming at the center of the circular channel, and 0.535 nN·m for swimming near the wall. Clearly, the \mathbf{x} -torque is the lowest for unbounded swimming and the highest for near-wall swimming, latter due to the traction forces between the swimmer and the cylindrical channel walls.

For the swimmer at the center of the circular channel, \mathbf{y} - and \mathbf{z} -forces have zero means with respect to time and have a phase shift in time due to rotation of the helical tail. For the swimmer near the channel wall, net forces in the \mathbf{y} - and \mathbf{z} -directions are negative and positive, respectively. The negative \mathbf{y} -force indicates that the swimmer with the left-handed helical tail is pushed to its left side (port) during its forward motion. Non-zero \mathbf{y} -force is clearly due to the traction force from the rotation of the swimmer near the wall. On the other hand, according to simulation results, a small positive force in the \mathbf{z} -direction indicates that the swimmer is pushed away from the wall, and there may be a stable position for the swimmer near the wall, similar to the ‘trapping’ of bacteria near walls [50, 69]. According to simulation results, normal-stress distribution around the swimmer as a whole contributes to the \mathbf{z} -force against the wall; individual contributions from the head and tail are comparable. Furthermore, in our ongoing computational studies, it is observed that the radial force increases for higher forward speeds when the motion is in the opposite direction as compared to the rotation (such as left-handed helices rotating in the positive direction or vice versa).

In Figure 5.20, normalized drag force on the spherical head of the swimmer is plotted against time. Drag force on the spherical head is normalized by the theoretical

drag force, $3\pi\mu d_h U$, on a sphere of diameter d_h , moving with velocity U in an unbounded fluid with viscosity μ . Averaged values over 12 different angular positions are obtained as 1.445 for unbounded, 5.928 for center, and 6.04 for near-wall swimming for base-case parameters. The difference between averaged values for swimmers inside the channel is very little. However, the difference between the unbounded swimmer and in-channel swimmers is more than fourfold. Moreover, the head drag for the unbounded swimmer is nearly 45 % larger than the theoretical drag for an isolated sphere; this increase is mostly due to the difference between flow fields for an isolated sphere and one with the helical tail. Lastly, results show that the drag force on the spherical head has the largest fluctuations due to variations of the axial velocity near the head for near-wall swimming (see Figure 5.17).

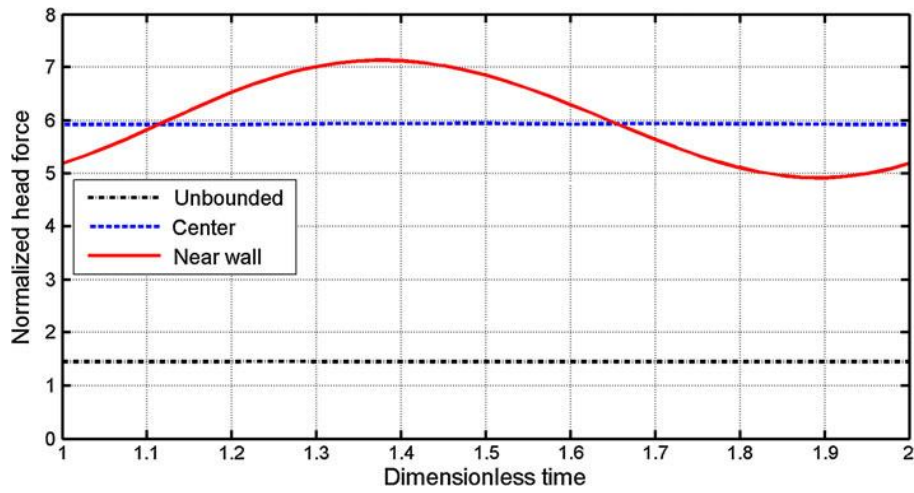


Figure 5.20 \mathbf{x} -force acting on the head normalized by the theoretical spherical drag ($3\pi\mu d_h U$) with respect to dimensionless time for unbounded (dash-dotted line), in-center (dashed line), and near-wall (solid line) swimmers.

In Figure 5.21, variations of time-averaged forces are plotted with respect to frequency (Figure 5.21a), amplitude (Figure 5.21b) and number of waves on the tail (Figure 5.21c) for near-wall swimming. Time-averaged forces on the swimmer in \mathbf{y} - and \mathbf{z} -directions and on the spherical head in the \mathbf{x} -direction increase linearly with the frequency (Figure 5.21a), with a constant factor multiplying the head-force in the \mathbf{x} -direction: about 2.23 for the \mathbf{y} -force and 0.33 for the \mathbf{z} -force. The ratio of the \mathbf{y} - and \mathbf{z} -forces is also constant, about 6.76, with respect to the frequency. Figure 5.21b illustrates that the \mathbf{y} -force on the swimmer remains significant due to the traction induced by the rotation even though the \mathbf{x} -force on the head and \mathbf{z} -force on the swimmer tends to zero

as the amplitude goes to zero. The magnitude of the x -force on the head and y - and z -forces on the whole swimmer increase with the wave amplitude (Figure 5.21b).

As for the dependence on the number of waves, the y -force increases with the increasing number of waves on the tail but the z -force tends to saturate (Figure 5.21c). The increase in the y -force with respect to both the amplitude and the number of waves is consistent with increasing traction force due to the rotation. However, the x -force on the head decreases as the number of waves increases (Figure 5.21c) due the decreasing swimmer speed (see also Figure 5.19c).

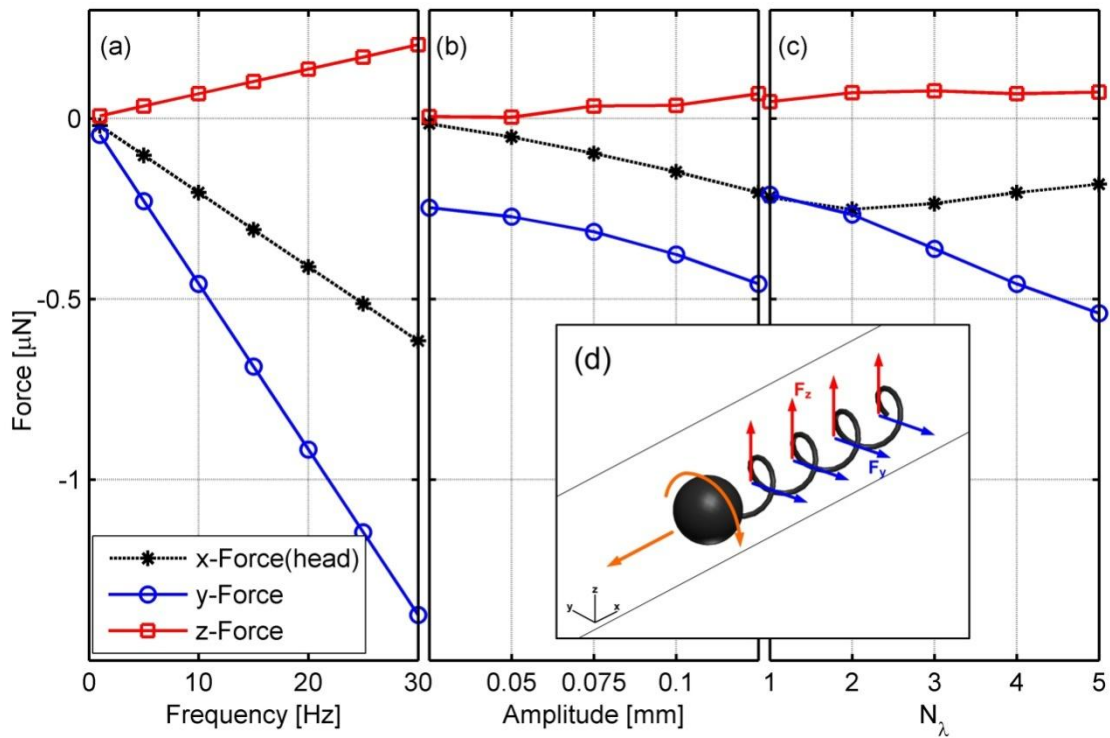


Figure 5.21 Time-averaged y - and z -forces for near-wall swimmers (solid lines with circles and squares) with respect to (a) frequency, (b) amplitude and (c) number of waves in comparison to drag force on the head (solid lines with asterisks). (d) Schematic representation of forces acting on the robot swimming near the wall.

Torques on swimmers in all directions are computed from the integration of the cross-product the position vector with respect to the center of mass of each swimmer and the stress tensor at the swimmer's surface for near-wall swimming. The position of the center of mass is calculated for each robot according to the geometry of the helical tail that varies with the amplitude and wavelength. For robots with small tail mass (small amplitude and large wavelength), swimmer's center of mass is closer to the head than for robots with large tail mass (large amplitude and small wavelength).

Magnitudes of the torques in \mathbf{x} - and \mathbf{z} -directions increase linearly with the frequency (Figure 5.22a). The \mathbf{x} -torque, which is the direction of rotation, is the largest; the \mathbf{z} -torque on the swimmer due to uneven traction between the head and tail of the swimmer is next in size (about 1.4 % of the \mathbf{x} -torque); whereas \mathbf{y} -torque is observed as zero. This result is somewhat consistent with the parallel-positioning of the microorganisms swimming near flat surfaces as observed by Lauga *et al.* [50]. As the amplitude increases, \mathbf{x} -torque increases as well due to increasing resistance to rotation, the \mathbf{y} -torque remains almost zero and \mathbf{z} -torque decreases and even changes its direction from positive to negative (Figure 5.22b). For small amplitudes, the positive \mathbf{z} -torque indicates that the traction force from the spherical head overcomes the traction force from the tail with respect to the center of mass of the swimmer which is closer to the head, hence the positive \mathbf{z} -torque is observed. On the other hand, the traction from the tail is larger than the traction from the head for larger amplitudes and leads to the negative \mathbf{z} -torque that forces the swimmer to turn clockwise with respect to the \mathbf{z} -axis as observed in the experiments.

The \mathbf{x} -torque remains almost constant as the number of waves increased to 2 from 1 (Figure 5.22c), and increases at a higher rate for larger number of waves than 2. For small wave numbers the \mathbf{x} -torque on the head is dominant and the effect from the tail is indiscernible. As the wave number increases, the \mathbf{x} -torque on the tail becomes important.

The \mathbf{z} -torque decreases with the increasing number of waves similarly to the behavior with respect to the amplitude. With the increasing number of waves on the helical tail, the traction force from the tail increases and dominates the one from the head and the \mathbf{z} -torque changes its direction (Figure 5.22c). The non-zero \mathbf{z} -torque causes the robot to change its alignment with the channel's axis; counter-clockwise when the number of waves is smaller than 4, and clockwise for N_λ equals 4 and 5. Thus, it is likely for the swimmer to follow a path, which is not parallel to channel's long axis, as observed in our experiments (Figure 5.22e).

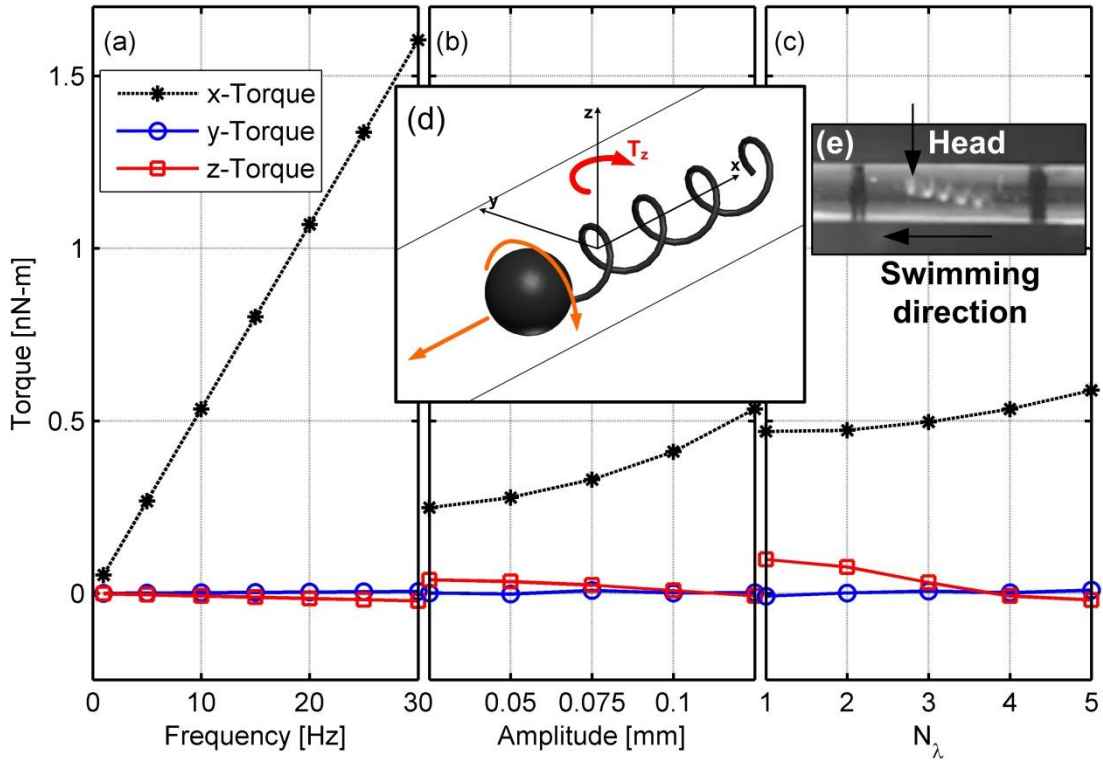


Figure 5.22 Time-averaged torques in y - and z -directions for near-wall swimmers (solid lines with circles and squares) with respect to (a) rotational frequency, (b) wave amplitude and (c) number of waves on the helical tail in comparison to the x -torque (dashed lines with asterisks). (d) Schematic representation of torques on the base-case robot swimming near the wall. (e) Top-view of the micro robot in experiments (actual robot has a right-handed helical tail, mirror-image is shown here).

5.3.2.4 Efficiency

Efficiency of low Reynolds number swimmers with flagellar propulsion is defined as the ratio of rates of work to linearly push the swimmer and to rotate the tail [7]. The net torque due to swimmer's rotational motion is well-defined and can be computed accurately. Nevertheless, since the net force on the swimmer in the direction of its motion is zero, an approximate definition of the efficiency is necessary. For swimmers with spherical heads, some authors typically use the ratio of the drag on the body to the total dissipation in the fluid [18, 42]. However, this approach neglects the tail resistance and is less meaningful for swimmers with relatively small heads compared to their tails. In (5.30), total force in the axial direction is calculated and set to zero in order to satisfy the free-swimming condition and to obtain the axial velocity; in essence, the total drag

of the swimmer is balanced by the propulsion force. Therefore, an alternative figure of merit is defined for the efficiency based on the net propulsion force in the swimming direction and calculated from the integration of the product of the stress tensor in the same direction and the Heaviside function that masks the stress. Then the efficiency is determined from:

$$\eta = \frac{|U| \int_S \sigma_{xj} H(\sigma_{xj}) dS_j}{2\pi f |T_x|} \quad (5.32)$$

Here, U is the linear velocity in the swimming direction, here \mathbf{x} -direction, f is the rotation frequency, T_x is the rotational torque in the axial direction, $H(\cdot)$ is the Heaviside step function that masks the stress tensor component in the swimming direction on the swimmer, i.e., $H(x) = x$ for $x > 0$ and $H(x) = 0$ for $x < 0$.

Efficiency values for in-center and near-wall swimming robots are shown in Figure 5.23. Efficiency stays constant as the frequency increases because of the linear relationship between the time-averaged \mathbf{x} -direction velocity and the rotational frequency for both positions of the robot. The near-wall swimming is more effective ($\sim 1.5\%$) compared to in-center swimming of the micro-robot ($\sim 1.21\%$) and the simulations show that free swimmer is slightly less efficient ($\sim 1.2\%$) than the in-channel swimmer. Efficiency values are on the order of 1% , as also stated by Purcell for helical swimmers in low Reynolds number flow regimes [7].

Change in the efficiency with respect to wave amplitude is presented in Figure 5.23b. Similar to the velocity, efficiency is proportional to the wave amplitude with the power > 1 for near-wall swimming micro-robot. As the wave amplitude increases, efficiency increases for both near-wall and in-center swimmers, yet the near-wall swimming is slightly more efficient than swimming at the center of the channel.

Increase in number of waves results in decrease in efficiency (Figure 5.23c). As the number of waves increases, friction over the tail also increases and since the velocity decreases, overall the efficiency of the robot decreases with the number of waves. However, we obtain the optimum value for $N_\lambda = 2$ similar to what is observed for the velocity of the swimmer.

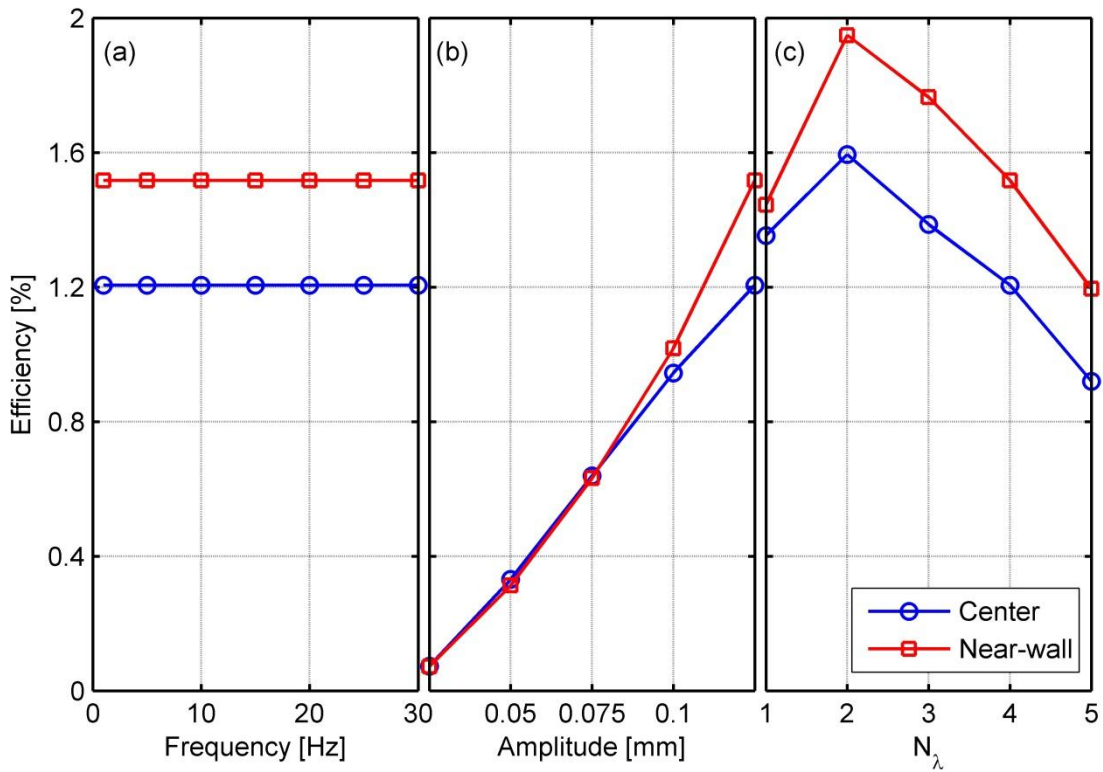


Figure 5.23 (a) Frequency, (b) wave amplitude and (c) number of waves dependence of efficiency for in-center (solid lines with circles) and near wall (solid lines with squares) swimming micro robots.

5.4 Flow Visualization

In this section, micro-PIV technique is explained which is used to visualize the flow field induced by the rotation of the helical tail of magnetic swimmers. In order to visualize cross-sectional flow fields around the tail and the head, a vertical channel is placed under the microscope. The channel is filled with micro-size fluorescent particle inserted glycerol. In typical applications, certain amount of micro spheres that are fluorescent or highly reflective are fed to the flow. Kinematical and dynamical properties of flow are not affected by the injected micro particles since they are extremely small in size and they have the same density as the working fluid. The important factor in PIV method is the light which has to be strong enough to make the micro particles detectable, thus usually laser or LED is used. The illuminated area is recorded by a digital camera, optical components and suitable lenses. Image processing methods are applied to the consecutive snap shots and the velocity vector profiles of the flow at those cross-sections are obtained from the displacements of the micro particles.

5.4.1 Experimental Setup

Magnetic swimmer consists of a cylindrical permanent $\text{Nd}_2\text{Fe}_{14}\text{B}$ magnet and non-magnetic copper wire. Copper wire is coiled up on another wire and adjusted for the desired number of waves. Permanent magnet and helical tail is fixed to each other with a strong adhesive. Permanent magnet has a diameter of 0.4 mm and length of 1 mm. Helical tail is made by 0.1 mm diameter wire and has 2 waves on 1 mm length.

The cylindrical channel having 1 mm diameter is manufactured by simply drilling a hole into a $20\text{ mm} \times 20\text{ mm} \times 20\text{ mm}$ Plexiglas cube (Figure 5.24). The cube is placed onto a lamella and magnetic swimmer is placed inside the channel which is filled with glycerol. Fluorescent micro particles having $1\mu\text{m}$ diameter is used as seeding particles and fed into the glycerol.

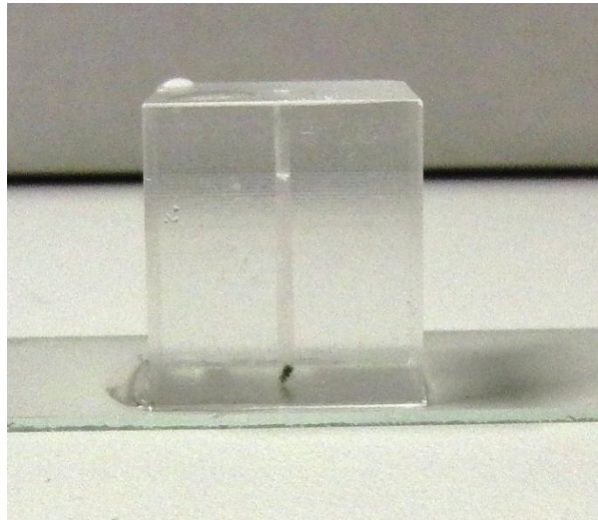


Figure 5.24 $20\text{ mm} \times 20\text{ mm} \times 20\text{ mm}$ Plexiglas cube on a lamella with a 1 mm diameter cylindrical channel and magnetic swimmer at the bottom

Two rectangular electromagnetic coil pairs are placed orthogonally on the microscope to obtain a rotating magnetic field vector along vertical direction (Figure 5.25). Small coils and large coils have 800 and 600 turns, respectively.

The glycerol filled cube is placed in the space between the electromagnetic coils, which are driven by Maxon ADS_E 50/5 4-Q-DC servo-mechanism amplifiers connected to NI-PCI 6733 high speed analog output device that transmits the current to the coils from the power supplies. In order to control the rotating frequency of magnetic field, LabView software interface is developed.

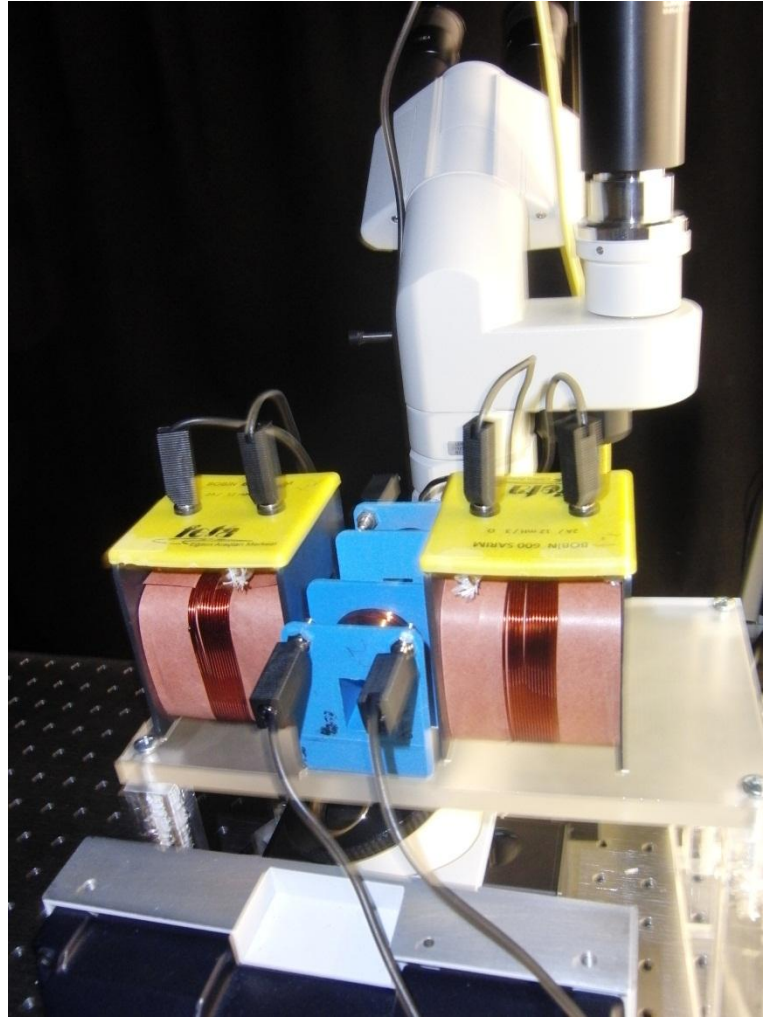


Figure 5.25 Electromagnetic coil pairs to produce rotational magnetic field along vertical axis placed on the Leica microscope.

5.4.2 Micro Particle Image Velocimetry Setup

Micro-particle image velocimetry (micro-PIV) is the preferred method to visualize the flow in micro scales, such as the flow induced by the rotation of a helical tail. One of the most important parameters of the PIV systems is dynamic speed range, which is defined as the ratio of the minimum and maximum velocity vectors that the system measures. PIV system having high dynamic speed range is required particularly generating vortex velocity vectors for turbulent flows. For this reason, double-frame PIV cameras and dual-cavity high power laser systems are developed and widely used. In typical applications, certain amount of micro spheres, which are fluorescent or highly reflective, are fed to the flow. Kinematical and dynamical properties of flow are not affected by the injected micro particles since they are extremely small in size and they

have the same density as the working fluid. The important factor in PIV method is the light which has to be strong enough to make the micro particles detectable, thus usually laser or high-intensity LED is used. The illuminated area is recorded by a digital camera, optical components and suitable lenses. Image processing methods are applied to the consecutive snap shots and the velocity vector profiles of the flow at those cross-sections are obtained from the displacements of the micro particles.

In our laboratory, double-frame micro-PIV imaging system consists of a cooling unit, a Neodymium-doped yttrium lithium fluoride (Nd:YLF) laser having a maximum output of 150W (DualPower, Dante Dynamics), a Phantom v130 high speed camera connected to Leica DMILM inverted microscope (Figure 5.26). Both the imaging system and illumination system are fixed to an optical table. This system is able to record two consecutive images in very short time intervals (50 ns - 7.5 ms) and perform time-resolved measurements at maximum 10 kHz.

Laser light, which is provided by dual-cavity Nd:YLF laser (Figure 5.27), transmitted to the inverted microscope with a liquid light guide. Laser can be turned on and off using the control unit in the cooling unit with triggering internally, or using the Dynamic Studio software [107] with triggering externally. Dynamic Studio software provides the opportunity to adjust the trigger rate, number of images and time between pulses as well as to post process obtained images to generate velocity vector plots.

The measurements are saved to the camera's hard-disk for initial investigation, and then they are transferred to the PC's hard-disc for further processing. Laser light illuminates the channel from one end; changing the focal distance of the microscope and thus changing the field of view, different layers perpendicular to the movement of the helical robot can be analyzed.



Figure 5.26 Double-frame micro-PIV imaging system consists of a cooling unit, a Neodymium-doped yttrium lithium fluoride (Nd:YLF) laser having a maximum output of 150W, a Phantom v130 high speed camera connected to Leica DMILM inverted microscope.



Figure 5.27 Dantec Dynamics DualPower dual cavity Nd:LYF laser.

5.4.3 Results

Experiments are conducted using a helical swimmer which is fabricated using nonmagnetic copper helix made of cylindrical wire (tail) and cylindrical $\text{Nd}_2\text{Fe}_{14}\text{B}$ permanent magnet (head). Radially magnetized cylindrical magnet having a diameter of 0.4 mm, is placed inside the helices, and a strong adhesive is used for rigid connection. The robot has 1.5 mm length and has 3 full waves on its 1-mm-length helical tail. Magnetic swimmer is rotated at 2 Hz and 8 Hz and the flow field at the tip of the tail and at the end point of the cylindrical magnet head is visualized. Fluorescent particles induced to the glycerol are 1 μm in size. Results of the micro-PIV experiments are compared with results obtained from simulations performed for a single robot used in these experiments.

Trigger rate, number of image pairs and time between pulses of the micro-PIV experimental setup are set to 508, 500 and 500 μs , respectively. Laser is operated at 1 kHz having a 50% of the output energy. Recorded images are then processed with a post-processing sequence of cross-correlation (at the tip of the tail) or adaptive correlation (at the end of the head), vector masking, range validation and moving average validation. Vector masking is used to mask the field outside of the channel and perform the analysis only in the field of interest which is the cross-section of the channel. Range validation is used to apply a filter to unexpectedly large velocity vectors by defining a maximum value limitation. Moving average validation is used to validate velocity vector maps by comparing each vector with the average vector in defined vicinity and replacing the ones that deviate too much from neighbors by the average of the neighbors to obtain a reasonable estimate for actual velocity vectors.

Figure 5.28 represents the comparison of micro-PIV and CFD results for helical swimmer rotating at 2 Hz at the at the end of the head (Figure 5.28a-b) and at tip of the tail (Figure 5.28c-d). Results obtained from experiments show that there is a rotational flow field in the channel (at the cross section). At 2 Hz, swimmer moves near the channel wall and resultant flow field at the end of the head is different than the one occurs at the tail tip. The swirling flow occurs behind the head is observed in CFD simulation results; however, it cannot be clearly seen in micro-PIV results because of the insufficient illumination. Another difference is the difference in the ratio between radius of the swimmer's head and radius of the channel for micro-PIV experiments and

CFD simulations. At the end point of the tail there are swirling flows both at the inner face of the tip and at the outer face of the tip between tail and channel wall. CFD results also indicates the same flow field with the micro-PIV results within the cross-section, however the place that swirling flows occurs is slightly different. The reason of this difference might be the imperfections on the helical robot tail used in the micro-PIV experiments, as well as the angular position of the tail, which might not be exactly same for micro-PIV and CFD. Maximum velocity in the cross section is measured as 2.8 mm/s which is in a good agreement with the linear velocity in the cross section, i.e. $2\pi fr_b \sim 3$ mm/s.

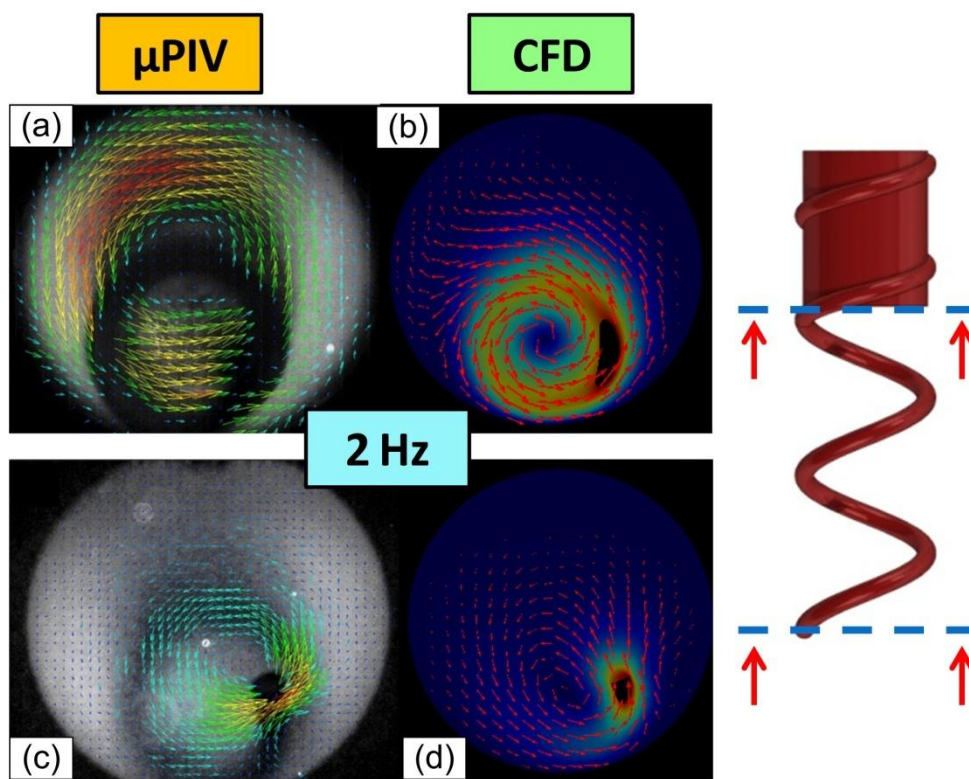


Figure 5.28 Velocity vector map obtained for 2 Hz (a) at the end of the cylindrical head from micro-PIV, (b) at the end of the cylindrical head from CFD, (c) at the tip of the tail from micro-PIV, (d) at the tip of the tail from CFD. Maximum velocities are measured from micro-PIV as 2.8 mm/s.

Similarly, micro-PIV and CFD results are compared for 8Hz at the end of the cylindrical head and at the tail tip and presented in Figure 5.29. At 8 Hz, swimmer moves in the center of the channel rather than near the channel wall. The swirling flow right behind the cylindrical head is not observed in micro-PIV because of the insufficient illumination. However the rest of the resultant flow field in the cross-

sectional area in the experiments can be well validated by CFD simulations. In addition, swirling flows around tail tip is observed in micro-PIV experiment results for 8 Hz as for 2 Hz, however in CFD simulation results only swirling flow occurs at the center of the cross-section (inner face of the tail tip). Maximum lateral (cross-sectional) velocity is measured as 11.2 mm/s and is higher for rotation frequency is equal to 8 Hz than to 2 Hz.

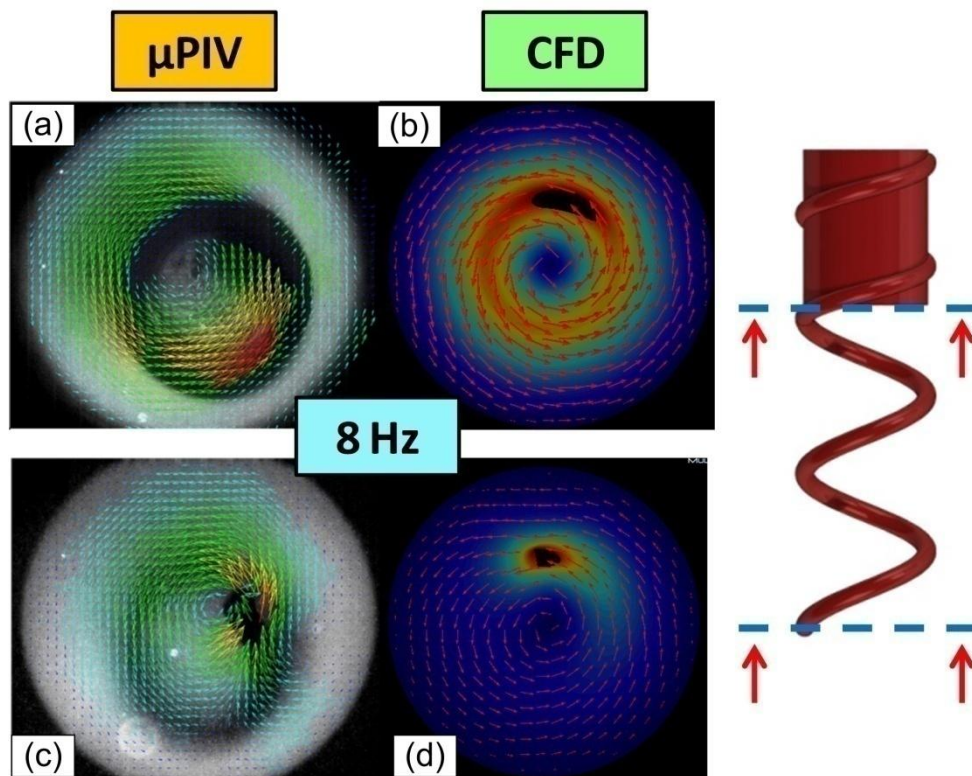


Figure 5.29 Velocity vector map obtained for 8 Hz (a) at the end of the cylindrical head from micro-PIV, (b) at the end of the cylindrical head from CFD, (c) at the tip of the tail from micro-PIV, (d) at the tip of the tail from CFD. Maximum velocities are measured from micro-PIV as 11.2 mm/s.

5.5 Discussion

Experiments with two micro swimming robots that have scales 0.36 mm and 0.41 mm in diameter and 2.17 and 2.45 mm in length, which are compatible with medical use in systems such as human circulatory, urinary, central nervous systems are presented. The micro swimmers used in experiments are made of permanent $\text{Nd}_2\text{Fe}_{14}\text{B}$ magnet heads and helical metal wire tails. Micro robots are actuated by external rotating magnetic fields and swimming behaviors are observed in glycerol- and water-filled

glass channels. To attain a rotational magnetic field, out of phase alternating currents are applied to two orthogonal electromagnetic coil pairs.

The range of the Reynolds number for experiments with glycerol shows that inertial effects are negligible similar to typical flow conditions of microscopic organisms. Thus, the linear relationship between rotating frequency and the velocity of the micro swimmer is observed for frequencies less than step-out frequency. The range of the Reynolds number for experiments in water is well above unity and up to 10 for the highest velocity observed in the experiments. Thus, clearly inertial effects are significant for mm-long micro robots swimming in water and similar fluids. Although a linear relation between frequencies and velocities are observed for up to 40 Hz, the micro robot travels slower in water between 20 Hz and 40 Hz than in glycerol owing to the significance of the inertial effects. At 20 Hz, micro robot travels approximately 1.4 times faster in glycerol than in water. At 30 Hz, the ratio is equal to 1.16, which is less than the former case due to the step-out effects.

Experiments conducted in glycerol indicated that the relative size of the head with respect to the tail's is important. The comparison of results measured from two different micro swimmers shows that the one with smaller head and longer tail travels faster. There are two outcomes from this observation: the first one is the drag force of the head must be minimal to increase the speed of the robot as also observed in [2], the second one is that the longer tail with mode helical turns (waves) improves the propulsion force of the tail.

Experimental data are confirmed that the motion along the channel depends on the actuation frequency: there exists a safe region where linear change in the actuation frequency affects the time-averaged forward velocity proportionally. As the magnetic actuation frequency increases, the magnetic torque cannot overcome the viscous resistance of the fluid. Then, the swimmer cannot rotate synchronously with the external magnetic field, and stops occasionally and even rotates in the opposite direction due to the variations in the instantaneous directions of the magnetic moment of the head and the external magnetic field. Thus, a nonlinear decrease in forward velocity with increasing frequency is observed.

Proposed RFT-based hydrodynamic model predicts the nonlinear decrease in forward velocity after step-out frequency observed as well as the linear relationship in between actuation frequency and time-averaged forward velocity; with a proper tuning of the normal drag of swimmer bodies. Lateral velocities, and thus \mathbf{yz} -trajectory, are

constrained numerically with proper modification of body and tail drag matrices with respect to swimmer position and orientation in the channel in order to include the near-wall effects of the cylindrical channel. It is observed that the required tuning on linear body drag is subject to proximity of the robot to solid boundaries.

Simulation results are presented for micro robots with helical tails swimming in circular tubes and compared with experimental results for a robot with approximately the same dimensions. Simulations are performed for two different radial positions of the robot in the channel: at the center and near the wall. The effects of frequency, wave amplitude, and number of waves on the forward velocity, forces on y - and z -directions, torques along x -, y - and z -axis and efficiency are studied for both radial positions.

Forward and backward flows induced by the tail's rotation and the motion of the swimmer form a bidirectional flow field around the helical tail and diminish within a short distance away from the swimmer. The axial velocity profiles around the helical tail for unbounded, in-center and near wall swimming cases are similar. However, due to the rotation of the helical tail, the squeezed fluid between channel boundaries and the swimmer is forced to move in opposite directions near the head. Forward velocity of the swimmer near the wall is larger than the one swimming at the center, which is also slightly faster than the unbounded swimmer agreeing well with the results presented by [51]. A linear relationship between the frequency and the time-averaged forward velocity of the swimmer is observed in simulations, which agree well with experiments for frequencies less than the step-out frequency for which the magnetic torque cannot overcome the rotational drag in experiments.

Forces acting on the swimmer in y - and z - directions vary significantly between the swimmers placed at the center and near the wall. For the swimmer placed along the axis of the channel at the center, y - and z -direction forces are nearly zero, unlike for the swimmer placed near the wall. Negative tangential force due to traction force shows that the swimmer is pushed sideways during its forward motion. For the swimmer near the wall, the y -torque is almost zero and the z -torque depends on the tail geometry, which also alters the position of the center of mass. A small positive z -torque for the swimmer used in experiments indicates that the swimmer has a tendency to travel with an angle with respect to the axis of the channel which is also observed in experiments. An appropriate metric for the efficiency of the micro-swimmer is proposed based on the propulsion force, and results show that near-wall swimmers are more efficient than

swimmers at the center; efficiencies are on the order of 1 %, which is expected for low Reynolds number swimmers.

Micro-PIV experiments are performed to visualize the flow field inside a cylindrical channel occurs as a result of the rotation of helical swimmers. It is observed that for near-wall and center swimmers, different flow fields at the tip of the tail and behind the head arise. The rotation of the helical swimmer causes a rotating fluid motion, which has effect on the motion of the swimmer, particularly at high rotational frequencies, since lateral fluid velocities are higher for larger rotational frequencies than smaller ones.

6 SWIMMING OF ARTIFICIAL SWIMMERS IN RECTANGULAR CHANNELS

In this chapter, swimming experiments of mm-sized robots in glycerol-filled rectangular channels are discussed in order to see the interaction between swimming robots and planar surfaces in a confined environment; robots are actuated by the rotating external magnetic field, which is generated by two counter-facing electromagnetic coil pairs. Experiments are carried out for two swimming magnetic helical robots which consist of heads made of cylindrical permanent magnets and rigid non-magnetic helical tails of different dimensions. The robots used in experiments have a body (head) radius of 400 μm and total length of 1.5 mm (swimmer no.1) and 1.9 mm (swimmer no.2), with these dimensions they simulates micro-fluidic regime.

In order to understand the flow field induced by the micro robot and the interaction of the micro robot with the channel wall, simulation-based analysis of the flow field is presented; forward, lateral and vertical velocities of the swimmer no.1 are calculated as a function of the position of the swimmer. Additional simulations are performed to calculate the traction and lift forces acting on the swimmers. A three-dimensional steady-state computational fluid dynamics (CFD) model is developed and solved with the commercial finite element software COMSOL Multiphysics [91].

6.1 Experimental Studies

6.1.1 Methodology

Microorganism-inspired helical swimmers similar to the ones mentioned in the previous chapter are fabricated using nonmagnetic copper helix made of cylindrical wire (tail) and cylindrical $\text{Nd}_2\text{Fe}_{14}\text{B}$ permanent magnet (head). Unlike the coupling mechanism that natural micro swimmers have, a rigid connection exists between head

and tail by means of which head and tail rotate in the same direction in rotational magnetic fields.

Two swimming robots with different dimensional parameters consist of a helical tail, which is made from a thin copper wire by simply winding it on another wire. Radially magnetized cylindrical magnet having a diameter of 0.4 mm, is placed inside the helices, and a strong adhesive is used for rigid connection. Helix is deformed plastically by stretching along its long axis to adjust desired number of waves, N_λ , on a fixed length, L_{tail} , (Figure 6.1). Dimensions of the robots are presented in Table 6.1.

Magnetic helical swimmers are placed inside glycerol-filled channels having rectangular cross section with dimensions of 1.3 mm in width and 1 mm in height (Figure 6.1). The viscosity and density of glycerol at room temperature are 1.412 Pa's and 1261 kg/m³, respectively. Reynolds numbers are calculated based on the forward motion of the swimmer and the rotation of the tail:

$$\text{Re}_{head} = \frac{\rho U d_b}{\mu} \quad (6.1)$$

$$\text{Re}_{tail} = \frac{\rho 2\pi f A d_{tail}}{\mu} \quad (6.2)$$

where the diameter of the head, d_b , and the velocity of the swimmer, U , are the length and velocity scales, respectively, for forward motion, the diameter of the wire, d_{wire} , and the tangential velocity of the tail, $2\pi f A$, are the length and velocity scales, respectively, for the rotational motion of the tail and A is the amplitude of the helical wave on the tail. For 1 Hz, Reynolds number for the forward motion of the head and the rotation of the helical tail are calculated as $0.45 \cdot 10^{-3}$ and $0.09 \cdot 10^{-3}$ for swimmer no.1 and $0.45 \cdot 10^{-3}$ and $0.15 \cdot 10^{-3}$ for swimmer no.2, respectively.

Table 6.1 Geometric parameters of the micro swimmers

Parameter	Swimmer no.1	Swimmer no.2
Wire diameter of the tail, d_{tail}	0.06 mm	0.09 mm
Length of robot, L	1.5 mm	1.9 mm
Diameter of cylindrical head, d_b	0.4 mm	0.4 mm
Length of cylindrical head	0.5 mm	0.8 mm
Number of waves, N_λ	2	3
Amplitude of waves, A	0.26 mm	0.29 mm

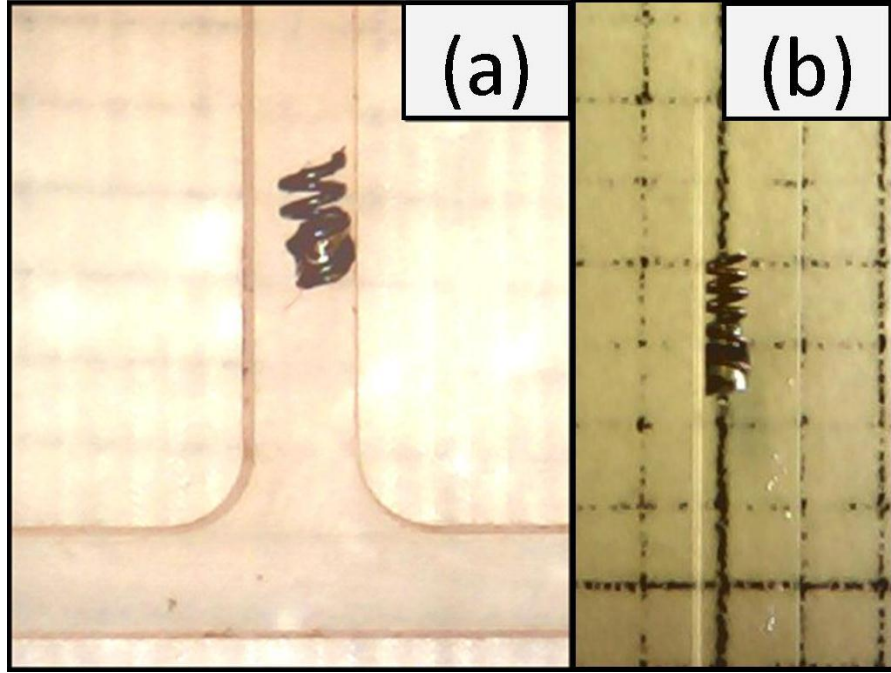


Figure 6.1 Millimeter size magnetic helical swimmers inside channels. (a) Swimmer no.1 (right-handed) and (b) swimmer no.2 (left-handed)

Three pairs of electromagnetic coils are placed along \mathbf{x} -, \mathbf{y} - and \mathbf{z} -axes for the propulsion and steering of untethered magnetic helical robots as commonly used in literature [2, 3, 12, 19, 20]. Cylindrical permanent magnets are radially magnetized and provide rotational motion due to the magnetic torque generated by the rotating magnetic field in the plane perpendicular to the centerline. The required magnetic torque, τ_M , for the synchronous rotation of the permanent magnet with the magnetic field is calculated from the cross product of the magnetic moment, \mathbf{m} , of the particle, which depends on the volume, V , and magnetization, \mathbf{M} , of the particle, and magnetic induction, \mathbf{B} , of the field, which depends on the permeability of free space, ζ_0 , and magnetic field, \mathbf{H} .

$$\tau_M = \mathbf{m} \times \mathbf{B} \quad (6.3)$$

where

$$\mathbf{m} = MV \quad \text{and} \quad \mathbf{B} = \zeta_0 \mathbf{H} \quad (6.4)$$

Thus, (6.3) can be rephrased as

$$\tau_M = \zeta_0 VMH \sin \theta \quad (6.5)$$

where θ is the angle between \mathbf{B} and \mathbf{m} . Magnetic field along the axis of a circular coil is derived from Biot-Savart law and depends on the radius of the coil, r_{coil} , number of the turns, N , current, I , and distance from the center along the axis of the coil, a .

$$H = \frac{NIr_{coil}^2}{2(r_{coil}^2 + a^2)^{3/2}} \quad (6.6)$$

Each electromagnetic coil is connected to one Maxon ADS_E 50/5 4-Q-DC servo-mechanism amplifiers, which are connected to NI PCI-6733 high speed analog output device, that are used to transmit the current to the coils from the power supplies. The currents applied to the \mathbf{x} -, \mathbf{y} -, and \mathbf{z} -axis coils are defined as $I_x = I_{x,0} \cos(2\pi ft)$, $I_y = I_{y,0} \cos(2\pi ft)$, and $I_z = I_{z,0} \sin(2\pi ft)$, respectively. A LabView software interface is constructed to control the motion of helical robots with a joystick by adjusting the magnitude and frequency of alternating currents. Motion of helical swimmers in channels is recorded with a 2.0 mega pixel CMOS digital microscope USB camera that has a recording rate of maximum 30 frames per second.

Translational and lateral velocities of helical swimmers are measured using MATLAB image processing tools. Properties of recordings, such as frame per second, length of the video and number of images, are obtained and each frame of the video is processed separately following a sequence including converting the frames from RGB to grayscale, detecting the intensity of each pixel, distinguishing helical swimmer by adjusting intensities of pixels and defining centroid of the helical swimmer (red dot in Figure 6.2). Forward and lateral velocities of the helical swimmer are calculated using the position change of the centroid.

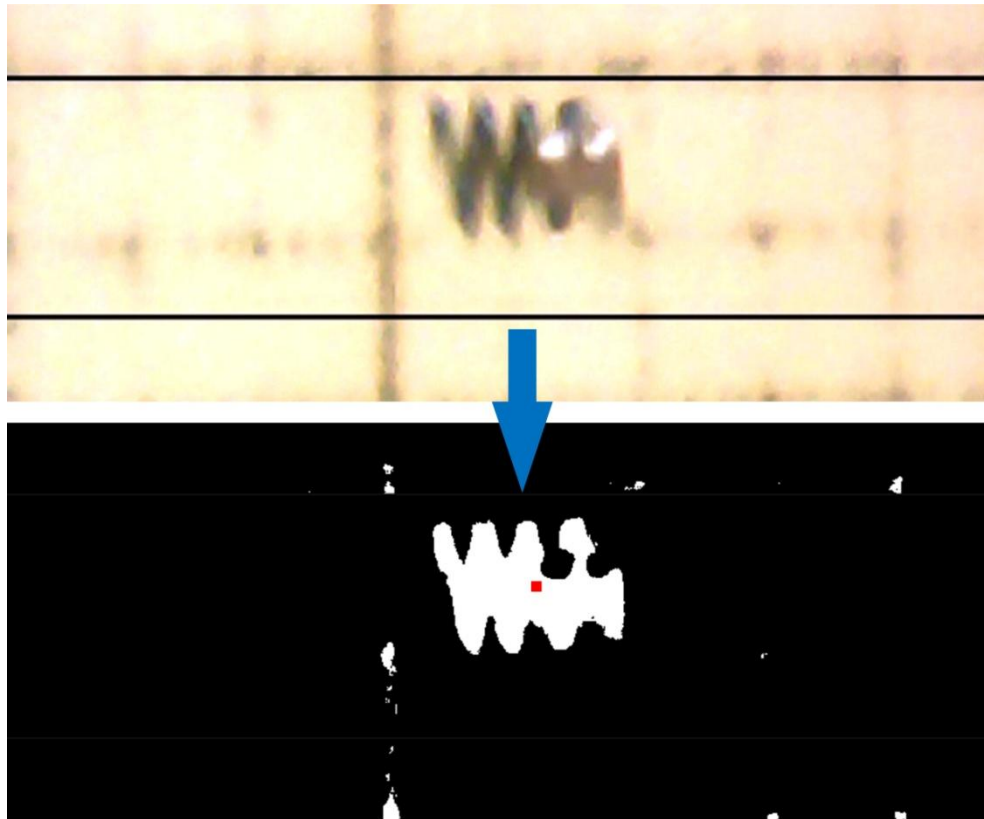


Figure 6.2 An image processing sequence of converting the frames from RGB to grayscale, detecting the intensity of each pixel, distinguishing helical swimmer by adjusting intensities of pixels and defining centroid of the helical swimmer is used to measure the forward and lateral velocities of micro swimmers.

6.1.2 Results

Propulsion as a result of the rotation of the helical tail is a well-known swimming mechanism for both natural and artificial micro swimmers. Inside rectangular channels, helical swimmers showed different swimming properties in experiments: forward motion due to the fluidic propulsion force and lateral motion due to the traction force near the solid wall. Swimmers tend to travel near solid walls due to their weight; a lift force from the wall balances the swimmer and avoids stiction to the wall and results in a very small clearance. Due to rotation, a net traction force emerges and acts as a lateral force on the robot and causes its sideways motion.

Linear and angular velocities of helical swimmers are obtained from the solution of the equation of motion. In addition to the propulsion force, traction force occurs, as well, due to the rotation of the tail when external magnetic torque is applied. Total drag

force and torque on the swimmer are as follows where subscripts p , d and ext denote propulsion, drag and external effects, respectively.

$$\begin{aligned}\mathbf{F}_d + \mathbf{F}_p + \mathbf{F}_{ext} &= 0 \\ \mathbf{T}_d + \mathbf{T}_{ext} &= 0\end{aligned}\tag{6.7}$$

Force and torque vectors due to hydrodynamic propulsion and fluid drag are constructed by the resistive force theory [18]: the force and torque vectors are obtained from the linear and angular velocity vectors with a linear resistance relationship as follows:

$$\begin{bmatrix} \mathbf{F}_{ext} \\ \mathbf{T}_{ext} \end{bmatrix} = \begin{bmatrix} \mathbf{F}_T \\ \boldsymbol{\tau}_M \end{bmatrix} = (\mathbf{C}_B + \mathbf{C}_T) \begin{bmatrix} \mathbf{u} \\ \boldsymbol{\Omega} \end{bmatrix}\tag{6.8}$$

where, for a full six degree of freedom motion, \mathbf{C}_B and \mathbf{C}_T are the resistance matrices of the body and tail, respectively. \mathbf{F}_{ext} is traction force and equals \mathbf{F}_T and \mathbf{T}_{ext} is the magnetic torque and equals $\boldsymbol{\tau}_M$.

In addition to the longitudinal motion, because of the traction due to the channel walls, lateral motion occurs. Wall effects on a swimmer moving at low Reynolds regime is examined in [52] in detail. As a result of the interaction with the channel wall, lateral motion occurs due to rotation of helical swimmer with the applied magnetic torque; equation of motion can be then written as:

$$\tau_M = F_T \cdot r_{hw} = b \cdot V = b \cdot \omega \cdot r_{hw}\tag{6.9}$$

where \mathbf{F}_T is the traction force, r_{hs} is the radius of the helical swimmer, b is the friction coefficient, V is the lateral velocity and ω is the angular velocity of the robot.

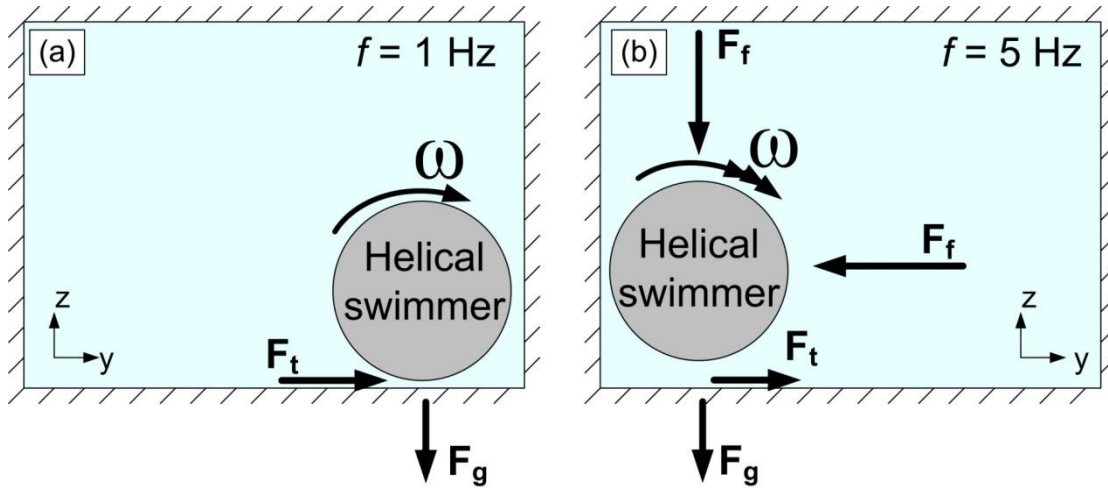


Figure 6.3 Motion of right-handed helical swimmer moving to the negative x -direction (swimmer no.1) or left-handed helical swimmer moving to the positive x -direction (swimmer no.2) inside rectangular channel when rotational frequency, f , equals (a) 1 Hz and (b) 5 Hz. In the figure, F_t , F_g , F_f and ω represent traction force, gravitational force, fluid force and angular velocity, respectively.

Experiments are performed when helical swimmer no.1 is rotated between 1 and 30 Hz in both directions (forward and backward swimming conditions) and smooth (glass) and rough (machined Plexiglas) surfaces. According to the experiments, forward and backward velocities are calculated and swimming modes at high and low frequencies are identified.

Forward and backward velocities of helical swimmer are calculated by dividing the travel distance to the travel time of helical magnetic swimmer using image processing tools of MATLAB (Figure 6.2 and Figure 6.4). Experiments performed when swimmers are moving forward and backward, indicate that surface roughness and swimming direction affect forward velocities of the helical swimmers. On glass surface, which is smooth, behavior of robot is stable and almost symmetrical with respect to zero frequency.

As the frequency increases, e.g. to 5 Hz, swimmer changes its lateral position inside the channel and begins to move towards the opposite side of the channel along with a fast forward motion reaching to a velocity of 0.35 mm/s (Figure 6.5). One reason for the lateral position change is the fluid force caused by the flow which is affected by rotation. This phenomenon is similar to the one observed in [50]; although the natural micro swimmers' head and tail rotating in reverse directions in the mentioned study, at high frequencies micro organism approach to the planar wall.

When the helical swimmer no.1 is moving between backward 7 Hz and forward 5 Hz, the linear velocity has a different behavior than the swimmer no.1 shows at other frequencies. Linear relationship between forward velocity and rotation frequency is observed for all frequency values; however, the slope varies as the frequency changes. When the frequency is more than 7 Hz during backward motion and more than 5 Hz during forward motion the behavior of the swimmer no.1 shows the same trend. When the helical swimmer no.1 is moving between backward 7 Hz and forward 5 Hz, an irregularity in the behavior of helical swimmer occurs particularly for backward motion because of the contact with the channel wall. In experiments, it is observed that at 3 Hz swimmer changes its position on the bottom wall of the channel according to the explained swimming modes with respect to the frequency for both forward and backward motion, since the lateral fluid forces overcome the traction force. In addition, at 7 Hz when moving backward and 10 Hz when moving forward, stable swimming behavior of helical swimmer changes and oscillations are observed during forward motion (Figure 6.4) which results with the change in measurements with respect to frequency after critical frequencies. When the frequency is above 5 Hz during backward motion and above 7 Hz during forward motion, the lifting force overcomes gravitational force and helical swimmer starts to follow an elliptical trajectory inside rectangular channel due to the resultant flow field. The frequencies at which the robot changes its behavior are named as “critical frequencies” that are 7 Hz and 5 Hz for backward swimming and forward swimming, respectively.

For rough surface, the critical frequencies are same as the smooth surface. The irregularity in the behavior of the swimmer between critical frequencies is observed in this case as well. In addition, when the frequency is above 25 Hz for backward motion and forward motion, magnitude of linear velocity decreases.

Another outcome of the experiments is that forward velocity being approximately zero during lateral motion of the swimmer from one corner of the channel to the other (Figure 6.4). On the other hand, when swimmer no.1 is rotating at low frequencies and moving forward along a corner without lateral motion, it has a forward velocity. For instance, at 1 Hz, during lateral position change of swimmer lateral velocity is equal to 1.6 mm/s and forward velocity is nearly zero. However when swimmer no.1 moves along a corner with zero lateral velocity, the forward velocity is measured as 0.07 mm/s. At 1 Hz, lateral velocity is measured as 1.6 mm/s which is close to $2\pi Af = 1.63$ mm/s where A is the wave amplitude and equals 0.26 mm.

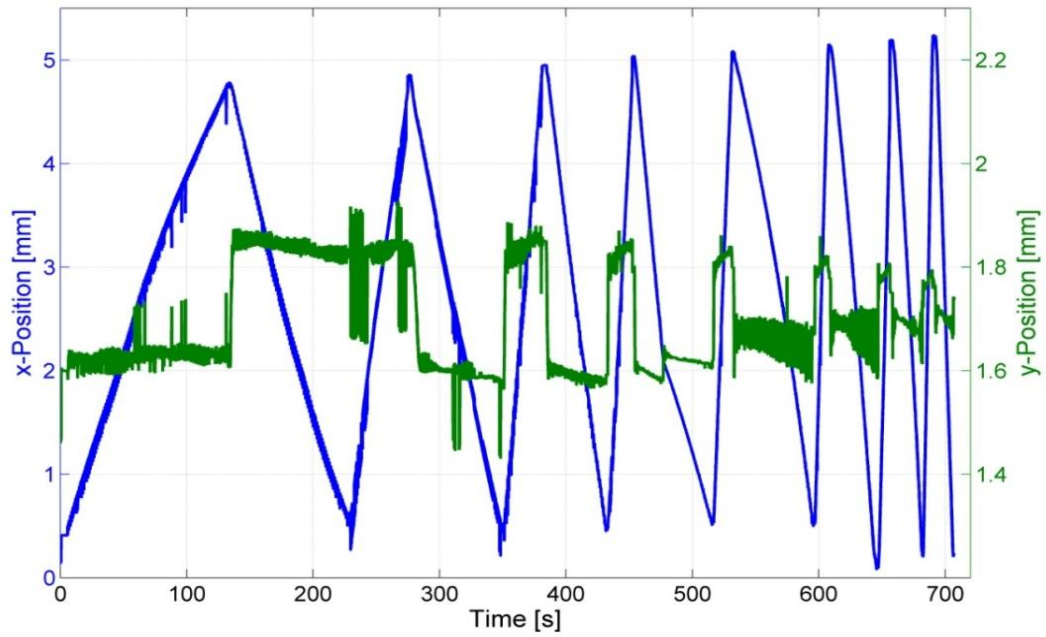


Figure 6.4 Position change of helical right-handed swimmer (no.1) in x -direction (blue line) and in y -direction (green line) inside rectangular channel during its motion.

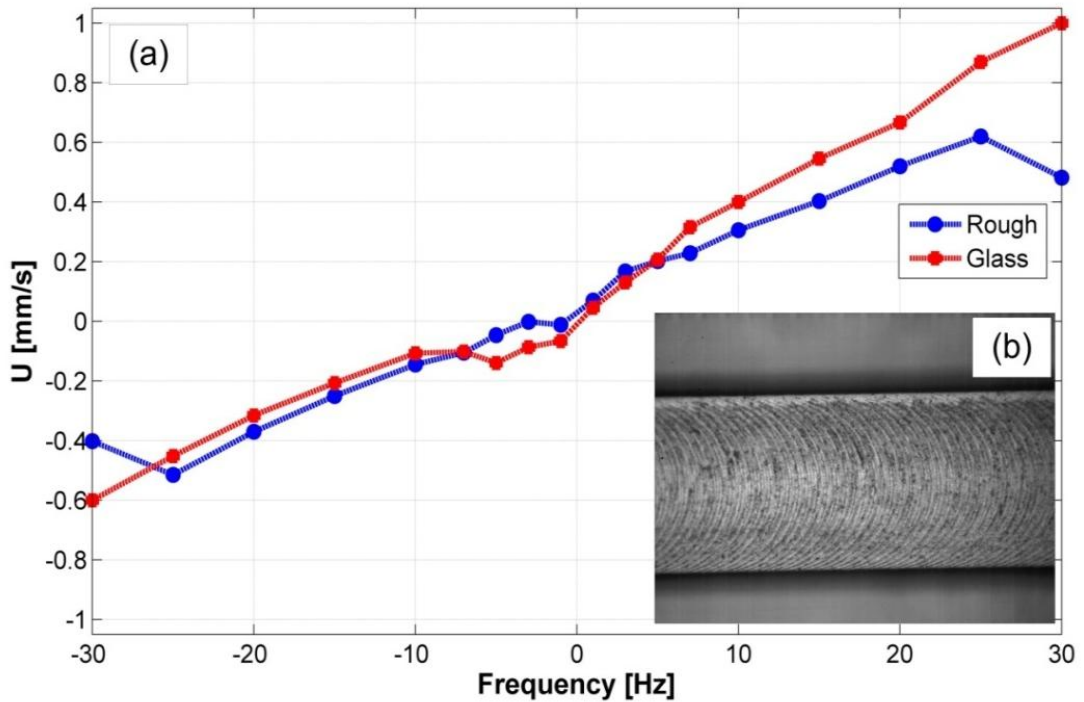


Figure 6.5 (a) Dependence of linear velocities of micro swimmer no.1 (right-handed swimmer) on rotation frequency and channel surface. Negative frequencies represent backward motion and positive frequencies represent forward motion. (b) Picture of rough-surface, width of the channel (rough surface) is equal to 1.3 mm.

When frequency of swimmer no.2 increases, the linear relationship between frequency and backward velocity prevails up to 7 Hz, after which a decrease is observed (represented by positive frequencies in Figure 6.6). The backward velocity at 10 Hz is measured less than the one at 7 Hz. Between 10 Hz and 30 Hz, backward velocity continues to increase nonlinearly. Similar behavior is observed for forward motion (represented by negative frequencies in Figure 6.6). The linear relationship between forward velocity and rotational frequency changes to nonlinear relationship when frequency is more than 5 Hz. In this case, between 5 Hz and 7 Hz, a sudden jump on the forward velocity is observed. The frequencies at which the robot changes its behavior are named as “critical frequencies” that are 5 Hz and 7 Hz for forward and backward swimming, respectively. The reason of the change in measurements with respect to frequency is that after critical frequencies, robot starts to move to the opposite side of the channel under the effect of the flow field; the fluid forces become dominant compared to the gravitational and traction forces.

For rough surface, the critical frequencies are different than the smooth surface. When frequency increases, for forward and backward motion, the critical frequency is measured as 3 Hz, after which an almost linear relationship between frequency and forward velocity is observed. When swimmer is moving forward, between 1 Hz and 7 Hz, the swimming behavior is not smooth. As the frequency increases up to 30 Hz in forward motion, the nonlinear relationship occurs between forward velocity and rotational frequency for values greater than 7 Hz.

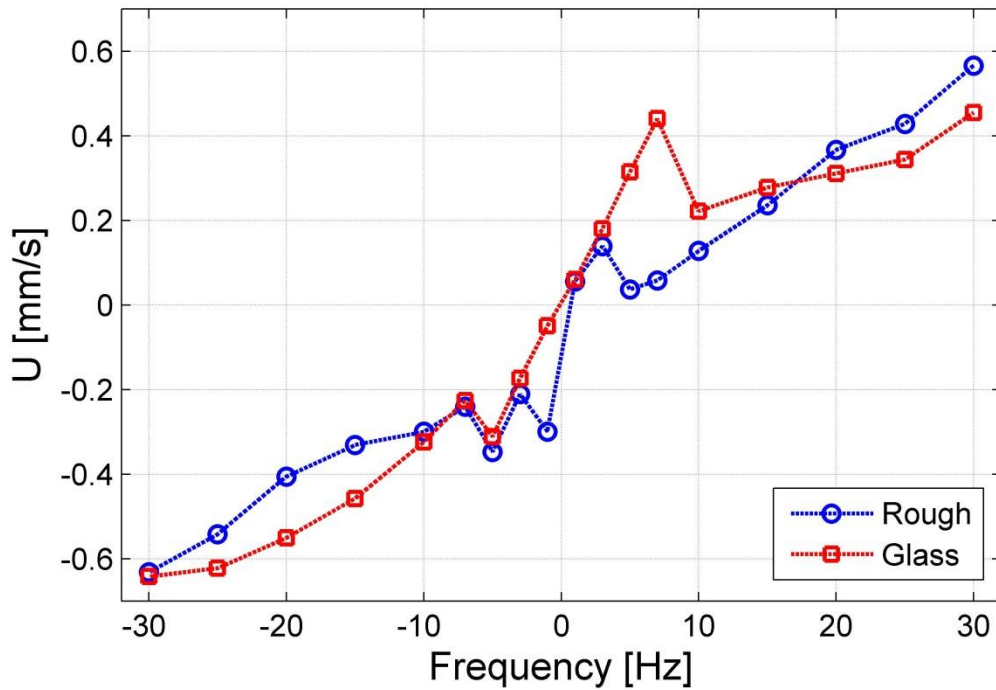


Figure 6.6 Dependence of linear velocities of left-handed swimmer (no.2) on rotation frequency and channel surface. Negative frequencies represent forward motion and positive frequencies represent backward motion.

Experiments with swimmer no.2 are performed on glass surface in order to eliminate possible effects of rough surface on the motion of the swimmer (Figure 6.7, 6.8 and 6.9). Three different frequencies (1 Hz, 2 Hz and 3 Hz) and three different starting positions (left, middle and right) are chosen for experiments to clarify the critical frequency and the optimal places in the channel. When swimmer is rotating with 1 Hz, regardless of the starting position, it moves to the side according to the rotation direction, which is positive y -direction, until it reaches to the boundary. After hitting the boundary, swimmer moves forward with along the vertical channel wall. When the sign of magnetic field changes, swimmer moves to the negative y -direction and it continues its motion along the sideways.

At 2 Hz, starting position becomes important for the helical swimmer's final path to follow. When swimmer starts its motion at the negative y -position or at the middle of the channel, it travels to the positive y - direction, however not until it reaches the corner. For both cases, final position stands between the channel wall and the mid-point of the channel. On the other hand, when it starts to travel at the positive y -corner or the channel, it does not change its position and continues to move along the channel wall. A similar behavior to the previous case is observed when the rotation direction of

magnetic field changes. When helical swimmer's initial position is positive y -corner or mid-point of the channel, it moves to the negative y -corner and stops at a distance to the channel boundary. However, when it starts its motion at the negative y -corner, then it continues to move along the channel wall. It is possible that a fluidic bump occurs between the corners and the mid-point of the channel, which prevents to move either direction, which results with two optimal positions of the helical swimmer in the channel.

The critical frequency for swimmer no.2 is 3 Hz, which is the frequency value to change the swimming behavior. When rotation frequency is equal to 3 Hz, regardless of the initial position, swimmer moves to the channel wall negative to the rotation direction, which is negative y -corner, and continues its forward motion along the channel wall. When the magnetic field changes its rotation direction, similar behavior is observed. The final position of the helical swimmer does not depend on the initial position; swimmer moves to the positive y -corner of the channel and travels along the channel boundary.

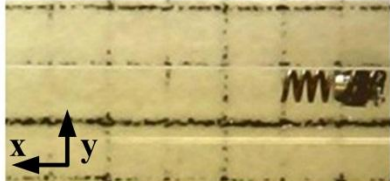
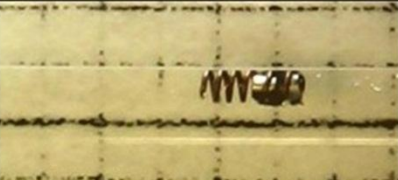
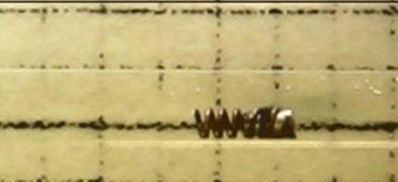
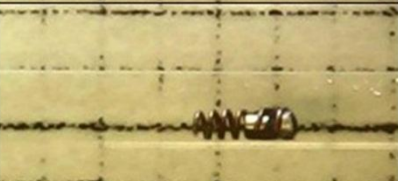
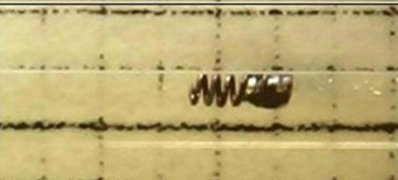
Frequency	Direction	Start	Finish
-1			
1			
-1			
1			
-1			
1			

Figure 6.7 Initial and final positions of the helical swimmers when rotating with a frequency of 1 Hz or -1 Hz, which represents moving forward and backward with a rotation frequency equal to 1 Hz, respectively. Three different initial positions are chosen: positive y-corner, mid-point, negative y-corner.

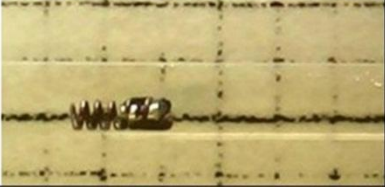
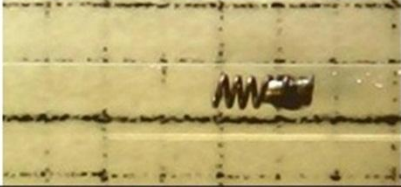
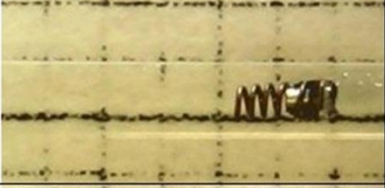
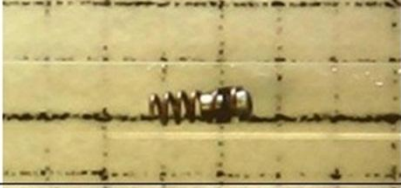
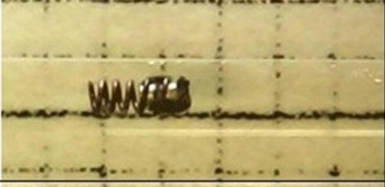
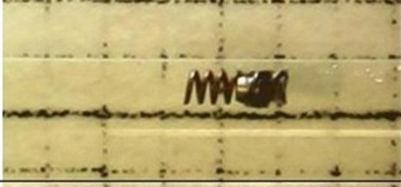
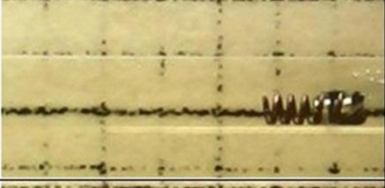
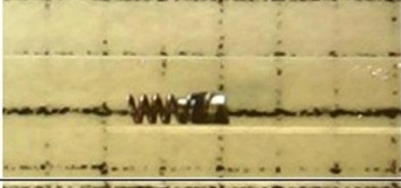
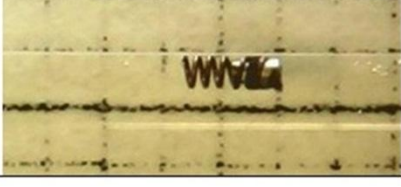
Frequency	Direction	Start	Finish
-2		 	
2			
-2			
2			
-2			
2			

Figure 6.8 Initial and final positions of the helical swimmers when rotating with a frequency of 2 Hz or -2 Hz which represents moving forward and backward with a rotation frequency equal to 2 Hz, respectively. Three different initial positions are chosen: positive y -corner, mid-point, negative y -corner.

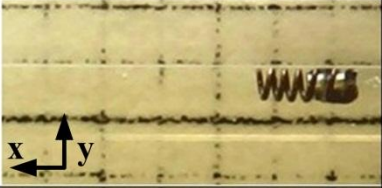
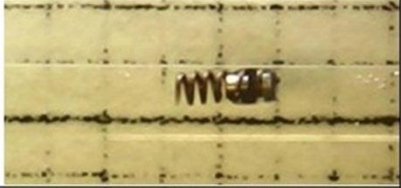
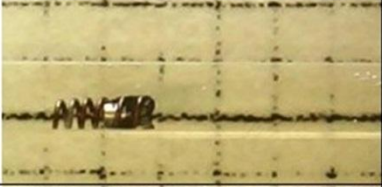
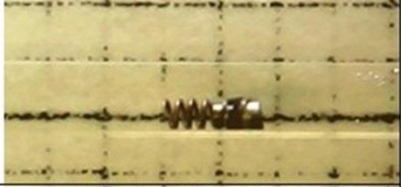
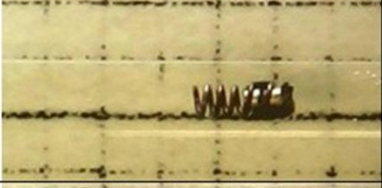
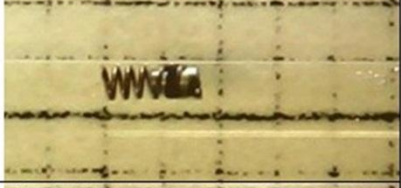
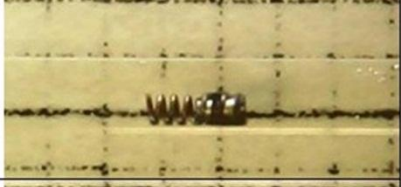
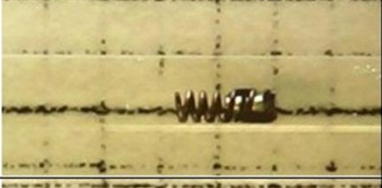
Frequency	Direction	Start	Finish
-3			
3			
-3			
3			
-3			
3			

Figure 6.9 Initial and final positions of the helical swimmers when rotating with a frequency of 3 Hz or -3 Hz. which represents moving forward and backward with a rotation frequency equal to 3 Hz, respectively Three different initial positions are chosen: positive y-corner, mid-point, negative y-corner.

6.2 CFD Studies

In order to fully understand the flow fields inside the channel due to faster rotation of the swimmer and which cause the swimmer change its lateral position in the channel as observed in the experiments, a computational model is necessary.

6.2.1 Methodology

Swimming of robot inside a rectangular channel filled with glycerol is simulated using a CFD model. The robot is modeled almost identically as the one used in the experiments with the union of a cylindrical head and a helical tail (Figure 6.10). Dimensions of the swimmer modeled here are scaled with the diameter of cylindrical head of the swimmer used in the experiments. Reynolds number used in scaling is the “frequency Reynolds number”, and calculated with a velocity scale, which is the multiplication of frequency of rotations, f , and diameter of cylindrical head, D_h :

$$\text{Re}_f = \frac{\rho d_b^2 f}{\mu} \quad (6.10)$$

Table 6.2 Geometric parameters of the channel and micro swimmer

Parameter	Actual Value	Dimensionless Value
Width of channel, W_{ch}	1.3 mm	3.25
Depth of channel, T_{ch}	1.0 mm	2.5
Length of channel, L_{ch}	6.0 mm	15
Wire diameter of the tail, d_{tail}	0.06 mm	0.15
Length of tail, L_{tail}	1.0 mm	2.5
Diameter of cylindrical head, d_b	0.4 mm	1

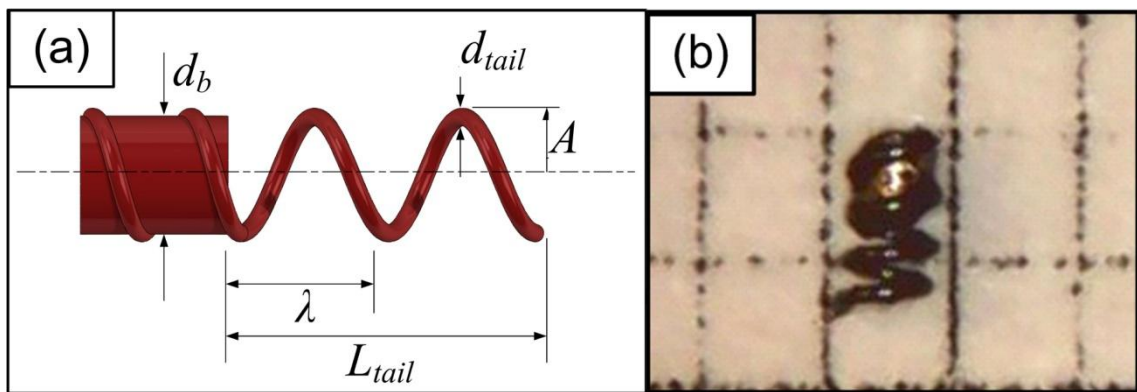


Figure 6.10 (a) Micro robot used in the experiments consists of a magnetic head and a metal right-handed helical tail. (b) Drawing of the micro robot in CFD model that consists of a cylindrical head and a right-handed helical tail.

Three-dimensional incompressible instantaneous flow is governed by viscous forces balanced by the pressure gradient subject to continuity since inertial forces are neglected due to the creeping flow regime at low Reynolds number:

$$\mu \nabla^2 \mathbf{u} - \nabla p = 0 \quad \text{and} \quad \nabla \cdot \mathbf{u} = 0 \quad (6.11)$$

where μ is viscosity, \mathbf{u} is the velocity vector and p is pressure.

In the absence of inertial forces, the flow induced by the rotation of the helical tail and the motion of the robot has no memory; instantaneous snapshot solutions of the velocity field and the pressure are obtained from (6.11) using boundary conditions for the given position of the robot and the helical tail. The centerline position of the wire, which forms a right-handed helical tail, is given by:

$$\mathbf{P}_{tail} = [x_{tail}, A \cos(kx_{tail} + \varphi), -A \sin(kx_{tail} + \varphi)] \quad (6.12)$$

where x_{tail} is the axial position of the helical tail measured from the joint, A is the amplitude (helical radius), $k = 2\pi/\lambda$ is the wave number, λ is the wavelength (helical pitch), and $\varphi = \omega t$ is the phase angle that corresponds to the rotation of the helix with angular velocity of ω .

The constraint equation for force-free swimming condition is specified as the zero-net force in three directions and forward, lateral and vertical velocities of the robot are obtained from the integration of fluid stresses over the surface of the robot in the related direction:

$$\int_{S_{tail} \cup S_{body}} \sigma \cdot \mathbf{n}_x dS = 0 \quad (6.13)$$

$$\int_{S_{tail} \cup S_{body}} \sigma \cdot \mathbf{n}_y dS = 0 \quad (6.14)$$

$$\int_{S_{tail} \cup S_{body}} \sigma \cdot \mathbf{n}_z dS = 0 \quad (6.15)$$

where σ is the stress tensor, \mathbf{n}_x , \mathbf{n}_y , \mathbf{n}_z are \mathbf{x} -, \mathbf{y} - and \mathbf{z} -components of the local surface normal, and $S_{tail} \cup S_{body}$ is the whole surface of the robot including its tail and body.

Similarly, for the unknown angular velocities along \mathbf{y} - and \mathbf{z} -axis, zero-net torque constraint is specified as an additional equation:

$$\int_{S_{tail} \cup S_{body}} [(z - z_{COM})(\boldsymbol{\sigma} \cdot \mathbf{n}_x) - (x - x_{COM})(\boldsymbol{\sigma} \cdot \mathbf{n}_z)] dS = 0 \quad (6.16)$$

$$\int_{S_{tail} \cup S_{body}} [(x - x_{COM})(\boldsymbol{\sigma} \cdot \mathbf{n}_y) - (y - y_{COM})(\boldsymbol{\sigma} \cdot \mathbf{n}_x)] dS = 0 \quad (6.17)$$

where $(x,y,z)_{COM}$ are $(\mathbf{x},\mathbf{y},\mathbf{z})$ -coordinates of the joint and $\mathbf{n}_{(x,y,z)}$ are \mathbf{x} -, \mathbf{y} - and \mathbf{z} -components of the surface normal.

6.2.1.1 Boundary conditions

At the inlet and outlet of the channel, the normal stresses are set to zero since they have open boundary conditions. The slip length between glass (solid) and glycerol (liquid) interfaces is less than 200 nm [21] and does not constitute a limiting issue in the experiments. Thus, the solid surfaces of the channel walls and the swimmer's surfaces have no-slip boundary conditions. Furthermore no-slip boundary conditions hold well in a variety of micro flows [22], and it is assumed that no-slip conditions remain valid for swimming of structures and organisms that are at least tens of microns long for channels that have similar dimensions. Thus, no-slip boundary conditions at the channel walls are:

$$\mathbf{u} = 0 \quad \text{at} \quad y = W_{ch} \quad \text{and} \quad z = T_{ch} \quad (6.18)$$

In order to simulate wall effects accurately, an additional viscous fluid layer, with a thickness of 0.02 mm is defined at the boundaries of the rectangular channel (Figure 6.11). The viscosity of the thin layer is 50000 more than the viscosity of fluid inside the channel.

The swimming robot moves with a forward velocity, U , lateral velocity, V , and vertical velocity, W , while the body and the tail rotate together with the same frequency. Therefore, no-slip moving-wall boundary conditions for the body and the tail are specified as:

$$\mathbf{u}(\mathbf{x}) = [U, V, W] + [0, y - w_{sw}, z - t_{sw}] \times [\Omega_x, \Omega_y, \Omega_z] \quad (6.19)$$

where w_{sw} and t_{sw} are the position of the robot in the \mathbf{y} -direction and \mathbf{z} -direction, respectively, and varied between 0 (centerline) and a value, which corresponds to a small gap between the body and the channel wall, and Ω_x, Ω_y , and Ω_z are the swimmer rotation rates.

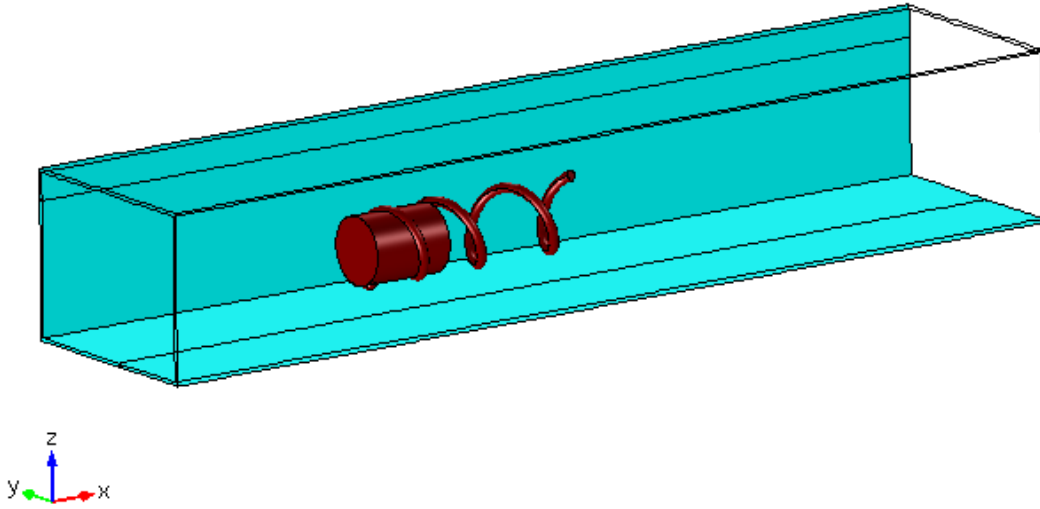


Figure 6.11 Helical swimmer placed in the rectangular channel and simulations are performed for different positions of the swimmer in the channel. A thin layer with high viscosity represents the channel walls.

6.2.1.2 Simulation parameters

Governing equations given by (6.11) subject to constraint equations (6.13) to (6.17) and boundary conditions (6.18) and (6.19) are solved with the finite-element method (FEM) software, COMSOL Multiphysics [91].

The finite-element model consists of approximately 175000 tetrahedral elements and 1100000 degrees of freedom. The linear system of equations is solved using the PARDISO direct solver. For each configuration of the tail and the radial position of the robot the average velocity and the body rotation rate are obtained from 12 different angular positions in $\pi/6$ increments; each simulation takes about 20 minutes on a high end workstation with 12 cores operating at 2.7GHz and sharing 96GB of RAM.

In simulations, position of the robot in the channel is varied along \mathbf{y} - and \mathbf{z} -axes.

Only one quarter of the channel is taken in the consideration, however, in order to verify the symmetry, additional simulations are performed through the channel. Without additional simulations, 42 simulations are conducted with 7 and 6 points defined along **y**- and **z**-axis, respectively. At the swimmer's closest positions to the wall, swimmer is tangent to the viscous fluid layer and the distance between channel and swimmer is equal to 0.02 mm. Furthermore, to calculate fluid forces acting on the swimmer at low and high rotational frequencies, two additional simulations are performed to calculate forces; one when traction forces are applied on the swimmer (swimmer is tangent to the viscous fluid layer) and one when swimmer is right above the viscous fluid layer (where fluid forces are dominant).

6.2.2 Results

In experiments, when helical swimmer rotates with 1 Hz, it is moving next to the channel wall, thus in simulations swimmer is tangent to the viscous layer to model the exact situation; distance between channel wall and swimmer, w_d , equals 20 μ m. Flow field and pressure distribution around the head of the swimmer for this case is presented in Figure 6.12. Swimmer is rotating in clock-wise direction to move forward along negative **x**-direction and the resultant flow field is in counter-clockwise direction. Since the swimmer is in touch with the viscous fluid layer, fluid cannot pass from where positive pressure occurs to where negative pressure exists. In this case, it is observed that traction forces are dominant compared to the fluid forces, thus swimmer rolls on the boundary like a wheel.

Experiments performed at higher frequencies, i.e. 5 Hz, shows that helical swimmer is not under the effect of traction forces since it moves along opposite corner of the previous case (Figure 6.3). Thus, simulations are performed with a distance between swimmer and channel walls, w_{dy} and w_{dz} , which is equal to, 30, 40, 70, 109, 214 and 424 μ m in **y**-direction (w_{dy}) and 30, 40, 70, 114 and 274 μ m in **z**-direction (w_{dz}). Simulation results show that pressure distribution within the channel is similar to the previous case; however, the pressure values are lower and decreasing with the increase in w_{dy} and w_{dz} (Figure 6.13).

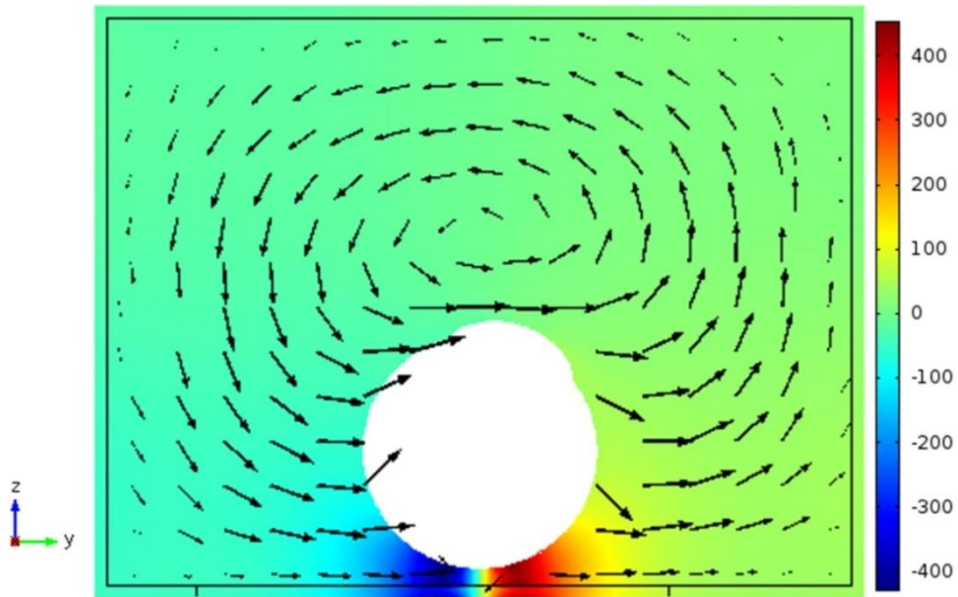


Figure 6.12 Flow and pressure field around the head of the helical swimmer inside rectangular channel while helical swimmer is rotating with 1 Hz and is in contact with viscous boundary layer. Color bar shows the pressure distribution in Pa in the cross-sectional plane.

Resultant clock-wise flow field represents that the fluid inside the rectangular channel is affected by the rotation of the swimmer (Figure 6.13). It can be concluded that when swimmer lies on the bottom of the channel (negative z -side), if the lifting force acting on the swimmer due to its high rotation frequency is enough to push it away from the channel boundary to the positive z -axis, resultant flow field is effective on the position change of helical swimmer in the rectangular channel (towards the negative y -corner of the channel). According to the magnitude of the lifting force, which increases with the frequency, swimmer can move against the gravity force and follow an elliptic trajectory with the effect of the resultant flow field. This behavior is observed in experiments when helical swimmer is rotating at a specific frequency which depends on the surface roughness and moving direction.

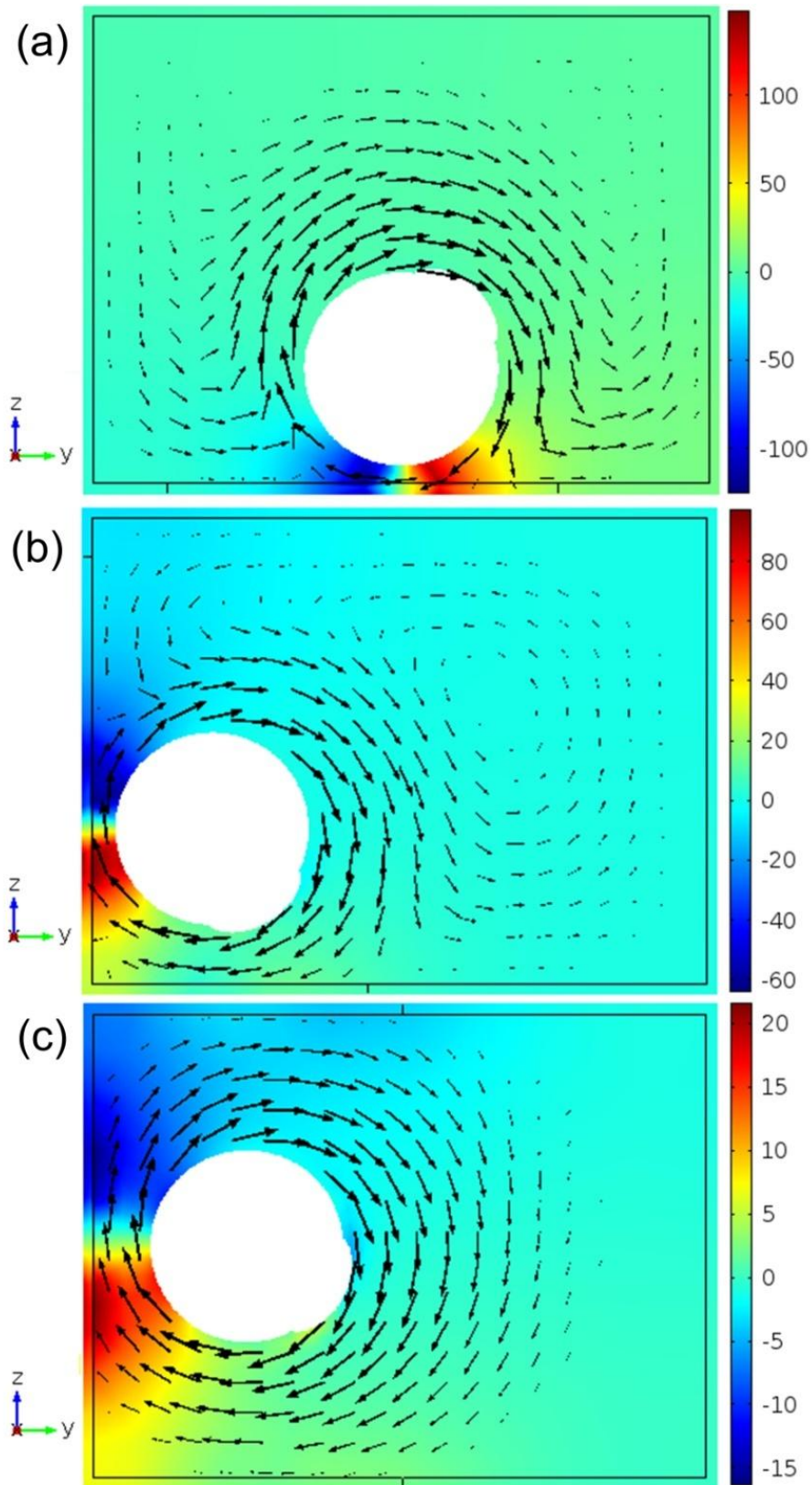


Figure 6.13 Flow and pressure fields around the head of the helical swimmer inside rectangular channel while helical swimmer is away from the channel boundaries with a distance of (a) $w_{dy} = 424 \mu\text{m}$, $w_{dz} = 30 \mu\text{m}$, (b) $w_{dy} = 40 \mu\text{m}$, $w_{dz} = 114 \mu\text{m}$, (c) $w_{dy} = 109 \mu\text{m}$, $w_{dz} = 274 \mu\text{m}$ to simulate the rotation at higher frequency values. Color bar shows the pressure distribution in Pa in the cross-sectional plane.

In CFD simulations, lateral and vertical positions of swimmer are varied and effects of the position of the swimmer in rectangular channel on the lateral, vertical and forward speed are studied. Position of the swimmer is adjusted so that the swimmer is tangent to the viscous fluid layer next to channel boundary which represents the channel wall. A mesh structure with the 42 position points are formed in the quarter of the channel, however, according to simulation results, there is symmetry about y -axis and z -axis.

The forward velocity of the micro swimmer is investigated in Figure 6.14 for one quarter of the channel. At the middle of the channel, the velocity distribution is even and calculated around 0.085 mm/s. When the distance between channel wall and the swimmer decreases, forward velocity increases up to a point where distance is equal to 0.02 mm and viscous fluid layer starts. There is an optimum point at the corners of the channel (navy regions in Figure 6.14), where forward velocity reaches its maximum value which is calculated approximately as 0.145 mm/s and this is the maximum velocity that the swimmer can reach at 1 Hz according to simulation results. The minimum forward velocities occur at the channel boundary where swimmer is tangent to the channel wall. At the corner of the channel, where swimmer touches both surfaces parallel to y - and z -axes, forward velocity is larger than the velocity calculated at a position where swimmer is tangent to only one surface and calculated approximately as 0.06 mm/s, which is close to the forward velocity measured in experiments for 1 Hz.

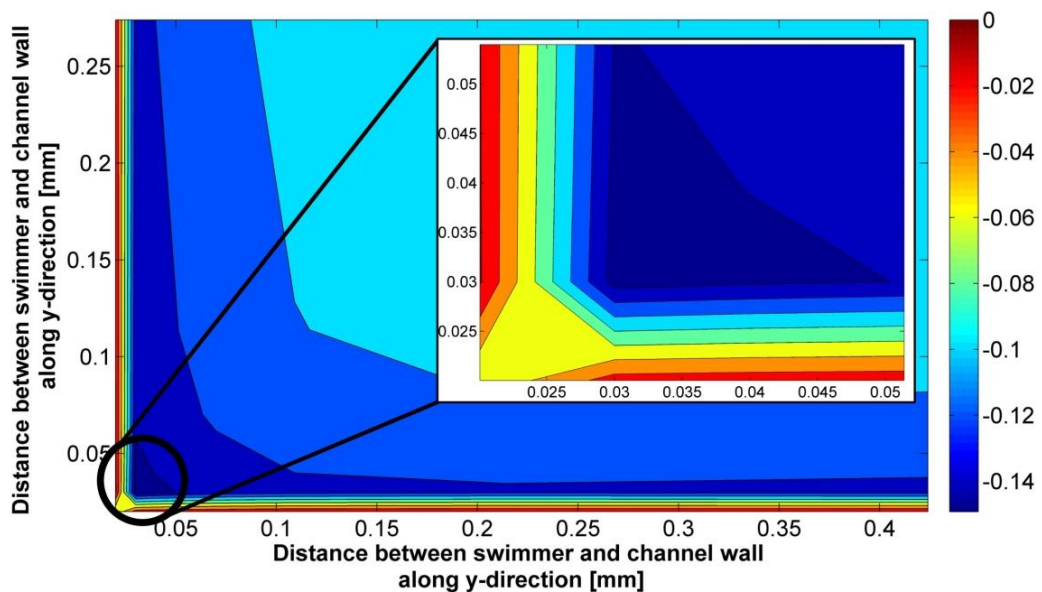


Figure 6.14 Linear (forward) velocities of micro swimmer with respect to its position inside rectangular channel. Only one quarter of the channel is presented and color bar shows the velocity values in mm/s..

Lateral (y -direction) and vertical (z -direction) velocities are presented in Figure 6.15 and Figure 6.16, respectively. At different positions in the channel without being tangent to any wall, y -direction velocity of the helical swimmer has a value smaller than zero, however, as the swimmer touches the viscous fluid layer in z -direction, i.e. w_{dz} is equal to 0.02 mm, a sudden increase is observed due to the traction forces. Maximum y -direction velocity is calculated as 1.58 mm/s and it is a sufficient approximate to the linear velocity of the swimmer in y -direction, which is calculated as $2\pi A f = 1.63$ mm/s, where B_0 is the helical wave amplitude and f is the rotation frequency. The positive y -direction velocity which occurs when w_{dz} is equal to 0.02 mm, indicates that as the swimmer rotates clock-wise according to its propulsion direction, it moves to positive y -direction with the traction force on charge, such as a rolling wheel. When swimmer is tangent to the vertical wall of rectangular channel, the lateral velocity has a positive value close to zero, which indicates that swimmer tends to move away from the wall in positive y -direction. As the swimmer reaches to the bottom of the channel and becomes tangent to both surfaces, i.e. w_{dy} and w_{dz} are both equal to 0.02 mm, lateral velocity increases to 0.5 mm/s.

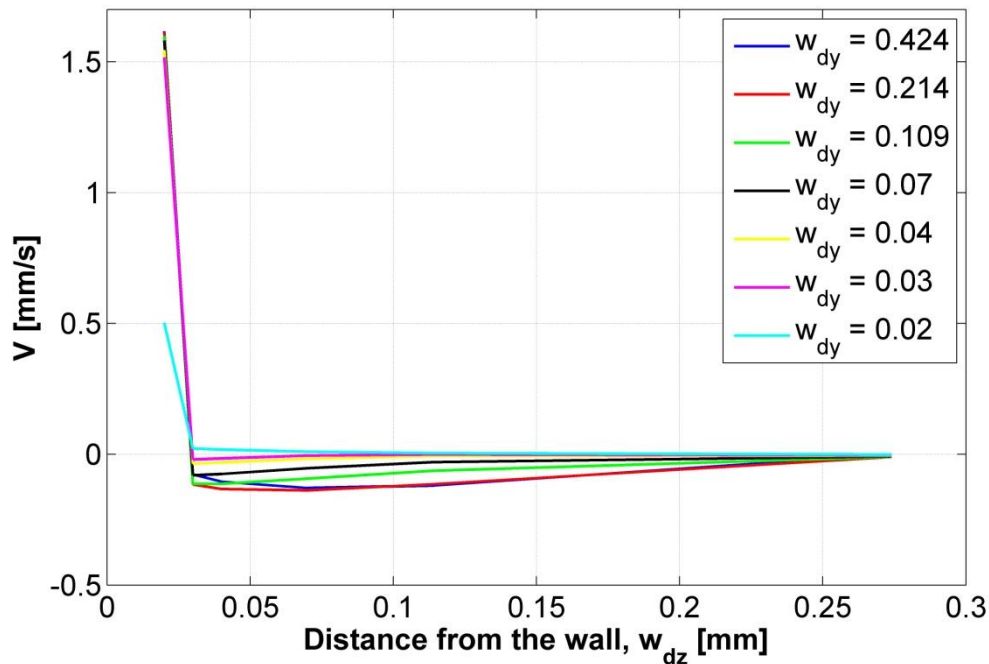


Figure 6.15 Dependence of lateral velocities of micro swimmer on the position inside the channel.

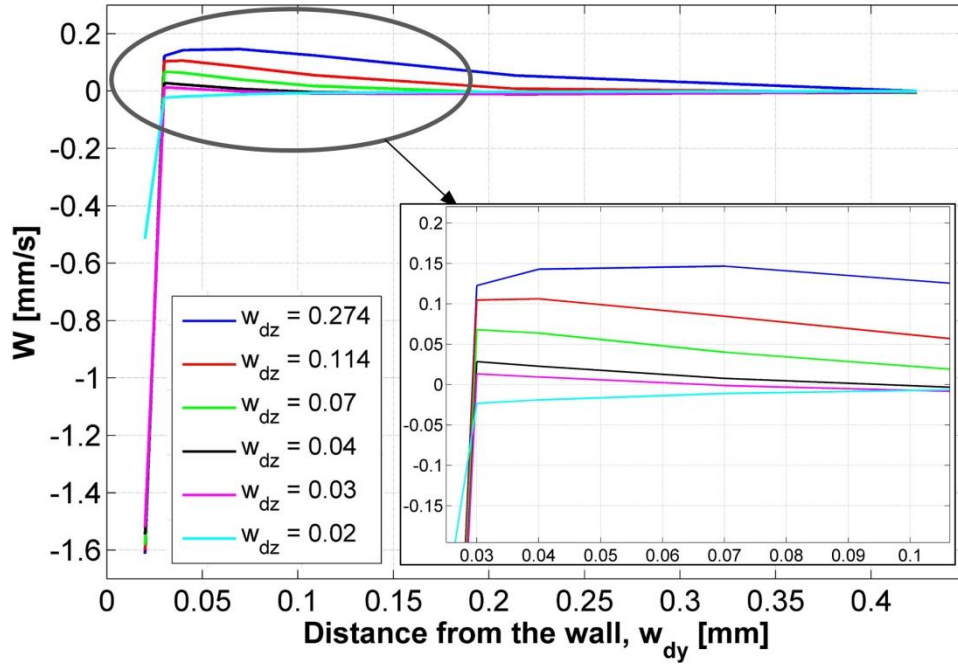


Figure 6.16 Dependence of vertical velocities of micro swimmer on the position inside the channel.

Vertical (z -direction) velocities are positive for w_{dz} is greater than 0.07 mm and w_{dy} is greater than 0.02 mm. Negative z -direction velocity is obtained when the distance between channel wall and swimmer is minimum (0.02 mm) for all w_{dy} values. The minimum z -direction velocity value is 1.6 mm/s which is close to the linear velocity of the swimmer when it is in contact with the viscous fluid layer, $2\pi Af = 1.63$ mm/s. Negative value of the z -direction velocity which occurs when the swimmer is in contact with the viscous fluid layer, indicates that the helical swimmer rolls to negative- z -direction with the effect of traction forces. When the distance between vertical channel wall and helical swimmer, w_{dy} , decreases, an increase in vertical velocity is observed until w_{dz} is equal to 0.02 mm. When swimmer is tangent to the lateral (bottom) wall of rectangular channel, the vertical velocity has a negative value close to zero, which indicates that swimmer tends to move towards the wall in negative z -direction. As the swimmer reaches to the side (vertical wall) of the channel and becomes tangent to both surfaces, i.e. w_{dy} and w_{dz} are both equal to 0.02 mm, vertical velocity increases to -0.5 mm/s.

In experiments performed on glass surface, it is observed that, swimmer changes its position when rotating at 3 Hz and the stability of swimming motion is corrupted at 7 Hz for both backward and forward motions, which are called critical frequencies. In

order to clarify the critical frequency values, additional simulations are performed where helical swimmer is tilted with an angle of 5° about y -axis, since it is noted by Shum *et al.* [69] that the optimum orientation of swimmers with rotating tails depends on the swimmers geometry, particularly the aspect ratio; i.e. swimmers with spherical heads have a strong tendency to move towards the wall while swimming near a plane boundary whereas the swimmers with elongated head has a positive stable tilt angle when boundary accumulation is present. Although the swimmer studied in this study is different from bacteria in terms of being a one-link swimmer instead of having counter rotating head and tail, still both conditions are present for the helical swimmer; the swimmer has a cylindrical (elongated) head and boundary accumulation because of gravity forces is seen. Thus, an extra simulation is performed where the swimmer is tilted by 5° and forces are calculated and presented in Figure 6.17.

The mass of the helical magnetic swimmer is calculated as 0.58×10^{-6} gr and the gravity force acting on the swimmer is calculated with (6.21) where g is the gravitational constant.

$$F_g = mass \times g = 0.58 \times 10^{-6} \times 9.81 = 5.68 \times 10^{-6} N \quad (6.20)$$

When the gravitational force is greater than the lifting force, which occurs as a result of rotation of the swimmer, helical swimmer moves on the channel surface, thus traction force is the dominant lateral force acting on the swimmer. Calculated lift force from the CFD simulations for helical swimmer is 0.13×10^{-6} N for a frequency value equals 1 Hz. The change in lift force acting on the helical swimmer with respect to the frequency is presented in Figure 6.17. At a certain frequency between 6 Hz and 7 Hz both forces come to a balance, as a result, it is expected that the swimmer moves away from the channel wall in positive z -direction as the frequency further increases. Within the channel, the resultant rotating flow field which occurs as a result of the rotation of the swimmer is rotating in the same direction as the swimmer. When fluid forces are dominant over traction force on the helical swimmer, it starts to move with the fluid until the swimmer reaches the channel corner; this behavior is observed at 3 Hz in experiments. In addition to this behavior, when frequency increases to a certain value, swimmers begin to stroll around the channel along the channel boundaries, only if the vertical lift force is sufficient enough. The lift force is calculated for the swimmer at the

corner as 1.18×10^{-6} N for 3 Hz and it is not enough to move the swimmer in positive z -direction against gravitational force. For 7 Hz, at which the unstable motion of helical swimmer is observed in experiments, lift force calculated from the simulations is greater than the weight of the swimmer, hence for the frequency values greater than 7 Hz, it is expected that the motion of helical swimmer is not smooth and under the effect of fluid flow inside the rectangular channel.

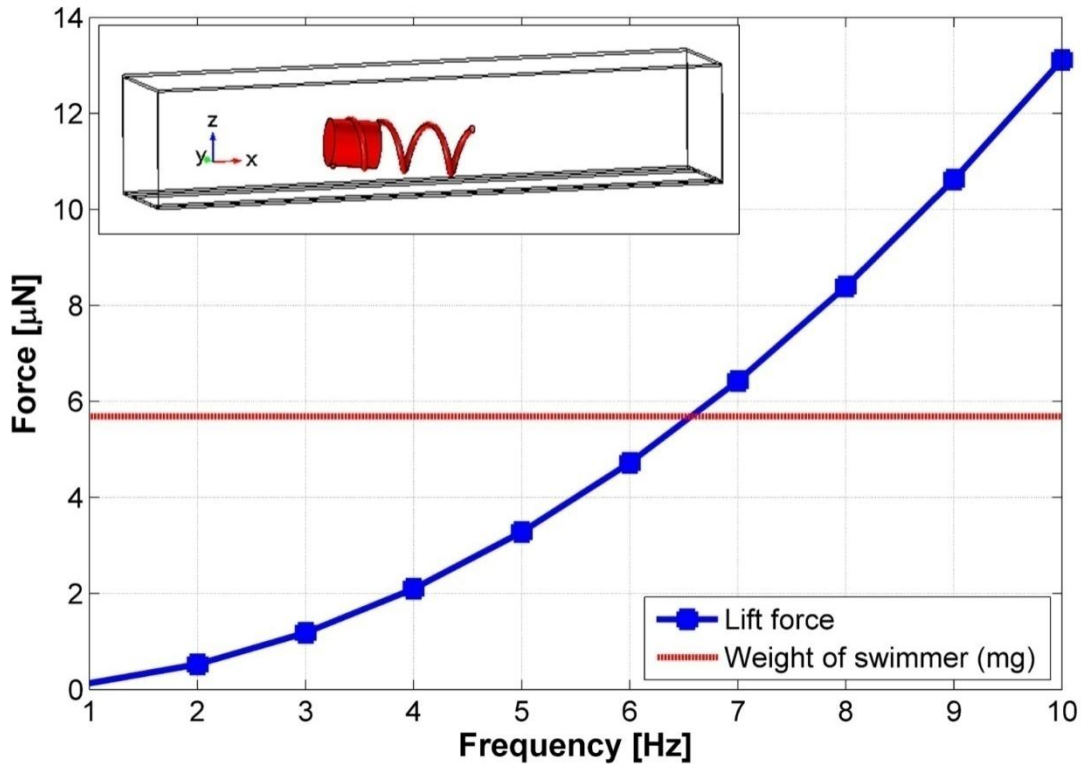


Figure 6.17 Dependence of lifting force acting in z -direction on rotation frequency for the case swimmer is rotated about y -axis by 5° which is shown in the inset.

Angular velocities for different positions of the helical swimmer in y - and z -directions are presented in Figure 6.18 and Figure 6.19, respectively. Rotation of the swimmer about the y - and z -axis corresponds to the pitch (angle of attack) and yaw (heading angle) angles. In CFD simulations, helical swimmer is aligned parallel to x -axis, i.e. yaw and pitch angles are set to zero, and angular velocities are calculated based on the torque-free swimming condition.

When swimmer is not tangent to the channel wall, resultant positive angular velocities in y -direction indicates that swimmer is forced to move its head upwards. When the distance between channel wall and helical swimmer in y -direction equals 0.02 mm, i.e. swimmer is tangent to the viscous fluid layer, the angular velocity in y -

direction increases whereas for w_{dy} greater than 0.02 mm it is decreasing. At the corner of the channel, when both w_{dy} and w_{dz} are equal to 0.02 mm, y -direction angular velocity is nearly zero; however a slight positive angular velocity in z -direction indicates that swimmer tends to move closer to the wall. Positive y -direction angular velocities shows that swimmer tends to pitch up from the wall when it is not tangent to the wall, nevertheless when swimmer is in contact with the viscous fluid layer in z -direction, i.e. $w_{dz} = 0.02$ mm, negative angular velocities in y -direction indicates that helical swimmer tends to pitch down to the bottom wall of the channel.

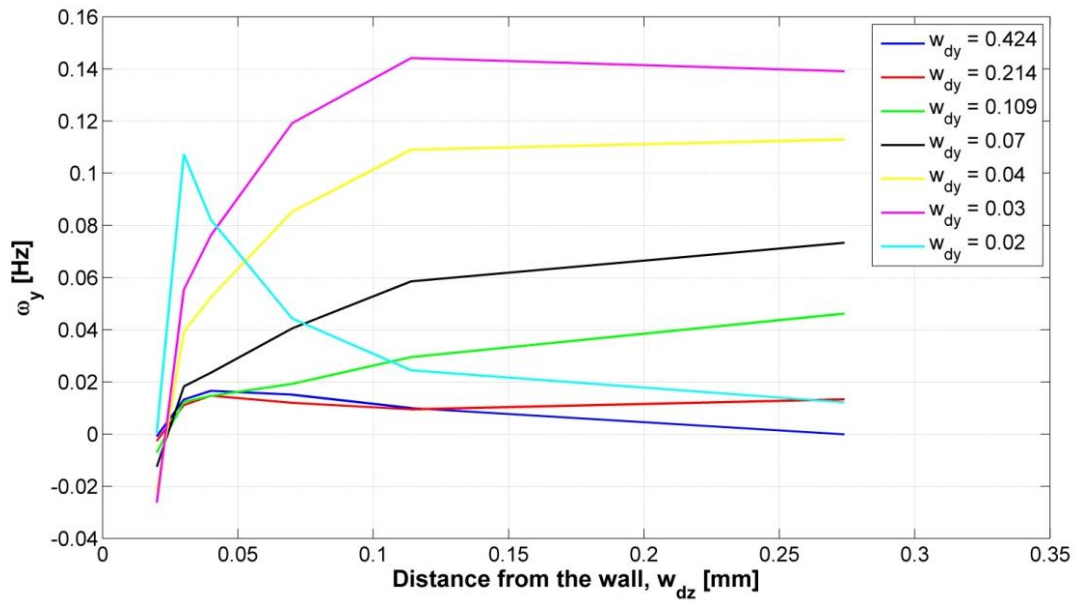


Figure 6.18 Dependence of angular velocities about y -axis on helical swimmer's position inside rectangular channel.

Angular velocities in z -direction show differences in terms of sign for different positions of the helical swimmer. When swimmer is away from the channel walls, i.e. w_{dy} is greater than 0.07, the angular velocities stays positive with respect to w_{dz} , which indicates that the helical swimmer is forced to turn left (head to port). On the other hand, when w_{dy} is between 0.07 and 0.02, angular velocities in z -direction switches sign from negative to positive as swimmer approaches to the bottom wall in z -direction. An exception occurs for w_{dy} is equal to 0.02, which is the case that the helical swimmer is tangent to the viscous fluid layer in y -direction. Angular velocities are negative for this case, until the swimmer reaches to the corner and is tangent to both walls in y - and z -directions, which indicates that swimmer tends to move toward the channel wall.

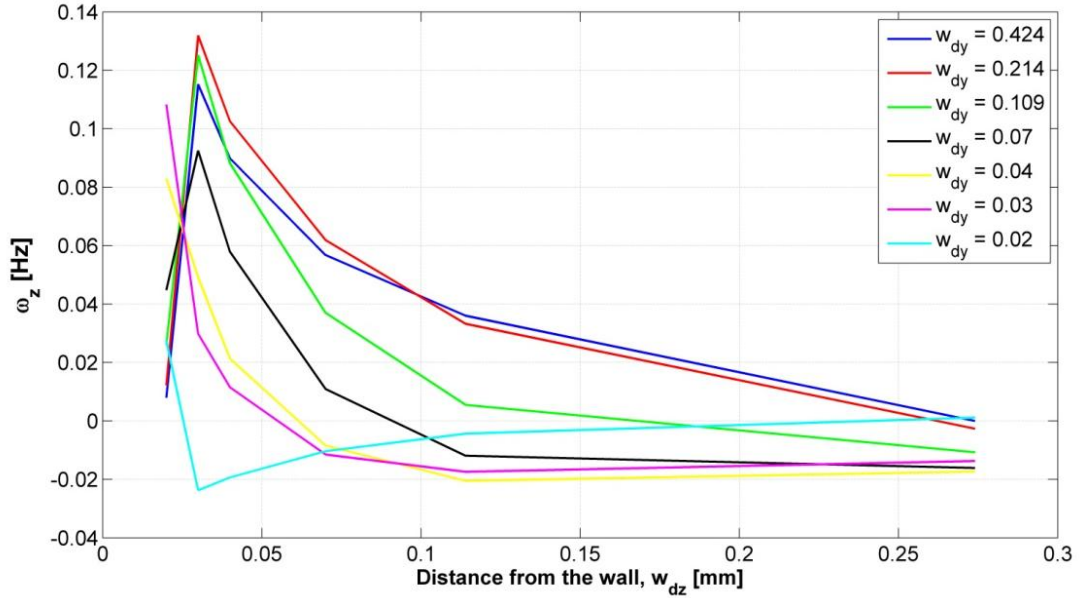


Figure 6.19 Dependence of angular velocities about \mathbf{z} -axis on helical swimmer's position inside rectangular channel.

6.3 Discussion

Experiments with two micro swimming robots, that have scales 0.4 mm in head diameter and 1.5 and 1.9 mm in length, are presented. The micro swimmers used in experiments are made of permanent $\text{Nd}_2\text{Fe}_{14}\text{B}$ magnet heads and helical metal wire tails. Micro robots are actuated by external rotating magnetic fields and the swimming behaviors are observed in glycerol-filled rectangular channels.

In experiments with rectangular channels, helical swimmers exhibited two different swimming modes, which depend on the rotation frequency: forward motion due to the fluidic propulsion force and lateral motion due to the traction force near the solid wall. Swimmers tend to travel near solid walls due to their weight; a lift force from the wall balances the swimmer and avoids stiction to the wall and results in a very small clearance. Due to rotation, a net traction force emerges and acts as a lateral force on the robot and causes its sideways motion.

Rotation frequency is an important parameter on swimming modes. At low frequencies, e.g. 1 Hz, as a result of the traction force, swimmer first moves to one side of the channel according to the rotation direction and then continues forward motion at the sideways near the channel wall. As the frequency increases, e.g. to 5 Hz, swimmer changes its lateral position inside the channel and begins to move towards the opposite

side of the channel along with a fast forward motion due to the fluid force caused by the flow which is affected by rotation. The critical frequencies at which the robot changes its behavior are obtained from experiments for smooth surfaces for swimmer no.1 as -7 Hz and 5 Hz for backward and forward motion, respectively.

Experiments with swimmer no.2 are performed on glass surface in order to eliminate possible effects of rough surface on the motion of the swimmer. Three different frequencies (1 Hz, 2 Hz and 3 Hz) and three different starting positions (left, middle and right) are chosen for experiments to clarify the critical frequency and the optimal places in the channel and the effect of initial position of the robot on its swimming motion. When frequency is equal to 2 Hz, a fluidic bump is observed between the corners and the mid-point of the channel, which prevents to move both directions and results with two optimal positions of the helical swimmer in the channel.

Simulation results are presented for swimming micro robot no.1 traveling in rectangular channels. Simulations are performed for 42 different places of the robot in the channel. In order to eliminate numerical difficulties for robots almost touching the wall, a highly viscous fluid layer, whose viscosity is 50000 more than the viscosity of fluid inside the channel, with a thickness of 0.02 mm is introduced at the boundaries of the rectangular channel. According to simulation results, when the distance between the channel wall and the swimmer decreases, the forward velocity increases up to a point where distance is equal to 0.02 mm and viscous fluid layer starts. There is an optimum point at the corners of the channel, where forward velocity reaches its maximum value which is calculated approximately as 0.11 mm/s.

7 SENSING AND APPLICATION OF ARTIFICIAL SWIMMERS IN CHANNELS

In this chapter, navigation of helical swimmers inside rectangular channels is demonstrated by using the direction and the frequency of the rotating magnetic field as controls. The swimmer is navigated through Y-shaped and T-shaped channels with the help of a radially-magnetized permanent-magnet head and by changing the rotation axis of the externally applied magnetic field. In addition, high and low frequency swimming modes explained in previous chapter are used to avoid obstacles inside channels.

To control the position of the swimmer perpendicular to the direction of the forward motion inside rectangular channels bias currents are applied to pairs of electromagnetic coils in addition to the sinusoidal current that provides the rotation of the magnetic field. Experiments are performed by taking the advantage of different swimming modes of the swimmer in rectangular channels at different rotational frequencies.

Experiments using Hall-effect sensors are performed to detect the position of helical magnetic swimmer in cylindrical channels by measuring the strength of the magnetic field of the permanent magnet head. Two magnetic Hall-effect sensors are placed next to each other and measurements are taken for a time interval while magnetic helical swimmer is moving inside a glycerol-filled cylindrical channel placed on to the sensors.

7.1 Moving In Channel Networks

7.1.1 Methodology

A simple procedure is used to make right-handed helices from a thin copper wire (here, with a diameter of 0.06mm) by winding it on another thick wire (here, with a diameter of 0.48 mm) (Figure 6.1a). Desired wavelength or the number of waves on a

fixed length is adjusted by stretching the helices to deform plastically. Radially magnetized cylindrical magnets with 0.4 mm diameter and 0.5 mm length are placed inside the helices, and secured with a strong adhesive. The helical swimmer used in the experiments has 2 full waves on its tail and is 1.5 mm long in total. Tail length is 1 mm and wavelength is calculated as 0.5 mm (Figure 6.1). Since permanent magnets are magnetized in the radial direction, the magnetization vector is perpendicular to the long axis of the swimmer, and it is rotating with the rotating external magnetic field.

The magnetic helical swimmer is placed inside different channel structures in sequence. Three different channel patterns were made of acrylic glass (plexiglass) by micro machining. The Y-shaped channel (Figure 7.1a) and T-shaped channel (Figure 7.1b) have rectangular cross section with a cross sectional dimensions of 1.3 mm in width and 1 mm in height. Channels were then filled with glycerol, whose viscosity and density are 1.412 Pa's and 1261 kg/m³, respectively, at room temperature. Experimental setup used for navigation experiments is explained in Chapter 6 and the setup and its components can be seen in Figure 7.2.

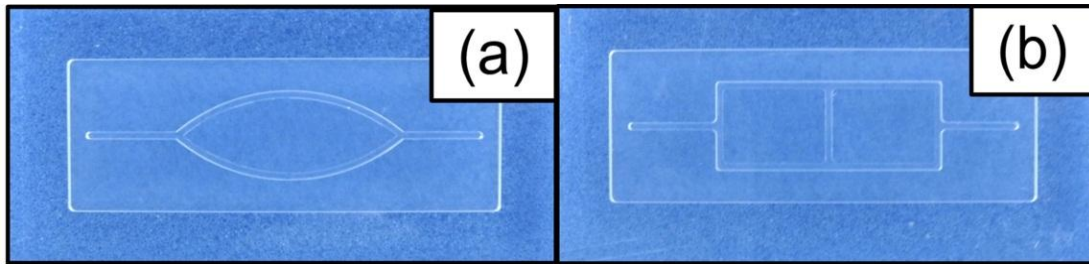


Figure 7.1 Channel structures with (a) Y-shaped connections and (b) T-shaped connections.

Helical swimmers can be propelled back and forth by using two orthogonal electromagnetic coil pairs. Third coil pair is used to control the direction of magnetic field vector and the direction of the motion of the swimmer. The frequency ($f_{x,1} = f_{x,2}; f_{y,1} = f_{y,2}; f_{z,1} = f_{z,2}$; where subscripts x , y , and z denotes the axes and 1 and 2 denotes the coil number of a pair) and magnitude of the applied current ($I_{x,1} = I_{x,2}; I_{y,1} = I_{y,2}; I_{z,1} = I_{z,2}$) to the coils are the same for mutual (bilaterally placed) coils, whereas, the current applied to the orthogonally placed coils have the same frequency ($f_x = f_y = f_z$) but different current magnitudes ($I_x \neq I_y \neq I_z$) to provide the same magnetic field strength ($B_x = B_y = B_z$) (Figure 7.3). A phase shift exists on the supplied current between the coil pairs placed along the z -axis and the coil pairs placed along the x - and y -axes to ensure the magnetic field to rotate (see Figure 7.2 and Figure 7.3). Helical swimmers rotate in sync with the

magnetic field by means of the magnetic torque on permanent magnet heads, and moves forward due to the propulsion force.

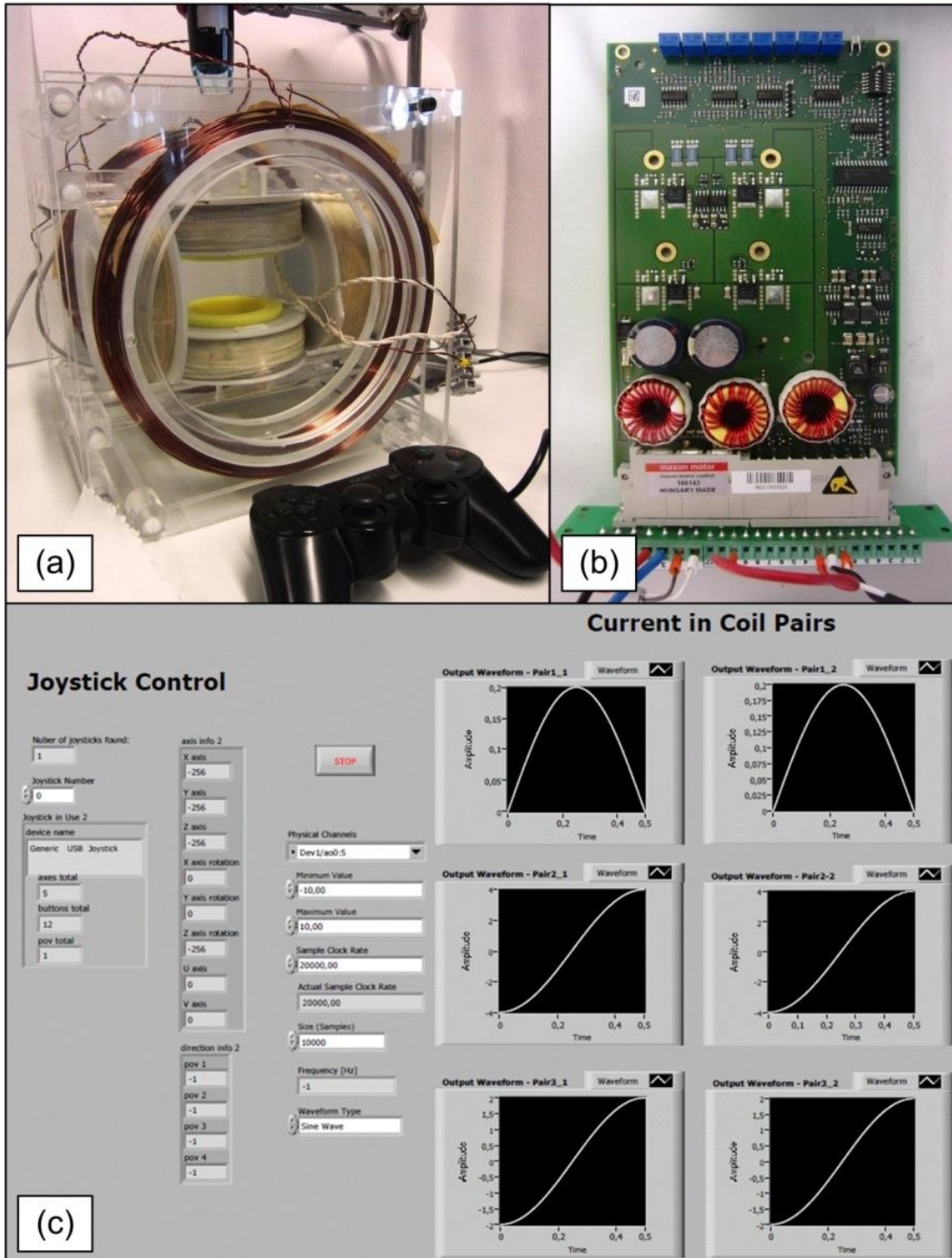


Figure 7.2 Experimental setup consists of (a) orthogonally placed three electromagnetic coil pairs (b) which are driven by Maxon Motor Drives connected to a NI-DAQ and controlled by a joystick (c) using Labview.

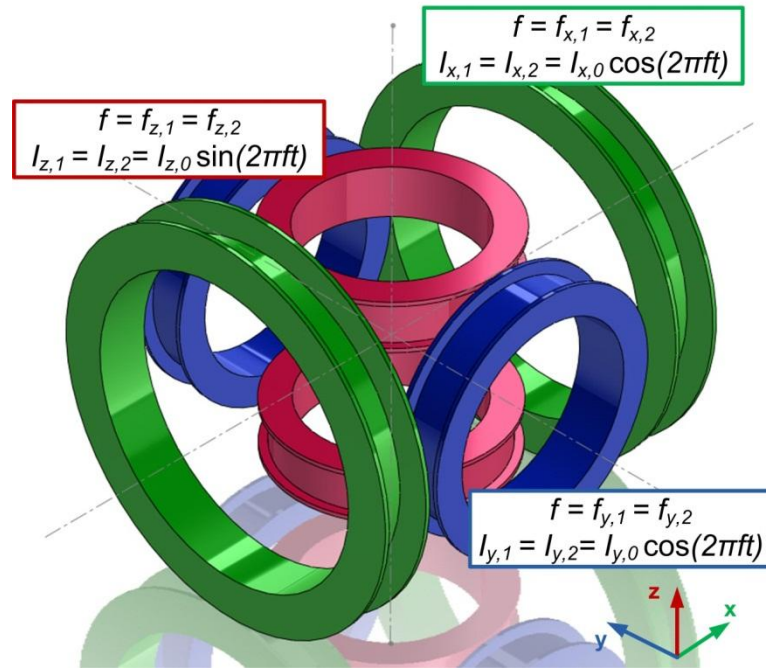


Figure 7.3 Orthogonally placed three electromagnetic coil pairs are driven with same frequency but with different currents. Coils placed in **x**- and **y**- direction are in phase whereas **z**-direction coil pair has a 90° phase shift.

Inside rectangular channels, the swimming modes of helical swimmers are explained in Chapter 6. Swimmers tend to travel near solid walls due to forces such as weight; a lift force from the wall balances the swimmer and avoids stiction to the wall and results in a very small clearance during the forward motion. The hydrodynamic lift force is observed only at high rotation rates of the swimmer. At low rotation rates, the lift force is not high enough to overcome the weight; therefore, a net traction force emerges, acts as a lateral force on the robot due to its rotation, and causes its roll, which is a sideways motion (Figure 7.4).

Three controls are applied to the open-loop system. First, on-off control is applied to start and stop the rotational motion of the helical swimmer. Swimmer can rotate with the applied frequency with sufficient magnetic field strength to overcome the rotational drag, and can be stopped at the desired location. Second control is the frequency of the rotating magnetic field, which is used to adjust the forward speed of the robot at high frequencies. Lastly, the third control is the direction of the magnetic field vector, which is used to control the direction of the motion.

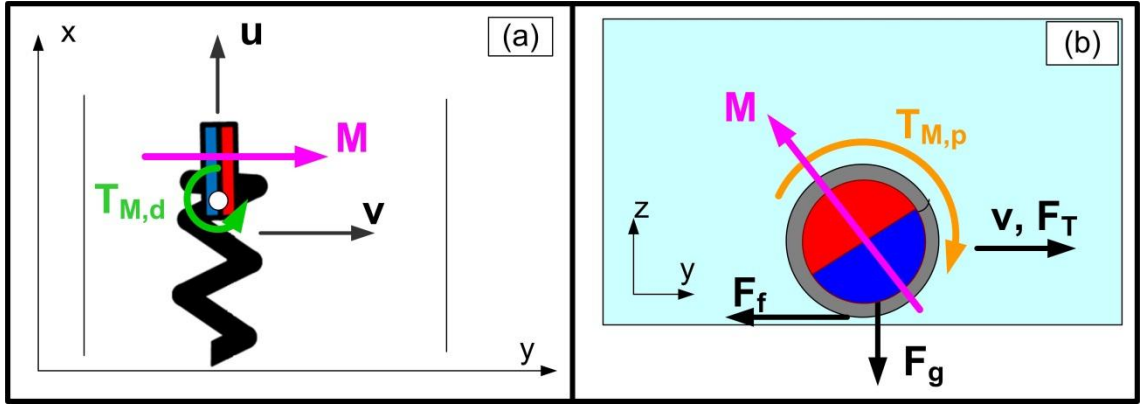


Figure 7.4 (a) Helical swimmer moves in positive x -direction with the applied positive rotational magnetic field along x -axis if the frequency is high. For low rotational frequencies lateral motion occurs also in positive y -axis. The torque applied for direction is represented with $T_{M,d}$, u is the velocity along x -axis and v is the velocity along y -axis. (b) Traction force, F_T , due to the applied magnetic torque, $T_{M,p}$, at low frequencies provides a velocity in lateral direction. F_f and F_g are friction and gravity forces, respectively

7.1.2 Results

7.1.2.1 Navigation in Y-shaped channels

Changing the direction of the helical swimmer is realized by changing the magnetic field vector in xy -plane (Figure 7.5a and Figure 7.5b) applied by the electromagnetic coil pairs. As explained in detail in [20], for an axially magnetized cylindrical magnetic particle, the magnetization vector is perpendicular to the long axis and follows the external magnetic field vector. The angle between two arms of Y-shaped channel is measured as 70° at the beginning of the junction. The resultant magnetic field vector in xy -plane should be rotated 35° either in positive or negative direction; depending on the desired direction that the robot is steered (Figure 7.5a). In order to move the swimmer backwards, direction of the rotational frequency is altered.

7.1.2.2 Navigation in T-shaped channels

Similar to the previous case, direction of the magnetic field vector is altered on the xy -plane to satisfy a resultant vector, which is perpendicular to the desired direction of motion. In order to alter the direction of the rotating magnetic field by 90° , the

current in the coil pairs which are situated along y -axis is set to zero instead of I_y , and current in the coil pairs situated along x -axis is set to I_x instead of zero. In channels with flat surfaces it is possible to change head and tail's position using the T-junction (Figure 7.5b).

7.1.2.3 Obstacle avoidance

The two swimming modes of helical swimmer are also used for avoiding an obstacle inside a rectangular channel. When the swimmer moves forward, it travels along the left hand side of the channel if the rotation frequency is high, and it proceeds to the right hand side as a result of the traction force as soon as the rotation frequency is lowered. The rolling motion is used to change the lateral position inside the channel as an alternative to manipulation of the magnetic field for navigation around obstacles. In Figure 7.6a, schematic representation of this scenario is presented, with the snapshots taken from the experiments for a similar situation (Figure 7.6).

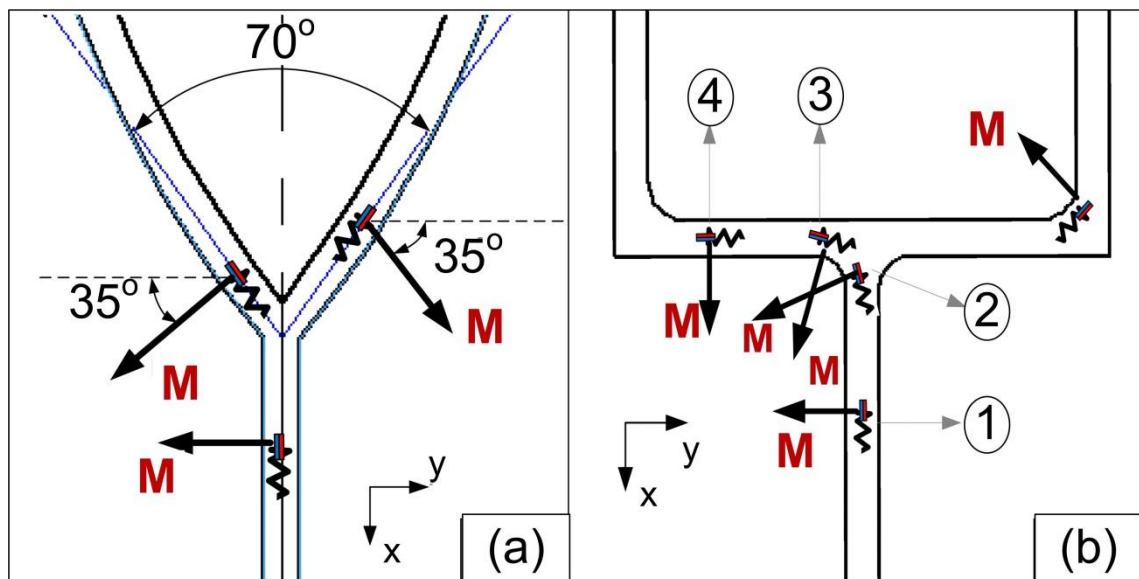


Figure 7.5 Motion of the helical swimmer inside (a) Y-shaped and (b) T-shaped rectangular channels. Magnetization of the permanent magnet on the helical swimmer is always perpendicular to the helix axis; net torque on the swimmer is due to the cross-product of the externally applied magnetic field with the magnetization of the head.

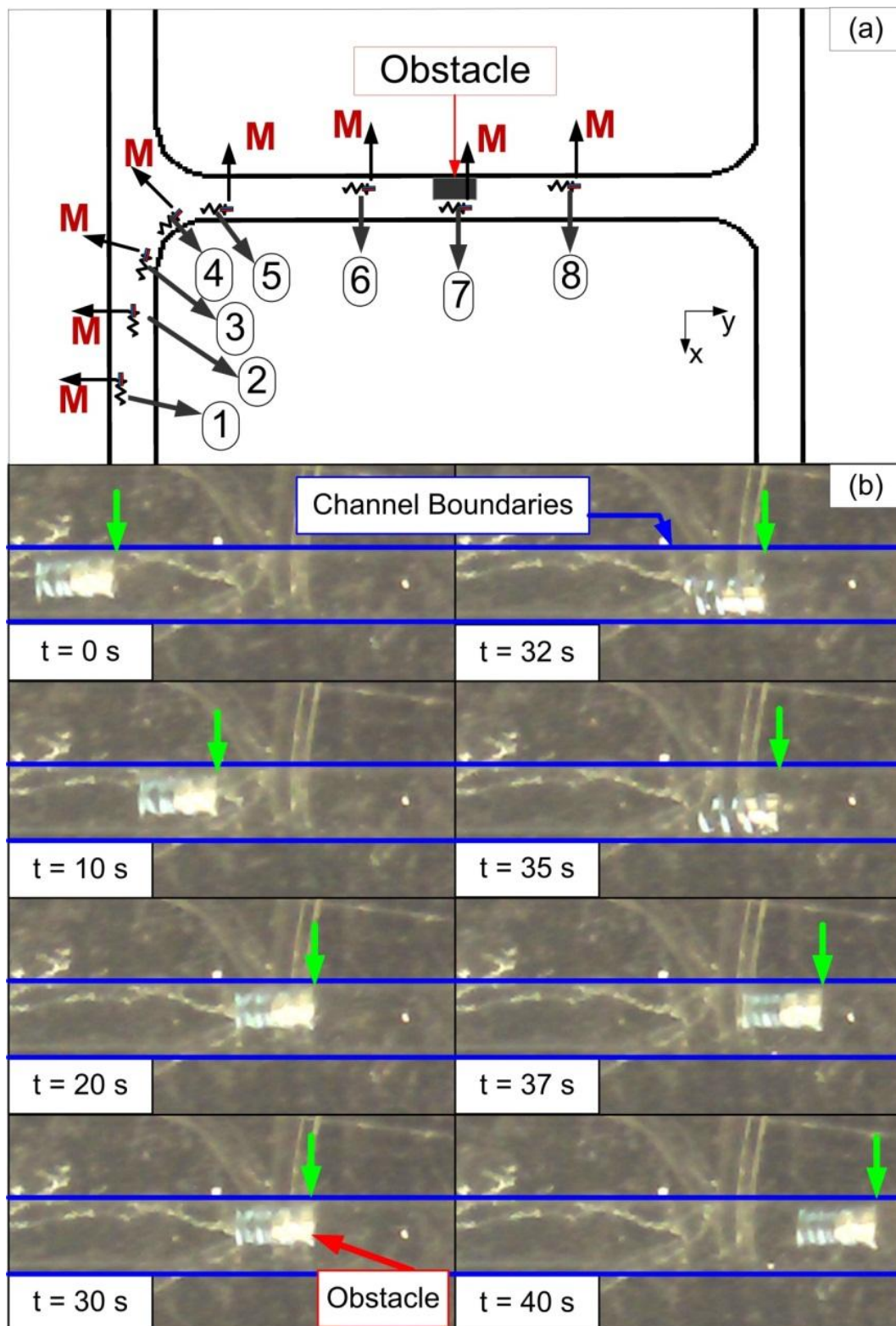


Figure 7.6 (a) Schematic representation of motion of helical swimmer inside rectangular channel when it comes across an obstacle. (b) Snapshots of forward motion of the helical swimmer placed inside rectangular channel. Green arrows show the position of the helical swimmer. Rotation frequency is 5 Hz. When $t = 20$ s swimmer does not move forward although it continues it is rotating at the same frequency. After $t = 30$ s, the frequency is dropped to 1 Hz and swimmer started to move in lateral direction, thus it avoided the obstacle.

7.2 Magnetic Navigation

A new methodology is developed to control the lateral position of the magnetic helical swimmers inside rectangular channels. The same experimental setup, which consists of orthogonally placed electromagnetic coils, Maxon ADS_E 50/5 4-Q-DC servo-mechanism amplifiers and NI PCI-6733 high speed analog output device, is used for the experiments. The magnetic helical swimmer manufacturing process is explained and dimensions are given in Chapter 6.1.1, which is named as swimmer no.2.

In order to obtain forward motion, rotating magnetic fields are applied and magnetic swimmer rotates in sync with the external rotating magnetic field. However, the lateral position of the swimmer depends on the magnitude of applied rotational frequency, due to which, swimmer moves under the effect of either traction forces, when the swimmer is very close to the wall or fluid forces sufficiently away from the wall. To change the lateral position, magnetic swimmer is pulled with a DC field, strength of which should be more than the traction force at low frequencies and fluid force at high frequencies. DC field is applied with a square wave, strength and duty cycle of which are the important parameters.

First part of the experiments is to understand the effect of the duty cycle on which the DC field is applied. Experiments are performed on glass surface when rotation frequency is equal to 1, 2 and 3 Hz, with two different initial positions, right (positive y-axis) and left (negative y-axis) of the channel. The maximum duty cycle that current can be set to zero without interrupting the rotation motion is determined as around 20%. In order to be on the safe side, second part of the experimental studies is performed by setting the duty cycle to 15%.

Additional DC current is applied only to the y-axis electromagnetic coil pair in a square wave form which has the same frequency and duty cycle with the sinusoidal current. Magnitude of the DC current is another important parameter besides duty cycle and it is equal to a constant times the magnitude of the sinusoidal current, i.e. $I_{0,DC} = c \cdot I_0$. Experiments are performed when c is equal to 1.5, 2, 2.5, 3.75, and 5 (Figure 7.7).

When the frequency is equal to 1 Hz and the duty cycle is equal to 15%, applied DC current is not sufficient to generate a pulling force that can overcome the traction force, which is calculated as 31.3×10^{-6} N from CFD simulations. Similar behavior is observed for the frequency is 3 Hz; generated magnetic force is not sufficient to

overcome fluidic forces. For these two cases, initial position does not have an effect on the results.

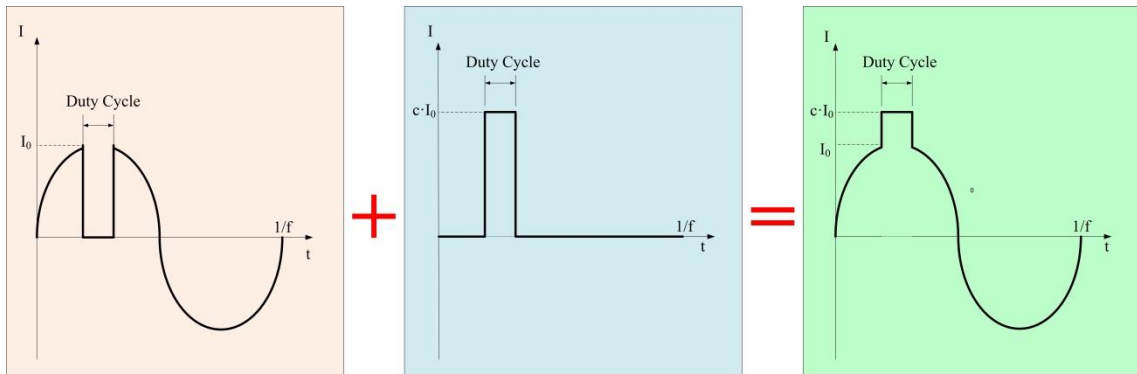


Figure 7.7 Applied current to the y-axis electromagnetic coil pair to change the lateral position of the swimmer. Magnitude of the sinusoidal current is multiplied with a constant “c” to determine the magnitude of DC current.

When rotation frequency is equal to 2 Hz, the initial lateral position of the micro swimmer is maintained applying a magnetic force against the traction force and changed by applying a reverse magnetic force. Figure 7.8 represents some scenarios and the minimum magnetic field force to be applied to obtain these results. In the first case, swimmer is in the positive y -side of the channel initially and it starts to rotate with the applied magnetic field to move in the positive x -direction. If the applied field is without an addition of square wave, swimmer would move to the negative y -direction with the affecting traction force as explained in previous chapter. The square wave having a magnitude of 1.5 times sinusoidal wave generates a force which is enough to keep the swimmer at the positive y -side of the rectangular channel. In the second case, swimmer starts its motion in positive y -side of the rectangular channel moving to the negative x -direction. Lateral position of the swimmer is changed when the magnitude of the DC current is five times larger than the magnitude of sinusoidal current; for smaller valued of DC current it is not possible to change swimmer's lateral position. For the third case, swimmer is positioned at the negative y -side of the rectangular channel initially, and travels to the positive x -direction. If there is no DC current provided to the electromagnetic coils, swimmer would continue its motion at negative y -side of the channel. However, a DC current twice as large as the sinusoidal current makes the swimmer change its lateral position within the rectangular channel. Fourth case is similar to the first one. Magnitude of the necessary DC current in order to keep the swimmers initial position (which is negative y -side of the channel) and overcome traction forces is 1.5 times the magnitude of AC current.

Min. c	Direction	Start	Finish
1.5	←		
5	→		
2	←		
1.5	→		

Figure 7.8 Some scenarios and the minimum magnetic field force to be applied to maintain the initial lateral position with a magnetic force against traction force or to change the lateral position of the micro swimmer by applying a reverse magnetic force. “Min.c” refers to the ratio between magnitudes of DC current and sinusoidal current. “Start” and “Finish” refer to the initial and final position of the magnetic swimmer, respectively.

When the frequency is equal to 1 Hz, fluid forces are smaller, the traction force is larger and lift force is smaller compared to the case where frequency equals 2 Hz. When the frequency is equal to 3 Hz, fluid forces are dominant over the traction forces with the help of the larger lift force. For the case in which the rotational frequency is equal to 2 Hz, resultant lift force is more than the one occurs at 1 Hz, thus traction is not as dominant. In addition, resultant fluid forces are not as effective as the ones at 3 Hz, thus swimmer does not change its position. As a result, at 2 Hz, with a 15% duty cycle, swimmer's lateral position is changed by applying DC magnetic fields. The dimensional parameters of the helical tail and magnetic head are significant due to which resultant forces change, thus navigation parameters can be affected. The parameters of this study is valid only for a robot having the same dimensional parameters as the one represented here, however, with the appropriate parameter setting, lateral positions of magnetic helical swimmers can be changed by applied DC magnetic fields.

7.3 Sensing

7.3.1 Methodology

Medical procedures such as opening clogged arteries or targeted drug delivery are potential applications for helical micro swimmers. It is important to detect the position of micro swimmer once it is injected a living organism, in order to perform controlled navigation accurately. Helical swimmers used in experimental studies explained in this thesis contain a permanent magnet as in similar artificial swimmers proposed in literature [3, 20, 105, 106], thus magnetic field sensing is an applicable method for aforementioned applications.

The experimental setup consists of electromagnetic coil pairs explained in Chapter 6 is used for sensing experiments. In order to measure the magnetic field change, Hall-effect sensors are chosen with an interface kit connected to the PC via USB cable to read the measured data (Figure 7.9). Hall-effect sensors measures at every 30 millisecond and a Visual Basic code is used to record the data measured during the experiments.

Hall-effect magnetic sensors are made smaller in size for experiments. Two sensors are placed next to each other. A helical swimmer having a radially magnetized cylindrical magnet head is injected into a glycerol-filled glass channel which is placed on the sensors (Figure 7.10).

7.3.2 Results

Experimental results are presented in Figure 7.11 with respect to time. Initial measured value of Hall-effects sensor no.1 and sensor no.2 are $8 \cdot 10^{-4}$ T and $3 \cdot 10^{-4}$ T, respectively. When $t = 50$ s, electromagnetic coil pairs are turned on with a frequency of 4 Hz. Sinusoidal magnetic field values indicate that positive and negative current is supplied to the electromagnetic coil pairs to generate a rotating magnetic field. Change in magnetic field values are first observed for the sensor no.2 around $t = 80$ s as swimmer moves forward and passes sensor no. 2. Around $t = 95$ s the system is turned off for a short time and turned on with -8 Hz, thus swimmer moves backward and passes from sensor no.2 for the second time, where a second peak is observed.

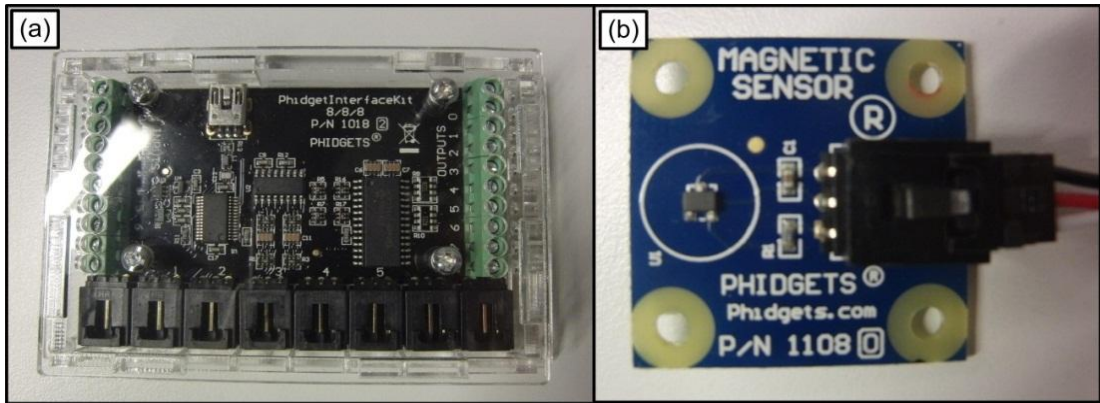


Figure 7.9 (a) Phidget Interface Kit 8/8/8 board (b) Phidget 1108 Hall-effect magnetic sensor

As swimmer gets away from sensor no.2 and moves closer to sensor no.1, the change in magnetic field strength cannot be detected until the swimmer is just next to the Hall-effect sensors. The change in measured data starts approximately 10 seconds before measuring the maximum change, which is not sufficient to detect the exact place of the swimmer between two sensors places with 13 mm distance. Second peak that sensor no.1 measures, is due to the swimmer's motion in reverse direction. Same procedure is repeated with 8 Hz rotational frequency between $t = 175$ s and $t = 270$ s. According to the results, swimmer has a higher velocity when rotating with 8 Hz than with 5 Hz, thus, Hall-effect sensors can also be used for velocity measurements of robots swimming in channels.

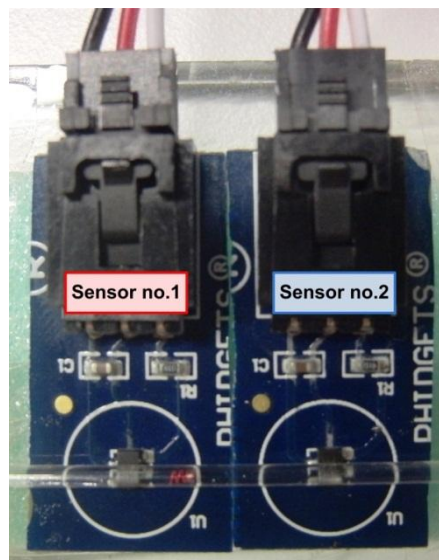


Figure 7.10 Magnetic helical swimmer is placed inside a glycerol-filled glass channel which is placed onto the Hall-effect magnetic sensors.

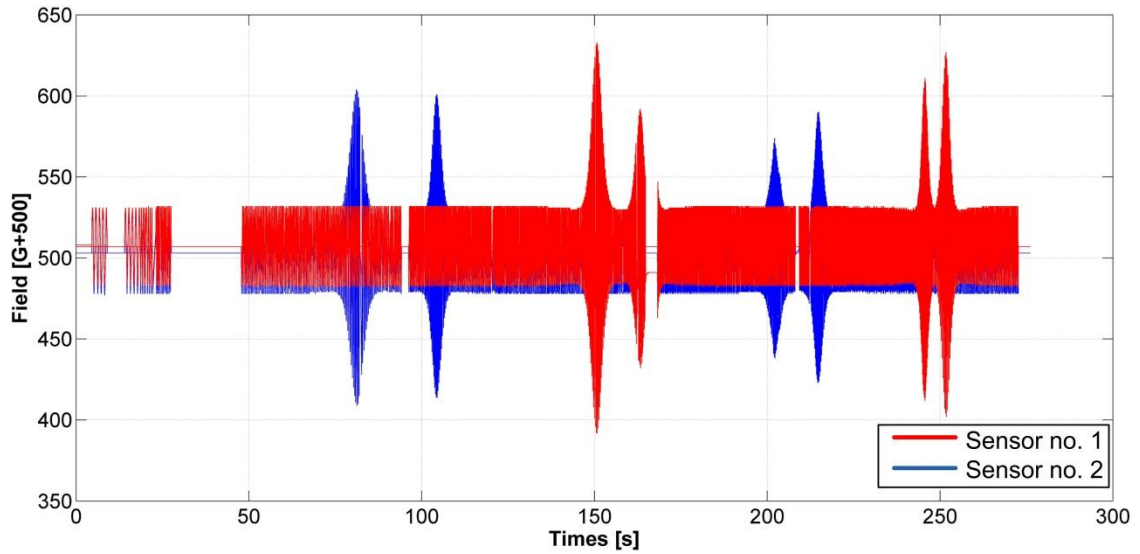


Figure 7.11 Magnetic field values with respect to time obtained from Hall-effect sensors

7.4 Discussion

Sensing of magnetic micro swimmers is an important topic to detect, control and navigate them inside channels precisely. Hall-effect sensors are used for magnetic field measurements in the experiments and it is demonstrated that the magnetic field can be measured by Hall-effect sensors as well as the magnetic swimmers can be detected while traveling close to them.

Navigation of helical swimmers inside rectangular channels is demonstrated by using the direction and the frequency of the rotating magnetic field as controls. The swimmer is navigated through Y-shaped and T-shaped channels with the help of a radially magnetized permanent magnet head and by changing the rotation axis of the externally applied magnetic field. In literature, most of the experimental works on swimming helical micro robots use three pairs of electromagnetic coils to navigate swimmers on a plane or in a volume by means of changing the direction of externally applied rotating magnetic field. In addition to the direction control achieved by changing the external magnetic field direction, another mechanism is used to change the swimming direction of swimmers on a plane. It is observed that due to traction forces, magnetic swimmer exhibits a rolling motion at lower frequencies, thus lateral motion takes place in addition to the forward motion. Helical swimmer is driven to the desired place and stopped at a desired location inside Y- and T-shaped channels. It is

demonstrated that possible obstacles inside channels and on the way of swimming robots can be negotiated inside rectangular channels.

A demonstration of changing lateral positions of magnetic helical swimmers is presented with applied DC magnetic fields introduced by a square waveform field with a defined duty cycle. By adjusting the parameters such as duty cycle and magnitude of DC magnetic field strength, it is possible to overcome traction of fluid forces and change the lateral position of magnetic helical swimmers.

8 CONCLUSION

Recent improvements on the micro-electro-mechanical-systems (MEMS) give the possibility to accomplish a great number of purposes, particularly in the areas of micro-fluidic, biomedical and chemical applications. The idea of developing micro swimming tools to perform minimally invasive surgical operations, such as diagnosis, targeted therapy, drug delivery and removing material from human body, makes micro-fluidics an interesting field among these applications. Researches about micro robot development and characterization became popular particularly in the last decade and it has been understood that micro robots have the potential to dramatically change many aspects of medicine by navigating inside the blood vessels or other channels in body to perform targeted diagnosis and therapy [1]. There are already a number of research groups working on the motion of bacteria and bio-inspired swimming machines in different environments such as fluid filled pools or near plane boundaries. However, in-channel behavior of these future surgical tools is still an area to be investigated in detail.

This thesis focuses on the in-channel swimming behavior of bio-inspired and artificial swimmers with helical tails inside viscous fluid filled channels in order to point out the differences from unbounded swimming and the points to be considered in designing micro swimmers and developing their control algorithms.

Experimental and computational fluid dynamics (CFD) studies are performed using bio-inspired two link cm-scale swimmers with helical tails in cylindrical channel are presented in Chapter 4. In this chapter, a CFD model is developed, validated with the experiments and used to study effects of the radial position of the robots as well as the wavelength and wave amplitude of the helical tails on the swimming speed, efficiency and forces acting on the body inside circular channels. Radial position of the robot is very important in the hydrodynamic analysis of in-channel swimming: first, the radial position of the robot can be controlled, for example, by magnetic forces albeit crudely when necessary; and second, in cases when the radial position cannot be controlled and governed by other forces acting on the robot, its effects need to be

understood well and incorporated in simple hydrodynamic relationships, such as the resistive force theory [23], in analytical models that incorporate all the forces acting on the robot, e.g. as in [52]. Contact forces arise when swimmer touches the rigid cylindrical wall is neglected in this study, since they produce a sudden impact and do not affect the swimming behavior as observed in experiments; neither tails of the robots stop rotating, nor an irregularity in the forward velocity is observed. Experiments are conducted with a bio-inspired cm-scale robot inside a circular channel filled with a silicone oil to mimic the low Reynolds number swimming conditions of small scale organisms [89]. The numerical model is based on the solution of three-dimensional Stokes equations subject to no-slip boundary conditions on the body and the tail of the robot and on channel walls as widely used in earlier/similar studies [7, 38, 51, 54]. Our approach is valid for scales greater than about 100 nm where the continuum hypothesis remains valid and no-slip boundary conditions hold. Simulations results for robots swimming near the wall agree well with experimental results, where the robots swim very close to the channel wall. In addition, CFD simulation results show that bio-inspired swimming robots swim faster near the wall than at the center and there is an optimal wave number value that robots reach higher swimming speeds. Moreover, up to 25% increase in efficiency is observed for robots traveling near the wall compared to the robots traveling at the center of the channel.

Artificial one link mm-scale magnetic swimmers with helical tails are used to perform experiments inside fluid-filled cylindrical channels which are presented in Chapter 5. Swimming experiments of mm-sized micro robots in glycerol and water-filled mini channels that are actuated by a rotating external magnetic field generated by two pairs of counter facing electromagnetic coils are presented. Experiments are carried out for two swimming micro robots which consist of heads made of permanent magnets and rigid helical tails of different dimensions, which simulate micro-fluidic regime since the same flow conditions as micro-scale rotation arise when they are in glycerol-filled mini channels. Moreover, a 6-dof time-dependent hydrodynamic model is built based on RFT including: a novel technique to implement cylindrical channel effects, and magnetic step-out frequency phenomena. Experimental results are used to validate the proposed hydrodynamic model with appropriate tuning of body resistance coefficients due to irregular shapes of the magnetic heads and the overall flow conditions that differ from simple viscous drag on the body, which is commonly used

to obtain analytical body resistance coefficients. Experiments performed with one-link magnetic helical swimmers confirmed that the motion along the channel depends on the actuation frequency. Proposed RFT-based hydrodynamic model predicts the nonlinear decrease in forward velocity after step-out frequency as well as the linear relationship between actuation frequency and time-averaged forward velocity; addressing magnetization misalignment, rotational misalignment and wall effects.

In addition to the experiments and theoretical studies, Chapter 5 includes CFD simulations of the artificial one link swimmer and visualization of the flow inside the cylindrical channel using micro-PIV. Simulation-based analysis of the flow field induced by the one-link swimmer inside a circular channel is performed to calculate hydrodynamic forces and torques acting on the swimmer and the swimming efficiency as a function of the wavelength and amplitude of the helical tail and the radial position of the swimmer. A three-dimensional steady-state CFD model is developed and solved with the commercial finite-element software COMSOL Multiphysics [91]. Furthermore, micro-Particle Image Velocimetry (micro-PIV) method is used to visualize resultant flow fields due to the rotation of helical micro swimmers inside cylindrical channels for different rotational frequencies. CFD simulation results show that one-link swimmers travel faster near the wall than at the center of the channel and there is an optimal wave number where efficiency reaches its maximum value. Forces calculated from CFD simulations showed that swimmer is pushed sideways during its forward motion due to traction force. In addition, torque in \mathbf{z} -direction depends on the tail geometry which also alters the position of the center of mass. Micro-PIV experiments are performed to visualize the flow fields and it is observed that rotation of the robot causes a rotating fluid motion.

In the experiments performed using helical micro robots near plane boundaries, it is observed that two motion mechanisms are used for forward and lateral motion, which are explained in Chapter 6. Experiments are performed using helical magnetic micro swimmers inside rectangular channels on rough and smooth surfaces and at different angular velocities to study the effects of surface roughness and rotation frequency on the forward velocity. Micro robots are placed inside glycerol-filled rectangular channels move forward due to the rotation of helical tails in the direction of helical axis and move laterally by rolling due to the wall traction. Moreover, high and low frequency behavior of micro robots inside rectangular channel differs due to the resultant flow fields. In CFD models, a viscous fluid layer is proposed to simulate the wall and

simulations are validated with experiments. Calculated translational and angular velocities are used to predict the position and orientation of the micro swimmers inside rectangular channels. CFD simulations show that at low frequencies swimmer is under the effect of traction forces, however at high frequencies fluid forces are dominant.

In the last chapter, experiments on magnetic sensing and controlled navigation of magnetic helical swimmers are investigated to understand how magnetic micro swimmers can be controlled in conduits. Controlled navigation of magnetic swimmers are performed inside channels and channel networks by taking advantage of motion mechanism and by taking rotation frequency, current supplied to the electromagnetic coils and direction of magnetic field as control inputs. Lateral position change of magnetic helical swimmers inside rectangular channels is demonstrated by applying DC magnetic fields introduced as a square waveform field with a defined duty-cycle. Last but not least, Hall-effect sensors are used to predict the position of micro swimmer inside channel by measuring magnetic field strength.

8.1 Contributions

Design and control of micro-robots for in vivo medical applications can benefit greatly from the results and detailed analysis presented in this thesis. First of all, in-channel experiments performed with bio-inspired and artificial swimmers indicates that proximity of the micro robots to the channel boundaries affects the forward swimming speed. In addition characterization studies showed the dependencies of swimming parameters such as translational and angular velocities and efficiencies on the geometric parameters of helical tails such as wavelength and number of waves of the helical tail.

CFD is a useful tool that gives point-wise velocity distribution in the flow and the complete stress tensor on the boundaries, which are difficult to obtain directly by means of experiments. The three-dimensional time-independent CFD-models governed by the Stokes flow, which is valid for low Reynolds number regime valid for small length scales, are used to analyze the flow field for the flow inside channels due to the motion of two-link and one-link swimmers with helical tails. Validation of CFD models are performed by macro and micro scale experiments.

In experiments performed using magnetic micro swimmers, the linear

relationship between the actuation frequency of the magnetic field and the forward velocity of the micro robot is observed up to step-out frequency, after which forward velocity decreases nonlinearly with increasing actuation frequency as also presented in literature. However, effect of surface roughness studied in this thesis points out that surface roughness is a swimming parameter which changes the motion of the micro robots.

Motion mechanism of micro robots observed in experiments is a finding was not reported in literature. Experiments showed that motion mechanisms of micro robots, which are moving forward and rolling sideways, can be used to overcome obstacles inside channels.

The relationship between forward velocity and angular velocity of an unbounded micro swimmer is well understood, however, the relationship between the resultant flow fields inside channels occur due to the rotation and the motion of micro robots has not yet studied. Effect of the flow field on the motion of micro robots at higher frequency values is investigated by experiments and CFD simulations and flow fields inside channels are visualized using micro-PIV system.

Lastly, proposed magnetic control method provides to change the lateral position of the micro robots inside channels as well as to control and navigate micro robots inside channel networks.

8.2 Future Work

In this thesis, in-channel swimming behavior of micro robots is investigated using experiments, theoretical models, CFD simulations and micro-PIV experiments. Although the contributions of this thesis will be important in designing micro robots and developing control algorithms, there are still a number of questions to be answered to use micro swimming robots as surgical tools.

The micro swimming robots are planned to be used inside living bodies, thus materials that will be used to manufacture micro robots are important. Bio-compatible or bio-degradable materials can be studied in designing micro robots considering the application field. It is known that human body shows different reaction mechanism to foreign creatures and micro robots need to stay safe while performing their tasks. In addition, design of micro robots according to the application area is important. Micro

robots are planned to be used in many different surgical operations, such as targeted drug delivery, biopsy or opening clogged arteries, and each requires certain capabilities to achieve the given tasks.

In the experiments performed in this thesis, the fluid inside channels is still, however, blood has a flow velocity which differs according to the veins. It is important to perform experiments inside channels having a fluid flow and navigate micro robots with or against the fluid flow and study the effects on the motion of the micro robots.

The veins or arteries inside human body are not perfectly cylindrical and are not rigid. First, behavior of micro robots inside flexible channels or inside channels with variable cross-sections should be investigated. Second, micro robots with flexible tails can be studied for specific applications such as drug delivery, for their capability to proceed forward in narrow channels.

The experiments performed in rectangular channels showed the importance of the surface roughness on the swimming characteristics of the helical one-link swimmers. More investigations on the effects of surface roughness are necessary to build accurate and precise control strategies for swimmers moving inside channels with different surface characteristics.

Swimming in nanometer scales, gravitational effects, close contact with channel walls and non-Newtonian behavior of bodily fluids are outside the scope of this work. Fully coupled solution of Stokes equations with those limitations remains a challenge.

9 REFERENCES

- [1] B. J. Nelson, I. K. Kaliakatsos and J. J. Abbott, "Microrobots for Minimally Invasive Medicine," *Annual Reviews of Biomedical Engineering*, vol. 12, pp. 55-85, August 2010.
- [2] L. Zhang, J. Abbott, L. Dong, K. Peyer, B. Kratochvil, H. Zhang, C. Bergeles and B. Nelson, "Characterization of the Swimming Properties of Artificial Bacterial Flagella," *Nano Letters*, vol. 9, no. 10, pp. 3663-3667, 2009.
- [3] A. Ghosh and P. Fischer, "Controlled Propulsion of Artificial Magnetic Nanostructured Propellers," *Nano Letters*, vol. 9, no. 6, 2009.
- [4] S. Martel, "Collective Methods of Propulsion and Steering for Untethered Microscale Nanorobots Navigating in the Human Vacular Network," *J. Mech. Eng. Science*, pp. 1505-1513, 2010.
- [5] J. Edd, S. Payen, B. Rubinsky, M. Stoller and M. Sitti, "Biomimetic Propulsion for a Swimming Surgical Micro-Robot," in *Proceedings of the International Conference on Intelligent Robots and Systems*, Las Vegas, USA, 2003.
- [6] B. Behkam and M. Sitti, "Design Methodology for Biomimetic Propulsion of Miniature Swimming Robots," *Journal of Dynamic Systems, Measurement, and Control*, vol. 123, pp. 36-43, 2006.
- [7] E. M. Purcell, "Life at Low Reynolds Number," *American Journal of Physics*, vol. 45, no. 1, pp. 3-11, 1976.
- [8] J. P. Armitage and R. M. Macnab, "Unidirectional, intermittent rotation of the flagellum of *Rhodobacter sphaeroides*," *Journal of Bacteriology*, vol. 169, no. 2, pp. 514-518, 1987.
- [9] T. Atsumi, Y. Maekawa, T. Yamada, I. Kawagishi, Y. Imae and M. Homma, "Effect of viscosity on swimming by the lateral and polar flagella of *Vibrio alginolytius*," *Journal of Bacteriology*, vol. 178, no. 16, pp. 5024-5026, 1996.
- [10] H. C. Berg, *Random walks in biology*, Princeton: Princeton University Press, 1993.
- [11] W. R. DiLuzio, L. Turner, M. Mayer, P. Garstecki, D. B. Weibel, H. C. Berg and G. M. Whitesides, "*Escherichia coli* swim on the right-hand side," *Nature*, vol 435, no. 30, pp. 1271-4, 2005.

- [12] J. J. Abbott, K. E. Peyer, M. C. Lagomarsino, L. Zhang, L. Dong, I. K. Kaliakatsos and B. J. Nelson, "How Should Microrobots Swim?," *The International Journal of Robotics Research*, vol. 28, no. 11-12, pp. 1434-1447, November/December 2009.
- [13] B. Watson, J. Friend and L. Yeo, "Modeling and testing of a piezoelectric ultrasonic micro-motor suitable for in vivo micro-robotic applications," *Journal of Micromechanics and Microengineering*, vol. 20, pp. 115018-115034, 2010.
- [14] W. Gao, S. Sattayasamitsathit, K. M. Manesh, D. Weihs and J. Wang, "Magnetically powered flexible metal nanowire motors," *J. Am. Chem. Soc.*, vol. 132, pp. 14403-14405, 2010.
- [15] T. S. Yu, E. Lauga and A. E. Hosoi, "Experimental investigations of elastic tail propulsion at low Reynolds number," *Physics of Fluids*, vol. 18, p. 091701, 2006.
- [16] B. Behkam and M. Sitti, "E.Coli Inspired Propulsion For Swimming Microrobots," in *Proceedings of IMECE'04 International Mechanical Engineering Conference and R&D Exposition*, Anaheim, CA, 2004
- [17] T. Honda, K. I. Arai and K. Ishiyama, "Micro swimming mechanisms propelled by external magnetic fields," *IEEE Transactions on Magnetics*, vol. 32, no. 5, pp. 5085-5087, September 1996.
- [18] S. J. Lighthill, "Mathematical Biofluidynamics," *Society for Industrial and Applied Mathematics*, 1975.
- [19] A. W. Mahoney, N. D. Nelson, E. M. Parsons and J. J. Abbott, "Non-ideal behaviors of magnetically driven screws in soft tissue," *IEEE/RSJ Intelligent Robots and Systems (IROS) 2012*, Vilamoura, 2012.
- [20] L. Zhang, J. J. Abbott, L. Dong, B. E. Kratochvil, D. Bell and B. J. Nelson, "Artificial bacterial flagella: fabrication and magnetic control," *Applied Physics Letters*, vol. 94, pp. 064107-13, February 2009.
- [21] N. Coq, O. duRoure, J. Marhelot, D. Bartolo ve M. Fermigier, "Rotational dynamics of a soft filament: Wrapping transition and propulsive forces," *Physics of Fluids*, vol. 20, p. 051703, 2008.
- [22] B. Chen, S. Jiang, Y. Liu, P. Yang and S. Chen, "Research on the Kinematic Properties of Sperm-Like Swimming Micro Robot," *Journal of Bionic Engineering*, vol. 7, pp. S123-S129, 2010.
- [23] M. J. Kim, J. C. Bird, A. J. Van Parys, K. S. Breuer and T. R. Powers, "A macroscopic scale model of bacterial flagellar bundling," *PNAS*, vol. 100, no. 26, pp. 15481-15485, December 2003.
- [24] M. S. Sakar, C. Lee and E. P. Arratia, "Flagellar Dynamics in Viscous Fluids," *Phys. of Fluids*, vol. 21, p. 09107, 2009.
- [25] S. Martel, O. Feldoul, J. -B. Mathieu, A. Chanu, S. Tamaz, M. Mohammadi, M. Mankiewicz and N. Tabatabaei, "MRI-based medical nanorobotic platform for the control of magnetic nanoparticles and flagellated bacteria for target interventions in human capillaries," *International Journal of Robotics Research*, vol. 28, pp. 1169-1182, 2009.

- [26] C. Yu, J. Kim, H. Choi, J. Choi, S. Jeong, K. Cha, J. Park and S. Park, "Novel electromagnetic actuation system for three-dimensional locomotion and drilling of intravascular microrobot," *Sensors and Actuators A*, vol. 161, pp. 297-304, 2010.
- [27] H. Choi, K. Cha, J. Choi, S. Jeong, S. Jeon, G. Jang, J. Park and S. Park, "EMA system with gradient and uniform saddle coils for 3D locomotion of microrobot," *Sensors and Actuators A*, vol. 163, pp. 410-417, 2010.
- [28] M. P. Kummer, J. J. Abbott, B. E. Kratochvil, R. Borer, A. Sengul and B. J. Nelson, "OctoMag: An electromagnetic system for 5-DOF wireless micromanipulation," *IEEE Trans. on Robotics*, vol. 26, no. 6, pp. 1006-1017, 2010.
- [29] T. W. R. Fountain, P. V. Kailat and J. J. Abbott, "Wireless control of magnetic helical microrobots using a rotating permanent magnet manipulator," *IEEE International Conference on Robotics and Automation*, 2010.
- [30] S. H. Kim, S. Hashi and K. Ishiyama, "Methodology of dynamic actuation for flexible actuator and biomimetic robotics application," *IEEE Trans. on Magnetics*, vol. 46, no. 6, pp. 1366-1369, 2010.
- [31] T. Okada, S. Guo and Y. Yamauchi, "A wireless microrobot with 3DOFs in pipe for medical applications," *Proc. of the IEEE/ICME Int. Conf. on Complex Medical Engineering*, China, 2011.
- [32] T. Okada, S. Guo and Y. Yamauchi, "Design of a wireless hybrid in-pipe microrobot with 3DOFs," *Proc. of the 2011 IEEE Int. Conf. on Mechatronics and Automation*, China, 2011.
- [33] Q. Pan, S. Huo and T. Okada, "A novel hybrid wireless microrobot," *Int. J. Mechatronics and Automation*, vol. 1, no. 1, pp. 60-69, 2011.
- [34] S. Sudo, S. Segawa and T. Honda, "Magnetic swimming mechanism in a viscous liquid," *Journal of Intelligent Material Systems and Structures*, vol. 17, pp. 729-736, August-September 2006.
- [35] R. Dreyfus, J. Baudry, M. L. Roper, M. Fermigier, H. A. Stone and J. Bibette, "Microscopic artificial swimmers," *Nature*, vol. 437, p. 862/865, October 2005.
- [36] S. Tottori, L. Zhang, F. Qui, K. K. Krawyck, A. Franco-Obregon and B. J. Nelson, "Magnetic helical micromachines: fabrication, controlled swimming and cargo transport," *Advanced Materials*, vol. 24, pp. 811-816, 2012.
- [37] S. Schuerle, S. Pane, E. Pellicer, J. Sort, M. D. Baro and B. J. Nelson, "Helical and tubular lipid microstructures that are electroless-coated with CoNiReP for wireless magnetic manipulation," *Small*, vol. 8, no. 10, pp. 1498-1502, 2012.
- [38] E. Lauga and T. R. Powers, "The hydrodynamics of swimming microorganisms," *Reports on Progress in Physics*, vol. 72, pp. 529-540, 2009.

- [39] S. G. I. Taylor, "Analysis of the Swimming of Microscopic Organisms," *Proc.R. Soc. Lond.*, vol. 209(A), pp. 447-461, 1951.
- [40] J. Gray and G. J. Hancock, "The propulsion of sea-urchin spermatozoa," *Journal in Experimental Biology*, vol. 32, pp. 802-814, 1955.
- [41] C. Brennen and W. H., "Fluid Mechanics of Propulsion by Cilia and Flagella," *Annual Review of Fluid Mechanics*, vol. 9, pp. 339-398, 1977.
- [42] J. J. Higdon, "The hydrodynamics of flagellar propulsion: helical waves," *Journal of Fluid Mechanics*, vol. 94, no. 2, pp. 331-351, 1979.
- [43] C. H. Wiggins and R. E. Goldstein, "Flexive and propulsive dynamics of elastica at low Reynolds number," *Physical Review Letters*, vol. 80, no. 17, pp. 3879-3882, 1998.
- [44] M. Manghi, X. Schlagnerger and R. R. Netz, "Propulsion with a rotating elastic nanorod," *Physical Review Letters*, vol. 96, p. 068101, 2006.
- [45] E. E. Keaveny and M. R. Maxey, "Spiral swimming of an artificial microswimmer," *Journal of Fluid Mechanics*, vol. 598, pp. 293-319, 2008.
- [46] O. Raz and A. M. Leshansky, "Efficiency of cargo towing by a microswimmer," *Physical Review E*, vol. 77, p. 055305, 2008.
- [47] D. F. Katz, "On the propulsion of micro-organisms near solid boundaries," *Journal of Fluid Mechanics*, vol. 64, pp. 33-49, 1974.
- [48] D. Katz, J. Blake and S. Paveri-Fontana, "On the Movement of Slender Bodies Near Plane Boundaries at Low Reynolds Number," *Journal of Fluid Mechanics*, vol. 72, pp. 529-540, 1975.
- [49] J. R. Blake, "Singularities of viscous flow," *J. Eng. Math.*, vol. 8, no. 2, pp. 113-124, 1974.
- [50] E. Lauga, W. DiLuzio, G. Whitesides and H. Stone, "Swimming in Circles: Motion of Bacteria Near Solid Boundaries," *Biophysics Journal*, vol. 90, pp. 400-412, 2006.
- [51] B. U. Felderhof, "Swimming at low Reynolds number of a cylindrical body in a circular tube," *Physics of Fluids*, vol. 22, pp. 1136041-1136046, 2010.
- [52] L. Arcese, M. Fruchard and A. Ferreira, "Endovascular magnetically guided robots: navigation modeling and optimization," *IEEE Trans. on Biomedical Engineering*, vol. 54, no. 5, pp. 977-987, December 2011.
- [53] T. Goto, S. Masuda, K. Terada and Y. Takano, "Comparison between Observation and boundary Element Analysis of BacteriumSwimming Motion," *JSME International Journal*, vol. 44, no. 4, pp. 958-963, 2001.
- [54] M. Ramia, D. L. Tullock and N. Phan-Thien, "The role of hydrodynamic interaction in the locomotion of microorganisms," *Biophysical Journal*, vol. 65, no. 2, pp. 775-778, 1993.
- [55] E. Lauga, M. P. Brenner and H. A. Stone, "Microfluidics: The No-Slip Boundary Condition," *Handbook of Experimental Fluid Dynamics*, C. Tropea, A. Yarin and J. F. Foss, Dü, Springer, 2007.

- [56] J. Eijkel, "Liquid slip in micro- and nanofluidics: recent research and its possible implications," *Lab on a Chip*, vol. 7, pp. 299-301, 2007.
- [57] Y. Zhu and S. Granick, "Limits of the hydrodynamic no-slip boundary condition," *Physical Review Letters*, vol. 99, no. 10, p. 106102(4), 2002.
- [58] D. C. Tretheway and C. D. Meinhart, "Apparent fluid slip at hydrophobic microchannel walls," *Physics of Fluids*, vol. 14, no. 3, pp. L9-12, March 2002.
- [59] C. -H. Choi, K. J. A. Westin and K. S. Breuer, "Apparent fluid slip in hydrophilic and hydrophobic microchannels," *Physics of Fluids*, vol. 15, no. 10, pp. 2897-2902, October 2003.
- [60] C. Cottin-Bizonne, S. Jurine, J. Baudry, J. Crassous, F. Restagno and E. Charlaix, "Nanorheology: an investigation of the boundary condition at hydrophobic and hydrophilic interfaces," *The European Physical Journal E*, vol. 9, pp. 47-53, 2002.
- [61] C. Neto, R. Evans, E. Bonaccorso, H. -J. Btt and V. S. J. Craig, "Boundary slip in Newtonian liquids: a review of experimental studies," *Reports on Progress in Physics*, pp. 2859-, 2005.
- [62] D. R. Absolom and L. A. C. G. Hawthorn, "Endothelialization of polymer surfaces," *Journal of Biomedical Materials Research*, vol. 22, pp. 271-285, 1988.
- [63] P. B. van Wachem, T. Beugeling, J. Feijen, A. Bantjes, J. P. Detmers and W. G. van Aken, "Interaction of cultured human endothelial cells with polymeric surfaces of different wettabilities," *Biomaterials*, vol. 6, pp. 403-408, 1985.
- [64] C. D. F. Honig and W. A. Ducker, "No-slip hydrodynamic boundary condition for hydrophilic particles," *Physical Review Letters*, vol. 98, p. 028305, January 2007.
- [65] G. Karniadakis, A. Beskok and N. Aluru, *Microflows and Nanoflows: Fundamentals and Simulation*, Springer, 2005.
- [66] M. C. van Loosdrecht, J. Lyklema, W. Norde, G. Schraa and A. J. Zehnder, "The role of bacterial cell wall hydrophobicity in adhesion," *Applied and Environmental Microbiology*, vol. 53, no. 8, pp. 1893-1897, August 1987
- [67] D. Daffonchio, J. Thaveesri and W. Verstraete, "Contact angle measurement and cell hydrophobicity of granular sludge from upflow anaerobic sludge bed reactors," *Applied and Environmental Microbiology*, vol. 61, no. 10, pp. 3676-3680, October 1995.
- [68] D. J. Smith, E. A. Gaffney, J. R. Blake and J. C. Kirkman-Brown, "Human sperm accumulation near surfaces: a simulation study," *J. Fluid Mech.*, vol. 621, pp. 289-320, 2009.
- [69] H. Shum, E. A. Gaffney and S. D. J., "Modeling bacterial behaviour close to no-slip plane boundary: the influence of bacterial geometry," *Proceedings of Royal Society A*, vol. 466, pp. 1725-1748, 2010.

- [70] R. W. Colman, V. J. Marder, A. W. Clowes, J. N. George and S. Z. Goldhaber, *Hemostasis and Thrombosis: Basic Principles and Clinical Practice*, Lippincott Williams and Wilkins, 2005.
- [71] B. Liu, T. R. Powers and K. S. Breuer, "Force-free swimming of a model helical flagellum in viscoelastic fluids," *PNAS*, vol. 108, no. 49, pp. 19516-19520, December 2011.
- [72] R. Adrian, "Particle-Imaging Techniques for Experimental Fluid Mechanics," *Ann. Rev. Fluid Mech.*, vol. 23, pp. 261-304, 1991.
- [73] R. J. Adrian, "Twenty Years of Particle Image Velocimetry," *Exp. in Fluids*, vol. 39, pp. 159-169, 2006.
- [74] H. Nasibov and S. Baytaroglu, "Recent advances in digital particle image velocimetry methods for flow motion analysis," *International Journal of Metrology and Quality Engineering*, vol. N 1, pp. 21-28, 2010.
- [75] E. G. Drucker and G. V. Lauder, "Experimental hydrodynamics of fish locomotion: functional insights from wake visualization," *Int. Comp. Biol.*, vol. 42, pp. 243-57, 2002.
- [76] F. E. Fish and G. V. Lauder, "Passive and Active Flow Control by Swimming Fishes and Mammals," *Annu. Rev. Fluid Mech.*, vol. 38, pp. 193-224, 2006.
- [77] G. V. Lauder and P. G. A. Madden, "Advances in comparative physiology from high-speed imaging animal and fluid motion," *Annu. Rev. Physiol.*, vol. 70, pp. 143-16, 2008.
- [78] C. Gurlek and B. Sahin, "Particle image velocimetry studies around a rectangular body close to a plane wall," *Flow Measurement and Instrumentation*, vol. 21, pp. 322-329, 2010.
- [79] C. Ozalp, A. Pinarbasi, M. S. Fakiler and B. Sahin, "PIV measurements of flow through a sudden contraction," *Flow Measurement and Instrumentation*, vol. 18, pp. 121-128, 2007.
- [80] J. G. Santiago, S. T. Wereley, C. D. Meinhart, D. J. Beebe and R. J. Adrian, "A particle image velocimetry system for microfluidics," *Experiments in Fluids*, vol. 25, pp. 316-319, 1998.
- [81] M. J. Kim, M. J. Kim, J. C. Bird, J. Park, T. R. Powers and K. S. Breuer, "Particle Image Velocimetry Experiments on a Macro-Scale Bacterial Flagellar Bundling," *Exp. in Fluids*, vol. 37, pp. 782-788, 2004.
- [82] M. M. Mielnik and L. R. Saetran, "Micro Particle Image Velocimetry - an overview," 2004.
- [83] B. Akselli, V. Ciftci, A. Kholmatov and H. Nasibov, "Experimental study of laminar flow in microchannels through micro-PIV measurements," in *International Metrology Conference, CAFMET*, Cairo, Egypt, 2010.
- [84] H. Nasibov, A. Kholmatov, B. Akselli and V. Ciftci, "Investigation of LED illuminated digital micro-particle-image velocimetry measurements," in *Interntional Metrology Conference CAFMET*, Cairo, Egypt, 2010.

- [85] R. Adrian, «Dynamic ranged of velocity and spatial resolution of particle image velocimetry,» *Meas. Sci. Technology*, vol. 8, pp. 1393-1398, 1997.
- [86] A. P. Berke, L. Turner, H. C. Berg and E. Lauga, “Hydrodynamic attraction of swimming microorganisms by surfaces,” *Physical Review Letters*, vol. 101, p. 038102, 2008.
- [87] D. Giacché, T. Ishikawa and T. Yamaguchi, “Hydrodynamic entrapment of bacteria swimming near a solid surface,” *Physical Review E*, vol. 85, p. 056309, 2010.
- [88] J. -B. Mathieu and S. Martel, “In vivo validation of a propulsion method for untethered medical microrobots using a clinical magnetic resonance imaging system,” *Proc. in IEEE/RSJ International Conference on Intelligent Robots and Systems*, 2007.
- [89] A. G. Erman, *Untethered bio-inspired helical swimmer in channels*, 2011.
- [90] A. G. Erman and S. Yesilyurt, “Swimming of onboard-powered autonomous robots in viscous fluid filled channels,” in *IEEE International Conference on Mechatronics (ICM2011)*, Istanbul, Turkey, 2011.
- [91] COMSOL-AB, "Comsol multiphysics modelling guide," COMSOL, Stockholm, 2012.
- [92] F. Z. Temel and S. Yesilyurt, “Simulation-based analysis of micro-robots swimming at the center and near the wall of circular channels,” *Microfluidics and Nanofluidics*, vol. 14, no. 1-2, pp. 287-298, January 2012.
- [93] G. K. Batchelor, *An Introduction to Fluid Dynamics*, Cambridge University Press, 2000.
- [94] H. Bruus, *Theoretical Microfluidics*, Oxford Master Series in Condensed Matter Physics, Oxford University Press, 2008.
- [95] M. Scherge and S. Gorb, *Biological Micro- and Nano-Tribology*, Springer, 2001.
- [96] F. Z. Temel, O. Erin, A. F. Tabak and S. Yesilyurt, “Bio-inspired micro robots swimming in channels,” *Proc. of the 13th Mechatronics Forum International Conference (Mechatronics 2012)*, Linz, Austria, 2012.
- [97] B. H. Happel J., *Low Reynolds number hydrodynamics with special applications to particulate media*, Hingham, MA: Kluwer Boston, Inc., 1983.
- [98] O. C. Zienkiewicz and R. L. Taylor, *The Finite Element Method: Its Basis and Fundamentals*, Elsevier, 2005.
- [99] S. J. Lighthill, “Flagellar hydrodynamics: the John von Neumann lecture,” *SIAM Review*, vol. 18, no. 2, pp. 161-230, April 1976.
- [100] C. Pawashe, S. Floyd and M. Sitti, “Modeling and experimental characterization of an untethered magnetic micro-robot,” *The International Journal of Robotics Research*, vol. 28, no. 8, pp. 1077-1094, August 2009.

- [101] D. Jiles, Introduction to Magnetism and Magnetic Materials, 2nd ed., London: Chapman & Hall, 1998.
- [102] A. F. Tabak and S. Yesilyurt, "Validated reduced order models for simulating trajectories of bio-inspired artificial micro-swimmers," *Proc. in ASME FEDSM-ICNMM2010*, 2010.
- [103] A. J. Hanson and H. Ma, "Visualizing flow with quaternion frames," *Proc. of the Conference on Visualization '94*, Washington D.C., 1994.
- [104] L. F. Shampine and M. K. Gordon, Computer Solution of Ordinary Differential Equations: the Initial Value Problem, San Francisco: W. H. Freeman, 1975.
- [105] J. -B. Mathieu and S. Martel, "Magnetic microparticle steering within the constraints of an MRI system: proof of concept of a novel targeting approach," *Biomedical Microdevices*, vol. 9, pp. 801-808, 2007.
- [106] L. Zhang, K. E. Peyer and B. J. Nelson, "Artificial bacterial flagella for micromanipulation," *Lab on a Chip*, vol. 10, no. 17, pp. 2203-2215, 2010.
- [107] Dantec Dynamics, Dynamic Studio Software Manual, 2011.